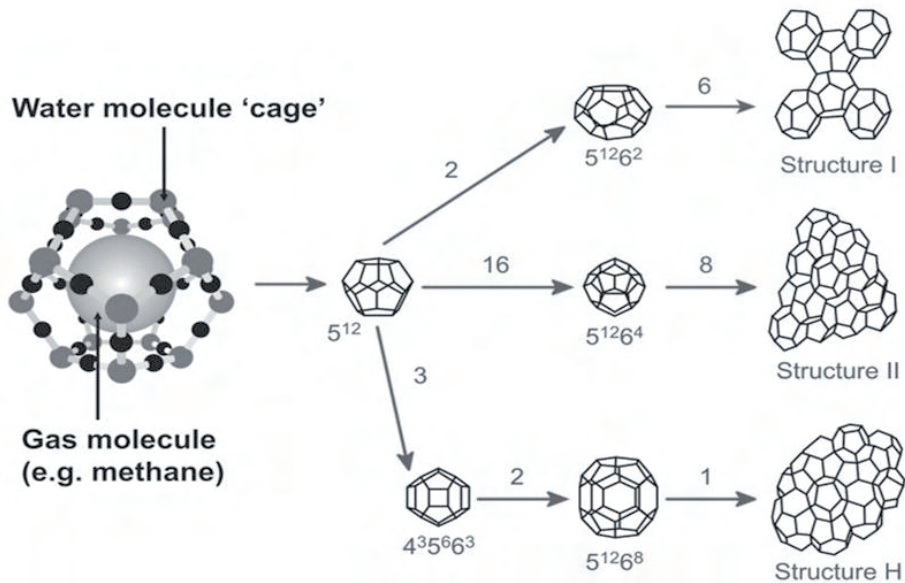


Experimental investigation and molecular simulation of gas hydrates



Lars Jensen
Ph.D. Thesis
2010

Experimental investigation and molecular simulation of gas hydrates

Lars Jensen
Ph.D. Thesis
2010

Copyright©: Lars Jensen
2010

Address: Center for Energy Resources Engineering
**Department of Chemical and
Biochemical Engineering
Technical University of Denmark**
Søltofts Plads, Building 229
DK-2800 Kgs. Lyngby
Denmark

Phone: +45 4525 2800

Fax: +45 4525 4588

Web: www.kt.dtu.dk

Print: **J&R Frydenberg A/S**
København
December 2010

ISBN: 978-87-92481-29-0

Preface

This thesis I have submitted as partial fulfillment of the requirements for a Ph.D. degree at the Technical University of Denmark. My thesis consists of 4 papers, 4 conference and workshop contributions and a detailed report (this work) covering all the work I have done during the study. I carried out most of the work at the Center for Energy Resources Engineering located in the Department of Chemical and Biochemical Engineering during the period 2007-2010. Part of the work I did at the Center for Hydrate Research at Colorado School of Mines where I spent 4 months as a visiting scholar during winter/spring 2009.

The work has been financed through a Ph.D. scholarship from the Technical University of Denmark and in part also by the Danish Research Council for Technology and Production Sciences through the project "Gas Hydrates - from Threat to Opportunity".

The topics covered in my thesis span from experimental investigation of gas hydrates to molecular simulation of hydrate systems. The diversity in the studied subjects is a result of pursuing my own ideas and goals and at the same time keeping an open mind to input and suggestions from outside.

During my Ph.D. study I have been in contact with quite a few people and each of them has contributed with invaluable knowledge and ideas making the study even more interesting. For this reason there are also a lot of people I would like to thank. First of all I would like to thank my two supervisors Nicolas von Solms and Kaj Thomsen for their useful guidance and especially for giving me the freedom to pursue my own ideas - This has been much appreciated.

I would like to thank Prof. Hans Ramløv from Roskilde University Center for supplying a range of the ice-structuring proteins used in my studies of kinetic hydrate

inhibition. From Unilever I would like to thank Deryck Cebula and Chris Sidebottom (former Unilever) for supplying samples of the ocean pout HPLC12 ice-structuring protein also used in these studies.

From Colorado School of Mines I would like to thank Profs. Dendy Sloan and Carolyn Koh for giving me the opportunity to spend four months at the Center for Hydrate Research. It was a great privilege to work with some of the best researchers in the field of gas hydrates. Thanks to Profs. Amadeu Sum and David Wu for supervising the molecular simulation project. I'm very happy that you suggested I look into this new, interesting and fast developing research area. I would also like to thank Scott Wierzchowski for taking his time, though being very busy working at Shell, helping me with the simulations. I would like to thank Jimmy Mulligan for helping me with the high pressure DSC experiments. Thanks to all the Hydrate Busters at the Center for Hydrate Research for making it such a wonderful and fun stay and in particular to Matthew Walsh who helped me with a lot of practicalities after arriving to Colorado School of Mines. Thanks for your great mood and humor. I'm glad that we are now not only dear colleagues but also good friends.

Finally I would like to thank my wife Theresa and our small daughter Johanne for your patience and for following me overseas to Colorado to experience new things in a time that had already been rich on experiences and challenges being a newly started family.

Kgs. Lyngby, August 2010



Lars Jensen

Summary

Gas hydrate formation in subsea transmission pipelines is the leading deepwater flow assurance problem and is listed as the major technical problem in offshore energy development. Traditionally the formation of gas hydrates in oil and gas pipelines has been prevented by injection of large amounts of antifreeze such as methanol or glycol. Alternatively the formation of gas hydrates can be controlled, using small amounts of polymeric compounds (kinetic inhibitors), which instead of inhibiting the formation thermodynamically work by slowing the formation rate (kinetics). However using kinetic hydrate inhibition requires a detailed knowledge of the nucleation and growth of gas hydrates and how these processes are influenced by pressure and temperature in relation to the phase equilibria and not least kinetic inhibitors.

In this thesis the phase equilibria, the nucleation and growth of gas hydrates have been investigated using experimental approaches and theoretical models. The purpose has been to make clear which physical parameters are especially important for the location of the phase equilibria and how the formation kinetics are influenced by the thermodynamic state of the system and the presence of kinetic inhibitors.

The phase equilibria of various hydrate forming systems were measured experimentally and calculated using Monte Carlo simulation; a molecular simulation tool which is very useful for studying the behavior and physical properties of complex fluid systems. The method has not been applied before to study phase equilibria of hydrate systems; however it is shown to be very useful for calculating the temperature and pressure dependence of the hydrate melting point, the hydrate equilibrium composition and the hydrate melting enthalpy. These results are encouraging since they suggest that molecular simulation may be suitable for predicting hydrate properties which are very difficult to access experimentally.

The results of the kinetic studies shows that the formation of gas hydrate is very similar to heterogeneous crystallization processes and that the nucleation period (induction time) can be prolonged significantly if kinetic inhibitors are present in the aqueous phase. This effect is mainly ascribed to the absorbance of inhibitor molecules on any impurities in the solution. This could for example be small dust particles (not the hydrate nuclei themselves) which cause the nucleation energy barrier to increase. In general the nucleation rate of structure I hydrate is much faster than for structure II hydrate; an effect which might be related to the higher pressures required to form structure I hydrate.

The growth studies of gas hydrates from pure water show that the growth rate is limited by the mass transfer of gas molecules from the gas phase to the aqueous solution. However where effective kinetic inhibitors are present the growth is (to begin with) controlled by intrinsic kinetics, i.e. by the hydrate surface reaction rate. This effect is ascribed to an effective coverage of the hydrate surface by adsorbed inhibitor molecules which decrease the hydrate surface area whereby the growth rate reduces. Although the growth rate during this period is very slow the kinetic inhibitors will eventually be overgrown by hydrate whereby the growth becomes mass transfer limited again.

Studies of how the nucleation and growth of gas hydrates are influenced by kinetic inhibitors include a class of biological molecules often referred to as antifreeze proteins. Antifreeze proteins are so named because they inhibit the nucleation and growth of ice in certain plants and animals living in cold environments, helping them to survive. The results of these studies show that antifreeze proteins are very effective kinetic hydrate inhibitors and in some cases even better than some of the synthetic inhibitors used in the oil industry today. Since antifreeze proteins are regarded as environmentally benign, as opposed to synthetic inhibitors, applying them as hydrate inhibitors can contribute to making the production of oil and gas greener. This is however only possible if the antifreeze proteins can be produced in large scale and at a price which is competitive.

Resumé

Gashydratdannelse i undersøiske transmissionslinjer udgør det største procestekniske problem under indvinding af olie og gas på store havdybder. Traditionelt forhindres gashydratdannelse i transmissionslinjerne ved injektion af store mængder af antifrostvæske, typisk metanol eller glykol. Alternativt kan gashydratdannelse hæmmes med små doser af polymerer (kinetiske inhibitorer), som i stedet for at forhindre dannelsen termodynamisk virker ved at sænke dannelseshastigheden (kinetikken). Anvendelse af kinetisk hydratinhibering kræver dog et indgående kendskab til kimdannelsen og væksten af gashydrater og hvorledes disse processer påvirkes af tryk og temperatur i forhold til faseligevægten og ikke mindst tilstedeværelsen af kinetiske inhibitorer.

I denne afhandling undersøges faseligevægten, kimdannelsen og væksten for forskellige hydratdannende systemer vha. eksperimentelle tilgangsvinkler og teoretiske modeller. Formålet er at afdække hvilke fysiske parametre, som er betydningsfulde for faseligevægtens beliggenhed, samt hvorledes dannelseskinetikken påvirkes af systemets termodynamiske tilstand og tilstedeværelsen af kinetiske inhibitorer.

Faseligevægten for forskellige hydratdannende systemer blev målt eksperimentelt og beregnet vha. Monte Carlo simulering; et værktøj, som er specielt anvendeligt til at studere fysiske egenskaber for komplekse molekylære systemer. Metoden har ikke tidligere været anvendt i ligevægtsstudier af gashydrater, men viser sig yderst anvendelig i beregningen af eksempelvis hydratsmeltepunktets temperatur- og trykafhængighed, hydratsammensætningen ved ligevægt og hydratets smeltevarme. Disse resultater er opløftende da molekylesimulering derved en mulig metode til at indhente informationer omkring gashydraters egenskaber, som ellers er svære eller umulige at måle eksperimentelt.

Resultaterne af kinetikstudierne viser at gashydratdannelsen har flere lighedspunkter med heterogene krystallisationsprocesser, samt at kimdannelsesperioden (induktionstiden) forlænges betydeligt ved tilstedeværelsen af kinetiske inhibitorer i vandfasen. Forlængelsen af induktionstiden skyldes at inhibitorerne adsorberer på overfladen af urenheder, som forefindes i systemet, eksempelvis små støvpartikler (dog ikke kimene selv), hvilket bevirker at energibarrieren for hydratudfældning hæves. Generelt viser studierne at dannelsen af struktur I hydrat er væsentlig hurtigere end dannelsen af struktur II hvilket kan skyldes at det kræver et væsentlig højere tryk at danne struktur I.

Vækststudierne af gashydrater i rene vandige opløsninger viser at væksthastigheden er begrænset af masseoverførslen af gasmolekyler fra gasfasen til den vandige opløsning. Tilstedeværelsen af kinetiske inhibitorer i vandfasen medfører dog at gashydratvæksten indledningsvis kontrolleres af reaktionshastigheden mellem gas og vand på hydratoverfladen. Dette er en konsekvens af at inhibitorerne adsorberer på overfladen af hydratet, hvorved hydratets overfladeareal mindskes og væksthastigheden sænkes. På trods af at væksthastigheden i denne periode er meget langsom vil inhibitorerne i sidste instans tildækkes helt med hydrat, hvorved væksten igen kontrolleres af overførslen af gas mellem de to faser.

I studierne af hvorledes kimdannelsen og væksten af gashydrater påvirkes af kinetiske inhibitorer indgår en gruppe af biologiske molekyler, der populært benævnes antifryseproteiner. Antifryseproteinerne udmærker sig ved at hæmme kimdannelsen og væksten af is i visse planter og dyr, som lever i kolde egne, og er dermed stærkt medvirkende til at sikre disse organismers overlevelse. Resultaterne af studierne her viser, at antifryseproteiner er særdeles effektive kinetiske inhibitorer og i visse tilfælde endnu bedre end de bedste syntetiske inhibitorer, som anvendes i olieindustrien i dag. Da antifryseproteinerne samtidig anses som miljøvenlige stoffer, til forskel fra de fleste syntetiske inhibitorer, kan deres anvendelse som kinetiske hydratinhibitorer bidrage til at gøre produktionen af olie og gas lidt grønnere. Dette kan dog kun lade sig gøre hvis antifryseproteinerne kan produceres i tilpas store mængder og til en pris, som er konkurrencedygtig.

Publications

Papers

1. Lars Jensen, Kaj Thomsen, Nicolas von Solms, Inhibition of structure I and II gas hydrates using synthetic and biological kinetic inhibitors, accepted in Energy Fuels.
2. Lars Jensen, Kaj Thomsen, Nicolas von Solms, Scott Wierzchowski, Matthew R. Walsh, Carolyn A. Koh, E. Dendy Sloan, David T. Wu, Amadeu K. Sum, Calculation of the liquid water-hydrate-methane vapor equilibria from molecular simulations, *J. Phys. Chem. B.* 114, 2010, 5775-5782.
3. Lars Jensen, Hans Ramløv, Kaj Thomsen, Nicolas von Solms, Inhibition of methane hydrate formation by ice-structuring proteins, *Ind. Eng. Chem. Res.* 49, 2010, 1486-1492.
4. Lars Jensen, Kaj Thomsen, Nicolas von Solms, Propane hydrate nucleation: Experimental investigation and correlation, *Chem. Eng. Sci.* 63, 2008, 3069-3080.

Papers 2, 3 and 4 which have already been published can be found in the appendices.

Conference Proceedings

1. Lars Jensen, Kaj Thomsen, Nicolas von Solms, Scott Wierzchowski, Matthew R. Walsh, Carolyn A. Koh, E. Dendy Sloan, David T. Wu, Amadeu K. Sum, The stability of methane hydrate from molecular simulation, Proceedings of properties and phase equilibria for product and process design, Suzhou, China, May 16-21 2010.
2. Lars Jensen, Kaj Thomsen, Nicolas von Solms, Scott Wierzchowski, Matthew R. Walsh, Carolyn A. Koh, E. Dendy Sloan, David T. Wu, Amadeu K. Sum, Monte Carlo simulation of the three-phase equilibria of water-hydrate-methane, CECAM/ACAM workshop on molecular simulation of clathrate hydrates, Dublin, 6-8 May 2010
3. Lars Jensen, Han Ramløv, Kaj Thomsen, Nicolas von Solms, Inhibition of gas hydrate formation by low-dosage, environmentally benign inhibitors, Proceedings of the 2nd annual gas processing symposium (ISBN: 987-0-444-53588-7), Doha, Qatar, January 9-11 2010.
4. Lars Jensen, Kaj Thomsen, Nicolas von Solms, Propane hydrate nucleation: Experimental investigation and correlation, 6th International Conference on Gas Hydrates, Vancouver, Canada, July 6-10 2008.

Abbreviations

AA	Anti agglomerants
AFP	Antifreeze protein
ALTA	Automated lag time apparatus
CAPEX	Capital expenditure
DSC	Differential scanning calometry
EPC	Electronic pressure controller
Erfc	Error function
FL	Frenkel & Ladd
GDI	Gibbs-Duhem integration
GROMACS	GRoningen MACHine for Chemical Simulations
ISP	Ice-structuring protein
KHI	Kinetic hydrate inhibitor
LDHI	Low-dosage hydrate inhibitor
L-H-V	Liquid-Hydrate-Vapor
LJ	Lennard-Jones
MC	Monte Carlo
MCHydrate	Monte Carlo Hydrate simulation
MD	Molecular Dynamics
MFC	Mass flow controller
MW	Molecular weight
NPT	Constant molecule number, pressure, temperature
NVT	Constant molecule number, volume, temperature
OF	Objective function
OPEX	Operating expenditure
OPLS	Optimized potentials for liquid simulations

PVCap	Polyvinylcaprolactam
PVP	Polyvinylpyrrolidone
Re _A	Agitation Reynolds number
RPM	Rotations per minute
SCP	Subcooling point
SGMC	Semigrand Monte Carlo
sI,sII,sH	Structure I, II and H
SLE	Solid-liquid equilibria
SLV	Solid-Liquid-Vapor
SRK	Soave-Redlich-Kwong
THI	Thermodynamic inhibitor
TI	Thermodynamic integration
TIPS	Transferrable intermolecular potential functions
TPI	Test particle insertion
vdWP	van der Waals and Platteeuw
VLE	Vapor-Liquid Equilibria

Symbols

a	Ewald summation convergence parameter
a_S, a_L	Interaction energies between methane molecules
A	Helmholtz free energy
A_{L-V}	Liquid-vapor interfacial area
A_p	Particle surface area
B	Thermodynamic parameter
B^*	Birth rate
c	Shape factor
C	Concentration
C_J	Langmuir constants
D^*	Death rate
f	Fugacity
G	Gibbs energy
G^*	Growth rate
h	Planck's constant
H	Enthalpy
\mathbf{H}	H matrix
H_E, H_{IE}	Einstein crystal Hamiltonians
J	Nucleation rate
k	Mass transfer coefficient
$k_{L-V}^l a_{L-V}$	Gas dissolution rate
k_H	Henry's constant
k_r	Intrinsic reaction rate constant
K	Kinetic constant
\mathbf{K}	Lattice vector in Fourier space

K^*	Overall transfer coefficient
$K_{g,n}$	Adsorption constant
L	Lattice parameter
m	Growth number
M	Molecular mass
N^*	Number of building units constituting a hydrate nucleus
N	Number of molecules
P	Pressure
q	Molecular partition function/charge
Q	Canonical/Isothermal-isobaric partition function
r_c	Cutoff radius
r_i	Cartesian coordinate
r_{OO}	Distance between the oxygen sites of two molecules
R^*	Critical radius of nucleus
s_i	Coordinates in simulation box units
S	Supersaturation ratio
t	Time
T	Temperature
u_{elec}	Electrostatic term in intermolecular pair potential
u_{L-J}	Lennard-Jones term in intermolecular pair potential
U	Intermolecular energy
v_h	Volume of hydrate building unit
v_{hw}	Volume of water in the hydrate
Δv_e	Volume difference between water molecule in solution and in hydrate
V	Volume
x_i	Mole fraction
y_i	Mole fraction in vapor phase
Z	Configurational partition function for hydrate
z	Compressibility factor
β	$1/k_B T$
γ_i	Activity coefficient
Γ	Semigrand partition function

ε	Depth of potential well
ε_0	Permittivity of vacuum
θ	Occupancy
κ	Dielectric constant
λ	Coupling parameter
Λ	Thermal wavelength
μ_i	Chemical potential
μ_n	N'th moment of the particle size distribution
$\Delta\mu$	Supersaturation
ρ	Density
σ	Surface energy/molecule diameter
φ	Fugacity coefficient
ϕ	Particle size distribution
ψ	Contact factor
ω	Angle
ζ	Fraction of crystals born

Contents

Preface.....	III
Summary.....	V
Resumé.....	VII
Publications.....	IX
Abbreviations.....	XI
Symbols.....	XIII
1 Introduction	18
1.1 Overview of the PhD project.....	23
2 Nucleation of gas hydrates	25
2.1 Hydrate nucleation theories.....	26
2.2 Driving force for hydrate nucleation.....	29
2.3 Studying hydrate nucleation.....	30
2.4 Induction times of propane hydrate nucleation.....	33
2.4.1 An induction time model for gas hydrates.....	34
2.4.2 Experimental section.....	37
2.4.3 Results and discussion.....	39
2.5 Improving induction time measurements for kinetic hydrate inhibitor testing....	47
2.5.1 Experimental section.....	48
2.5.2 Results and discussion.....	51
2.6 Evaluation of kinetic hydrate inhibitors using high pressure differential scanning calometry.....	60
2.6.1 Experimental section.....	61
2.6.2 Results and discussion.....	65
3 Growth of gas hydrates	69
3.1 Hydrate growth theories.....	70

3.2	Studying hydrate growth.....	73
3.3	Growth of structure I and II gas hydrates.....	75
3.3.1	Experimental section.....	75
3.3.2	Results and discussion.....	78
4	Molecular simulation of gas hydrates	87
4.1	Molecular simulation and gas hydrates.....	88
4.2	Basics of statistical mechanisms and molecular simulation.....	90
4.3	Phase equilibria of systems containing solids.....	96
4.4	Phase equilibria of hydrate forming systems.....	97
4.5	Chemical potentials of the fluid phases.....	99
4.6	Chemical potentials of water and methane in the hydrate.....	102
4.7	Potential models and simulation details.....	105
4.8	Results and discussion.....	110
4.8.1	Stability of the model hydrate.....	111
4.8.2	The vapor-liquid equilibria of methane-water.....	113
4.8.3	Gibbs free energies of the hydrate phase.....	116
4.8.4	The three-phase equilibria of sI methane hydrate.....	117
4.8.5	The three-phase equilibria of stoichiometric structure I methane hydrate.....	121
4.8.6	The three-phase equilibria of stoichiometric structure II methane hydrate.....	124
4.8.7	Estimation and calculation of the hydrate dissociation enthalpy.....	128
5	Conclusions and recommendations	133
5.1	Conclusions.....	133
5.2	Recommendations for future work.....	135
	References	137
Appendix I:	Paper 2.....	147
Appendix II:	Paper 3.....	155
Appendix III:	Paper 4.....	162
Appendix IV:	Apparatus operations.....	174
Appendix V:	MCHydrate.....	184

Chapter 1

Introduction

Clathrate hydrates, are ice-like inclusion compounds that form at low temperatures (T) and high pressures (P) with nonpolar guest molecules trapped (enclathrated) inside hydrogen-bonded water cages. Hydrates are relevant in a variety of scientific and industrial contexts, including climate change modeling, carbon dioxide sequestration, hydrocarbon extraction, hydrogen and natural gas storage, separation and refrigeration technologies, marine biology, and planetary surface chemistry. Clathrate hydrates formed from small gas molecules are commonly referred to as gas hydrates and depending on the type of gas molecule and the thermodynamic conditions, gas hydrates will form different structures. The three most known structures formed from gas molecules are the structure I (sI), structure II (sII) and structure H (sH) hydrate which are shown in Figure 1.1.¹

sI hydrate consists of two types of cages; a small cage consisting of 12 pentagonal rings (5^{12}) of water, and a larger cage consisting of 12 pentagonal and two hexagonal rings ($5^{12}6^2$). sII hydrate also consist of two types of cavities; the small 5^{12} cage and a larger cage consisting of 12 pentagonal and four hexagonal rings ($5^{12}6^4$) of water. sH hydrate consists of three types of cages; the 5^{12} cage, a larger $5^{12}6^8$ cage and an intermediate cage consisting of 3 squares, 6 pentagonal and three hexagonal rings ($4^35^66^3$) of water. While hydrates formed in nature seem to favor formation of sI, those found in artificial systems, like for instance oil and gas pipelines most often form sII. sH is only favored when a heavy hydrocarbon such as methylcyclohexane is present with methane and water.

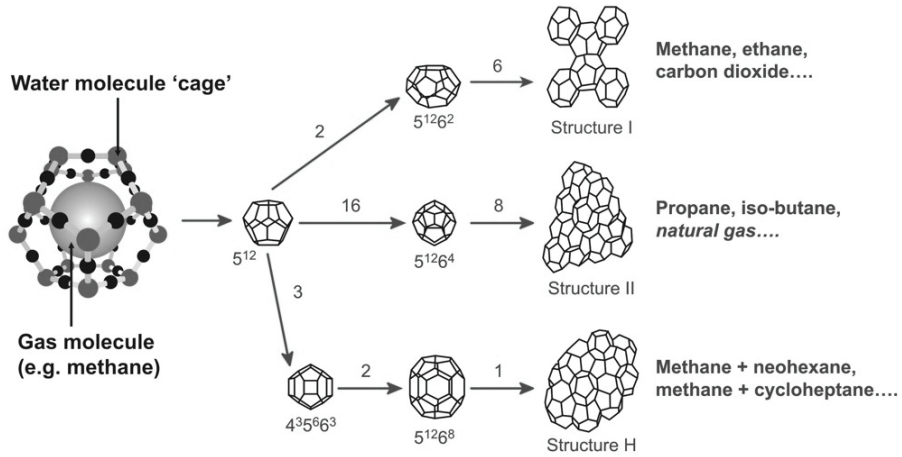


Figure 1.1. The three structures of gas hydrates.¹ The hydrate unit cell for structure I and II is composed of two types of cages while the structure H unit cell is composed of three types of cages. The type and number of cages constituting the unit cell is indicated by the numbers.

Because it is not possible for all cages to be occupied by a guest molecule hydrates always have more water than the stoichiometric composition. The ratio between the guest molecule and water bound in the cage lattice usually ranges from 6-19 moles of water for each mole of hydrate former, with typical fractional occupancies of the smaller cages between 0.3 and 0.9 whereas the large cage occupancy is close to unity. This variation causes clathrate hydrates to be called “non-stoichiometric hydrates” to distinguish them from stoichiometric salt hydrates.²

Gas hydrate formation is a problem that the oil and gas industry is very concerned about: Oil and gas transmission lines, tie-backs, and off-shore process equipment are prone to being blocked by hydrates, causing potential hazards and/or economic loss (a number of case studies related to this can be found in the literature^{2,3}). Hydrates are the leading (compared to wax, asphaltenes, scale) deepwater flow assurance problem by an order of magnitude⁴ and in a survey among 110 energy companies, flow assurance was listed as the major technical problem in offshore energy development.⁵

To assess whether a pipeline or other installation in connection with hydrocarbon extraction is at risk of hydrate formation, incipient hydrate formation conditions have been predicted using thermodynamic models like the van der Waals and Platteeuw (vdWP) model.^{6,7} In case precautions against hydrates are required traditionally the

formation of hydrates has been prevented by adding thermodynamic hydrate inhibitors (THIs) such as methanol and glycol to reduce the equilibrium hydrate formation temperature to below the temperature of operation. In Figure 1.2 an example where thermodynamic inhibition is necessary to prevent hydrate formation in a water wet gas pipeline is shown. The figure shows the P - T profile of a 60 km long natural gas pipeline running between the well and the production platform. In the figure the three-phase liquid water-hydrate-vapor (L-H-V) equilibrium curve of water and natural gas is also shown to indicate in which P - T regime hydrate formation can be expected. On the left side of the three-phase equilibrium curve gas hydrate coexists with water or gas while on the right side of the curve only water and gas coexist. By adding methanol in various mass fractions to the water phase it can be seen that the three-phase equilibrium curve is shifted to lower temperatures, i.e. the hydrate free area is increased. For the case depicted in Figure 1.2 up to 30 wt % methanol has to be added to the pipeline to ensure that it is operated outside the hydrate region.

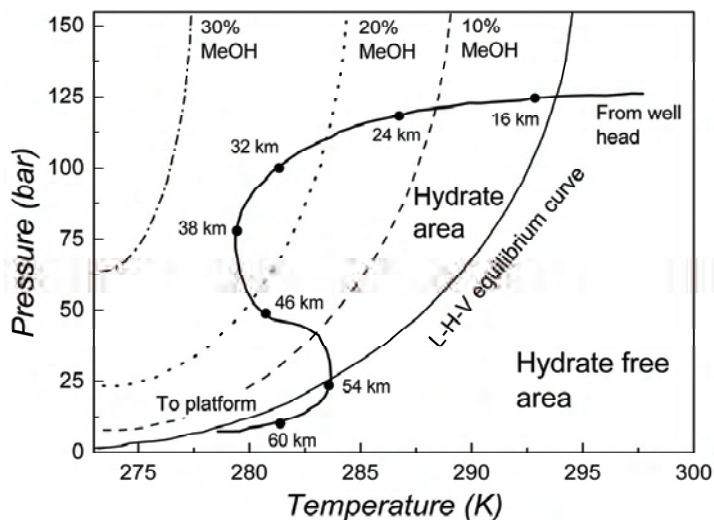


Figure 1.2. The P - T profile of a wet natural gas pipeline going from the well head to the production platform. The three-phase liquid-hydrate-vapor (L-H-V) equilibrium curve for the system composed of natural gas, water and methanol is also shown.³

After being injected to the pipelines the THIs are either disposed of to sea with the production water or regenerated by distillation and recycled to the injection point.

Though the figure illustrates a single example it is not unusual that the amount of THIs needed to avoid hydrate formation may reach 50 wt % in the water-rich phase⁸ and it is not uncommon that the yearly expenses related to hydrate prevention in large gas production facilities may reach several million dollars.^{4,9}

For these reasons, a particular interest in finding low-dosage hydrate inhibitors (LDHIs) has arisen. LDHIs are usually dosed at a concentration of about 0.1–1.0 wt % (active component) based on the water phase. The term covers two classes of hydrate inhibitor compounds namely kinetic hydrate inhibitors (KHI) and anti-agglomerants (AAs).

An AA enables the hydrates to form as a transportable nonsticky slurry of hydrate particles dispersed in the liquid hydrocarbon phase. In particular different surfactant molecules have been shown to be quite effective as AAs.¹⁰ KHIs inhibit the nucleation and growth of gas hydrates thus allowing transportation of reservoir fluids at hydrate favorable condition for a certain period of time before hydrates start to form. The water soluble polymer polyvinylpyrrolidone (PVP) was one of the first compounds identified as a KHI followed shortly by polyvinylcaprolactam (PVCap) which has been proven more efficient than PVP and for this reason has become the standard against which other KHIs are compared.¹⁰

The idea behind using LDHIs to prevent hydrates is that if the hydrate kinetics/stickiness is known, and can be controlled, that is, by adding LDHIs, it may then be possible to operate the oil and gas pipelines at hydrate favorable conditions, while still ensuring that hydrates will not have time to nucleate, grow or agglomerate sufficiently to cause flow blockage. The best AAs have been shown to prevent hydrate agglomeration at 10-20 K subcooling while the best KHIs can prevent hydrate nucleation down to 10 K subcooling.¹⁰ The subcooling is a measure of the driving force for hydrate formation here represented as the isobaric difference between the hydrate equilibrium temperature and the operating temperature. As will be explained in Chapter 2 other measures for the driving force can be applied.¹¹⁻¹⁶

The use of LDHIs offers several benefits to hydrocarbon extraction compared to THIs. One obvious advantage comes from handling much smaller inhibitor volumes resulting in less storage space required, lower inhibitor injection rates and less manpower needed to

handle the inhibitor. Considering the flammability and toxicity of THIs a substitution with LDHIs may also offer certain health and safety benefits. Such changes to the process may lead to significant cost reductions in the operational expenses (OPEX). However LDHIs have the biggest economic impact when designed into oil and gas production systems often affording multi-million dollar reductions in capital expenditure (CAPEX).¹⁷

KHIs have been used in oil field applications to prevent hydrate formation since 1996.^{18,19} By the end of 2005 there were estimated to be 50-70 field applications of LDHIs, the majority of these related to KHIs¹⁰ and primarily located in the North Sea, the Gulf of Mexico, South America and the Middle East.¹⁹⁻²⁵ At the beginning of 2000 sales of PVCap-based polymers for KHI applications were on the order of 300-500 ton per year, thus the amount of KHI used in field applications worldwide is by no means insignificant.¹⁰ Nevertheless, their use has been limited owing to their cost or because of environmental restrictions. For example in the Danish and Norwegian sectors of the North Sea approval of LDHIs and new production chemicals in general can only be achieved if they show at least 20-60 % biodegradability.²⁶ None of the KHIs on the market today possess this level of degradability thus there is currently a need for greener LDHIs, in particular with the North Sea sector in mind. Furthermore there is a large potential for green production chemicals in general as the oil and gas industry focuses on continuous replacement of production chemicals with greener alternatives.^{27,28,29}

Design of green LDHIs might benefit from knowledge of the hydrate formation mechanism. Laboratory measurements have been unsuccessful in identifying the molecular mechanism of hydrate formation because of inability to precisely target the time and spatial domain of a nucleation event, which may occur in nanoseconds and on the nanometer length scale.^{30,31} Because classical molecular dynamics (MD) simulations can follow the nanoscale trajectories of molecules, MD has been the preferred technique to investigate the formation of hydrates.³²⁻³⁸ Only until very recently spontaneous nucleation of hydrates from molecular simulations had never been observed. However the pioneering work by Walsh and coworkers in this area has allowed a detailed look into the formation mechanism of gas hydrate; information which may be valuable in the development of new and more effective KHIs.³⁹

1.1 Overview of the Ph.D. project

The topics covered in this PhD project can be divided into two parts; an experimental part and a theoretical part. The experimental part focuses on the three-phase equilibria of different hydrate systems and the nucleation and growth of sI and sII gas hydrates. In particular the effect of polymeric KHIs like PVP and PVCap on the nucleation and growth rates of hydrates have been investigated and compared to novel KHIs such as antifreeze proteins (AFPs) or ice-structuring proteins (ISPs) a name which is sufficiently general to cover the range of natural functions and potential applications. ISPs are compounds that exist naturally in fish, insects and plants living at cold conditions and cause freeze resistance of the plasma and cell material of these living species.⁴⁰ ISPs found in winter flounder formed the background of KHI development projects at Shell in the early nineties and was what made them look at protein-like water-soluble polymeric amides such as PVP as KHIs. While they did not see any great KHI potential in ISPs more recently it has been shown that ISPs from winter flounder and spruce budworm are also capable of retarding the nucleation and growth of methane hydrate and clathrate hydrates formed from tetrahydrofuran.⁴¹⁻⁴⁴

In part the motivation for investigating the KHI potential of ISPs is that there is a need for “greener” alternatives to the KHIs applied by the oil and gas industry today. It is also likely that ISPs are more effective KHIs compared to PVP and PVCap; due to their preference to attach to ice/inorganic surfaces, an ability which has been developed through millions of years of evolution.⁴⁵

The ISPs which have been subject to investigation in this work are those found in the ocean pout (*Zoarces americanus*), the meal worm (*Tenebrio molitor*) and in the bark beetle (*Raghium mordax*).

To perform the experimental nucleation and growth studies of gas hydrates and investigate the effect of the selected ISPs and KHIs various experimental setups and methodologies have been applied. The nucleation studies were performed using two existing high pressure stirred cells and high pressure differential calorimetry. A part of the nucleation data obtained experimentally has been interpreted using a recently developed induction time model for gas hydrates. This allows the study of certain microscopic properties of gas hydrates and how these are influenced by the presence of KHIs or changes in the thermodynamic state. Chapter 2 summarizes the results of the nucleation studies.

The growth experiments were carried out using a new experimental set-up designed to measure the growth rate of various hydrates at constant pressure and temperature. Though the type of experiment is rather simple compared to other apparatuses⁴⁶⁻⁵¹ it can provide a more accurate estimate of the growth rate of gas hydrates - even at the very low rates obtained when efficient KHIs are present. The results of these studies are presented in Chapter 3.

The theoretical study is a part of a larger molecular simulation study of gas hydrates done in collaboration with the Center for Hydrate Research at Colorado School of Mines. The aim of the study has been to calculate the three-phase L-H-V equilibria for a system composed of methane and water. Calculation of two component three-phase equilibria from molecular simulation has not been attempted before, thus part of the study deals with developing the methodology to perform the calculations. The main findings of this study are presented in Chapter 4.

The main conclusions and recommendations for future work are presented in Chapter 5.

Chapter 2

Nucleation of gas hydrates

While time-independent hydrate properties, such as the three-phase equilibria of hydrate forming systems are well understood, hydrate time-dependent phenomena such as nucleation and growth are much more challenging to deal with. Understanding hydrate nucleation trends is essential for a fundamental scientific understanding of the formation process but is also important for the design and testing of KHIs. As mentioned in Chapter 1 KHIs delay the nucleation and usually also decrease the crystal growth rate of gas hydrates. The nucleation delay time (induction time), is the most critical factor in field applications, since this will indicate whether hydrate formation is likely to take place during the production and transportation of oil and gas or not.

This chapter gives an overview of some of the theories behind the nucleation of gas hydrates and how nucleation can be studied experimentally. An extensive experimental study on the nucleation of gas hydrates has been performed using different experimental set-ups and methods. The aim has in part been to identify some of the important factors influencing the nucleation process and for this purpose a recently proposed nucleation model for gas hydrates has been utilized for interpretation of the nucleation data. The other part of the study mainly focuses on how it is possible to improve the reproducibility of nucleation experiments and in particular for nucleation experiments involving KHIs.

2.1 Hydrate nucleation theories

Nucleation is a microscopic stochastic phenomenon where water molecules form clusters (nuclei) around gas molecules. These clusters will grow and disperse until they reach some critical size. The nucleation process of gas hydrates may have direct analogies to crystallization processes such as precipitation of salts from solution.⁵² Like salt solutions, hydrate solutions are also metastable. Metastability (also called the thermodynamic spinodal) in salt crystallization has been hypothesized to occur through supersaturation, that is for each solvent-solute pair there exists a concentration-temperature relationship which defines the metastable limit.⁵³ A supersaturated solution is one in which the solvent contains more solute than can normally be accommodated at that temperature. The greater the degree of supersaturation, the more crystal nuclei will form in the solution. The metastability phenomenon is best explained by looking at a generalized concentration-temperature relationship for a solute in solution as shown in Figure 2.1A. At point P nuclei or crystals cannot form since the solution is superheated by an amount RP. Once the solid-liquid saturation line is passed, either through cooling or concentration, nuclei and crystals may or may not form in the metastable region. A metastable point Q is shown between point R and the crosshatched line CD indicates the spinodal. The spinodal line is crosshatched since it is system dependent.

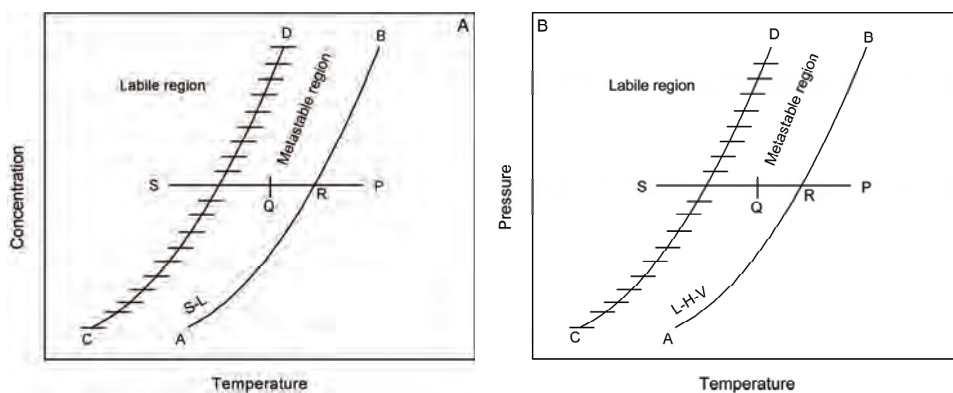


Figure 2.1. A) The generalized supersolubility diagram for crystal formation showing the solid-liquid (S-equilibrium line (AB) relative to the spinodal line (CD). B) The supersolubility diagram for hydrate forming systems showing the three-phase liquid-hydrate-vapor (L-H-V) equilibrium line (AB) and the spinodal line (CD).

An analogy to this generalized scheme can be made for hydrates and is shown in Figure 2.1B. The main difference between the two figures is that the concentration axis in Figure 2.1A has been replaced by a logarithmic pressure axis in Figure 2.1B. Typically hydrate nucleation and growth will occur within the metastable region before entering the spinodal region. If the spinodal region is entered hydrate nucleation and growth takes place rapidly due to the fact that the driving force (see section 2.2) has become very high. For hydrate forming systems held at conditions corresponding to the metastable region the driving force is not as high thus an induction period will appear before hydrate formation takes place.

It is the general perception that the nucleation process of gas hydrates has a stochastic nature¹² and that induction periods are quite hard to reproduce. This is in particular true at low driving forces^{54,55} i.e. as the hydrate forming conditions gets closer to line AB in Figure 2.1B. In particular the heterogeneous nature of the nucleation process is assumed to play an important role for the unsystematic nucleation events.^{56,57} It is well known that heterogeneous nucleation plays an important role in the formation of ice⁵⁸ and similar observations have been made for gas hydrates.¹⁵ This causes the induction time to be very sensitive to any heterogeneities in solution, i.e. presence of impurities in the hydrate forming system can cause induction times to become highly scattered.

There is very little information about the actual nucleation mechanism of gas hydrates because the experimental conditions (high pressure and low temperature) disfavor studying hydrate formation at the molecular level. Nevertheless several theories and hypotheses attempting to describe this process have been proposed. One of the earliest hypotheses, “the labile cluster hypothesis”, suggests that hydrate nucleation is a progression of small clusters of water and gas, agglomerating in an effort to reach a critical nucleus at which hydrate growth can continue. A conceptual picture of this is seen in Figure 2.2. At the starting point in (A), the pressure and temperature are at hydrate favorable conditions however only water molecules are present. It is seen here how typical hydrogen-bonding networks of water molecules in liquid water resemble the polygonal structure of the hydrogen bonded water molecules in hydrate cage faces.⁵⁹ Upon dissolution of gas into the water (B), labile clusters form immediately. These labile

clusters undergo agglomeration through face sharing (C), and finally through additional agglomeration, the labile clusters reach a critical size at which hydrate growth continues.

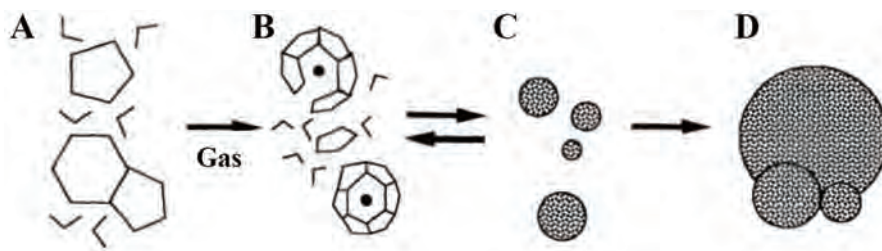


Figure 2.2. The hydrate formation mechanism proposed by Christiansen and Sloan.⁶⁰ (A) Pressure and temperature are at hydrate forming conditions but no gas is present. (B) Labile clusters form immediately upon gas dissolution into the water. (C) Agglomeration of labile clusters through face sharing thus increasing disorder. (D) When a cluster size reaches a critical value, hydrate growth begins.

In another hypothesis, nucleation is assumed to take place on the vapor side of the vapor-liquid interface. First gas molecules are transported to the interface and absorbed by the aqueous surface. At suitable adsorption sites water molecules will form first partial and then complete cages around the adsorbed gas molecules. Clusters will join and grow on the vapor side until the critical size is reached.^{61,62}

Other theories are based on observations made using molecular simulations of hydrate forming systems.⁶³ Molecular simulation enables the observation of molecule interactions at the molecular level and is thus very useful for studying crystallization phenomena such as the nucleation of gas hydrates. Very recently a simulation study of the system water and methane at low temperature and high pressure resulted in spontaneous nucleation and growth of methane hydrate.³⁹ Rare $5^{12}6^3$ cages were observed among the cage structures identified allowing the coexistence of sI and sII hydrate by creating an energetically favorable interface. A more detailed description and discussion of this study is provided in Chapter 4.

2.2 Driving force for hydrate nucleation

A number of driving forces for the formation of gas hydrates have been suggested in the literature for both single and multicomponent systems.¹¹⁻¹⁶ The total molar change in Gibbs free energy presented by Christiansen and Sloan¹³ is perhaps the most general driving force expression. A number of the proposed driving forces are summarized in Table 2.1. For an explanation of the different symbols used in the equations please see the list of symbols.

Table 2.1. Different driving forces proposed for the formation of simple and mixed gas hydrates. The text in the parentheses describes whether the expression is suitable for simple or multicomponent hydrate systems.

Ref.	Driving force	Expression
12	Fugacity (simple hydrate)	$f_i^{\text{exp}} / f_i^{\text{eq}} - 1$
13	Gibbs free energy	$\Delta G^{\text{exp}} = n_w(v_w - v_h)(P^{\text{eq}} - P) + RT \sum (n_i) \ln [f_i^{\text{eq}} / f_i]$
14	Subcooling (simple hydrate)	$T^{\text{eq}} - T^{\text{exp}}$
11	Chemical potential difference between water in hydrate and in liquid. (multicomponent hydrate)	$\frac{\Delta \mu_{\text{wat}}}{RT} = \sum_i v_i \ln \left(1 - \sum_j \theta_{j,i} \right) + \frac{\Delta \mu_0}{RT_0} - \int_{T_0}^T \frac{\Delta H_0 + \Delta C_p(T - T_0)}{RT^2} dT + P \frac{\Delta v}{\frac{1}{2}R(T + T_0)}$
15	Supersaturation Isothermal/Isobaric (simple hydrate)	$\Delta \mu = k_B T \ln \left[\varphi(P, T) P / \varphi(P^{\text{eq}}, T) P^{\text{eq}} \right] + \Delta v_e (P - P^{\text{eq}})$ $\Delta \mu = \Delta S_e \Delta T - (C_{p,e} / 2T_e) \Delta T^2$
16	Gibbs free energy (multicomponent hydrate)	$\Delta G = \Delta v_e (P - P^{\text{eq}}) - n_w k_B T \sum_i v_i \ln \left(\frac{1 - \sum_j \theta_{j,i}(T, P, y)}{1 - \sum_j \theta_{j,i}(T, P^{\text{eq}}, y)} \right)$

Apart from a few of the expressions proposed in literature limited justification has been provided for these driving forces. Furthermore it has been shown that some of the

different expressions are actually just special cases of the more general case as reviewed by Sloan and Koh.² The subcooling was one of the first driving forces to be used in the description of hydrate formation. The subcooling is the difference, at isobaric conditions, between the three-phase equilibrium temperature and the temperature of the hydrate forming system. The subcooling is basically proportional to the difference in fugacity or chemical potential between water in hydrate and in pure water at isobaric conditions and fixed gas phase composition as long as no hydrate formation has taken place.⁶⁴ However while the subcooling has also shown to be proportional to the supersaturation and the Gibbs free energy change at isobaric and isothermal conditions for simple hydrate formers the subcooling underestimates the driving force for multicomponent natural gas mixtures. For this reason it has been speculated whether the subcooling is actually suitable to use when for example assessing the effectiveness of KHIs.⁶⁵

2.3 Studying hydrate nucleation

Gas hydrate nucleation has been studied experimentally using different approaches and analytical expressions have been derived to describe the obtained data.^{54,55,57,64-73} For hydrate forming systems the driving force is found to have a significant impact on the induction period. At low driving force the induction period increases exponentially while at high driving forces the induction period disappears. A schematic plot of the induction time versus the driving force is shown in Figure 2.3. At high driving forces, (corresponding to the labile region in Figure 2.1B) hydrate forms instantaneously. In the metastable region an induction period appears before hydrate starts to form. The metastable region has in this case been divided into two; one at moderate driving forces and the other at low driving forces. The line indicating the induction time at low driving force is crosshatched indicating that the induction time becomes increasingly stochastic in this region.

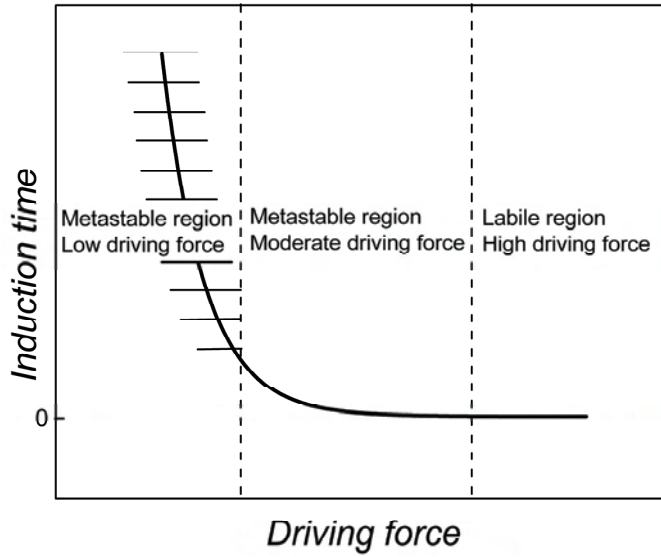


Figure 2.3. A typical relationship between the induction time of hydrate formation and the driving force. In the labile area instantaneous nucleation and growth occurs while in the metastable region an induction period appears before hydrate forms. The metastable region has been divided in two areas; at moderate and low driving forces. The crosshatched line at low driving forces symbolizes that the induction period becomes increasingly stochastic in this region.

Various methods have been applied in the laboratory to investigate nucleation of gas hydrates experimentally. While some methods rely on specific procedures others rely on application of specific experimental equipment. In Table 2.2 a list of some of the equipment types which have been used in hydrate nucleation studies are provided including a small description of the method and the advantages/deficiencies of using it.

These methods are all well suited for studying nucleation of gas hydrates, however at the same time all the methods have some undesirable features. Induction times found from stirred cell experiments lack reproducibility which is unfortunate since reproducible induction times will provide a better basis for assessing the impact of for example KHIs on the induction time.

Table 2.2. Description of three different methods which have been used in studying gas hydrate nucleation.

Method	Ref.	Description	Advantages/Deficiencies
Stirred Cell	12,14,64,68-72	Stirred cell experiments are conducted by mixing of water and gas under hydrate forming conditions. The time it takes from when the system is brought to hydrate forming conditions until hydrate forms is taken as the induction time.	Internal mixing in the cell provides renewal of the gas-liquid interface mimicking the flow of reservoir fluids in pipelines. Low reproducibility of measured induction times.
HP ALTA	55,67	High pressure automated lag-time apparatus (ALTA). Measures the subcooling point (SCP) of water “freezing” into hydrate by cooling a small liquid sample at a constant cooling rate.	Very small samples needed. Highly automated and fast. Gives statistically robust data sets within days. Requires a high degree of subcooling (12-17 K) to cause nucleation. No stirring of the liquid phase.
HP DSC	57,73	High pressure differential scanning calometry. Liquid and gas is charge to a small cell. When hydrate forms (exotherm) or dissociates (endotherm) a heat flow is detected. Experiments can be done at constant P and T or at a constant cooling rate.	Small samples needed. In constant cooling experiments good reproducibility is obtained. Requires very high subcoolings (25-30 K) to nucleate hydrate. No stirring possible. Isothermal induction time experiments have poor reproducibility.

While the ALTA method provides a statistically better result for the nucleation event of gas hydrates it does not measure the induction time directly but rather the subcooling (cooling the sample at a constant rate) at which hydrate nucleation appears with a probability of 50 %; referred to as the subcooling point (SCP). Constant cooling of the sample is also necessary to obtain reliable statistics for the formation of gas hydrates when using high pressure DSC. How these critical nucleation temperatures relate to the induction time is yet to be investigated, however one major deficiency of the ALTA and the high pressure DSC method is that there is no agitation of the liquid phase thus there is no renewal of gas-liquid interface. This is most likely the reason why very high subcoolings (30 K)^{57,67} are required to observe formation of hydrate with these methods compared to stirred cell experiments (>1 K).⁷² Since most KHIs only work at moderate

degrees of subcooling¹⁰ (10-15 K) stirred cell experiments have been preferred over constant cooling rate experiments to investigate the effect of KHIs.^{26,71,74,75}

Different steps can be taken to improve the reproducibility of the hydrate induction time obtained from stirred cell experiments. One such method is by forming hydrate from water which has already been subject to hydrate structures. If hydrate is melted at moderate temperatures the melted water is thought to contain residual hydrate structures which will act as precursors upon second hydrate formation. This phenomenon is sometimes also referred to as the “memory effect” of water.² Recently by using the hydrate precursor technique it has been shown that the reproducibility of the induction times obtained from stirred cell experiments, for uninhibited and kinetically inhibited systems, is significantly improved compared to induction times measured upon first hydrate formation.⁷⁵ Another way to improve the reproducibility of the hydrate induction time obtained from stirred cell experiments is by adding a defined amount of impurity to the aqueous phase thereby increasing the heterogeneity of the hydrate forming system. In heterogeneous nucleation the hydrate clusters grow in contact with a substrate which lowers the interfacial energy cost of further growth. In most hydrate forming systems there are small heterogeneities present, even for those that are assumed to be very pure, since it is almost impossible to avoid dust particles from entering in the system. Variation in particle content from experiment to experiment is probably one of the reasons why induction times appear to be stochastic. If a defined amount of impurity (for example silica with a certain size distribution) is introduced in the hydrate forming system this will add significantly to the total amount of impurities present compared to the unknown (dust) particles. Thereby the effect of the unknown particles is suppressed and in principle the induction time should become more reproducible.^{76,77}

2.4 Induction times of propane hydrate nucleation

The important factors influencing hydrate formation are difficult to study at the molecular level. Using crystallization theory it is however possible to relate macroscopic properties such as the hydrate induction time and supersaturation to microscopic properties such as

the size of the critical hydrate nucleus, the hydrate-water interfacial energy, the hydrate-substrate contact angle etc.

This section begins with a description of a newly proposed induction time model which will be applied to interpret induction time data of sII propane hydrate. The model will specifically be applied to investigate the influence of the driving force (supersaturation), the stirring rate and the presence of a KHI on the aforementioned hydrate properties.

2.4.1 An induction time model for gas hydrates

The induction time is not a fundamental physical characteristic of a system, but it is experimentally accessible and contains valuable information about the kinetics of a new phase nucleating. Most induction time models of crystallization processes are based on crystal growth theory in which the fitting parameters often are found to be system specific which is indeed also the case for hydrate forming systems.^{12,58}

Kashchiev and Firoozabadi have proposed an induction time model for gas hydrates based on crystallization theory which means that the model accounts for proportionality between the induction time and the nucleation rate.⁶⁶ The model is shown below:

$$t_i = K e^{-\Delta\mu/k_B T} (1 - e^{-\Delta\mu/k_B T})^{-3m/(1+3m)} \exp \left[\frac{4c^3 N_W^{H2} \sigma_{ef}^3}{27(1+3m)k_B T \Delta\mu^2} \right] \quad (2.1)$$

where K is a kinetic parameter, $\Delta\mu$ is the supersaturation, k_B is the Boltzmann constant, m is a number that relates to the growth type, c is a crystal shape factor, N_W^H is the number of water molecules in the hydrate and σ_{ef} is the effective surface energy between hydrate and solution. The model assumes that progressive nucleation is taking place, i.e. hydrate crystallites are continuously nucleated during the nucleation process, however the model can be modified to account for situations where instantaneous nucleation is taking place as well.⁶⁶

To calculate the interfacial properties of the hydrate forming system, i.e. the effective surface energy between hydrate and solution, the following expression has been substituted into eqn. (2.1):

$$B = \frac{4c^3 v_h^2 \sigma_{ef}^3}{27(k_B T)^3} \quad (2.2)$$

For heterogeneous nucleation σ_{ef} is given as:

$$\sigma_{ef} = \psi \sigma \quad (2.3)$$

where σ is the surface energy between hydrate and solution and ψ , assuming that hydrates form cap-shaped clusters on a solid substrate, is given as:

$$\psi = \left[(1/4)(2 + \cos \omega)(1 - \cos \omega)^2 \right]^{1/3} \quad (2.4)$$

with ω being the wetting angle. Other shapes of the hydrate can be assumed, i.e. spheres/cubes in the bulk or lenses at the gas-liquid interface by modifying the expression for ψ . However in this case cap-shaped clusters have been chosen since it has been shown that these are thermodynamically favored over both spheres and lenses.¹⁵ The driving force can be expressed as the supersaturation ratio, S :

$$S = \left[\frac{\varphi(P, T)P}{\varphi(P_e, T)P_e} \right] \cdot \exp \left[\frac{\Delta v_e (P - P^{eq})}{k_B T} \right] \quad (2.5)$$

where φ is the fugacity coefficient of the gas in the gas phase and P_e is the L-H-V three-phase equilibrium pressure. $\Delta v_e = N_w v_w - v_h$ is the difference between the volume of N_w water molecules in the solution, v_w , and the volume of a hydrate building unit in the hydrate crystal, v_h . A hydrate building unit consists of a single gas molecule and x water molecules, x depending on the hydrate structure. For propane hydrate $\Delta v_e = -1.370 \times 10^{-28} \text{ m}^3$.⁷⁸ Substituting this driving force expression into eqn. (2.1) yields:

$$t_i = K \left[S(S-1)^{3m} \right]^{-1/(1+3m)} \cdot \exp \left[\frac{B}{(1+3m) \ln^2 S} \right] \quad (2.6)$$

Plotting the induction times versus supersaturation ratios it is possible to obtain B and K from a regression of the data points as the slope and the intercept, respectively. If growth by volume diffusion of dissolved gas, through a stagnant layer formed around the nucleus is assumed then $m = 1$.⁶⁶ Eqn. (2.6) then becomes:

$$\ln \left[S^{1/4} (S-1)^{3/4} t_i \right] = \ln K + \frac{B}{4 \ln^2 S} \quad (2.7)$$

Other types of growth mechanisms can be assumed but in most cases these also result in $m = 1$. The number of building units that constitute a hydrate nucleus can be calculated using the expression:

$$N^* = \frac{2B}{\ln^3 S} \quad (2.8)$$

The size of the critical nucleus can be found from the relation¹⁶:

$$R^* = \frac{2\sigma N_w v_{hw}}{\Delta G} \quad (2.9)$$

where v_{hw} is the molecular volume of water in the hydrate (hydrate unit cell volume divided by the number of water molecules in the unit cell). The expression for ΔG , can for simple hydrate forming systems be reduced to:

$$\Delta G = N_i(T, P_e) k_B T \ln \left[\frac{\varphi(P, T) P}{\varphi(P_e, T) P_e} \right] + \Delta v_e (P - P_e) \quad (2.10)$$

N_i being the number of gas molecules in the unit cell. The induction time model can also be adapted to hydrate forming systems containing additives such as KHIs. This can be done by introducing a Langmuir type term in eqn. (2.6) taking into account adsorption of molecules on nucleation sites and on the surface of the growing hydrate. Eqn. (2.6) then becomes:

$$t_i = K \left[(1 + k_g C_a)^{3m} (1 + k_n C_a)^{1/(1+3m)} \right] \left[S(S-1)^{3m} \right]^{-1/(1+3m)} \cdot \exp \left[\frac{B}{(1+3m) \ln^2 S} \right] \quad (2.11)$$

where k_g and k_n (m^3) are adsorption constants and C_a (molecules/m^3) is the concentration of the additive in solution. This expression is valid for additive molecules that (i) do not adsorb on the surface of the hydrate nuclei, but adsorb on the surface of the growing hydrate crystallites, (ii) do not provide new nucleation sites in the system, and (iii) block existing nucleation sites by adsorbing at the solution/gas interface or onto the surface of the nucleation-active particles. For the derivation of this expression see the work by Kashchiev and Firoozabadi.⁶⁶ This expression is similar to eqn. (2.6) rearranged to a form from which the constants K and B can be obtained from a linear regression:

$$\ln \left[\frac{S^{1/4} (S-1)^{3/4} t_i}{(1+k_g C_a)^3 (1+k_n C_a)^{1/4}} \right] = \ln K + \frac{B}{4 \ln^2 S} \quad (2.12)$$

Applying this model for induction time data for systems containing KHIs it is possible to assess qualitatively and quantitatively how the nucleation process is affected by the presence of these additives.

2.4.2 Experimental section

Apparatus. The induction time measurements were conducted in a high-pressure stainless steel cell with a fixed volume of 66.5 cm^3 and a maximum working pressure of 150 bar. The cell allows for visual observation of hydrate formation through two sapphire windows. A safety valve is attached to the cell which opens when pressure exceeds an adjustable value (40-100 bar). The cell is attached to a gas reservoir and a vacuum pump. The temperature in the cell is controlled by circulating coolant (water-ethanol solution), in a jacket surrounding the cell. The temperature is monitored by using a platinum resistance probe, Pt-100 ($\pm 0.01 \text{ K}$), placed inside the cell. The pressure of the cell is monitored by a single pressure transducer (BD Sensors, 0-40 bar, 0.25 % FSO). The cell is placed on a stir plate which allows a stirring bar to rotate within the cell. The pressure and temperature in the cell can be recorded continuously on a computer. A schematic of the hydrate equilibrium cell is shown in Figure 2.4.

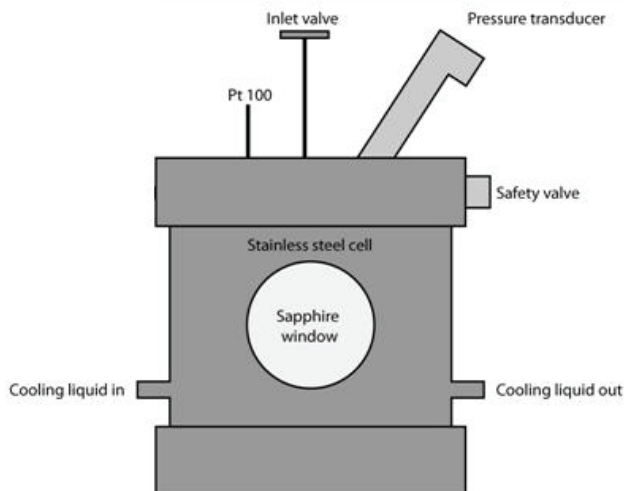


Figure 2.4. Schematic of the stainless steel hydrate cell used in the propane hydrate nucleation studies. The hydrate cell is attached to a gas supply unit and a vacuum pump. The temperature is controlled by a cooling bath. Data is collected continuously on a computer.

Methods. The cell was cleaned with deionized water and loaded with deionized water or deionized water containing PVP. A stirring bar was placed in the cell. The cell lid was screwed on and the cell evacuated using a vacuum pump for approximately 1 hour. The temperature bath was adjusted so the temperature in the cell was around 273.75 K. When the temperature in the cell was constant the propane gas was injected through the inlet until the desired pressure at the chosen temperature was reached. Three experimental series using deionized water were performed. For each series the stirring rate was altered in the range 200-500 rpm in order to investigate the effect of the stirring rate on the hydrate induction time. For experiments involving a KHI two experimental series at KHI concentrations of 0.050 wt% and 0.025 wt% were performed both at a stirring rate of 500 rpm. In all the experiments the pressure and temperature were recorded every 5 s.

Materials. The experiments were performed using deionized water ($0.6\mu\text{S}/\text{cm}$) and propane with a purity of 99.5 supplied by Intergas. As a KHI PVP (MW 10,000) supplied by Sigma-Aldrich was used.

2.4.3 Results and discussion

A total of 85 experiments investigating how the driving force influences the nucleation period of propane hydrate and investigating the role of the stirring rate have been performed. The series investigating the role of PVP in connection with propane hydrate nucleation involved 31 experiments. The data obtained in an experimental run can typically be represented as the pressure-time relationship shown in Figure 2.5. First the pressure drops due to gas dissolving in the water. Next the pressure becomes stable for a given period of time until it drops rapidly due to hydrate formation. The time where the pressure remains constant is here taken as the induction time. The following terminology has been applied in describing the initial cell pressure (P_0), the time for gas to dissolve in water (t_{Sol}), the pressure after gas dissolution (P_{Sol}) and the induction time (t_i).

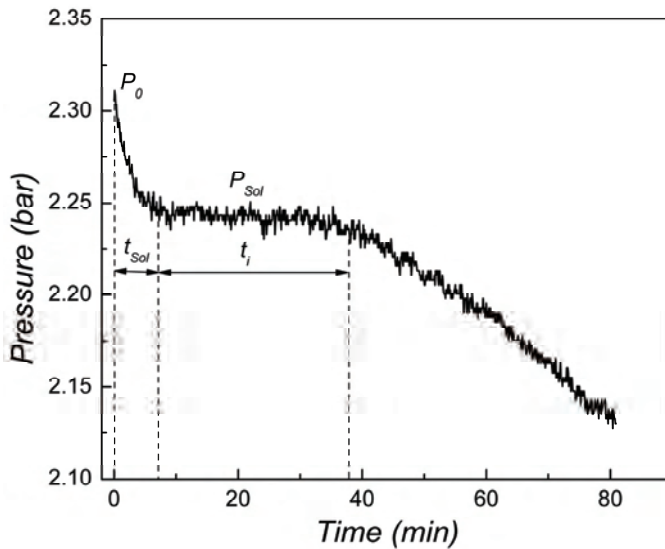


Figure 2.5. Typical pressure-time recording for a stirred cell experiment during which propane hydrate formation takes place.

P_0 , t_{Sol} , P_{Sol} and t_i have for each experiment been extracted from the recorded data and using these values the gas dissolution rate and the supersaturation ratio were calculated. In calculating the supersaturation ratio the fugacity coefficients of the gas were obtained using the SRK equation of state. The three-phase equilibrium pressures of propane hydrate were calculated using CSMGem at the experimental temperatures. CSMGem is a

program capable of calculating the thermodynamically stable hydrate structures and cage occupancy at specified pressure, temperature and composition by minimization of the Gibbs free energy of the system.⁷⁹ The gas dissolution rate $k_{L-V}^l a_{L-V}$ was determined using the two film theory neglecting the resistance on the gas side of the vapor-liquid interface:

$$\left(\frac{dx}{dt}\right) = k_{L-V}^l a_{L-V} (x_{L-V}^i - x) \quad (2.13)$$

where x_{L-V}^i is the gas solubility of the hydrate former in the liquid phase at the vapor-liquid interface and a_{L-V} is the vapor-liquid interfacial area per volume of dispersion (A_{L-V}/V_L). Integrating from $x = x_0$ at t_0 to the equilibrium concentration $x = x_{sol}$ at t_{sol} yields:

$$\ln\left(\frac{x_{L-V}^i - x_{sol}}{x_0 - x_{sol}}\right) = -k_{L-V}^l a_{L-V} t \quad (2.14)$$

The mole fraction of propane gas dissolved in water was in all cases calculated using the fugacity of the pure component in the vapor phase, f_i , and the Henry's constant, k_H :

$$x_i = \frac{f_i(P_{\text{exp}}, T_{\text{exp}})}{k_H} \quad (2.15)$$

Henry's constant was calculated using the empirical expression proposed by Chapoy et al.⁸⁰ given as:

$$\ln(k_H)(KPa) = 552.64799 + 0.078453T - \frac{21334.4}{T} - 85.89736 \ln(T) \quad (2.16)$$

The dissolution rate was then calculated using a least square analysis. It was assumed that the addition of PVP did not have any impact on the magnitude of Henry's constant as the concentration was very low. It was found that the dissolution rate was independent of the initial pressure in the pressure interval investigated here (2-5 bar). In Table 2.3 the calculated average dissolution rates of propane in water are shown as a function of the stirring rate and the agitation Reynolds number, Re_A . The Reynolds numbers are in the

intermediate range between laminar (<10) and turbulent (>10000), 500 rpm being very close to turbulent agitation. However, as the number only refers to the conditions in the vicinity of the impeller, it does not give any indication of how well the water-gas interface is stirred. From a visual point of view 200 rpm corresponds to a situation where a vortex on the water surface has just appeared and 500 rpm corresponds to a vigorous stirring of the water phase.

Table 2.3. Agitation Reynolds numbers (Re_A) and average dissolution rates $k_{L-V}^L a_{L-V}$ calculated from eqn. (2.13) at different stirring rates and concentrations of polyvinylpyrrolidone (PVP). The temperature was 273.75 K.

RPM	Re_A	$k_{L-V}^L a_{L-V}$ ($\cdot 10^3 \text{ s}^{-1}$)
500	8134	7.38
300	4881	2.66
200	3254	0.96
500 (0.050wt% PVP)	8134	5.98
500 (0.025wt% PVP)	8434	6.94

Addition of PVP causes the dissolution rate to lower slightly, the higher concentration causing the dissolution rate to decrease most. This could indicate that the polymer chains damp the turbulence in the liquid phase an effect which might be closely related to how certain polymers work as drag reducers in turbulent flow.

In Figure 2.6 and Figure 2.7 the propane hydrate induction times have been plotted as a function of the supersaturation ratio at different stirring rates and at different PVP concentrations, respectively. From Figure 2.6 the induction time can be seen to be more or less independent of the stirring rate when this is varied in the range of 300-500 rpm. The consistency in the data is quite good i.e. the data follows the expected pattern also shown in Figure 2.3. However for the 200 rpm experiments this tendency is not as regular i.e. the data points are more scattered. This indicates that in low convection systems nucleation events become increasingly random; an effect which might be ascribed to the lower vapor-liquid interfacial area or a less favorable distribution of gas in the bulk liquid phase.

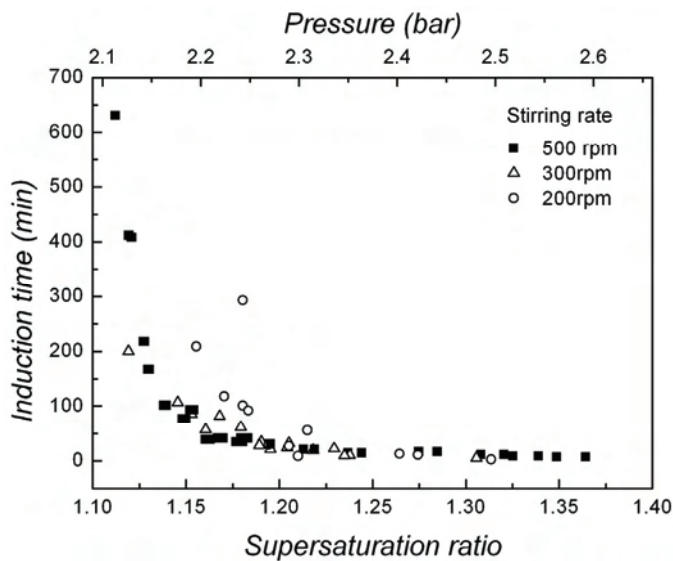


Figure 2.6. Plot of the induction time versus the supersaturation ratio at 273.75 K for propane hydrate at different stirring rates. The induction times measured at high stirring rates are very similar. At low stirring rate more scattering among the measured induction times is observed.

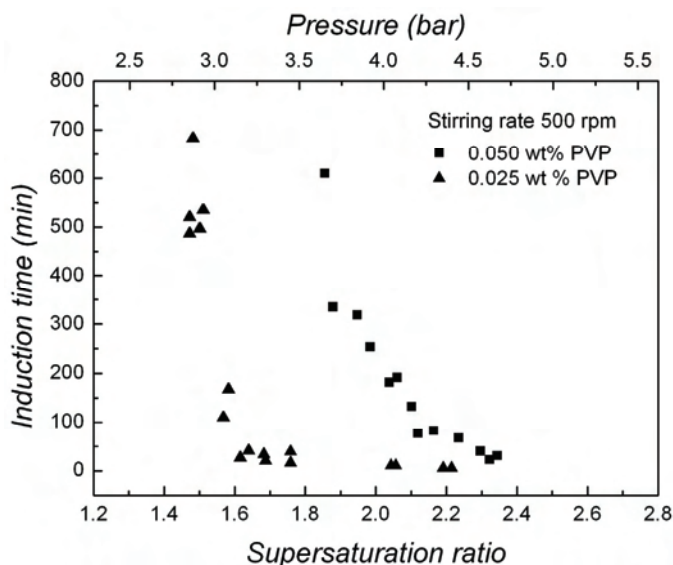


Figure 2.7. Plot of the induction time versus the supersaturation ratio at 273.75 K for propane hydrate for two different concentrations of polyvinylpyrrolidone (PVP) using a stirring rate of 500 rpm. When the concentration of PVP is increased the induction time of propane hydrate is increased.

When PVP is added in even very small amounts the induction time data is shifted to higher supersaturation ratios as seen in Figure 2.7 i.e. PVP works as a KHI as expected. There seems to be quite steady agreement among the two data sets, i.e. the higher PVP concentration data are shifted to the right with approximately the same value in the x-axis direction, ΔS , compared to the data at the lower PVP concentration. In Figure 2.8 the propane hydrate induction time at a stirring rate of 500 rpm has been plotted as a function of the supersaturation ratio given by eqn. (2.7).

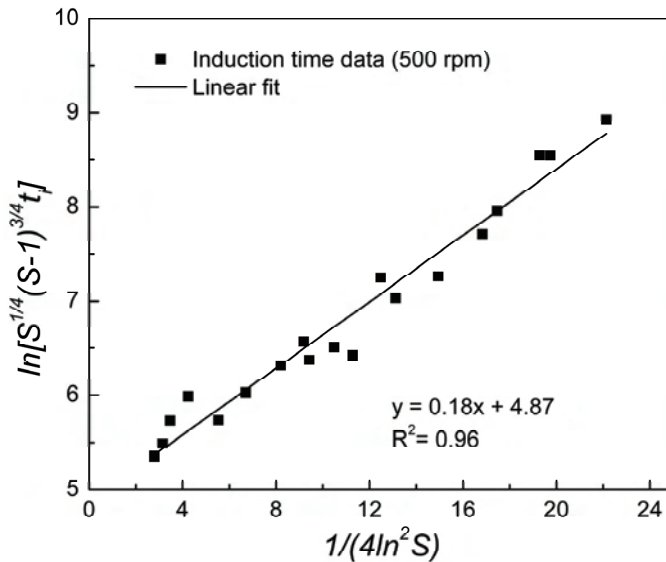


Figure 2.8. Linearized dependence of the induction time on the supersaturation ratio for nucleation of propane hydrate in aqueous solution at 273.75 K and 500 rpm. A very low degree of scattering in the measured data can be observed.

As seen the data shows a reasonably good linear dependence when plotted according to eqn. (2.7). The intercept and the slope of the best fit allows determination of the kinetic parameter K as $\ln(K) = 4.87$ s thus $K = 130.32$ s (4.56) while $B = 0.18$ (0.04) The values in parentheses state the standard deviation of K and B respectively. The magnitude of K is rather high for a process taking place on the molecular level; however it is likely that it indicates that the nucleation is following a polynuclear crystallization mechanism i.e. as the system undergoes a phase transition it allows the formation of statistically many nuclei.⁸² For an operative mononuclear mechanism and homogeneous nucleation very

low K values would be expected, <5 ns.⁶⁶ thus the result also seems to support that the nucleation mechanism is heterogeneous and that nucleation is taking place progressively. From eqn. (2.2) the hydrate/solution effective surface energy can be calculated by inserting $c^3 = 36\pi$ (cap-shaped hydrate nuclei on solid substrate), $v_h = 0.647 \cdot 10^{-27} \text{m}^3$ which is the volume of a propane hydrate building unit, thus it follows that $\sigma_{ef} = 1.11 \text{mJ/m}^2$. Such a low effective surface energy implies a heterogeneous nucleation mechanism is taking place (20mJ/m^2 for homogeneous nucleation of ice⁸³) thus the information about the nucleation mechanism given by both K and B agrees.

Using eqns. (2.3)-(2.10) the number of building units constituting the critical hydrate nucleus, the radius of the critical nucleus, the effective surface energy and the hydrate-substrate wetting angle was calculated at the different stirring rates. Calculation of the wetting angle was made under the assumption that the surface energy between hydrate and water, σ , is equal to the surface energy between ice and water. The results are summarized in Table 2.4.

Table 2.4. The number of building units constituting the hydrate nucleus and its critical size, the hydrate-solution effective surface energy and the hydrate-substrate contact angle. Numbers in parenthesis indicate the standard deviation.

RPM	S	N^*	R^* (nm)	K (s)	σ_{ef} (mJ/m ²)	ω (°)
500	1.11-1.36	294-13	4.10-1.50	130.92 (1.10)	1.11 (0.05)	10
300	1.12-1.31	255-19	3.90-1.68	118.73 (1.25)	1.12 (0.14)	10
200	1.16-1.31	341-55	4.35-2.34	69.85 (2.32)	1.58 (0.32)	13

When the stirring rate is decreased, K decreases most when going from 300 to 200 rpm whereas σ_{ef} is found to increase as stirring rate decreases. The standard deviations (numbers in parenthesis) of the K and σ_{ef} increases significantly when the stirring rate is lowered which is a result of the induction times becoming more scattered at the lower stirring rate.

The critical radius of the hydrate nucleus was found to vary between 1.50-4.35 nm which is slightly lower than those reported for the homogeneous nucleation of methane and ethane hydrate.⁸⁴ This result is however expected since heterogeneous nucleation will result in a smaller critical radius compared to homogeneous nucleation, thus again the results indicate that heterogeneous nucleation is taking place.

The surface energy in nucleation processes can in general be regarded as a dynamic surface energy and not an equilibrium surface energy.⁸⁵ This means that the surface energy is likely to depend on diffusion of gas molecules in the bulk and the geometry of the nuclei surfaces. Equilibrium conditions are reached more rapidly in fast stirred systems compared to stagnant systems. This suggests that the surface energy at a stirring rate of 500 rpm is closer to the equilibrium surface energy compared to the surface energies at 300 and 200 rpm. Consequently the surface energy found at the higher stirring rate should attain the lowest value which is also observed in Table 2.4. In literature the water-propane hydrate surface energy has been reported as 25mJ/m^2 from fitting experimental phase equilibrium data to the Gibbs-Thompson equation.⁸⁶ The water-carbon dioxide hydrate surface energy has been reported to be 1.5 mJ/m^2 using an approach very similar to the one used in this work. It is peculiar that the surface energy of water-propane found using the Gibbs-Thompson equation is even higher than the surface energy found for the homogeneous nucleation of ice bearing in mind that heterogeneous nucleation plays an important role in hydrate nucleation processes. Thus it can be speculated whether an equilibrium based model such as the Gibbs-Thompson equation is actually suitable for calculating properties which are more closely related to the kinetic mechanisms.

In Figure 2.9 the induction time data obtained from the experiments containing small amounts of PVP have been plotted according to eqn. (2.12). Typical values of $k_g = k_n = 10^{-18}\text{ m}^3$, also reported elsewhere in literature⁶⁶ have been used in the calculation of K and B . As seen there is a reasonably good linear relationship for the two data sets. In Table 2.5 the kinetic parameter, the number of building units constituting the critical hydrate nucleus, the radius of the critical nucleus, the effective surface energy and the hydrate-substrate wetting angle are shown.

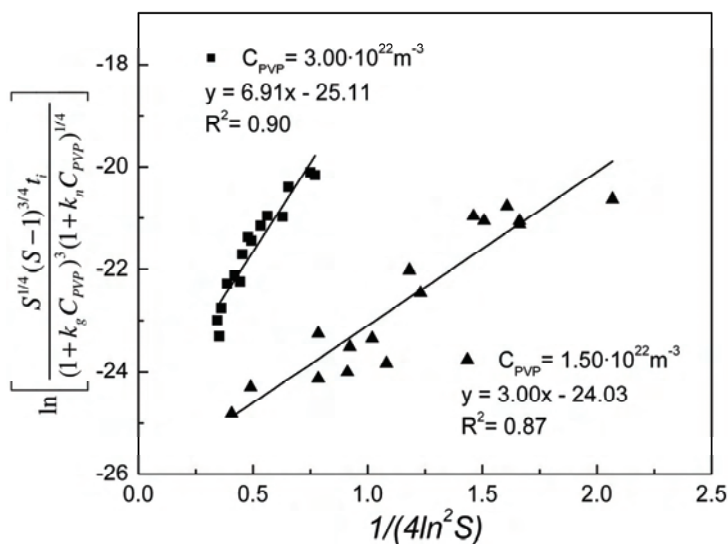


Figure 2.9. Plot of the induction time versus the supersaturation ratio for nucleation of propane hydrate in aqueous solutions containing polyvinylpyrrolidone (PVP) at 273.75 K and 500 rpm. When the PVP concentration is increased the slope increases whereas the intercept decreases.

As seen in the figure the induction times become decreasingly scattered as more PVP is added to the system.

Table 2.5. Critical size of hydrate nucleus, hydrate-solution effective surface energy and hydrate-substrate contact angle found using the induction time model on the nucleation data obtained from the nucleation experiments containing polyvinylpyrrolidone (PVP). Numbers in parenthesis indicate the standard deviation.

C. PVP (wt%)	S	N^*	R^* (nm)	K (s)	σ_{ef} (mJ/m ²)	ω (°)
0	1.11-1.36	294-13	4.1-1.50	130.92 (1.11)	1.11(0.05)	10.0
$1.50 \cdot 10^{22}$	1.42-2.19	143-12	3.33-1.57	$3.35 \cdot 10^{-12}$ (4.7310^{-14})	2.85(0.28)	20.4
$3.00 \cdot 10^{22}$	1.77-2.35	75-22	2.76-1.93	$9.44 \cdot 10^{-13}$ ($1.10 \cdot 10^{-14}$)	3.76 (0.33)	25.2

From the table it is seen that addition of PVP to the aqueous phase causes the kinetic constant K to decrease substantially compared to the K value found when no PVP is present. Actually the K value is even lower than when homogeneous nucleation is taking place ($K = 5$ ns). PVP is seen to cause the effective surface energy to increase with PVP concentration. This implies that adsorption of PVP on hydrate nuclei does not take place

as this would result in a decrease of the surface energy according to the equilibrium adsorption theory. It can also be argued that adsorption of PVP molecules on the nuclei surface is not possible because the lifetime of the nuclei is too short for the additive to reach them by diffusion and because their surface areas are too small.⁸⁷ The reasons why σ_{ef} increases when PVP is added could be many. It is possible that the contact angle between the hydrate nuclei and substrate will change if for example PVP adsorbs onto any nucleation sites on the substrate. Another possibility is that the additive itself is a type of nucleation site however less active compared to the original nucleation sites (by original is referred to the nucleation sites present in an aqueous solution not containing additives). The effective surface energy of the nuclei that forms on this type of substrate could indeed be different from that of nuclei forming on the original substrate. In fact if the substrate is less active this will result in a higher hydrate-solution effective surface energy and larger supersaturation/critical nucleus size ratios which are indeed also observed from Table 2.5.⁸⁷ As the model does not account for molecules that themselves act as nucleation sites this last consideration should be perceived only as a suggestion for the inhibiting mechanism of additives like PVP.

2.5 Improving induction time measurements for kinetic hydrate inhibitor testing

As was discussed in the introduction, using LDHIs to manage hydrate formation offers several advantages over TIs; for example low chemical usage and savings in OPEX and CAPEX. Even so their use in oil and gas field applications has been limited due to their cost or because of environmental restrictions.²⁶ Furthermore the oil and gas industry is traditionally rather conservative and has been slow to switch to LDHIs compared to TIs. While it is relatively fast, for example by using thermodynamic models, to obtain information about the amount of TI required to suppress the hydrate coexistence temperature, using LDHIs to prevent hydrate formation is associated with uncertainties arising from the stochastic nature of hydrate nucleation¹² exemplified by the relatively high scattering among the data points presented in Figure 2.6 and Figure 2.7. In this

context it is important to establish methods by which it is possible to obtain reliable information about the efficiency of LDHIs. This has already been realized by a few groups in academia and industry who have proposed methods for improving the reproducibility of hydrate induction times. This is very useful in the assessment of how effective KHIs are at preventing hydrate formation.^{57,75}

This section begins with testing three different experimental approaches to obtain more reproducible hydrate induction times from stirred cell experiments. Both sI and sII hydrate nucleation experiments have been conducted and the effect of NaCl and heptane as well as two KHIs on the induction time has been quantified. To investigate the effect of the driving force on the induction time and the performance of the KHIs the three-phase boundary of the various hydrate forming systems was measured experimentally.

2.5.1 Experimental section

Apparatus. The nucleation experiments were conducted in a high-pressure stainless steel cell with a volume of 280 cm³ and a maximum operating pressure of 100 bar. A schematic of the cell is shown in Figure 2.10. Gas can be charged or discharged through a valve which is attached to the cell lid. A Pt-100 (± 0.01 K) measures the temperature inside the cell and the pressure is measured using a pressure transducer (BD Sensors, 0-100 bar, 0.25 % FSO). The cell is surrounded by a cooling jacket and temperature in the cell is controlled by circulating coolant using a Julabo F25 cooling bath. A magnet bar is placed inside the cell which is rotated by a stir plate located below the cell ensuring that the liquid phase in the cell can be well agitated. Hydrate formation can be observed visually through two high quality glass windows. A safety valve is attached to the cell which will open if the pressure exceeds 100 bar.

Methods. Measurement of the hydrate dissociation point followed closely the procedure detailed by Tohidi and coworkers i.e. after hydrate had formed in the cell the temperature was increased in steps of 1 K while ensuring that equilibrium was obtained in each temperature step until the hydrate had completely melted.^{88,89}

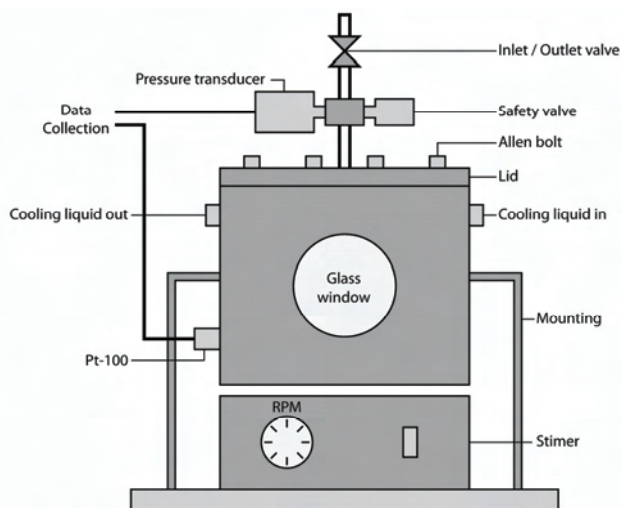


Figure 2.10. Schematic of the high pressure stainless steel cell in which the nucleation experiments of gas hydrates took place.

Three methods were applied when measuring the induction time of gas hydrate formation. Common for all three methods was that they were performed at constant temperature (≈ 277 K) although the pressure varied from experiment to experiment depending on the subcooling required. Hydrate formation was identified as a sudden decrease in the cell pressure as was shown in Figure 2.5. In all experiments the total liquid volume used was 60 cm^3 . In most cases only water was used. Where a liquid organic phase was present this constituted 50 % of the total volume. Before each experiment the cell was cleaned with deionized water and flushed several times with gas before the cell was loaded with liquid and pressurized to the experimental pressure. During an experimental run the pressure and temperature in the cell were recorded every 60 s using a computer. Each experiment was conducted 5 times. The first method (A) relied on simply mixing liquid and the gas of interest (stirring rate of 450 rpm) at the desired pressure and temperature and then waiting for hydrate to form. In the second method (B) a small amount of silica gel ($0.02 \text{ g}/60 \text{ cm}^3$ liquid) was introduced in the hydrate forming system, since it has been proposed that in particular the heterogeneous nature of the nucleation process is assumed to play an important role in the stochastic nature of gas hydrate formation as mentioned previously. The idea behind this procedure

is that the impurities added mask the effect that unavoidable impurities like dust particles have on the induction time whereby more reproducible induction times should be obtained. The third method (C) used was basically identical to the hydrate precursor procedure proposed by Duchateau and coworkers.⁷⁵ In the first stage hydrate formation was allowed to take place for 10 min to ensure that a small amount of hydrate had formed. The stirring was then stopped and the temperature increased to 2.5 K above the hydrate coexistence temperature. The hydrate was then allowed to melt for 2 hours and towards the end the liquid phase was inspected visually to observe if any visible crystals appeared in the liquid phase. After the hydrate had melted the temperature was decreased to around 277 K and stirring was started, signalling the beginning of an induction time measurement.

Materials. The experiments were performed using deionized water (0.6 μ S/cm). As a model system of seawater an aqueous solution of 3.5 wt % NaCl was prepared. The NaCl (>99.5% purity) was purchased from Merck. In the experiments investigating the effect of having a liquid organic phase present in the hydrate forming system heptane supplied by Sigma-Aldrich (>99% purity) was used. Methane (99.995 % purity) was used in the sI hydrate experiments and was supplied by AGA while natural gas was used in the sII hydrate experiments and was supplied by Air Liquide. The composition of the natural gas can be found in Table 2.6. As a model impurity silica gel grade 62 with a particle size of 60-200 mesh supplied by Sigma-Aldrich was used. The ISP used was type III HPLC12 (7.027 kDa) which can be identified in the fish ocean pout. The ISP has been produced from a yeast fermentation and was supplied by UNILEVER as a complex solution containing small amounts of salts, sugars and proteins (other than ISP) however in a concentration range that will not affect the phase boundary of ice or gas hydrates.⁹² PVCap (MW 21.4000) was kindly supplied as a dry purified formulation by the Center for Hydrate Research at Colorado School of Mines.

Table 2.6. Composition of natural gas.

Compound	Mole %
Oxygen	0.24
Nitrogen	3.68
Methane	87.81
Ethane	6.60
Propane	1.22
n-butane	0.17
i-butane	0.22
n-pentane	0.02
i-pentane	0.03
n-hexane	0.01

2.5.2 Results and discussion

In Figure 2.11 the three-phase coexistence curves of the sI and sII hydrate forming systems investigated in this work are presented in a pressure versus temperature plot. The hydrate coexistence points of methane hydrate have been taken from the literature⁹³ whereas the data points labeled NG (Natural Gas) were measured as a part of this work.

The figure shows that the sII natural gas hydrate is stable at significantly higher temperatures than the sI methane hydrate. Addition of NaCl to the aqueous phase (3.5 wt %) is seen to shift the hydrate phase boundary to lower temperatures (approximately 2 K) compared to the NG + water hydrate forming system i.e. the NaCl works as a thermodynamic inhibitor. When heptane is introduced in the system the phase boundary is also seen to shift to lower temperatures (3.5 K) compared to the NG + water system. In this case the shift is caused by a change in the gas phase composition, i.e. the solubility of the heavier natural gas compounds (e.g. propane etc.) in heptane is relatively larger compared to the solubility of the lighter compounds (e.g. methane). This has also been pointed out by other researchers.⁹⁴ When introducing both NaCl and heptane in the NG + water system the shift observed for the hydrate phase boundary is basically proportional to the combined individual effects of NaCl and heptane, respectively.

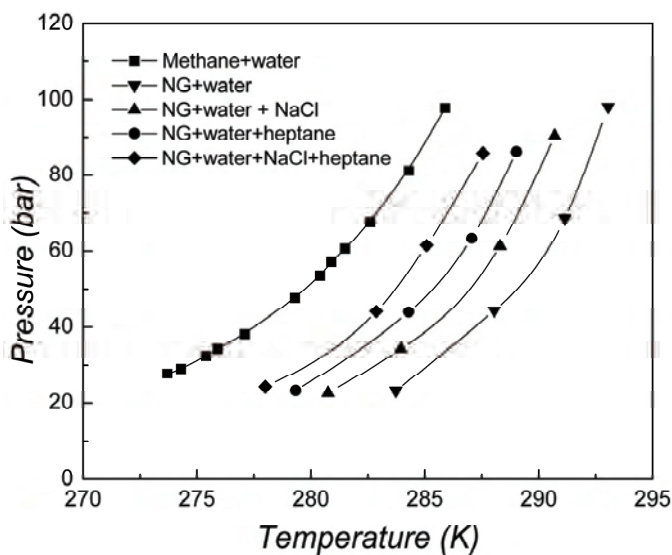


Figure 2.11. The three-phase coexistence curves of the various hydrate forming systems studied in this work. The data points shown for the methane hydrate coexistence curve have been taken from literature while the natural gas hydrate coexistence curves have all been measured experimentally as a part of this work. In the experiments involving NaCl a 3.5 wt % NaCl solution was used. In the experiments where heptane was introduced in the system the liquid phase consisted of 30 cm³ water and 30 cm³ heptane.

A third order polynomial expressing the coexistence pressure as a function of temperature has been fitted to the hydrate coexistence data and the polynomial coefficients, as shown in eqn. (2.17), found by this procedure are provided in Table 2.7:

$$P = aT^3 + bT^2 + cT + d \quad (2.17)$$

Using these coefficients the subcooling of the individual nucleation experiments has been calculated and used as a measure for the driving force for hydrate formation. Note that the coefficients are only valid for the pressure and temperature range for which they were obtained.

Table 2.7. Polynomial coefficients for use in eqn. (2.17) found by fitting a 3rd order polynomial to the hydrate coexistence data for the systems methane-water, natural gas - water, natural gas - 3.5wt % NaCl aqueous solution, natural gas – water - heptane. The volume fraction of water and heptane was 1:1.

System	<i>a</i>	<i>b</i>	<i>c</i>	<i>d</i>
CH ₄ +water	0.0133921	-10.9025232	2960.9782186	268248.18028
NG+water	0.1222138	-105.0686601	30113.7738150	2877334.78524
NG+water+NaCl	0.0526866	-44.6146610	12596.6461509	1185827.95907
NG+water+heptane	0.0776602	-65.8868017	18637.6835017	1757803.87416
NG+water+NaCl+heptane	-0.0037241	3.6802218	-1181.7666906	124146.53418

In Figure 2.12 the induction time measurements involving methane hydrate are presented. The error bars indicate the standard deviation of the induction time and the numbers in parenthesis are the relative standard deviations.

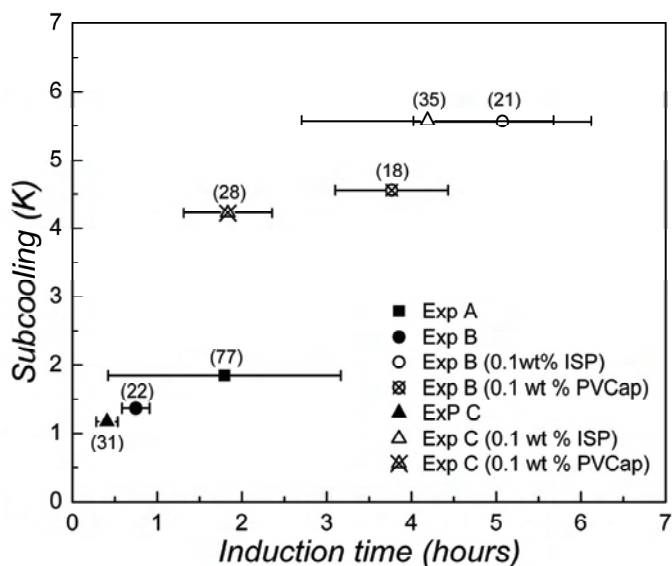


Figure 2.12. Plot of the subcooling versus the methane hydrate induction time. The concentration of the ocean pout ice-structuring protein (ISP) and polyvinylcaprolactam (PVCap) was 0.1 wt %. Each experimental point is based on 5 measurements from which the standard deviation (error bar) and the relative standard deviation (number in parenthesis) have been calculated. All experiments were performed around 277 K. It is clear that using method B and C drastically decreases the standard deviation of the induction time. Addition of ISP or PVCap prolongs the induction times though the subcooling has increased as well.

As seen the standard deviation of the methane hydrate induction time is quite significant when just mixing water and methane as done using method A. However adding small amounts of silica gel to the liquid phase as done in method B or by applying the hydrate precursor procedure as done in method C brings the standard deviation of the induction time down dramatically. It is also noted that using method B and C the induction time is shorter compared to the induction time obtained using method A despite the fact that the subcooling of experiments B and C was actually lower than the subcooling of experiment A. This is not surprising since to some extent the procedure applied in methods B and C corresponds to a type of crystal seeding - a well known technique to promote crystal formation.⁵⁸

Since methods B and C result in short induction times relative to the subcooling, using these methods will serve as a sterner test of the KHIs, thus the results obtained from these experiments will be more trustworthy in terms of better statistics and represent a worst case induction time, compared to the induction times obtained using method A. Addition of ISP or PVCap to the aqueous phase (0.1 wt %) is seen to prolong the induction times of methane hydrate and at the same time a significant increase in the subcooling is required to obtain hydrate formation within a reasonable time period, suggesting that both molecules are quite active KHIs. Addition of PVCap to the aqueous phase results in slightly shorter induction times, however also at slightly lower subcoolings compared to when ISP is added i.e. the ISP is a better KHI of methane hydrate compared to PVCap. Interestingly it is clear that the same good statistics of the induction times are obtained using methods B and C despite ISP and PVCap have been added, compared to the case when no inhibitors were present. Comparing the statistics obtained using method B and C it is seen that method B seems to result in slightly better reproducibilities of the induction time. The marginally worse statistics of the induction times obtained from method C are likely a result of difficulties in controlling the amount of hydrate precursors present in the aqueous solution after hydrate melting has taken place. If the number and size of hydrate precursors varies from experiment to experiment it will correspond to different degrees of crystal seeding and will most likely result in more scattered induction times. As has also been discussed elsewhere²¹ the induction time obtained using method C is relatively sensitive to the degree of superheating and melting time at which the initial melting

process takes place in order to produce the hydrate precursors - an observation which supports the preceding discussion.

Considering that method B is simpler and less time-consuming than method C, the induction time measurements for sII natural gas hydrate were performed using method B. In these experiments the effect of ISP and PVCap on the formation of sII hydrate was quantified. In some of the experiments deionized water was substituted with model seawater whereas in other experiments heptane was added to the hydrate forming system. This was done to test their effect on the induction time and on the performance of the KHIs. The results of these experiments are shown in Figure 2.13.

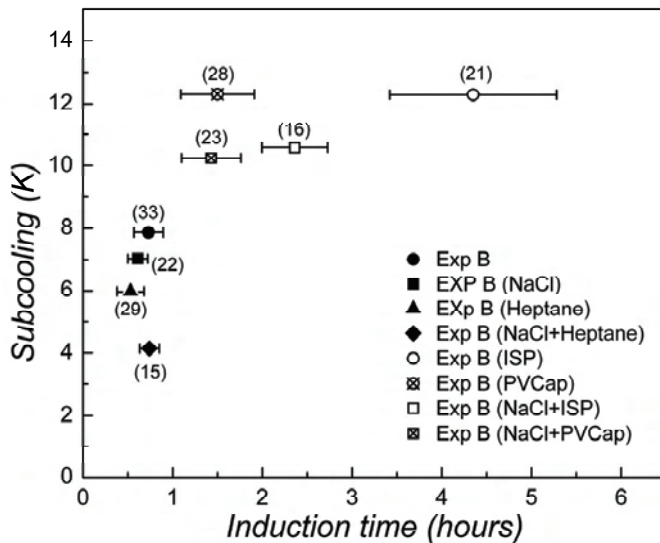


Figure 2.13. Plot of the subcooling versus the natural gas hydrate induction time. The concentration of ocean pout ice-structuring protein (ISP) and polyvinylcaprolactam (PVCap) was 0.1 wt %. The salt concentration was 3.5 wt %. The heptane to water ratio was 1:1 by volume. Each experimental point is based on 5 measurements from which the standard deviation (error bars) and the relative standard deviation (number in parenthesis) have been calculated. All experiments were performed around 277 K. As seen NaCl and heptane promote hydrate nucleation while PVCap and ISP inhibits the nucleation quite effectively.

First of all, it is worthwhile noticing that all experiments show equally good statistics thus the seeding procedure seems to be an appropriate method for improving the reproducibility of the hydrate induction time of sII hydrate formation as well. Another

interesting observation here is that apparently the subcooling required to form sII hydrate is much higher compared to the case of sI. Adding NaCl or heptane to the liquid phase causes the induction time to shorten a little while at the same time the subcooling is also seen to be lower compared to the case where only water and natural gas are present. When adding both NaCl and heptane to the hydrate forming system the subcooling at which hydrate formation is detected is even lower, while the induction time does not change significantly. This suggests that NaCl and heptane both act to promote hydrate formation i.e. NaCl, although working as a TI, increases the formation rate of hydrates, at the concentration used here. Similar observations have been made with low concentrations of methanol.⁹⁷

Only a very few studies have focused on the effect of liquid hydrocarbons on the formation kinetics of gas hydrates, and the conclusions reached from these studies are contradictory i.e. both increased⁹⁸ and decreased^{99,100} formation rates were observed when a liquid reservoir crude or a model system hereof is introduced in the hydrate forming system. This is perhaps not surprising since the compounds contained in reservoir crudes are many and varied, possibly including also natural kinetic hydrate inhibitors or promoters. On the other hand, when introducing only heptane as a liquid hydrocarbon model in a hydrate forming system, studies have only reported increased formation rates - in agreement with the findings in this work.^{98,101} Obviously heptane does not contain any promoters nor inhibitors so the increased formation rate must be ascribed to other effects. Possibly since the gas becomes relatively richer in methane when heptane is present, higher pressures are required to obtain the same subcooling, resulting in the increased formation rate despite the fact that sII formation is still favored.

In the induction time measurements involving KHIs it seems that the ISP is also a better KHI of sII hydrate compared to PVCap i.e. at the same inhibitor concentration (0.1 wt %) and at a similar subcooling (≈ 12 K) the ISP prevents hydrate formation for almost 4.5 hours whereas PVCap only prevents hydrate formation for 1.5 hours. When NaCl is present the ability of both ISP and PVCap to prevent hydrate formation is weakened. In Figure 2.13 this is seen as a decrease in the induction time compared to the experiments not containing NaCl while at the same time the subcooling in the NaCl containing experiments is around 2 K lower than in the experiments not containing NaCl. Such

observations have also been made previously for a system composed of natural gas + NaCl solution + PVCap.¹⁰² Though in that work NaCl was not observed to promote hydrate nucleation, based on the findings here we propose that the decrease in KHI activity of ISP and PVCap is due to the counteracting, promoting effect of NaCl. The reason why no induction time is reported for the systems containing heptane with either ISP or PVCap was that when heptane and ISP/PVCap was present it seemed that a hydrate slurry formed instantly and remained stable, i.e. the liquid phase containing the hydrate particles could be stirred for days, even for quite high subcoolings. This is a rather unexpected effect considering that ISP and PVCap are regarded as KHIs and not AAs.

Interestingly when comparing how the inhibitors perform for the sI and sII hydrate systems formed from pure water alone the trends are qualitatively rather similar, although with one important difference, namely that the subcoolings in the sII hydrate experiments are much greater compared to those required to form sI hydrate within a reasonably short period of time. This is also true even in the case where no inhibitors are present as also mentioned above i.e. methane hydrate formation is seen at subcoolings as low as 1-2 K while natural gas hydrate formation requires a subcooling of around 8 K. This indicates that the nucleation and formation rate of sII hydrate is much slower than sI. As mentioned above one explanation why sII hydrate formation is slower than sI could be due to the effect of pressure i.e. it requires a substantially higher methane pressure (45 bar at 277 K) to obtain 1-2 K subcooling compared to the pressure of natural gas (30 bar at 277 K) required to obtain 8 K of subcooling. One consequence of this is that there will be fewer gas molecules present at the gas-liquid interface where hydrate nucleation is hypothesized to take place, compared to when only methane is used as a hydrate former. It is also possible that the slow formation of sII hydrate arises from structural limitations: while the sI and sII hydrate lattice share the small 5¹² cage they differ in that the large cage of sII contains 4 hexagonal rings while the large cage of sI only contains two hexagonal rings. It has been speculated that this will cause the large cage of sII to have a larger energy barrier of formation compared to the large cage of sI.¹⁰³ If this is the case this would also explain why sII hydrate forms at a slower rate than sI hydrate.

Based on these considerations one could speculate that the reason why most KHIs are considered to perform best for sII hydrates (i.e. they are effective at a higher degree of subcooling) is likely to be due to sII having much slower formation kinetics compared to sI. This is true when methane is used as a sI former however the same conclusions have been reached from comparing formation rates (both induction time and growth rates) of sI ethane hydrate and a sII natural gas hydrate.¹⁰⁴ Consequently this suggests that the evaluation of the true inhibitor potential of KHIs might not be adequately described by just stressing the maximum subcooling at which the KHIs will be active since this will vary depending on the hydrate structure formed, gas composition etc. Using other driving force expressions will not alter this conclusion thus it is actually a bit difficult to discuss which driving force expression is more correct to use in the evaluation of KHI effectiveness as done in section 2.2. When testing the KHI activity it may be more informative to look at the excess subcooling/driving force that the hydrate forming system can tolerate upon introducing KHIs in the system. This is the idea behind a constant cooling rate experiment, although using this methodology, information about the induction time, which is crucial if the KHI is to be implemented in field applications, is lost. Instead one could choose an arbitrary reference point (any given pressure and temperature) for which a measurable induction time is obtainable. The effect of the KHI in terms of excess subcooling and prolonged induction time compared to this reference point might then make it easier to compare directly and quantitatively rank the activity of various KHIs. Using such an approach, looking at the results of method B, it is found that the difference in subcooling between the ISP inhibited and the uninhibited methane hydrate experiments ($5.48-1.17 = 4.31$ K) is almost identical to the difference in subcooling between the ISP inhibited and the uninhibited natural gas hydrate experiments ($12.04-7.90 = 4.14$ K). The differences in induction times between the inhibited and the uninhibited systems are found to be 4.32 and 3.63 hours for methane and natural gas, respectively. This suggests that the ISP is a slightly better KHI of methane hydrate compared to natural gas hydrate. For PVCap the excess subcooling and induction time prolongation for methane hydrate was 3.24 K and 3.01 hours, respectively while it was 4.38 K and 0.78 hours for natural gas hydrate. Given that there is almost 1 K difference in subcooling between the methane and natural gas hydrate experiments it is difficult to

determine which of the structures PVCap works best for. Previous studies have found that PVCap has worse subcooling performance for sI compared to sII¹⁰⁴ although in that work the faster formation rate of sI was not accounted for in reaching this conclusion. If a conclusion should be drawn from the results presented in this work, it seems that PVCap works more or less equally well for sI and sII hydrate.

As a final test of the KHI potential of ISP and PVCap the concentration was increased to 0.5 wt% which is close to the concentration at which KHIs are used in field applications.¹⁰ Stirred cell experiments using method B were performed at various pressures and at temperatures around 277 K to determine the subcooling range at which the induction time will vary in the time interval between 0 and 24 hours. 11 experiments were conducted for the PVCap and ISP systems. The results are shown Figure 2.14.

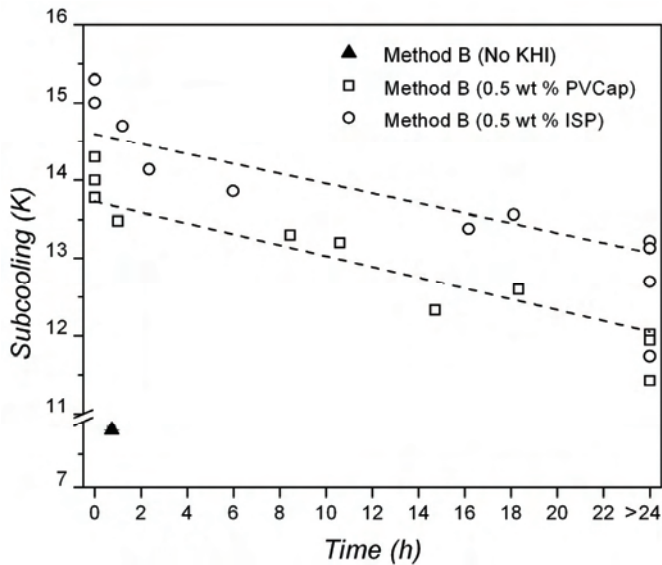


Figure 2.14. Plot of the subcooling versus the natural gas hydrate induction time using method B (adding silica as crystal seeds). The concentration of ISP and PVCap was 0.5 wt %. All experiments were performed around 277 K. The dashed line indicates the best fit of the data points which lie between an induction time of 0 and 24 hours.

For PVCap the subcooling at which the induction time exceeds 24 hours was found to be 12 K while for the ISP it was found to be 13.2 K i.e. again the ISP is found to perform better than PVCap as also observed in the previous experiments. In general the

subcooling versus induction time relationship follows the expected trend i.e. the higher subcooling yield lower induction times and also indicated by the negative slope of the best fit straight line of the data (dashed line in the plot). Obviously it is not possible to assess if this is also true in the low subcooling range since the experiments lasting more than 24 hours were terminated if hydrate had not yet formed. Interestingly the subcooling range for which the induction time goes from 24 to 0 hours for PVCap is much similar to what is found for the ISP i.e. 12 to 13.8 for PVCap and 13.2 to 15 K for the ISP also indicated by the two regressed lines having an almost similar slope. This also indicates that the ISP is indeed a better KHI than PVCap. It should however be pointed out that the PVCap used in this work has a rather high molecular weight and studies have shown that as the molecular weight of PVCap decreases it's efficiency as a KHI increases. Based on the findings it is proposed that if the ISP can be made available in large amounts and at a price comparable to PVCap it should be as good a KHI as PVCap but with one main advantage of being environmentally benign. Unfortunately it has not been possible to get information about the production of ISP or the possibility for scaling up the process and the effect that this will have on production costs.

2.6 Evaluation of kinetic hydrate inhibitors using high-pressure differential scanning calometry

When searching for new types of KHIs it is often advantageous to use equipment which allows carrying out fast tests using relatively small inhibitor amounts. One of the reasons for this is that when new KHI molecules are synthesized this process at the lab scale is often not optimized resulting in poor yields or low purities. This is in particular true for biological molecules such as ISPs. When a new ISP is discovered in for example an insect, the ISP is first extracted from hundreds of insects and then purified, leading to very small (microgram) yields. ISPs can be produced at a larger scale when expressed as recombinant proteins, however most often production of ISP by this method at the lab scale also results in quite small amounts (milligrams). For this reason testing the KHI

potential of these compounds using stirred cell experiments is not practical since the amount of KHI required is too large.

Apparatuses such as the ALTA or the high-pressure DSC have the advantage that they only need small sample loadings to study the nucleation of gas hydrates. However as also discussed in section 2.3 both the ALTA and the high-pressure DSC require a constant cooling rate procedure to obtain good statistics for the nucleation event and exactly how this relates to the induction time is yet to be investigated. Furthermore very high subcoolings (12-35 K) are required to facilitate nucleation using these methods and may result in the KHIs either being less or not active at all.

In this section, high-pressure DSC has been applied to study the nucleation of methane hydrate. This has been done using the hydrate precursor method (method C in section 2.51) to obtain nucleation events at lower subcooling and a better reproducibility of isobaric-isothermal induction time measurements. Using this method the effect of the subcooling on the induction time has been investigated and the KHI potential of two compounds was assessed. The KHIs used were PVCap and an ISP obtained from the Danish Bark beetle. This ISP has recently been discovered and it has shown to cause freeze resistance of water down to approximately 263.15K which makes it one of the most efficient ISP isolated to date, thus possibly having a high KHI potential.¹⁰⁵

2.6.1 Experimental Section

Apparatus. A high-pressure micro DSC (μ -DSC) VIIa¹⁰⁶ (Setaram Inc.) was used to conduct the nucleation experiments of methane hydrate. In Figure 2.15 a schematic of the experimental set-up is shown. The μ -DSC is connected to gas bottles through a high pressure panel through which gas can be charged to the sample and reference cells. Pressure in the cells can easily be increased or decreased by a piston hand pump.

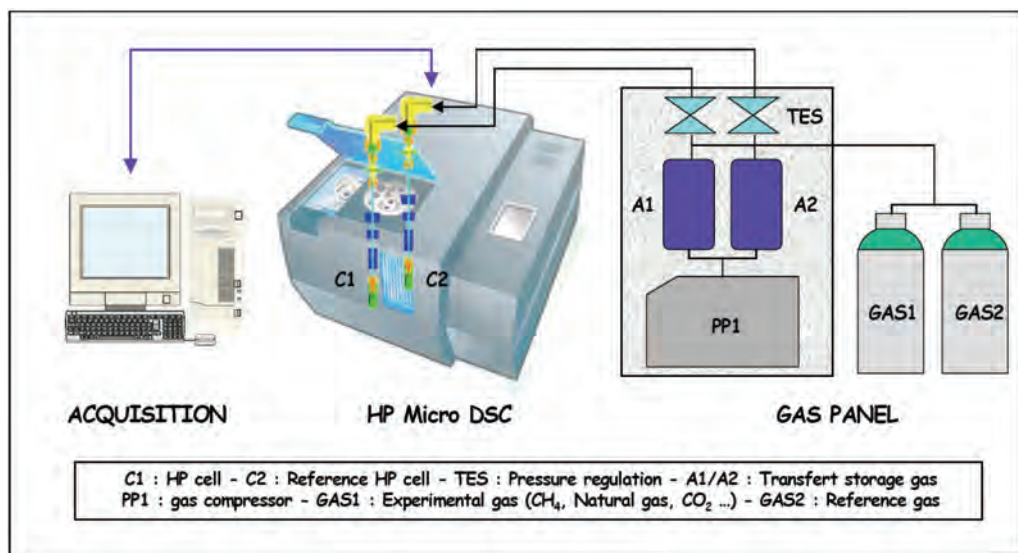


Figure 2.15. High-pressure micro differential scanning calorimetry (μ -DSC) VIIa with high-pressure panel and data acquisition.

The sample and reference cells of the μ -DSC are composed of Hastelloy C276, a metal alloy highly resistant to both oxidizing and reducing substances. Both cells are connected to the high pressure panel with twelve stainless steel 1/8" tubing. The volume of each cell is 0.5 cm³ with a maximum liquid loading of 0.2 cm³; the small sample volume is extremely advantageous because it diminishes heat transfer effects through the sample itself.¹⁰⁷ The furnace uses a two-stage Peltier thermo-element allowing the apparatus to operate in a temperature range from 228.15 to 393.15 K with an uncertainty of about +/- 0.1°C. The apparatus should never be held above 353.15 K or below 228.15 K. The resolution of the heat flow is 0.4 μ W.¹⁰⁷

The μ -DSC measures the temperature difference, ΔT , between the sample and the reference cells. ΔT is measured by thermocouples linked to each cell and the heat flow required to achieve a zero temperature difference between the cells, ΔT , is calculated.¹⁰⁸ As any change in enthalpy, such as a phase transition, of the sample occurs, a resulting heat flow change will be observed. From performing cycles of cooling and heating of the cells (enabled by Peltier elements) the heat flow is output as a function of time in a thermogram. An exothermic occurrence such as the freezing of ice will result in positive heat flow while an endothermic event such as ice melting will give a negative heat flow.

A schematic of the DSC thermogram is shown in Figure 2.16. The labels A and B correspond to the points at which the heat flow response departs from the baseline due to an exothermic and endothermic process taking place and can for pure substances such as simple hydrates be taken as the point of formation and dissociation, respectively.

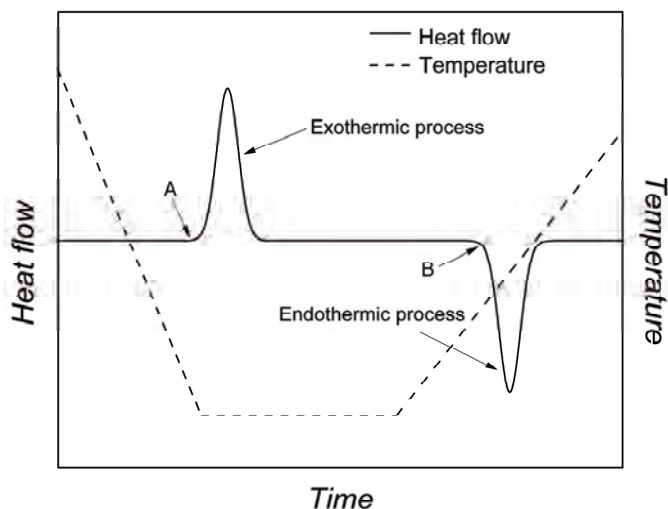


Figure 2.16. Typical differential scanning calorimetry thermogram of the crystallization and melting process. The exothermic peak indicates crystallization while the endothermic peak indicates melting.

Methods. The μ -DSC cell was loaded with between 30 and 50 mg of water or water containing PVCap or ISP. To obtain the most accurate nucleation results, proper loading of water into the sample cell is critical. The sample should be filled starting from the middle of the bottom of the cell taking care not to have any water on the cell walls. A slight meniscus should exist due to surface tension resulting in a relatively flat gas-water interface. Water on cell walls can cause multiple nucleation events to occur which is undesirable in terms of measuring the induction time of hydrate formation. Once water was loaded the lid of the cell was attached and the cell was placed in the μ -DSC. Methane gas (99.9%, Airgas) was charged to the sample and reference cells and the pressure was increased using the piston hand pump until the desired experimental pressure was obtained (100-200 bar).

Initially the sample was held at 313.15 K for three hours to allow methane saturation of the water. The temperature was then decreased to 248.5 K at a rate of 3 K/min. Once

the system reached the final temperature the temperature was held constant until nucleation occurred. In general 3 hours were found to be sufficient to obtain hydrate formation at the experimental pressures used in this work. The sample was then heated at a rate of 0.5 K/min to a temperature of about 2 K above the three-phase equilibrium temperature. The temperature was held constant at this superheating for 30-60 min to ensure that all hydrate melted. At these conditions as found in the stirred cell experiments in section 2.5 the water is likely to contain hydrate precursors which will promote hydrate nucleation once the sample is brought to hydrate favorable conditions again. The temperature was subsequently lowered to give the desired subcooling of the nucleation experiment. The typical temperature cycle and resulting heat flow response as a function of time is shown in Figure 2.17.

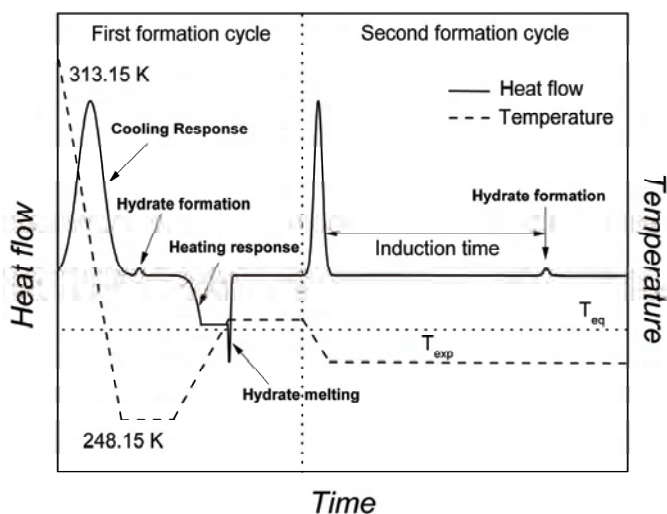


Figure 2.17. Heat flow and temperature as a function of time applied in a typical experiment utilizing the hydrate precursor method. Hydrate is first formed and melted in the first formation cycle to form hydrate precursors and then reformed in a second formation cycle during which the induction time measurement takes place.

From the figure it can be seen that upon cooling the sample to 248.15 K a large positive peak appears which is due to the heat flow response caused by the cooling process itself. After a short period of time a second heat flow signal is observed this time due to hydrate formation. The hydrate formation peak can often be observed as a small

separate peak, however in some cases it will appear as a shoulder on the cooling response peak if hydrate forms during a cooling ramp. Often this happens when cooling to very low temperatures is attempted. Upon heating the cell again a negative heat flow is observed as a response to the heating process itself. However as the three-phase equilibrium temperature of the hydrate is approached a second peak appears, because of the endothermic nature of the hydrate melting process. The temperature is maintained at moderate superheated conditions until all hydrate is melted i.e. until no heat flow signal from the melting process has been present for around 30 min. Then the temperature is decrease fast to the experimental temperature. During the second formation cycle the induction time of hydrate formation is measured as the difference in time between the points at which the μ -DSC reaches the experimental temperature until a peak due to hydrate formation occurs.

Materials. The experiments were performed using deionized water and methane with a purity of 99.97%. The PVCap (MW 21.4000) was kindly provided by the Center for Hydrate Research at Colorado School of Mines. ISP isolated from the Danish bark beetle was supplied by Prof. Hans Ramløv from Roskilde University.¹⁰⁵

2.6.2 Results and discussion

The experiments for pure methane hydrate were conducted at 100 bar. Hydrate was initially formed at 248.15 K maintaining the temperature constant for 3 hours. After this the temperature was slowly ramped to 288.15 K which is about 2 K above the three phase equilibrium temperature of methane hydrate. After 30-60 min hydrate was completely melted i.e. no heat flow, indicating melting was present. The temperature was subsequently lowered to the experimental temperature (in this case 276.15 K and 279.15 K) resulting in subcoolings of 10 K and 7 K, respectively. The results of the experiments can be seen in Figure 2.18. Only the second formation cycle is shown as the main point here is to measure the induction time.

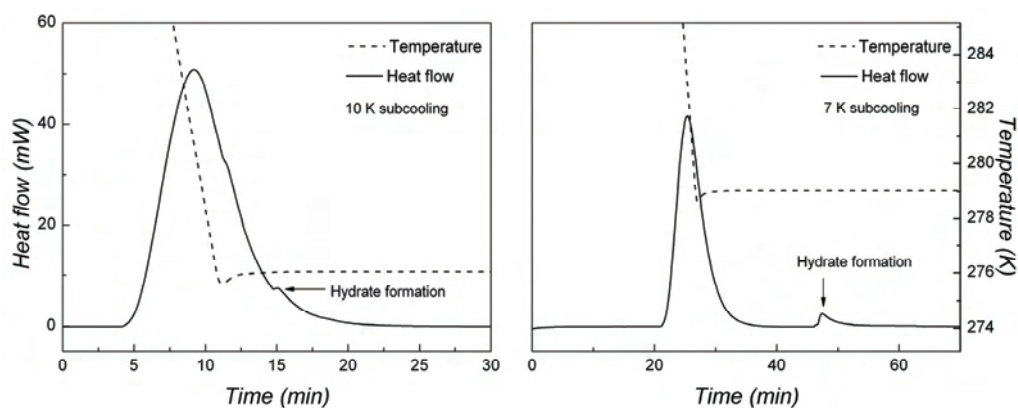


Figure 2.18. Thermograms of methane hydrate formation. Only the second formation cycle, from which the induction time is measured, is shown.

As seen in both cases hydrate formation is obtained after a relatively short time thus the precursor method seems to be quite an effective way to form hydrate in μ -DSC experiments at moderate degrees of subcooling. The experiment at 10 K subcooling is found to have an induction time of 4 min (formation peak seen as a small shoulder on the large cooling peak) while the experiment at 7 K subcooling has an induction time of 19 min (seen as a separate peak). After concluding the experiments the cell was heated up and a heat flow due to hydrate melting was in both cases found at the expected three-phase equilibrium temperature. This confirmed that the small peaks observed in Figure 2.18 were indeed due to hydrate formation. Though only two experiments were performed the results indicate that induction times obtained from isothermal μ -DSC experiments using the hydrate precursor method increase with decreasing driving force, in accordance with the trend observed in stirred cell experiments. Furthermore the fact that nucleation events were possible even at moderate degrees of subcooling makes the method promising in terms of testing/screening KHIs.

Isothermal nucleation experiments of methane hydrate in the presence of PVCap and ISP from the Danish bark beetle were performed at 150 and 200 bar. The procedure for the first hydrate formation cycle was the same as when no KHI was present. The experiments involving the ISP used a pressure of 200 bar and temperatures of 263.15–273.15 K resulting in subcoolings of 26.6–18.6 K. The concentration of the ISP in

aqueous solution was 0.015 wt%. The results of the experiments involving the ISP can be seen in Figure 2.19. Just as in the case where no inhibitor was present it can be seen that the nucleation follows the expected trend of increasing induction times as the subcooling decreases.

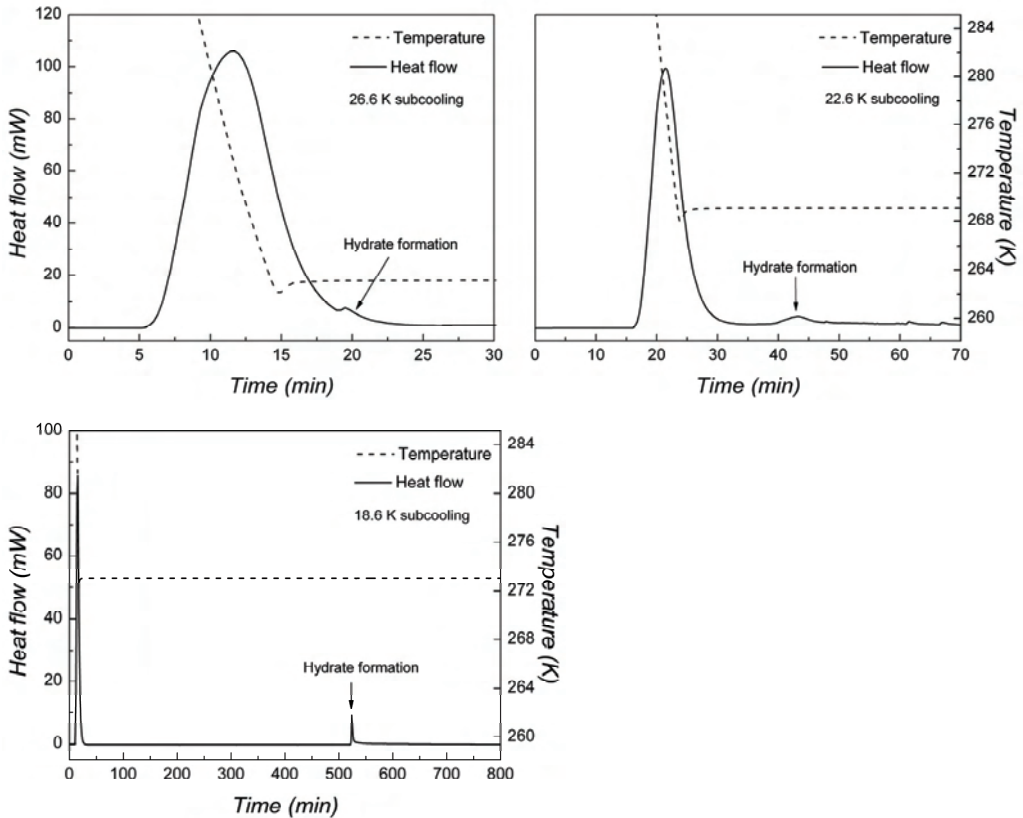


Figure 2.19. Thermograms of methane hydrate nucleation in the presence of ice-structuring protein (ISP) from the Danish bark beetle. Again it is seen that the induction time is prolonged as the subcooling decreases. However here it should be noted that the presence of ISP causes this relationship to be shifted to substantially higher subcoolings, compared to the case shown in Figure 2.17, indicating that the ISP is a quite effective kinetic hydrate inhibitor.

At a subcooling of 26.6 K the induction time is 5 min and at 22.6 K it is 16 min. At a subcooling of 18.6 K the induction time has increased to 500 min thus even though the subcooling is rather high the ISP is capable of prolonging the induction time of methane hydrate quite effectively. The samples was after hydrate formation was detected heated

up again to confirm that the heat signal observed was indeed due to hydrate formation. In all cases a melting peak around the expected hydrate dissociation point was observed. In none of the cases ice formation had appeared as this would have resulted in a melting peak around 273.15 K.

Experiments using a 1 wt% aqueous solution of PVCap were conducted at 150 bar and temperatures of 277.15 K and 281.15 K resulting in subcoolings of 8 K and 12 K, respectively. No hydrate formation was observed during the 15 hours that an experimental run lasted. This is maybe not surprising considering that the inhibitor concentration was significantly higher although the subcooling was lower, compared to experiments involving the ISP. Due to limited time available for conducting the high pressure μ -DSC experiments unfortunately it was not possible to perform PVCap experiments at lower concentrations and higher subcoolings to favor hydrate formation and enable a better comparison of the two KHIs.

Chapter 3

Growth of gas hydrates

Once hydrate has nucleated growth of hydrate crystals commence. While the growth rate of gas hydrates depends on most of the parameters which also influence the nucleation process (stirring rate, driving force, gas composition etc.) mass and heat transfer in particular become important. Since gas hydrates contain around 15 mole % of gas which is two orders of magnitude greater than the solubility of most gases in water it is obvious that transport of gas to the hydrate surface becomes very important. In some cases hydrate growth may also be controlled by the exothermic heat of formation i.e. in cases where the water and gas phases are stagnant.

As seen in Chapter 2 KHIs delay the onset of hydrate formation quite effectively. However they may also be capable of slowing the growth kinetics. Though the most critical parameter when using KHIs in oil and gas processing is the delay of hydrate formation, growth inhibition by KHIs may act as a second protection barrier against flow line blockage. If for example KHIs can suppress the growth sufficiently so that hydrate crystals do not grow and agglomerate to large masses it is possible that the hydrates can be transported as a non-plugging suspension.

In this chapter some of the basic theories behind the growth of gas hydrates will be presented along with an overview of some of the experimental techniques which can be used to study the growth of hydrates. The results of an experimental growth study of sI and sII hydrates and their inhibition by various KHIs is presented. For this purpose a high pressure stirred cell, modified to enable measurement of hydrate growth rates at constant temperature and pressure, was used.

3.1 Hydrate growth theories

The growth of gas hydrates can be considered to be the combination of three factors; i) the intrinsic kinetics of crystal growth at the hydrate surface, ii) mass transfer of components to the hydrate surface, iii) heat transfer of heat of formation away from the growing crystal.² At the microscopic level, like nucleation, the growth mechanism is the sum of several components which are indistinguishable at the macroscopic level. Similarly to the nucleation process, the growth mechanism at the microscopic level has not been studied in the laboratory due to experimental limitations. However at the macroscopic level the growth of gas hydrates is a property which can be accessed experimentally. In Figure 3.1 a typical relationship showing the amount of hydrate formed over time at the macroscopic scale is provided.

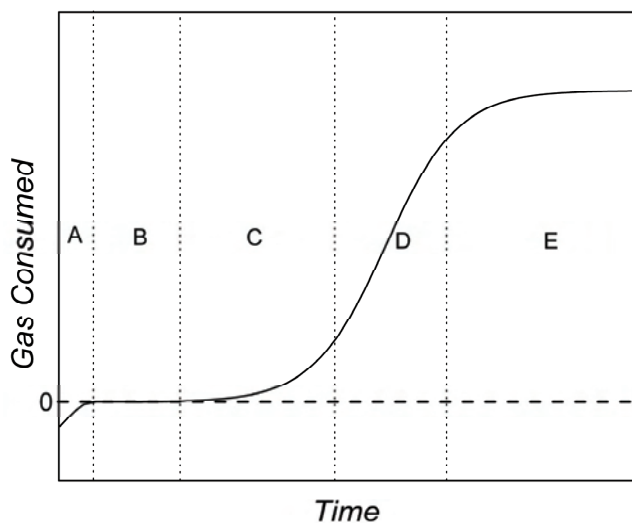


Figure 3.1. Typical relationship between the amounts of hydrate formed as a function of time here represented as the amount of gas consumed by the hydrate while growing. The horizontal dashed line indicates the basis line for the point where no hydrate has formed yet. Region A is the dissolution process of gas into the liquid (no hydrate formed yet). B is the nucleation period. C is the initial growth stage. D is the region of linear hydrate growth and E is the period where the growth levels off due to mass transfer limitations.

Firstly gas dissolves into the liquid (A) after which the nucleation period takes place (B) The dashed line placed on top of the nucleation period symbolizes the period at which no

hydrate formation has yet taken place.. The nucleation period ends once hydrate starts to grow i.e. as the continuous line starts deviating positively from the dashed horizontal line. The initial nonlinear growth period (C) is under normal circumstances very short and is simply the consequence of moving from nucleation to growth of hydrates. The initial growth period is followed by a longer period at which hydrate grows linearly (D) which has been the preferred period used in studying the growth of gas hydrates.^{14,84} Eventually hydrate formation will slow down due to mass transfer limitations i.e. limited availability of free water, lowering of surface area etc.

In most cases growth will initiate at the gas-liquid interface since the concentration of gas at the interface is significantly higher than in the bulk. The diffusion-reaction theory is the basis for describing such crystallization processes. Noyes and Whitney¹⁰⁹ proposed the following equation to describe the change in rate of crystal growth:

$$\frac{dm}{dt} = k_m A_p (C - C^{eq}) \quad (3.1)$$

where dm/dt is the growth rate (mass deposition over time), k_m is the coefficient of mass transfer, A_p is the crystal surface area, C is the concentration of solute in solution and C^{eq} is the solute equilibrium concentration. Later Berthoud and Valetton proposed that the growth of crystals was the result of two steps i.e. a diffusion process where solute molecules are transported from the bulk to the solid surface followed by a first order reaction when the solute molecules arrange themselves into the crystal lattice.^{110,111} The following modifications to eqn. (3.1) were subsequently proposed:

$$\frac{dm}{dt} = K^* A_p (C - C^{eq}) \quad (3.2)$$

With the overall transfer coefficient K^* given by:

$$\frac{1}{K^*} = \frac{1}{k_d} + \frac{1}{k_r} \quad (3.3)$$

where k_d is the mass transfer coefficient in the diffusion layer surrounding a crystal particle and k_r is the intrinsic rate constant for the surface reaction process. A similar type

of growth model can be used to describe gas hydrate growth, however certain modifications to eqn. (3.2) have to be made before the model becomes applicable for gas hydrate systems. It is useful to describe the rate process of hydrate growth in terms of gas consumed by the hydrate over time, dn/dt , since this is a direct indication of the amount of hydrate formed over time. Contrary to crystallizing systems such as salts in which only one interface exists (liquid-crystal) in gas hydrate forming systems there are two interfaces to deal with, namely the liquid-crystal and the liquid-vapor interface. Mass transfer of gas molecules from the vapor phase to the liquid through the liquid-vapor interface has shown to be of prime importance for the growth of gas hydrates in dynamic systems.⁹⁸ For this reason an additional term has been included in the overall transfer coefficient, K^* :

$$\frac{1}{K^*} = \frac{1}{A_p} \left(\frac{1}{k_d} + \frac{1}{k_r} \right) + \frac{1}{k_l A_{L-V}} \quad (3.4)$$

where k_l is the mass transfer coefficient in the liquid film and A_{L-V} is the liquid-vapor interfacial area. The product $k_l A_{L-V}$ can for example be determined experimentally from carrying out dissolution experiments such as those presented in section 2.4.3. The surface area of a hydrate particle is a function of the second moment of the particle size distribution and can be accessed from a population balance¹¹² or by laser scattering experiments.⁵¹ The solute concentration can be replaced by gas fugacities or the mole fractions of gas in water. Since the solvent (water) itself is used during the formation process this must also be accounted for in the expression. From these considerations the following model can be formulated:

$$\left(\frac{dn}{dt} \right)_{p,T} = C_{w0} K^* (x_{L-V}^i - x_{H-L}^i) \quad (3.5)$$

where C_{w0} is the initial concentration of water, x_{L-V}^i is the gas solubility in the liquid at experimental conditions, and x_{L-H}^i is the gas solubility in the liquid at L-H-V equilibrium conditions. This type of expression can be used to calculate the growth rate of simple gas hydrate forming systems at constant pressure and temperature. The model can easily be

extended to more than one hydrate forming component if the transport of components and their integration to the hydrate lattice are assumed to be independent of each other.

There has been some disagreement regarding the rate-limiting step for hydrate growth in stirred cells. While some consider the hydrate intrinsic kinetics, the left term in eqn. (3.4) to be the limiting step,^{49,51,84,113,114} others (Skovborg and Rasmussen¹¹ and Mork and Gudmundsson¹¹⁵) have proposed models that neglect the diffusion and reaction rate constant, and are solely based on mass transfer considerations i.e. they have only considered the rightmost term in eqn. (3.4). Based on the results of the growth studies obtained in this work the discussion on the rate-limiting step for hydrate growth in stirred cells is continued in section 3.4.2.

3.2 Studying hydrate growth

Different types of experimental techniques and equipment have been used to study the growth of hydrates. Such studies involve growth of single crystals mainly used for structural analysis^{116,117,118} or hydrate film growth at the water-hydrocarbon interface to provide insight into the growth mechanism.^{119,120} Other studies apply an approach very similar to the stirred cell nucleation experiment extracting information about the hydrate growth rate by measuring the amount of hydrate formed in the cell as a function of time. Table 3.1 summarizes the various stirred cell experiments which have been applied to study the growth of gas hydrates listing the advantages and deficiencies of the apparatus and method. The most simple stirred cell growth experiment is to observe the pressure drop in the cell upon hydrate formation. Since the driving force is decreasing during the experiment this will cause the growth rate also to decrease thus it is not possible to extract one rate constant specific for the system under investigation. Conducting the growth experiment at constant pressure and temperature it is possible to obtain a single rate constant for the formation process making it much easier to compare the effect of the driving force, gas composition and other parameters influencing the growth process. From such experiments it is only possible to get information about the overall growth rate (and maybe the gas dissolution rate) thus the contribution from the intrinsic kinetics to the total growth rate cannot be accessed. This is however possible by using laser

scattering capable of measuring the number and size distribution of the hydrate crystal suspension. Such apparatuses are quite expensive and some of them suffer from variable accuracy. Other analytical techniques can be combined with stirred cell experiments to provide further insight into the growth of gas hydrates, for example Raman spectroscopy.¹⁰²

Table 3.1. Description of different stirred cell experiments which have been applied in hydrate growth studies.

Method	Ref.	Description	Advantages/Deficiencies
Stirred cell (const. T)	98	From observing the pressure drop in the stirred cell caused by hydrate formation over a given period of time the growth rates of CH ₄ , C ₂ H ₆ , C ₃ H ₈ and mixtures hereof were determined.	Very simple experiment to conduct. The driving force of hydrate formation is not constant during the experiment meaning that a linear growth patterns is not observed. This type of experiment models the case of a shut-in pipeline (though stirring does simulate flow) rather than one in operation.
Stirred cell (const. P, T)	14,84, 121	Growth rates were measured at constant T and P. The growth of hydrate was observed as the amount of gas supplied to the cell to maintain a constant pressure. Growth rates have been measured for CH ₄ , C ₂ H ₆ and mixtures hereof.	This method requires additional pressure control valves and a flowmeter to measure the amount of gas which enters the cell during a growth experiment. The driving force is held constant during the experiment thus it is straight forward to assess how the driving force influences the growth rate.
Stirred cell + light scattering	49,51,76, 122,123,	Using particle size analyzers in combination with stirred cell experiments it is possible to calculate the intrinsic kinetics of gas hydrates. Particle size analysis can be done in-situ using focused beam reflectance measurement or externally by circulating the hydrate suspension through a particle size analyzer. Growth rates of hydrates formed from the following gases have been studied: CO ₂ , CH ₄ , C ₃ H ₈ , c-C ₃ H ₆ .	Allows study of the intrinsic growth rate of gas hydrates. Provides information about the critical size/surface area/number of hydrate particles during the growth period. Wide particle size distributions can be difficult to measure accurately. The method does not distinguish between hydrate particles nucleated at the water-gas interface and impurities which will cause errors to the particle sizes. Assuming spherical particles can lead to errors in size/surface area.

3.3 Growth of structure I and II gas hydrates

In this section the growth of methane hydrate and hydrate formed from natural gas is investigated. Previously growth studies of methane hydrate in the presence of KHIs have resulted in observations of a biphasic growth response, i.e. the growth initially followed a nonlinear pattern, however after a given period of time the growth pattern changed to linear.⁴⁴ Though this phenomenon has been reported it has never quantified or discussed in detail. In this section a careful analysis of the nonlinear hydrate growth caused by certain KHIs is provided. For this purpose a new experimental set-up to study hydrate growth at constant P and T has been designed.

3.3.1 Experimental Section

Apparatus. The growth experiments were conducted using a stainless steel hydrate equilibrium cell with a fixed volume of 66.5 cm^3 and a maximum working pressure of 150 bar. The complete experimental set-up can be seen in Figure 3.2.

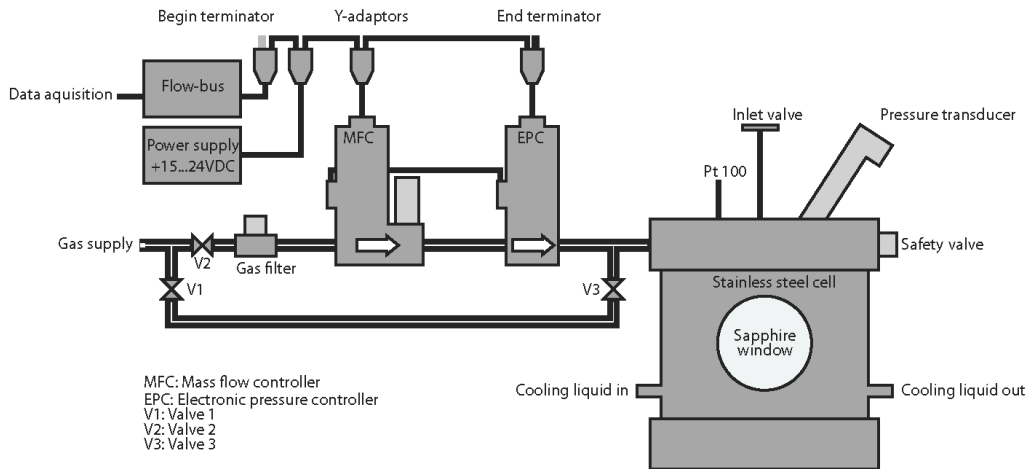


Figure 3.2. Experimental set-up showing the hydrate cell and the back pressure control and flow measurement system.

The cell allows for visual observation of hydrate formation through two sapphire windows. A safety valve is attached to the cell which opens when pressure exceeds an

adjustable value (40-100 bar). The pressure in the cell is monitored using a digital pressure sensor (EPC, Bronkhorst High-Tech) with a range of 0-100 bar (0.5% FSO). The pressure sensor is connected to a mass flow controller (MFC, Bronkhorst High-Tech El flow) with a flow range of 0-10 mln/min N₂ (2% FSO). An mln corresponds to 1 ml at 1 atm and 273.15 K. The MFC has a maximum working pressure of 100 bar and is attached to a gas filter which is attached to a gas reservoir.

The EPC and MFC work as an electronic back pressure control system which ensures that the pressure in the cell is maintained constant during an experimental run. The pressure sensor receives a digital set point from the flow-bus (High Tech RS232) and when the measured value becomes less than the set point value, i.e. pressure drops due to hydrate formation, an analog set point is sent to the mass flow meter. This causes the mass flow meter to open its valve, allowing gas to enter the cell based on the set-point. The backpressure system is PID-controlled and parameters are optimized for the systems of interest to ensure the best control. Data logging and instrument control is performed using the software FlowPlot and FlowView which is also supplied by Bronkhorst technologies. The gas supply can by-pass the backpressure control system by closing valve 2 and opening valve 1 and 3. This is done when starting up the experiment in order to quickly obtain the pressure needed in the cell.

The temperature in the cell is controlled by circulating coolant (water-ethanol solution), in a jacket surrounding the cell. The temperature is monitored by using a platinum resistance probe, pt-100 (± 0.01 K), placed inside the cell and an extra pressure transducer is attached to the cell to ensure that a constant pressure indeed is maintained during a run (BD Sensors, 0-100 bar, 0.5% FSO). The cell is placed on a stir plate which allows a stirring bar to rotate inside the cell. The pressure, temperature and the amount of gas supplied to the cell to maintain constant pressure in the cell is recorded continuously on a computer.

Methods. The cell was cleaned with water and loaded with 15 g of deionized water or water containing KHI. A stirring bar was placed in the cell. The cell lid was screwed on and the cell evacuated using a vacuum pump for approximately 1 hour. The temperature bath was adjusted so the temperature in the cell was around 277 K. Gas (methane or

natural gas) was injected into the cell, by by-passing the backpressure control system (valves 1 and 3 open and valve 2 closed), until the desired pressure was obtained.

When adding KHIs to the hydrate forming system nucleation periods can be prolonged quite significantly, as also discussed in Chapter 2, causing experiments to be very time consuming. Increasing the subcooling is one way to shorten induction times, however the effects that KHIs cause on the growth period are better expressed at low degrees of subcooling's. These requirements are contradictory, so to perform growth experiments at low degrees of subcooling we need to eliminate or shorten the nucleation period by other means. This was done by using the hydrate precursor method (method C) which was described in details in section 2.5.1. As these experiments were conducted at constant temperature slight modifications to the procedure were made i.e. forming and melting hydrate by increase and decrease in pressure rather than using the temperature. This at the same time provides a faster way to melt and form hydrate as pressure can rapidly be increased/decreased whereas it takes longer to change the system temperature. The procedure was as follows: The pressure was first increased to between 60 and 90 bar (depending on the gas used) ensuring relatively fast hydrate formation. After a short period of formation the pressure was lowered until a superheating of around 2 K was obtained whereby the hydrate would melt. During gas venting care must be taken not to form ice in the cell, however slowly releasing the gas only causes a minor drop in temperature and it never went below the ice point. The system was maintained at the superheated conditions for approximately 2 hours ensuring that all hydrate melted. Visually the liquid phase was inspected through the two sapphire windows and when the liquid phase was clear this was taken as an indication that all hydrate had indeed melted.

The pressure was then increased to the experimental pressure. Valves 1 and 3 were closed and valve 2 opened. A set-point, corresponding to the start pressure in the cell was given to the EPC. The experiment was then initiated by starting the stirring bar in the cell and starting the data acquisition. Data in terms of cell pressure, temperature and ml gas injected/min was acquired every 5 seconds.

The amount of gas injected to the cell was based on N₂ mln/min. This was subsequently converted to mln/min of methane gas using an empirical conversion factor provided by Bronckhorst technologies. The cumulative amount of methane injected to the

cell was found by integrating the output volume of the MFC over time using the trapezoidal rule. A detailed description of how to operate the equipment and perform the calculations is provided in appendix IV.

Each experimental run was repeated 3 times and the cumulative amounts of methane found for each run were combined to represent an average amount of gas consumed by the hydrate over time. The average gas consumption rate was then found by performing a linear regression of the combined data. Using the stoichiometric hydrate formulas of sI/sII the percentage of water converted from liquid water to hydrate has been calculated and used as a measure for the hydrate growth rate.

Materials. The experiments were performed using deionized water (0.6 $\mu\text{S}/\text{cm}$). Methane was supplied by AGA with a purity of 99.995 % while the natural gas was supplied by Air Liquide. The composition of the natural gas was provided in Table 2.6.

The KHIs used in this study were two ISPs i) the ocean pout ISP (for specifications see section 2.51) and the type III ISP (8.50 kDa) which can be identified in the meal worm. The meal worm ISP was found to have a relatively low purity of 10% determined from SDS-page¹²⁴ and by comparing hysteresis freezing points of various ISP solutions to literature values.¹²⁵ The two other KHIs used were PVP (MW 10,000) purchased from Sigma-Aldrich and PVCap (MW 21,400) which was kindly provided as a gift by the Center for Hydrate research at Colorado School of Mines.

3.3.2 Results and discussion

All the methane and natural gas hydrate growth experiments were performed at 277 K and under constant pressure. The back pressure control system ensured that the maximum deviation between the experimental pressure and the set-point pressure was never more than 0.25 %. Figure 3.3 shows the amount of water converted to methane hydrate as a function of time at a pressure of 56 bar and a temperature of 277 K. The data points are the averages obtained from 3 different experimental runs.

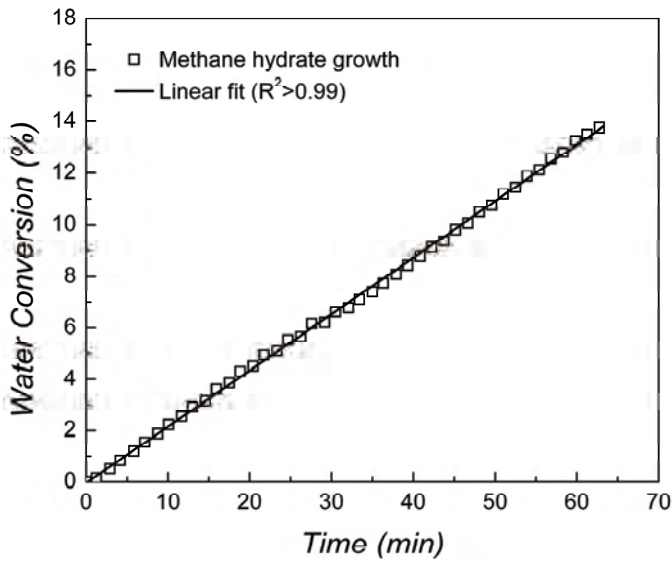


Figure 3.3 Fraction (%) of the initial amount of liquid water present converted into hydrate over time at 277 K, 56 bar and a stirring rate of 450 rpm. Solid points are the data combined from 3 experiments and the dashed line indicates the average conversion rate. As seen the reproducibility is very high given the R^2 is very close to unity.

As seen the growth of methane hydrate is linear as expected. In general low scattering among the data points is observed (the R^2 value of the linear fit of the data is very close to unity). In Figure 3.4 growth of methane hydrate from an aqueous solution containing 0.10 wt% PVCap is shown. In this case the growth pattern can be seen to be quite different than the one shown in Figure 3.3 formed from pure water i.e. initially a nonlinear growth period appears which at a given point becomes linear. The initial nonlinear growth period will be designated as growth period 1 in the following while the linear growth period will be designated as growth period 2. The distinction between growth periods 1 and 2 is quite apparent in the plot and the interface between the periods is found at around 540 min. The solid line in growth period 1 indicates the average water conversion and is based on a second-order polynomial. The dashed line in growth period 2 indicates the average water conversion found by linear regression. In Figure 3.5 the water conversion rate has been plotted as a function of time for methane hydrate formed from an aqueous solution containing small amounts of the ocean pout ISP.

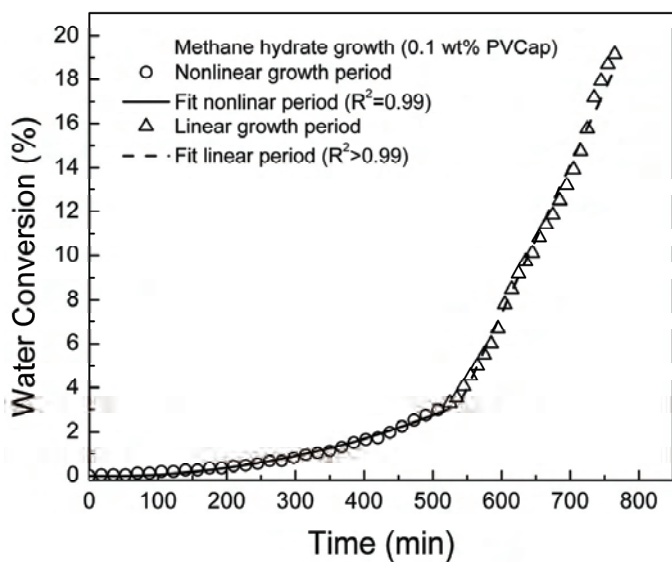


Figure 3.4. Methane hydrate growth from an aqueous solution of 0.10wt% polyvinylcaprolactam (PVCap) at 277 K, 56 bar and a stirring rate of 450 rpm. The solid and dashed lines indicate the average growth rate.

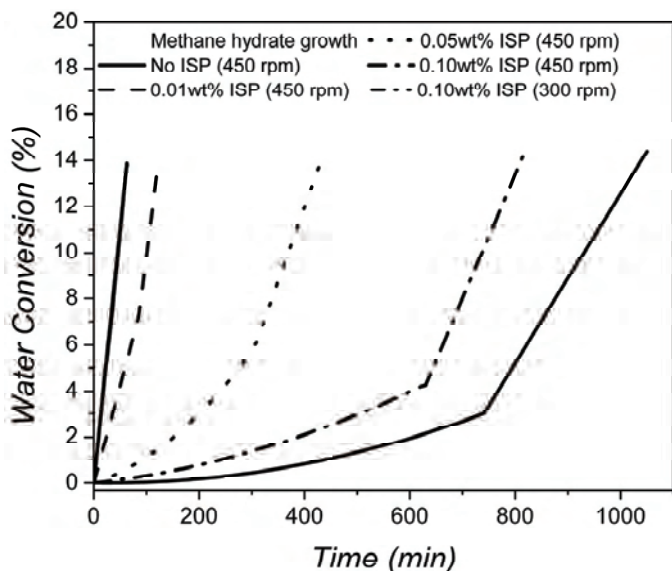


Figure 3.5. Methane hydrate growth from an aqueous solution of ice-structuring protein from the ocean pout (ISP) in concentrations between 0.01-0.1 wt% at 277 K, 56 bar and stirring rates of 300 and 450 rpm. The lines shown have been obtained from a polynomial and linear regression of the raw data with R^2 values comparable to those shown in Figure 3.4.

As seen the ISP also causes the growth of methane hydrate to be split up in two stages. Both growth periods are seen to be highly dependent on the ISP concentration i.e. increasing the ISP concentration will prolong growth period 1 and decrease the growth rate of period 2. At a stirring rate of 300 rpm growth period 1 is extended whereas the water conversion rate during growth period 2 decreases compared to the 450 rpm case.

Table 3.2 list the results of the methane hydrate growth experiments involving the various KHIs investigated. The amount of water converted to hydrate during growth period 1 has been listed for the cases where the KHI triggered the staged growth pattern. The growth rate of methane hydrate i.e. the percentage of water converted per minute has been calculated for growth period 2 for the various KHIs and the last column indicates how much the growth rate of period 2 has been decreased due to the KHIs.

Table 3.2. The percentage of water converted during growth period 1(GP 1), measured water conversion rates (%/min) during growth period 2 (GP 2) and the percentage of growth rate inhibition for the various systems investigated at 56 bar and 277 K.

System	C. (wt%)	RPM	GP 1 Conversion (%)	GP 2 Conversion rate (%/min)	GP2 Inhibition (%)
No KHI		450		0.218 ($8.70 \cdot 10^{-5}$)	
Ocean pout ISP	0.01	450	8.00	0.182 ($1.43 \cdot 10^{-3}$)	17
Ocean pout ISP	0.05	450	6.13	0.065 ($1.37 \cdot 10^{-4}$)	70
Ocean pout ISP	0.10	450	4.27	0.054 ($9.95 \cdot 10^{-5}$)	75
Ocean pout ISP	0.10	300	2.95	0.037 ($1.06 \cdot 10^{-4}$)	
Meal worm ISP	0.004	450		0.152 ($3.05 \cdot 10^{-4}$)	30
PVP	0.10	450		0.133 ($2.10 \cdot 10^{-4}$)	39
PVCap	0.10	450	3.53	0.067 (1.2410^{-4})	69

It is noted that only the ISP from the ocean pout and PVCap trigger a staged growth of methane hydrate. At a concentration of 0.10 wt % PVCap and the ocean pout ISP inhibit the growth of methane hydrate quite substantially and almost equally well, which can also be seen by comparing the data points of Figure 3.4 and Figure 3.5. PVP and the meal worm ISP only decrease the growth rate to a minor extent. While the concentration of the meal worm is probably too low to observe any significant effect on the growth rate, for PVP, where the concentration is as high as for both PVCap and ocean pout ISP this indicates that it is quite an inefficient KHI. The reason why no inhibition percentage of

growth period two can be seen for the ocean pout ISP experiment conducted at a stirring rate of 300 rpm is that no methane hydrate growth experiments at this stirring rate were conducted.

As mentioned earlier there has been some disagreement regarding the rate-limiting step for hydrate growth in stirred cells i.e. some have considered the hydrate intrinsic kinetics, while others propose that the growth is solely mass-transfer limited. To contribute to this discussion the staged growth of methane hydrate is analyzed using the overall transfer coefficient, K^* presented in eqn. (3.4) as a starting point. The relationship between the hydrate surface area and the hydrate growth rate can be found from a population balance. The population balance for a stirred batch reactor can be expressed as:

$$\frac{d\phi}{dt} + M \frac{d\phi}{dr} = B^* - D^* \quad (3.6)$$

where ϕ (m) is the particle size distribution, t (s) is the time, M (m/s) is the linear growth rate, independent of the of the particle size, r is the radius and B^* and D^* are the birth and death rates including primary and secondary nucleation, agglomeration and breakage. Clarke and Bishnoi have shown using a light scattering apparatus that the number of particles almost remains constant once hydrate started to grow which is supported by the observations of Bylov who saw a slight linear increase of the particle number in time during the growth of gas hydrates.^{49,76} Assuming that the number of hydrate particles during the growth period is constant eqn. (3.6) can be written as:

$$\frac{d\phi}{dt} + M \frac{d\phi}{dr} = 0 \quad (3.7)$$

Eqn. (3.7) can be transformed into a set of ordinary differential equations:

$$\frac{d\mu_n}{dt} = nM\mu_{n-1} \quad (3.8)$$

where μ_n is the n'th moment of the particle size distribution. The particle surface area can be expressed in terms of the second moment of the particle size distribution, μ_2 assuming that the particles are spherical:

$$A_p = 4\pi\mu_2 \quad (3.9)$$

Solving eqn. (3.8) for $n = 2$, the following expression for the second moment of the particle size distribution is obtained:

$$\mu_2 = \mu_0^0 G^2 t^2 + 2\mu_1^0 Gt + \mu_2^0 \quad (3.10)$$

where $\mu_0^0, \mu_1^0, \mu_2^0$ are the initial number, size and surface area of particles, respectively. Substituting eqns. (3.9) and (3.10) into eqn. (3.4), the overall transfer coefficient can be expressed as:

$$\frac{1}{K^*} = \frac{1}{4\pi(\mu_0^0 M^2 t^2 + 2\mu_1^0 Mt + \mu_2^0)} \left(\frac{1}{k_d} + \frac{1}{k_r} \right) + \frac{1}{k_l A_{L-V}} \quad (3.11)$$

Expressed in this form it be seen that the particle surface area is a quadratic function of time. Thus for a crystallizing system which is controlled by intrinsic kinetics it is expected that the nature of the macroscopic growth rate will be nonlinear. While KHIs, as discussed in section 2.4.3, cannot adsorb on the surface of a hydrate nucleus they have been shown capable of adsorbing to the surface of a growing hydrate crystal.¹²⁶ Effective KHIs will thus be capable of minimizing the surface area of the hydrate particle, A_p . If this is the case $A_p \ll A_{L-V}$ and as a result the intrinsic kinetics will play the dominant role for the growth of gas hydrates according to (3.4) and explains why the growth profile initially exhibits a nonlinear nature. At some point the KHIs may be overgrown by hydrate thus $A_p \gg A_{L-V}$ which results in the growth of the hydrate becoming mass-transfer limited and the growth profile becomes linear. This is at least how the staged growth can be explained from a theoretical point of view. It is however likely that both the intrinsic kinetics and the mass-transfer contribute to the overall growth of hydrates at the same time. At least this is what could be speculated from looking at the dependence of the nonlinear growth period on the concentration of the ISP as shown in Figure 3.5. As seen the nonlinear growth period becomes increasingly linear as the ISP concentration decreases. Decreasing the stirring rate, which will decrease the mass transfer contribution, makes growth period 1 even more nonlinear which seems to support the

idea that the overall growth kinetics of gas hydrates is a result of competing effects of intrinsic kinetics and mass transfer considerations.

In the experiments using natural gas as the hydrate former the stirring rate was increased to 700 rpm compared to the experiments done using methane. This was done because the hydrate formation rate was very low, thus increasing the stirring led to a faster hydrate formation rate. It is however also possible to increase the formation rate by increasing the driving force, however in these studies, as discussed previously, it is desirable to keep the driving force low to moderate in order to study the effect of KHIs on the growth of gas hydrates.

In Figure 3.6 the growth of sII hydrate formed from the natural gas is shown. As seen the data again shows a high degree of linearity as also found for the sI methane hydrate.

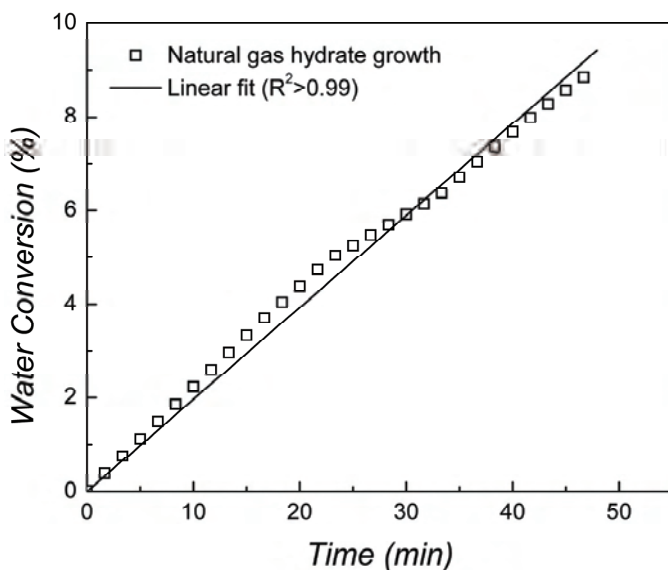


Figure 3.6. Growth of hydrate formed from a natural gas. The plot shows the fraction (%) of the initial amount of liquid water present converted into hydrate over time at 277 K, 34 bar and a stirring rate of 700 rpm. The data points are the data combined from 3 experiments and the solid line indicates the average conversion rate.

Table 3.3 summarizes the results of obtained from the sII hydrate growth experiments. Only the two KHIs, the ocean pout ISP and PVCap, which were the most efficient growth inhibitors of sI hydrate were included in this study. Again the KHIs cause the growth

pattern to change from solely linear to staged, suggesting that the mechanism by which they inhibit sI and sII is similar, i.e. by effective coverage of the hydrate surface.

Table 3.3. The percentage of water converted during growth period 1 (GP 1), measured water conversion rates (%/min) during growth period 2 (GP 2) and the percentage of growth rate inhibition for hydrate formed from a natural gas at 34 bar and 277 K.

System	C. (wt%)	Stirring rate (rpm)	GP 1 Conversion (%)	GP 2 Conversion rate (%/min)	GP 2 Inhibition (%)
No KHI	-		-	0.200 ($4.18 \cdot 10^{-6}$)	-
Ocean pout ISP	0.025		2.50	0.098 ($2.88 \cdot 10^{-7}$)	51.0
Ocean pout ISP	0.050	700	1.92	0.021 ($6.36 \cdot 10^{-7}$)	89.5
PVCap	0.050		4.80	0.220 ($1.71 \cdot 10^{-4}$)	0
PVCap	0.100		1.62	0.0054 ($7.36 \cdot 10^{-6}$)	97.3

For the sI and sII systems not containing any KHIs almost identical growth rates were found despite the fact that the stirring rate and subcooling in the sII hydrate experiments (8.7 K, 700 rpm) were higher than in the sI experiments (3.8 K, 450 rpm). In general the ISP and PVCap seem to perform equally well for the sII hydrate. In terms of how much hydrate is formed during growth period 1 and to what extent the growth rate of period 2 is decreased by the KHIs it is found that the sII hydrate is marginally more inhibited compared to the sI. The results found here are in accordance with the results found in section 2.5 for the nucleation of sI and sII hydrates, namely that the formation kinetics of sI are much faster than sII. From the growth results it is not obvious for which structure the KHIs work best due to the different stirring rates used in the experiments and also due to the aforementioned different formation rate but based on these results they seem to work about equally well.

To sum up the conclusions which can be drawn from these growth studies i) The growth of sII hydrate is significantly slower than sI; ii) under normal circumstances the surface area of the hydrate particles is much higher compared to the gas-liquid interfacial area ($A_p \gg A_{L-V}$) thus mass transfer of gas molecules from the gas phase to the liquid phase will dominate the hydrate growth pattern; ii) when effective KHIs are present and capable of adsorbing on the surface of the growing hydrate, the surface area of the hydrate becomes smaller than the gas-liquid interfacial area ($A_p \ll A_{L-V}$) thus the intrinsic

kinetics will dominate the hydrate growth pattern, iii) Though either mass transfer or intrinsic kinetics can dominate the growth of hydrates under certain circumstances it is likely that the growth pattern for any case is a result of contributions from both. The findings here suggest that for special cases the contribution from either one can be very small.

Chapter 4

Molecular simulation of gas hydrates

Computer simulation has become a widely used tool to study the physical properties of molecular systems. Primarily Monte Carlo (MC) and Molecular Dynamics (MD) simulations have been used to conduct such studies.

In MC simulations molecules are moved randomly from an initial configuration having the consequence that the current position is only affected by the previous configuration. The energy of the system is calculated using appropriate potential models for the molecules in the system. If the total energy of the system is minimized when going from an old to a new configuration the move is accepted. If the total energy of the system increases the change in configuration is accepted with a probability proportional to the Boltzmann distribution.^{127,128} For each new configuration thermodynamic properties are calculated and accumulated in sums usually running over several millions of configurations.

MD simulation, in contrast to the MC method, integrates Newton's equations of motion over time for each molecule in the system. Averages generated by the MD method are time averages. The positions and velocities of each molecule are advanced to their new positions in time according to the integration algorithm. The net force acting on each molecule is calculated from the configuration of the molecule and the potential model used. The resultant force and hence the acceleration acting on each molecule is

used to correct values given in the previous step. From integration of the forces over several thousands (or millions) of time steps molecule trajectories are produced from which time-averaged macroscopic properties can be calculated.

In this chapter some of the basic concepts behind molecular simulations are presented and applied to study various thermodynamic properties of methane hydrate.

4.1 Molecular simulation and gas hydrates

Tester and coworkers were the first to apply molecular simulation using the MC technique to study the physical behavior of gas hydrates.¹²⁹ From their simulations they concluded that the Lennard-Jones (LJ) potential can adequately describe the guest-host interactions in simple hydrate systems. Tse and coworkers were the first to use MD simulations to study hydrates.^{130,131,132} Calculating vibrational frequencies of hydrates and ice they were capable of explaining the differences and similarities in certain physical properties (heat capacity; thermal conductivity) between hydrate and ice.

In terms of more practical applications molecular simulations have been used to investigate the vdWP statistical theory which with great success has been applied to calculate three-phase equilibria of various hydrate forming systems.^{6,7} In one study, based on MD simulations, it was found that in particular the repulsive interactions from the guest molecules are important for stabilizing the hydrate lattice.¹³³ In another study it was shown from MC simulations that the physical significance of the vdWP theory can be improved if long-range guest-host interactions are included (the original version neglects these interactions) without losing the accuracy of the model.¹³⁴

MD simulations have been preferred compared to MC simulations when studying gas hydrates. This is perhaps not surprising because MD simulation can calculate time-dependent phenomena as well as thermodynamic properties.¹³⁵ MC simulations only allow for evaluation of time-independent properties such as phase behavior and free energies.^{134,136} Experimentally time-dependent properties like nucleation and growth are very difficult to study compared to time-independent properties, at least this is true when studying the mechanisms of gas hydrate nucleation and growth at the molecular level. Nevertheless various mechanisms have been proposed for the nucleation and growth of

gas hydrates as was discussed in chapter 2 and 3. Unfortunately, the available experimental evidence does not differentiate between the different nucleation and growth models. MD simulations could possibly provide such information. MD simulations have already been conducted to gain information about the nucleation and growth mechanisms of gas hydrates. However common to all these studies is that hydrates either grow or form hydrate from a hydrate crystal seed already present in the system whereby information about the true mechanisms may be lost.^{34,63,137}

Very recently nucleation and growth of methane hydrate was successfully achieved from a bulk solution of methane and water:³⁹ Excluding interfacial concentrations, before cooling the initial mole fraction of methane in water was 0.0015, or one percent of that in a hydrate. During the first microsecond of simulations several networks of water were formed around the dissolved methane molecules only to disappear again. After a long simulation (> 1 microsecond) spontaneous nucleation took place leading to extensive growth of gas hydrate. Analysis of the hydrate structures formed revealed both sI and sII motifs which were enabled through the formation of a $5^{12}6^3$ cage. The $5^{12}6^3$ cage has also been identified in another MD simulation study of methane hydrate though growth in that case was not observed directly from a melt but from a system composed of a melt and hydrate phase at the beginning of the simulation.¹³⁸

From experiments, it is well-known that the driving force of gas hydrate formation is strongly dependent on the degree of subcooling or overpressurization relative to the hydrate equilibrium formation temperature or pressure which has also been demonstrated in this work. Therefore, it is evident that the driving force, in terms of subcooling/overpressurization, must also be well-defined when considering the formation of gas hydrates from molecular simulations. Nonetheless, all simulation studies to date have arbitrarily set a temperature and pressure, in the absence of knowledge about the actual hydrate phase boundary for the specific molecular models used. In the work of Moon et al.³⁴ and Zheng et al.¹³⁷ they even use the term subcooling when discussing the observed effect of temperature on the induction time and the formation of hydrate-like structures. Still they did not determine the three-phase equilibria of the hydrate forming system using the appropriate potential models.

With these considerations in mind, a procedure has been established to calculate the three-phase equilibrium of liquid water-methane hydrate-methane vapor from molecular simulations. The potential models used to represent water and methane were similar to those used in the nucleation and growth simulations by Walsh et al.³⁹ thus will allow a direct determination of the thermodynamic state of those simulations. The procedure has been applied to determine the hydrate coexistence conditions for both sI and sII methane hydrates since both structures were observed in the MD simulations. The hydrate equilibrium composition was calculated from the simulations and compared to those predicted by the vdWP theory and the effect of hydrate being a non-stoichiometric compound has been analyzed in relation to the profile and location of the hydrate phase boundary. Furthermore the enthalpy of hydrate dissociation was determined directly from simulations and indirectly from the simulated hydrate phase boundary using the Clapeyron equation.

Before going into detail about how to arrive at the three-phase equilibria of a hydrate forming system from MC simulations a small introduction to statistical mechanics and molecular simulation will be presented. It is not the intention to fully explain the theory behind molecular simulation but rather to provide a glimpse into the simulation box - which for people not familiar with molecular simulations - often appears black.

4.2 Basics of statistical mechanics and molecular simulation

When studying phase equilibria using molecular simulation in particular two ensembles are very useful, namely the isothermal-isobaric ensemble (NPT) and the canonical ensemble (NVT). The N, V, P and T indicate that the number of molecules, volume and either pressure or temperature are held constant during the simulation. In the NVT ensemble the Helmholtz free energy is related to the partition function, Q , as follows:¹³⁹

$$A = -k_B T \ln(Q(NVT)) = -k_B T \ln \left(\frac{q^N}{N!} \times \int \exp[-\beta U(\mathbf{r}_1, \omega_1, \dots, \mathbf{r}_N, \omega_N)] d\mathbf{l} \dots dN \right) \quad (4.1)$$

where $\beta=1/k_B T$, and k_B is Boltzmann's constant, U is the intermolecular energy of the whole system, q is the molecular partition function and $d\Omega$ stands for $d\mathbf{r}_i d\omega_i$, where $d\mathbf{r}_i=dx_i dy_i dz_i$. The location of molecule i is given by Cartesian coordinates, $\mathbf{r}_i(x_i, y_i, z_i)$ of the reference point and a normalized set of angles defining the orientation of the molecule (ω_i). Eqn. (4.1) is often referred to as the workhorse of equilibrium statistical mechanics. For a nonlinear molecule the molecular partition function can be written as:

$$q = q_t q_r q_v q_e \quad (4.2)$$

where $q_t=q_t/V$ is the translational partition function and q_r, q_v , and q_e are the rotational, vibrational and electronic partition functions, respectively. q_r, q_v , and q_e are dimensionless and for phase equilibria calculations it is assumed that they are the same in coexisting phases. For this reason their precise value does not affect phase equilibria and it can simply be assumed that their value is a constant (set to 1 for convenience). q_t has units of inverse volume and is usually denoted as the inverse thermal wavelength ($1/\Lambda^3$), $\Lambda = h/\sqrt{2\pi m k_B T}$ where h is Planck's constant and m is the molecular mass.

The other ensemble, useful in the studying phase equilibria, is the NPT ensemble from which the Gibbs free energy, G , can be obtained as:

$$G = -k_B T \ln(Q(NPT)) \quad (4.3)$$

where Q is given as:

$$Q(NPT) = \frac{q^N \beta^P}{N!} \int \exp(-\beta P V) dV \times \int \exp[-\beta U(\omega_1, \mathbf{s}_1, \dots, \mathbf{s}_N, \omega_N; \mathbf{H})] V^N \times d\mathbf{s}_1 d\omega_1 d\mathbf{s}_N d\omega_N \quad (4.4)$$

Here \mathbf{s}_i are the coordinates of the reference point of molecule i in simulation box units. The conversion from simulation box units to Cartesian coordinates can be performed via the \mathbf{H} matrix $\mathbf{r}_i = \mathbf{H}\mathbf{s}_i$ (the volume of the system is the determinant of the \mathbf{H} matrix).

As described previously in MC simulations the molecules are moved around randomly in a rigid container (simulation box). One problem that arises from this is that many of

the molecules, at any given point during the simulation, will be located adjacent to the simulation box wall thus not experiencing the same forces as the molecules in the bulk. This problem is overcome by introducing periodic boundary conditions, using a system which is replicated an infinite number of times in each of the three dimensions of the simulation box.¹⁴⁰ As a molecule moves in the original system, its corresponding image in each of the replicate systems also moves in the same way. The result is that as a molecule leaves the system through one wall, the molecule will enter the system through the opposite wall.

In contrast to MD simulations which include both kinetic and potential energies in the acceptance criteria, in MC simulation only the potential energy is considered. To calculate the intermolecular potential energy, U_{Pot} , of a given system in principle it is necessary to calculate the interaction energies between all molecules in the system:

$$U_{Pot} = \frac{1}{2} \sum_{i,j,n} 'u(|\mathbf{r}_{ij} + \mathbf{n}L|) \quad (4.5)$$

where $u(r)$ is the intermolecular potential between two pairs of molecules, L is the diameter of the periodic simulation box (assumed cubic for convenience) and \mathbf{n} is an arbitrary vector of three integer numbers. The prime over the sum indicates that the term where $i = j$ is to be excluded when $\mathbf{n} = 0$ to exclude self interactions. Though many different types of pair potentials exist, the one that probably has been most extensively applied in molecular simulations of non-polar molecules is the Lennard-Jones (LJ) potential, u_{LJ} , which is given by:

$$u(r)_{LJ} = 4\varepsilon \left[\left(\frac{\sigma}{r} \right)^{12} - \left(\frac{\sigma}{r} \right)^6 \right] \quad (4.6)$$

where ε is the depth of potential well, σ is the molecule diameter and r is the distance between two molecules.

Theoretically all molecules in a system containing N molecules should be accounted for when calculating the intermolecular energy of the system. In practice, however for systems containing hundreds of molecules many of the $N-1$ molecules will have a negligible effect on the molecule in question. For this reason it is common practice to

consider only the molecules within a certain distance of the molecule in question. Beyond this distance the interactions are said to be cut off. For the molecules that are near the system boundary, the closest molecule will not be contained in the original system, but rather their corresponding images in the replicated boxes. This can however be accounted for using the “minimum image convention”.¹⁴¹

The maximum allowable cutoff radius, r_c , for a cubic box of length L is $L/2$, although a cutoff radius of 2.5σ is normally sufficient to obtain converged results in three dimensional simulations¹⁴² since the LJ potential asymptotes rapidly to zero for distances greater than 2.5σ (the long-range attractive term decays with $1/r^6$). Because of this very fast decay, the error introduced by this truncation is quite small, generally less than two percent.¹²⁷ Furthermore the error that the truncation induces is easily corrected by adding a simple long-range correction term (tail contribution) to eqn. (4.5).¹⁴³ This correction assumes that the pairwise distribution function, $g(r)$, is unity beyond the cutoff distance and the long-range potential contribution, u^{tail} , may then be calculated by:

$$u^{tail} = 2\pi\rho \int_{r_c}^{\infty} u(r)r^2 dr \quad (4.7)$$

where ρ is the average density of the system. When the simulation includes polar molecules this causes much greater problems in connection to long-range interactions. The Coulomb interactions only decays with $-1/r$ and the error introduced by using truncation plus tail contribution even with a cutoff radius of several Angstroms is appreciable (5-15%). A general rule of thumb is that the tail contribution diverges unless $u(r)$ decays faster than $1/r^3$.¹²⁸ The most favored method for dealing with the long-range contributions from Coulomb interactions to the potential energy in a system with boundary conditions is the Ewald summation method.¹⁴⁴ The contribution of the Coulomb interactions to the potential energy of the system can be described by:

$$u(r)_{Coul} = \frac{1}{2} \sum_{i=1}^N q_i \phi(r_i) \quad (4.8)$$

where q_i is the charge of particle i and $\phi(r_i)$ is the electrostatic potential at the position of particle i :

$$\phi(r) = \sum'_{j,n} \frac{q_j}{|\mathbf{r}_{i,j} + \mathbf{nL}|} \quad (4.9)$$

where the prime on the summation indicates that the sum is over all periodic images \mathbf{n} and over all particles j , except $j = i$ if $\mathbf{n} = 0$. For simplicity of notation all factors of $4\pi\epsilon_0$ have been omitted (ϵ_0 is the permittivity of vacuum). Eqn. (4.8) cannot be used to calculate the electrostatic energy because it contains a poorly converging sum. To improve the convergence of (4.8) it is assumed that each particle i with the charge q_i is surrounded by a Gaussian charge distribution of opposite sign, such that the total charge of this cloud exactly cancels q_i . The charge distribution screens part of the charge resulting in the interactions become short-ranged. It is of course necessary to make a correction for adding these potentials (it is not the aim to evaluate the potential in term of a set of screened charges), which is done by adding another charge distribution with the same sign as the original charges. In Figure 4.1 the idea behind the Ewald summation method is shown.

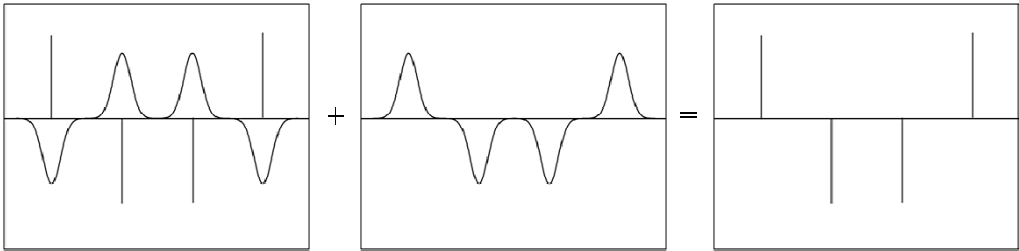


Figure 4.1. The general idea behind the Ewald summation method to calculate long-range Coloumb interactions. A charge distribution (Gauss) is added to the system which screens part of the original charge (left). To obtain overall charge equality a charge distribution of opposite sign is added for compensation (middle). The resulting charge thereby becomes equal to the initial charge (right).

The compensating charge distribution varies smoothly in space and is periodic. Thus it can be represented by a (fast converging) Fourier series. In short, the idea behind Ewald summation can be explained as; i) Sum screened particle interaction in real space, ii)

subtract compensating potential in Fourier space. Mathematically the contribution from the Coulomb interactions to the potential energy can be represented by 4 individual parts:

$$\begin{aligned}
 U_{\text{Coul}} = & \frac{1}{2V} \sum_{\mathbf{k} \neq 0} \frac{4\pi}{k^2} |\rho(\mathbf{k})|^2 \exp\left(\frac{-k^2}{4\alpha}\right) && \text{Fourier contribution} \\
 & - \left(\frac{\alpha}{\pi}\right)^{3/2} \sum_{i=1}^N q_i^2 && \text{Self - potential correction} \\
 & + \frac{1}{2} \sum_{i \neq j}^N \frac{q_i q_j \text{erfc}\left(\sqrt{\alpha} r_{ij}\right)}{r_{ij}} && \text{Real space contribution} \\
 & + \frac{2\pi}{(2\kappa' + 1)V} \left| \sum_{i=1}^N \mathbf{r}_i q_i \right|^2 && \text{Boundary effects}
 \end{aligned} \tag{4.10}$$

where $k = (2\pi/L)\mathbf{l}$ and $\mathbf{l} = (l_x, l_y, l_z)$ are the lattice vectors in Fourier space, α (convergence parameter) characterizes the width of the compensating Gaussian charge distribution width = $\sqrt{2/\alpha}$, $\text{erfc} = \left(2/\sqrt{\pi}\right) \int_0^x \exp(-u^2) du$ is the error function and κ' is the dielectric constant. The choice of α is determined by considerations of computational efficiency and accuracy which can be done from a short simulation.¹⁴⁵ The computational effort for standard Ewald summation scales as $N^{3/2}$ thus the approach becomes prohibitively expensive for large systems. For systems containing large numbers of molecules ($N > 10^5$) other methods such as the particle-particle/particle-mesh (scales as $N \log N$) or the fast multipole method (scales as N) can be applied.

This was a very brief introduction to some of the concepts in molecular simulation, however for a more thorough explanation of the theory see references 127 and 128. For a more detailed description of the Ewald summation method see De Leeuw et al.^{146,147,148} In the next section a brief review of the methods which until now have been used to calculate solid-liquid-vapor (SLV) equilibria will be presented. The advantages and disadvantages of the different methods will be discussed in the context of applying them for calculating two component three-phase equilibria.

4.3 Phase equilibria of systems containing solids

Prediction of three-phase, SLV equilibria of a binary gas-water system from molecular simulation is a time consuming process. It requires the calculation of the solid, liquid and vapor free energies at the temperature of interest.¹⁴⁹ The coexistence point is found as the intersection of solid, liquid and vapor isotherms in the pressure-chemical potential plane.¹⁵⁰ In principle the Gibbs-ensemble MC method could be used to calculate SLV equilibria however it is limited by the need to perform molecule exchanges which maintain equal chemical potentials.¹⁵¹ At high densities the molecule transfer step has a very low probability for acceptance thus the method has never been used for calculating SLV equilibria.¹²⁷ Instead thermodynamic integration (TI) can be used to calculate the fluid phase free energies or alternatively the test particle insertion (TPI) method could be applied.¹⁵² The free energy of a solid can be determined using the so-called Einstein crystal method proposed by Frenkel and Ladd (FL) which has more or less become the standard method for calculating free energies of solids.¹⁵³ The advantage of using these methods is that they are well established and documented in the literature and straight forward to use. The disadvantage is that it requires a lot of simulations to arrive at a coexistence point and the simulations of especially water and hydrate phases are relatively time consuming.

Alternatively the Gibbs-Duhem integration (GDI) method can be used to equate and evaluate the chemical potentials of coexisting phases.¹⁵⁴ Compared to many other simulation techniques, GDI has the advantage of being independent of insertions and/or removals of molecules. This makes the method especially suitable for calculation of phase equilibria including solid phases.¹⁵⁵⁻¹⁶² By combining the Gibbs-Duhem equations of coexisting phases it is possible to derive a so-called Clapeyron equation which describes monovariant phase coexistence. The original Clapeyron equation relates the vapor pressure changes with temperature for two phases to remain at coexistence. However the Clapeyron equation applies to any type of coexistence situation, as long as the number of degrees of freedom is 1. From molecular simulation it is possible to evaluate the Clapeyron equation thus each simulation yields one point on the coexistence line. The GDI method is however incapable of giving directly an arbitrary coexistence point, thus other methods have to be applied to determine this initial point. While the GDI

method has been successfully applied to calculate pure component solid-liquid equilibria (SLE)¹⁶³ and vapor-liquid equilibria (VLE)¹⁶⁴ it has never been applied to three-phase equilibria of binary systems thus it will require time to develop and test this method. In any case the GDI method can only be applied after determination of a single point on the three-phase L_W -H- V_M coexistence line so while using the TI approach to calculate chemical potentials and free energies of all phases is tedious and time-consuming it seems the best choice for calculating the L_W -H- V_M equilibria.

4.4 Phase equilibria of hydrate forming systems

For two component (water and methane) three-phase equilibrium, the chemical potentials (μ) of both species in all phases are equal at a given temperature and pressure, that is:

$$\begin{aligned}\mu_W^L &= \mu_W^H = \mu_W^V \\ \mu_M^L &= \mu_M^H = \mu_M^V\end{aligned}\quad (4.11)$$

where, the subscripts W and M refer to the water and methane, respectively. At equilibrium conditions, dense ordered (hydrate), dense disordered (liquid) and low density (vapor) phases coexist; thus TI along multiple paths is required to obtain all the necessary chemical potentials provided in eqn. (4.11). For each phase at a specified temperature and pressure, the chemical potential of each species varies with the composition in that phase. This is illustrated for the solid hydrate phase in Figure 4.2, which plots the methane and water chemical potentials versus the number of methane molecules (hydrate occupancy) at a fixed temperature, pressure and number of water molecules.

Similar plots exist for the liquid and vapor phases. For a given temperature and pressure, equality of chemical potentials between two phases for each species, that is two-phase equilibrium, will occur only at a specific composition in each phase. In accordance with Gibbs phase rule, three-phase equilibrium can then only occur at the coexistence temperature at a given pressure (or coexistence pressure at a given temperature). At three-phase coexistence conditions, the composition in the hydrate phase in equilibrium with

the gas phase will be the same as the hydrate composition in equilibrium with the liquid phase.

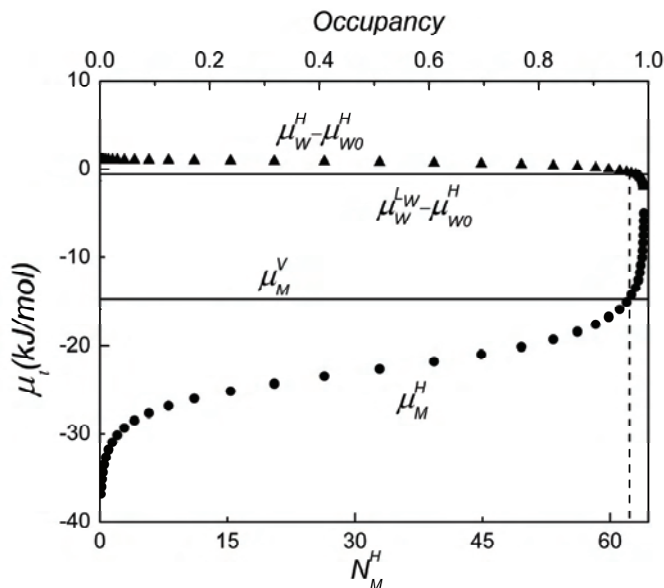


Figure 4.2. Chemical potential of methane in the vapor phase (bottom solid line), methane in the hydrate (filled circles), water in the liquid phase (top solid line), and water in the hydrate phase (filled triangles), plotted as a function of the hydrate occupancy. A thermal wave length of 1\AA was used in calculating the chemical potential for all phases. The number of methane molecules, in the hydrate has a maximum of 64, corresponding to a $2\times 2\times 2$ structure I hydrate unit cell. The temperature and pressure here are on the three-phase coexistence curve (298.9 K, 100 bar), and therefore, the condition of equal chemical potentials is satisfied at the same hydrate composition, as shown by the vertical dashed line.

Considerable simplifications can be made, however, when a phase at coexistence is nearly pure. The accuracy of this approximation can be assessed by VLE simulations and is found to be extremely good for the system studied here as detailed in section 4.8.2. In the present case this implies that for a given pressure, the coexistence temperature can be determined as that temperature for which the hydrate composition that satisfies $\mu_W^{Lw} \approx \mu_W^{Lw,0} = \mu_W^H$ is the same hydrate composition that satisfies $\mu_M^V \approx \mu_M^{V,0} = \mu_M^H$. Figure 4.2 illustrates this condition of equal water and equal methane chemical potentials at a given composition (dashed vertical line) required to locate the three-phase equilibrium for

a methane hydrate system. The chemical potential of water in the liquid phase and of methane in the vapor phase are shown as horizontal lines in the plot, as these are fluid phase properties independent of the occupancy of methane in the hydrate. Equating these two pairs of chemical potentials is thus sufficient to determine the coexistence temperature, pressure and hydrate composition. The remaining two chemical potential conditions, $\mu_w^H = \mu_w^V$ and $\mu_M^H = \mu_M^L$, serve to determine the (dilute) compositions of the minority species in the fluid phases.

In the following sections a detailed description of the equations and simulation types required to obtain each of the chemical potentials in eqn. (4.11) is presented.

4.5 Chemical potentials of the fluid phases

The chemical potential for a mixture can be expressed as:

$$\mu_i(T, P, x_i) = \mu_i^0(T, P) + RT \ln(\gamma_i x_i) \quad (4.12)$$

Where μ_i^0 is the pure component (methane or water) chemical potential at the mixture temperature, R is the gas constant, T is temperature, P is pressure, x_i is the mole fraction of the pure component and γ_i is the activity coefficient of species i in the mixture. For nearly pure phases $x_i \approx 1$ for the majority species, and the Lewis-Randall rule $\gamma_i = 1$ applies. The chemical potential of a pure component is found from thermodynamic integration (TI). If the chemical potential at one pressure is known, then the chemical potential at any other pressure along an isotherm can be found as:

$$\frac{\mu_i(T, P_2)}{k_B T} = \frac{\mu_i(T, P_1)}{k_B T} + \int_{P_1}^{P_2} \frac{1}{\rho_i k_B T} dP \quad (4.13)$$

where ρ_i is the number density. Likewise, along an isobar, the temperature dependence of the chemical potential is given as:

$$\frac{\mu_i(T_2, P)}{k_B T_2} = \frac{\mu_i(T_1, P)}{k_B T_1} - \int_{T_1}^{T_2} \frac{H_i}{k_B T^2} dT \quad (4.14)$$

where H_i is the molar enthalpy. The starting point of the thermodynamic integration can be chosen arbitrarily, however, the ideal gas is often a convenient choice given that its chemical potential can be calculated analytically; the ideal gas chemical potential is given by:

$$\frac{\mu_i^{\text{id}}}{k_B T} = \ln(\rho_i \Lambda^3) \quad (4.15)$$

where $\Lambda = h/\sqrt{2\pi M k_B T}$ is the thermal wavelength, and M is the molecular mass; this term cancels out when comparing chemical potentials between phases in equilibrium. An example of how an integration path for a given fluid can be constructed in order to calculate the chemical potential is shown in Figure 4.3. The integration starts at 1 bar and 800 K going up isothermally to 330 bar and from that isobarically down to a temperature of 400 K from where the pressure is decreased to 100 bar isothermally. At this pressure the chemical potential of the fluid can then be calculated in a temperature interval of interest for determining the three-phase equilibria of gas hydrates. It is important that integration to the state of interest is done without crossing a first order phase transition (melting, vaporization, solid state transitions) to ensure that the integration path remains reversible. The integration steps in temperature and pressure are chosen to be sufficiently small so that a smooth integration curve is obtained.

From NPT simulations it is possible to obtain both the density and the enthalpy of the fluid (methane or water) of interest thus choosing suitable steps in pressure and temperature (for accurate integration a smooth curve in density or enthalpy versus pressure or temperature must be obtained) enables the calculation of the chemical potentials.

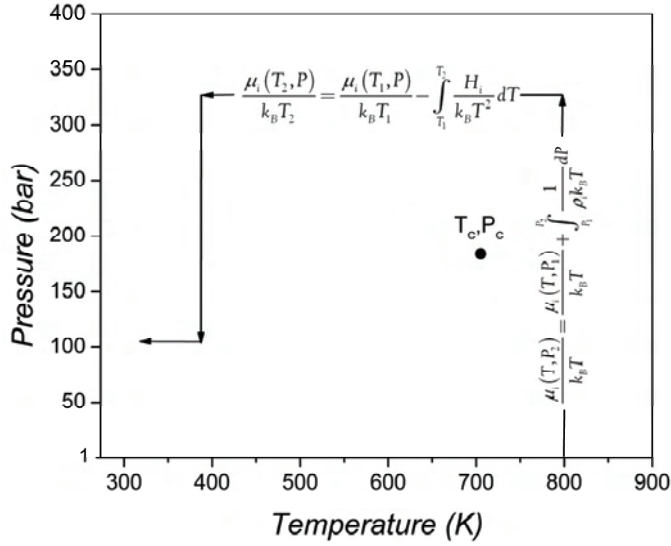


Figure 4.3. Integration path from a supercritical state to determine the chemical potential of a fluid at any given state. The starting point (1 bar and 800 K) corresponds to a near ideal state and performing the integration in suitable steps in pressure and temperature it is possible to move up around the critical point of the fluid and down to the area of interest, thereby creating a reversible integration path.

For testing the assumption that the chemical potentials of the pure phases are good approximations to the chemical potentials of the phases with dissolved methane or water, the fluid solubilities were calculated. The mole fraction of a compound in the gas phase (y_i) for near-ideal conditions can be well-described in terms of the partial pressure of the compound:

$$y_i = \frac{P_i}{P} \quad (4.16)$$

where the total pressure, P , is the sum of the partial pressures. Likewise, the solubility of a small nonpolar molecule in an aqueous phase (x_i) is well-described by Henry's law, which is given by:

$$k_{H,i} = \frac{P_i}{x_i} y_i \quad (4.17)$$

Henry's constant, $k_{H,i}$, can also be related to the excess chemical potential of the solute, $\mu_i^{\text{ex},\infty}$, by:

$$k_{H,i} = \rho_s k_B T \exp(\beta \mu_i^{\text{ex},\infty}) \quad (4.18)$$

where ρ_s is the solvent density. The excess chemical potential of the solute can be calculated from TPI simulations.¹⁵² The change in chemical potential resulting from the solubility calculations at various temperatures and pressures can then be compared in magnitude relative to the pure phase approximations.

4.6 Chemical potentials of the hydrate phase

Calculation of chemical potentials in the hydrate phase follows closely the procedure outlined by Wierchowski and Monson,¹³⁴ which is summarized here. The calculation proceeds first by the generation of a hypothetical empty hydrate and calculation of the chemical potential of water therein. Secondly the change in chemical potential of both water and methane due to the introduction of methane in the hydrate at various compositions is found from thermodynamic integration. The latter is carried out using semigrand MC (SGMC) simulations while the chemical potential of the hypothetical empty hydrate is calculated using a modified version of the FL Einstein crystal method.¹⁵³ In the following this method will just be referred to as the FL method.

Since SLE does not end in a critical point there exist no reversible paths from the solid to the ideal gas that do not cross a first order phase transition. However it is possible to construct a reversible path from the solid to other states (than the ideal gas) of known free energy. One such method is the FL method which is based on thermodynamic integration of the Helmholtz free energy, taking a reversible path to the system of interest from a classical Einstein crystal for which the Helmholtz free energy can be calculated analytically.

The hypothetical empty hydrate may be viewed as a metastable ice phase, however although it is not thermodynamically stable, it is a mechanically reproducible stable state in MC simulations thus the FL method is suitable for calculating its free energy.

Slight modifications to the method have been introduced to treat the orientational degrees of freedom and the effect of fixed center of mass for the hydrate.^{165,166} The starting point is defining the Einstein crystal Hamiltonian:

$$H_E(\lambda_T, \lambda_R) = \sum_{i=1}^N \left[\lambda_T (\mathbf{r}_i - \mathbf{r}_i^{(0)})^2 + \lambda_R \left(\sin^2 \omega_{a,i} + \left(\frac{\omega_{b,i}}{\pi} \right)^2 \right) \right] \quad (4.19)$$

where λ_T and λ_R are force constants, \mathbf{r}_i gives the Cartesian coordinates of molecule i , and $\mathbf{r}_i^{(0)}$ gives the coordinates for a molecule i in the reference lattice. $\omega_{i,a}$ and $\omega_{i,b}$ are angles describing the orientational displacement of molecules with respect to the reference lattice. Eqn. (4.19) defines a classical Einstein crystal and the free energy can be determined by combination of analytical and numerical methods. If H_E is added to the Hamiltonian, H_0 , the Hamiltonian of an interacting Einstein crystal is obtained:

$$H_{IE}(\lambda_T, \lambda_R) = H_0 + H_E(\lambda_T, \lambda_R) \quad (4.20)$$

For large values of λ_T and λ_R the system behaves like an Einstein crystal only being slightly perturbed by the interactions in H_0 . For zero values of λ_T and λ_R the system behavior is solely determined by H_0 . Thermodynamic integration is used to determine the free energy change associated with changing the force constants from zero to values sufficiently large where the system is close to being an Einstein crystal. The Helmholtz free energy of the system can be written as:

$$A = A_E + (A_{IE} - A_E) + (A_{CM} - A_{IE}) + (A - A_{CM}) \quad (4.21)$$

where A_E is the free energy of the Einstein crystal, A_{IE} is the free energy of an interacting Einstein crystal and A_{CM} is the free energy of the hydrate but with the center of mass fixed. Indeed all quantities in eqn. (4.21) except A refer to a system with fixed center of mass. A_E can be written as $A_E = A_{E,T} + A_{E,R}$ with:

$$A_{E,T} = -k_b T \ln \left[N^{\frac{3}{2}} \left(\frac{\pi k_b T}{\lambda_T} \right)^{\frac{3(N-1)}{2}} \right] \quad (4.22)$$

being the contribution from the translational motion and:

$$A_{E,R} = -Nk_b T \ln \left\{ \int_0^1 \exp \left[-\frac{\lambda_R}{kT} (1-y^2) \right] dy \right\} \int_0^1 \exp \left[-\frac{\lambda_R}{kT} (1-y'^2) \right] dy' \quad (4.23)$$

is the contribution from the rotational motion with $y = \cos\alpha$ and $y' = (\gamma/\pi)$ where α and γ refer to the Euler angles describing the molecular orientation. The difference between a noninteracting and an interacting Einstein crystal is found using:

$$A_{IE} - A_E = -k_b T \ln \left\langle \exp \left[\frac{H_0}{k_b T} \right] \right\rangle_{H_E(\lambda_T, \lambda_R)} \quad (4.24)$$

with $\langle \rangle_{H_E(\lambda_T, \lambda_R)}$ indicating a canonical ensemble average evaluated for a system with Hamiltonian $H_E = (\lambda_T \lambda_R)$. The third term in eqn. (4.21) is found using a coupling parameter integration over λ_T and λ_R . The final term in eqn. (4.21) is given by $A - A_{CM} = \ln(V/N)$. For a thorough review of calculating the free energies of solids using the Einstein crystal method see Vega et al.¹⁶⁷

Once the Helmholtz free energy for the hydrate is known, the chemical potential of water in the empty hydrate is found as:

$$\mu_{w0}^H = \frac{A + PV}{N_w^H} \quad (4.25)$$

where N_w^H , V , and P are the number of water molecules, volume, and pressure of the empty hydrate, respectively. Specifying the fully occupied hydrate it is likewise possible to calculate its free energy.

To obtain a relationship between the water and methane chemical potentials as a function of the hydrate composition (filled circles and triangles in Figure 4.2) methane is introduced into the empty hydrate lattice (or deleted from the fully occupied lattice) at fixed values of methane chemical potential, μ_M^H , by performing N_wPT SGMC simulations. In this case the hydrate lattice will work as an absorbent and the absorbed methane will be in equilibrium with methane outside the absorbent (the reservoir). The equilibrium

condition is that the chemical potential of the absorbed methane and that of the reservoir must be equal.¹²⁸ Using this technique for each value of the methane chemical potential, the number of methane molecules in the hydrate, N_M^H , can be calculated as an ensemble average (filled circles in Figure 4.2).

The Gibbs-Duhem relation for two-component system implies that the change in the water chemical potential depends on the change in the methane chemical potential, namely that at constant temperature and pressure, $N_W^H d\mu_W^H + N_M^H d\mu_M^H = 0$. The water chemical potential in the hydrate can thus be obtained as:

$$\mu_W^H - \mu_{W0}^H = -\frac{1}{N_W^H} \int_{\mu_{M0}^H}^{\mu_M^H} N_M^H d\mu_M^H \quad (4.26)$$

and plotted versus N_M^H (filled triangles in Figure 4.2) at the desired temperature and pressure. Finally, the Gibbs free energy of the hydrate at any given composition can be expressed as:

$$G_H = N_M^H \mu_M^H + N_W^H \mu_W^H = N_M^H \mu_M^H + N_W^H \mu_{W0}^H - \int_{\mu_{M0}^H}^{\mu_M^H} N_M^H d\mu_M^H \quad (4.27)$$

The Gibbs free energies obtained from eqn. (4.27) using the SGMC approach can be compared to the values obtained directly from thermodynamic integration using the FL method, thus serving as a validation of the SGMC method.

4.7 Potential models and simulation details

As described in section 4.2, to calculate the potential energy of the molecular system it is necessary to use a potential model representing the interactions between molecules. In this case the TIP4P/ice potential model was used to model water molecules.¹⁶⁸ The term ‘‘TIPS’’ comes from Transferable Intermolecular Potential function and it is a class of potentials originally developed for water, ethers and alcohols.¹⁶⁹ The TIP4P/ice potential belongs to a class of four sited potential models which have been shown very successful in capturing many features of the complex behavior of water.^{170,171,172}

Three of the four sites are placed at the oxygen and hydrogen atom positions, respectively. The fourth site, often called the M site, is coplanar with the O and H sites and is located at the bisector of the H-O-H angle as shown in Figure 4.4:

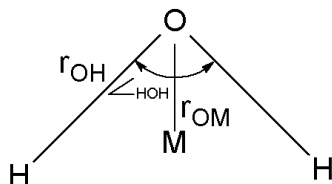


Figure 4.4. The characteristic shape of the transferable intermolecular potential function of water. The parameters may vary depending on the model.

An important feature of the model is that the oxygen site carries no charge, but contributes to the LJ term. Conversely, the H and M sites are charged, but do not contribute to the LJ term. As a consequence of the molecular geometry and potential definitions there are four unknown parameters to determine, namely the well depth, ε , and the molecular diameter, σ , in the LJ term, the hydrogen site charge (or the M site charge $q_H = -1/2q_M$) and the distance, r_{OM} between the oxygen and the M site. In the table below three different TIP4P potential models are listed.

Table 4.1. Parameters for different variants of the transferable intermolecular potential function.

Model	q_H (e)	r_{OH} (Å)	\angle_{HOH} (deg)	r_{OM} (Å)	ε/k_B (K)	σ (Å)
TIP4P	0.52	0.9572	104.52	0.15	78.12	3.153
TIP4P/2005	0.5564	0.9572	104.52	0.1546	93.20	3.3589
TIP4P/ice	0.5897	0.9572	104.52	0.1577	106.1	3.1668

The TIP4P/ice potential model accurately describes the SLE of hexagonal ice and liquid water up to 2000 bar and captures most of the trends observed in the phase diagram for other ice types. Considering that hydrate is also a solid with a crystal structure mainly composed of water molecules, it is plausible that the TIP4P/ice model together with a suitable model for the gas molecules should be capable of describing the thermodynamic properties of gas hydrates.

Methane molecules were modeled using the united-atom Lennard-Jones representation using the optimized potentials for liquid simulations (OPLS) which has been parameterized using isobaric-isothermal MC simulations to give accurate liquid densities and heats of vaporization for short alkanes at atmospheric pressure.¹⁷³ The OPLS parameters for methane are shown in Table 4.2. Note that these only contain parameters for the LJ term since methane is non-polar.

Table 4.2. Lennard-Jones (energy and size) parameters for the optimized potentials for liquid simulations (OPLS) of methane.

Model	ϵ/k_B (K)	σ (Å)
OPLS	148.50	3.7300

The critical temperatures and pressures for methane and water as found from the OPLS and TIP4P/ice potential models are shown in Table 4.3 along with those found experimentally. As seen there is very good agreement between the experimental and calculated critical point of methane which is not surprising since the model has been optimized to methane density data. The reason why there is disagreement between the experimental and calculated critical point of water is because the TIP4P/ice model as mentioned earlier has been parameterized to SLE thus the parameters may not necessarily be suitable for modeling the VLE of water.

Table 4.3. Critical temperature and pressure for water¹⁷⁴ and methane¹⁷⁵ as predicted from the TIP4P/ice and the OPLS potential models. The numbers in parenthesis are experimental values.¹⁷⁶

177

Model	TC (K)	PC (bar)
TIP4P/ice	705 (647.1)	184 (220.6)
OPLS	190.6 (190.6)	45 (46)

The methane and water molecules will not only interact with themselves but also interact with each other. These cross interactions were accounted for using the Lorentz-Berthelot combining rule.^{178,179}

$$\epsilon_{ij} = \sqrt{\epsilon_{ii}\epsilon_{jj}} \quad (4.28)$$

$$\sigma_{ij} = \frac{\sigma_i + \sigma_j}{2} \quad (4.29)$$

The MC simulations used the standard Ewald summation method for the long-range electrostatic forces.^{180,181} Similarly, an Ewald summation approach was applied to evaluate the long-range dispersion (LJ) interactions using a lattice sum method.¹⁸² A convergence parameter, α , of $4/L$ was used, where L is the lattice parameter for hydrate in question. For all simulations the cut-off radius was 10 \AA corresponding to 2.7σ and 3.2σ for methane and water, respectively.

Before running any of the simulations required for calculating the three-phase equilibria the accuracy of the MC simulation package used in this work (MCHydrate^a) was tested against GROMACS, which is a commercially available and very well tested simulation tool.¹⁸³ To validate the accuracy of MCHydrate the initial potential energy of an empty hydrate crystal at a given pressure and temperature was calculated using MCHydrate and GROMACS. The result is shown in the table below. As seen the agreement between the potential energy found using the two methods is excellent.

Table 4.4. Comparison of initial potential energies calculated with MCHydrate and GROMACS.

MCHydrate (kJ/mol)	GROMACS (kJ/mol)	MCHydrate/ GROMACS
-67.11652	-67.11750	0.99999

The dispersion and electrostatic energies found using MCHydrate are in 99.94% and 99.98% agreement with those calculated from GROMACS, thus the MCHydrate simulation package is capable of calculating the potential energy of molecular systems correctly.

The following procedure was applied for running the simulation to calculate the chemical potentials of water and methane in the fluid and hydrate phase; For the fluid phase either 500 water or methane molecules were placed in the simulation box. The enthalpy and density of the fluid phase were obtained from *NPT* simulations. Typically 50,000-100,000 equilibration cycles were performed followed by 100,000-250,000

^a Made available by Center for Hydrate Research, Colorado School of Mines

simulation cycles to obtain converged averages of the densities and enthalpies. A simulation cycle corresponds to a set of N trial moves, where N is the number of molecules in the system. The block averaging technique was used to calculate statistical uncertainties and in most cases a block average of 10,000 cycles was used. By performing NPT simulations in small steps of temperature and pressure, the chemical potential of water and methane was obtained from eqn. (4.13) and (4.14) by integration using the trapezoidal rule.

Using the methodology described by Bennett¹⁸⁴ TPI simulations were performed in the NPT ensemble to obtain the solvent (water) densities and solute (methane) excess chemical potentials, $\mu_M^{\text{ex},\infty}$, from which Henry's constants were obtained. The Bennett method was used as it has been reported to offer improved accuracy over the Widom method.^{185,186} For these simulations 500 water molecules were first equilibrated for 100,000 cycles after which four stages of more than 500,000 cycles were performed. In the first stage, insertions of test particles were performed with five insertions attempted per cycle, and in the following three stages the particles were deleted.

The empty sI or sII hydrate lattice consisted of 368 and 1088 water molecules, respectively both corresponding to $2 \times 2 \times 2$ hydrate unit cells; NPT simulations were performed with 20,000 equilibration cycles and 200,000 cycles for averaging. The densities obtained from these simulations were used as input to the SGMC and FL simulations. The SGMC simulations were conducted over a range of methane chemical potentials (μ_M^H) from states in the neighborhood of the zero-occupancy hydrate (an initial value of $\mu_M^H = 36.83$ kJ/mol is used in this work) up to states describing a fully occupied hydrate (single occupancy of cages). Eqn. (4.26) was integrated using the trapezoidal rule in intervals of $\delta\mu_M^H = 0.837$ kJ/mol. Initially SGMC simulations were performed to obtain plots of the hydrate occupancy, θ , versus the methane chemical potential starting from both an empty and a full hydrate to identify if any mismatches in the curves are observed as pressure or temperature varies. Disagreement between the obtained curves is critical since this will result in eqn. (4.26) no longer being valid, thus the simulations serve to locate the boundary conditions for which phase equilibrium calculations can be performed.

The third simulation type involved the calculation of the chemical potential of water in the zero-occupancy hydrate ($\mu_{\text{w}0}^{\text{H}}$), which according to eqn. (4.26) is necessary for calculating the chemical potential of water in the occupied hydrate, ($\mu_{\text{w}}^{\text{H}}$). In addition, ($\mu_{\text{w}0}^{\text{H}}$) is used for calculating the Gibbs free energy of the hydrate at any given composition according to eqn. (4.27). The Helmholtz free energy of the empty and full hydrate was found using the FL method. It was assumed that the hydrate is proton-disordered but that the contribution to the free energy disorder is independent of the molecular interactions and approximated by the residual entropy of ice as determined by Nagle¹⁸⁷ For the sI hydrate the coordinates of the oxygen atoms for the perfect crystal used in specifying the Hamiltonian, $H_E(\lambda_T, \lambda_R)$, were those given by McMullan and Jeffrey.¹⁸⁸ For the sII hydrate the coordinates of the oxygen atoms for the perfect crystal were those specified by Mac and McMullan.¹⁸⁹

The orientations associated with the perfect crystal were determined by carrying out a search over the water molecule orientation to determine the configuration of lowest potential energy and dipole moment. Calculation of $A_{\text{CM}} - A_{\text{IE}}$ was determined using a 20 point Gaussian quadrature. The force constants used in the FL method were $\lambda_T = 25000 k_B T \text{\AA}^2$ and $\lambda_R = 25000 k_B T$. Simulations were performed for 5,000 equilibration cycles and 50,000 cycles for averaging.

For a detailed description on how to run simulations with MCHydrate (simulation input and output files etc.) see appendix V.

4.8 Results and discussion

In the following subsections a summary of the results of the fluid and hydrate phase MC simulations will be provided. First the results of a stability study of methane hydrate will be presented. The purpose of this study was to determine in which temperature and pressure regions the hydrate structure was in a stable state. Next the results of the chemical potential and Gibbs free energy calculations will be presented and based on these results the three-phase equilibria of water – hydrate – methane is determined. Based on the equilibrium calculations the hydrate composition was determined and discussed in

the context of the Langmuir adsorption theory. Assuming hydrate was stoichiometric (fully occupied) the three-phase equilibria was determined again to assess the effect of accounting for composition in equilibrium calculations. Finally the enthalpy of hydrate dissociation was calculated directly from simulations and indirectly from the equilibrium data using the Clapeyron equation.

4.8.1 Stability of the model hydrate

To determine in which temperature and pressure region the hydrate structure can be regarded as stable, SGMC simulations to obtain a relationship between the hydrate occupancy and the methane chemical potential, were performed over a broad range of pressures and temperatures. Such a relationship should in principle yield a smooth s-shaped curve and deviation from this shape will indicate that the hydrate structure has started to destabilize. Simulations were done starting from both an empty and a fully occupied hydrate at similar thermodynamic states.

First the temperature dependence of the occupancy relationship was investigated at 100 bar in the temperature range 250-400 K. The results are displayed in Figure 4.5A-D. In Figure 4.5A and B it can be seen that large temperature steps of 50 K are required to observe a noteworthy change in the occupancy relationship while small steps of 5 K have an insignificant effect on this relationship. In Figure 4.5C and D filling of the hydrate was attempted starting from an empty and a fully occupied hydrate at 300 K and at 400 K. At 300 K the two curves match perfectly (as expected) however at 400 K the curves do not match at occupancies below 0.55. The reason for this mismatch is that when only a few methane molecules are available for going into the small and large cages, part of the hydrate lattice will destabilize, corresponding to a melting process. The result indicates that the stability of the hydrate is at some sort of a boundary condition and in such a case it is no longer possible to obtain either the free energy of the hydrate nor the chemical potential of the water in the hydrate.

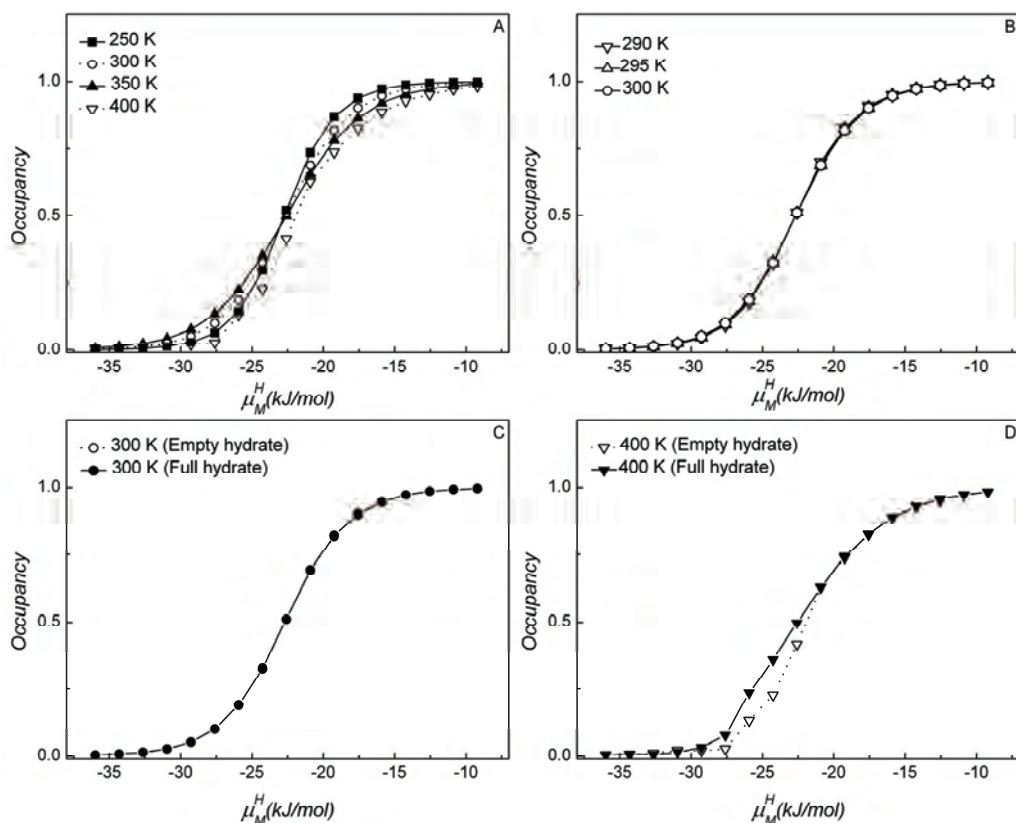


Figure 4.5. A) Temperature dependence of the hydrate occupancy (θ) versus the methane chemical potential (μ_M^H) relationship in a broad temperature range (250-350 K) and 100 bar. B) Temperature dependence of θ versus μ_M^H in a narrow temperature range (290-300 K) at 100 bar. C+D) θ versus μ_M^H starting the SGMC simulations from an empty and full hydrate at 300 K and 400 K both at 100 bar.

A similar study has been carried out at 300 K and pressures ranging from 200-10000 bar. The results can be seen in Figure 4.6A and B. The results show that the occupancy relationship is only weakly affected by changes in pressure i.e. only a small difference is observed when going from 200 to 5000 bar. At 10000 bar unexpected trends in the curve are seen and running SGMC simulations from an empty and a fully occupied hydrate reveal a hysteresis-like pattern as also observed at 100 bar and 400 K. The occupancy of the hydrate is seen to drop quite significantly when going from 5000 to 10000 bar

indicating that the high pressure exerted on the hydrate causes the cages to compress whereby some of the cages become incapable of enclathrating gas molecules.

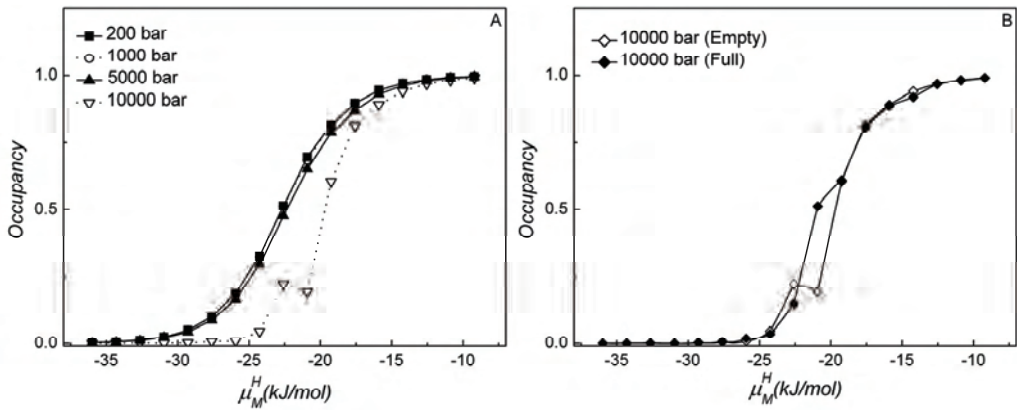


Figure 4.6. A) Pressure dependence of the hydrate occupancy, (θ) versus methane chemical potential (μ_M^H) relationship in a broad pressure range (100-10000 bar) and 300 K. B) Hydrate occupancy (θ) versus methane chemical potential (μ_M^H) relationship starting the SGMC simulations from an empty and full hydrate at 10000 bar and 300 K.

From this small study it can be concluded that the model hydrate shows high stability with respect to pressure and temperature and the conditions required to destabilize the hydrate are much higher than the expected three-phase equilibrium conditions. Thus destabilizing effects will not influence the equilibrium calculations.

4.8.2 The vapor-liquid equilibria of methane-water

To test the accuracy of assuming that the fluid phases are pure, VLE calculations of the fluid phases have been performed at 100 bar and in the temperature range 275-310 K. The solubility of methane in water was found from TPI simulations and the fraction of water in the vapor phase was estimated using eqn. (4.16) and vapor pressure data for water modeled using TIP4P/ice for the water partial pressure.¹⁹⁰ Since the water vapor pressures obtained from TIP4P/ice have only been reported in the temperature range 300-650 K, the data was extrapolated down to 275 K as seen in Figure 4.7. Since the vapor

pressures nearly linear in the $\log P$ versus $1/T$ plane, the error resulting from the extrapolation should be relatively small.

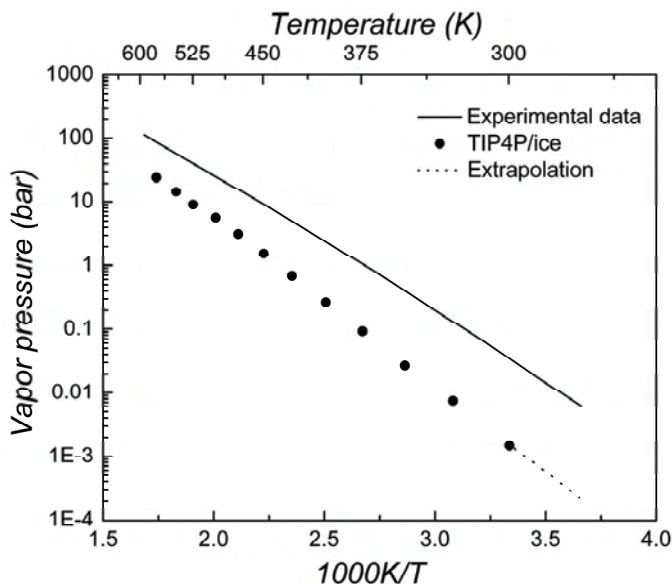


Figure 4.7. Vapor pressure of water found experimentally (solid line)¹⁹¹ and from molecular simulation using the TIP4P/ice potential model (filled circles).¹⁹⁰ The dotted line is the extrapolation of vapor pressures found by simulation to lower temperatures.

As seen from the figure the vapor pressures predicted by the TIP4P/ice potential model are substantially lower than the experimental vapor pressures. In the higher temperature region the TIP4P/ice underestimates the vapor pressure by a factor 4 while in the lower temperature region the deviation becomes even more significant (factor 25). In Table 4.5 the results of the VLE calculations along with the experimental values are provided. Experimental Henry's constants were calculated using a semiempirical correlation based on a best fit of experimental data in the temperature range 273.15-633.15 K.^{192,193} The experimental fractions of water in the vapor phase have been calculated using experimentally determined vapor pressures of water.¹⁹¹

Table 4.5. Vapor-liquid equilibria for the binary water-methane system at 100 bar and in the temperature range 275-310 K from experiments and Monte Carlo simulation. Numbers in parenthesis are standard deviations.

T (K)	$k_{H,M}$ (kbar)		x_M		$\gamma_W (\cdot 10^4)$	
	Sim.	Exp.	Sim.	Exp.	Sim.	Exp.
275	34 (5)	24	0.0030	0.0042	0.0257	0.7037
280	39 (5)	27	0.0025	0.0037	0.0372	0.9775
290	35 (6)	34	0.0028	0.0029	0.0766	1.8538
300	59 (6)	41	0.0017	0.0025	0.1540	3.4402
310	102 (12)	47	0.0010	0.0021	0.3024	6.2558

As seen from Table 4.5 the TIP4P/ice water model in combination with the OPLS potential model for methane predicts the solubility of methane in water to be around 30-50 % less than experimental values while the amount of water in the vapor phase is on the order of 20-25 times lower than experimental values. Low solubilities of methane in water modeled using other versions of the TIP4P potential model have previously been reported, thus providing additional support for the results presented here.^{194,195}

According to eqn. (4.12), the change in the chemical potential of the majority species when accounting for fluid phases mixing is $RT\ln x_i = RT\ln(1-x_j) \approx -RT(x_j)$, where $x_j \ll 1$ is the mole fraction of the minority species. Since the fluid phases are nearly pure, the activity coefficient is extremely close to unity. Therefore it is obvious from eqn. (4.12) that accounting for mixing will have a greater effect on the chemical potentials in the liquid than in the vapor since the mole fraction of methane in water is on the order of 100-1000 times larger compared to the mole fraction of water in the vapor. In Table 4.6, the pure component chemical potential of water found from TI and the additional excess contribution to the total chemical potential due to the dissolved methane is shown at 100 bar in the temperature range 275-310 K. It is evident that the contribution from mixing to the chemical potential of water is negligible compared to the pure water chemical potential (the mixing contribution to the chemical potential is less than the standard deviation from the combined TI steps that were used to calculate the pure water chemical potential). From these results it can be concluded that the fluid phases can be considered pure for the purpose of using the chemical potentials for determining the three-phase L-H-V equilibrium of methane hydrate.

Table 4.6. Pure component chemical potential of water and the contribution to the chemical potential from accounting for solubility of methane in water. Numbers in parenthesis are the standard deviations.

T (K)	μ_w^0 (kJ/mol)	$RT \ln(x_w)$ (kJ/mol)
275	-43.887 (0.06)	-0.00683 (0.0010)
280	-43.676 (0.06)	-0.00593 (0.0008)
290	-43.276 (0.06)	-0.00684 (0.0012)
300	-42.895 (0.07)	-0.00426 (0.0004)
310	-42.553 (0.07)	-0.00253 (0.0003)

4.8.3 Gibbs free energies of the hydrate phase

The Gibbs free energies of the zero-occupancy and fully-occupied hydrates were found directly using the FL method. The results obtained from SGMC simulations, together with eqn. (4.27), can also give the Gibbs free energy of a fully occupied hydrate provided that the empty hydrate free energy is also known. Typical results obtained from SGMC simulations correspond to the filled circles in Figure 4.2, which shows the methane hydrate occupancy as a function of the chemical potential of methane in the hydrate. Another method for calculating the free energy of the hydrate is by using the Gibbs-Helmholtz equation. The Gibbs-Helmholtz equation describes the temperature dependence of the free energy at isobaric conditions:

$$\frac{G}{T} - \frac{G_0}{T_0} = - \int_{T_0}^T \frac{H}{T^2} dT \quad (4.30)$$

where G_0 the isobaric free energy of the hydrate found at the temperature, T_0 , and H is the molar enthalpy of the hydrate. H comes from an individual NPT simulation while the starting point of the integration (G_0 , T_0) comes from a FL simulation.

Using these three methodologies; i) the temperature dependence of the empty and fully occupied hydrate has been determined and ii) a consistency check of the TI approach from the empty to the fully occupied hydrate has been performed. Both types of consistency checks have been performed at 100 bar and in the temperature interval 285-300 K and the results are shown in Table 4.7.

Table 4.7. Gibbs free energy in kJ per mole of water of an empty and a fully occupied hydrate calculated with the FL method (FL). The full hydrate value calculated from an empty hydrate reference by thermodynamic integration is also shown (TI). The temperature dependence of the Gibbs free energy of the hydrate has been calculated using the Gibbs-Helmholtz (G-H) relation. A thermal wavelength, $\Lambda = 1 \text{ \AA}$ has been used. Calculations were performed at 100 bar and the specified temperature. Numbers in parenthesis are standard deviations.

T (K)	G_{Empty}^H (FL) (kJ/mol)	G_{Empty}^H (G-H) (kJ/mol)	G_{Full}^H (FL) (kJ/mol)	G_{Full}^H (G-H) (kJ/mol)	G_{Full}^H (TI) (kJ/mol)
285	-42.40 (0.11)	-42.39 (0.06)	-46.26 (0.06)	-46.29 (0.06)	-46.34 (0.11)
290	-42.09 (0.05)	-42.10 (0.06)	-45.98 (0.06)	-45.99 (0.06)	-46.03 (0.05)
295	-41.81 (0.06)	-41.80 (0.06)	-45.69 (0.07)	-45.70 (0.06)	-45.75 (0.06)
300	-41.51 (0.06)	-41.51 (0.06)	-45.40 (0.07)	-45.40 (0.06)	-45.45 (0.06)

As shown in Table 4.7 there is good agreement between the FL and TI methods for obtaining the Gibbs free energy of a fully occupied hydrate indicating that these two independent methods are consistent. These results are also in good agreement with a previous study.¹³⁴ The isobaric temperature dependence of the Gibbs free energy as found from performing individual FL simulations is in very good agreement with the dependence calculated using the Gibbs-Helmholtz equation. Besides confirming that the temperature dependence of the hydrate found using the FL method is consistent with the Gibbs-Helmholtz equation the result is useful in the sense that simulation time can be saved. The time required to obtain the hydrate enthalpy from an *NPT* simulation is significantly shorter compared to the time required to obtain the hydrate free energy from a FL simulation. This means that only one FL simulation at each pressure is needed to calculate G_0 followed by 3-4 *NPT* simulations to capture the free energy temperature dependence instead of 3-4 FL simulations to obtain the same result.

4.8.4 The three-phase equilibria of structure I methane hydrate

To obtain the L_W -H- V_M three-phase equilibrium temperature at a given pressure, it is necessary to satisfy the constraint on the equality of the chemical potential for each species in each phase as shown in eqn. (4.11), and with the same hydrate composition, as discussed earlier. Based on the fact that the fluid phases can be assumed pure, the

following objective function (OF) describing the difference in the methane occupancies at which the chemical potentials of each species are equal has been constructed:

$$\text{OF} = N_M(\mu_M^V = \mu_M^H) - N_M(\mu_W^{L_w} = \mu_W^H) \quad (4.31)$$

Conditions for equilibrium are met when the OF has a value of zero. In practice, the OF is calculated at constant pressure for different temperatures covering the region for which the equilibrium temperature is expected to lie within. Figure 4.8 shows the values of the objective function for the temperatures explicitly considered in the simulations at the fixed pressure of 100 bar.

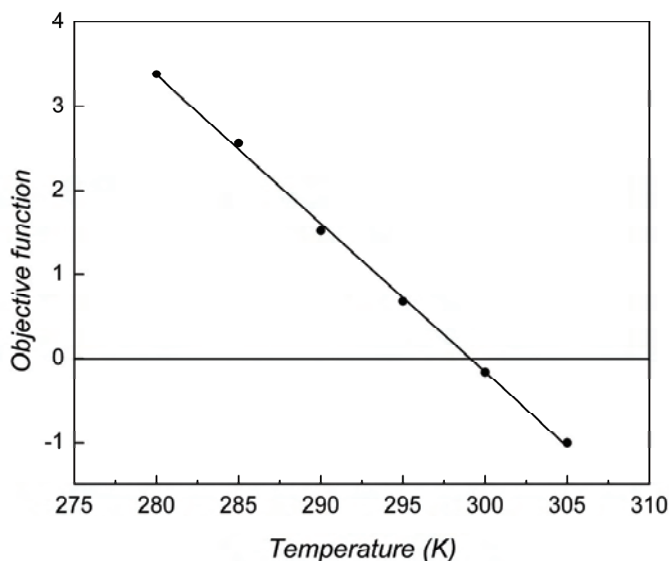


Figure 4.8. Value of the objective function defined by eqn. 4.31 at the different temperatures explicitly considered at 100 bar (filled circles). Line corresponds to the best fit of the points. The objective function has an interpolated value of zero (condition for equilibrium) for the liquid water-hydrate-methane vapor equilibrium at 298.9 K.

The objective function is linear with temperature in the range examined, thus allowing interpolation to obtain the temperature for which the objective function is zero. The same procedure was applied to determine the equilibrium temperature at the other pressures.

Based on this procedure, the calculated L-H-V three-phase equilibrium temperatures in the pressure range 20-500 bar are shown in Figure 4.9 along with experimental data. It can be seen that the linear behavior of the experimental data is also shown by the simulation data. The simulation data is also seen to be shifted to higher temperatures, thus the molecular models predict a larger stable area of methane hydrate compared to experimental observations.

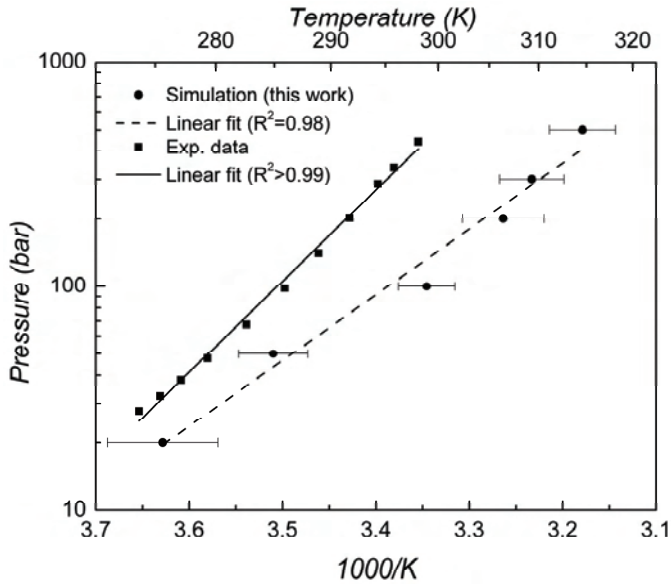


Figure 4.9. Pressure-temperature phase diagram for the liquid water-methane hydrate-methane vapor system comparing experimental data (filled squares)⁹³ and simulations results (filled circles). The hydrate structure is structure I. The straight lines correspond to the best fit of the data as found from regression. The error bars on the points found from simulation correspond to uncertainty in the temperature estimated from the standard deviations of μ_M^H , μ_M^V , $(\mu_W^{Lw} - \mu_{W_0}^H)$, and $(\mu_W^H - \mu_{W_0}^H)$.

It is seen that the linearity of the experimental data is also shown by the simulation data though the degree of linearity of the simulation data is not as high as that of the experimental data. Interestingly both the experimental and simulation data show a three-phase equilibrium temperature that bends off towards lower temperatures (deviates from linear behavior) as pressure drops below 100 bar. This might be an effect of the hydrate becoming increasingly non-stoichiometric as pressure decreases.

Figure 4.10 shows the fractional (small/large cage) and total equilibrium hydrate occupancy as a function of pressure, as determined from the simulations. As seen in the figure, the occupancy increases as the equilibrium pressure increases. It has previously been shown that the occupancy, $\theta_{J,i}$, of cavity i by type J molecules follows a Langmuir adsorption relation which has also been applied in the vdWP theory to model the cavity filling as a function of pressure and temperature. The Langmuir relation describing the filling of cages is given by:

$$\theta_{J,i} = \frac{C_{J,i} f_J}{1 + C_{J,i} f_J} \quad (4.32)$$

where, $C_{J,i}$ are the temperature dependent Langmuir constants found from fitting experimental data and f_J are the fugacities of molecule J . Using the Langmuir constants for methane as reported by Munck and coworkers,¹⁹⁶ the fractional and total occupancies of methane hydrate as a function of the equilibrium pressure are also plotted in Figure 4.10. It should be noted that the occupancy found at each pressure is at the corresponding L-H-V three-phase equilibrium temperature as found from either simulation or experiment. As seen in the figure, there is a good agreement between the trends observed in the occupancy found from simulation and those predicted by the Langmuir adsorption relation applied in the vdWP theory. Similar observations for the methane and propane hydrate occupancies as function of pressure have been presented in the literature.^{197,198}

In general, the occupancies found from simulations are slightly lower compared to those predicted by the vdWP theory. Compared to that of the large cages, the occupancy of the small cages is seen to be more strongly dependent on the pressure, both as calculated from simulation and from the vdWP theory. At the same time, the small cage occupancies found from simulations deviate more from those predicted by the vdWP theory when compared to the relative deviation in the large cage occupancies.

The small/large cage occupancy ratios found from simulations were between 0.89-0.98, and the hydration numbers were found to vary between 6.15-5.82 in the pressure region investigated; both of these quantities are not only within the limits reported from theoretical studies, but also within the experimentally reported values.^{2, 199-205}

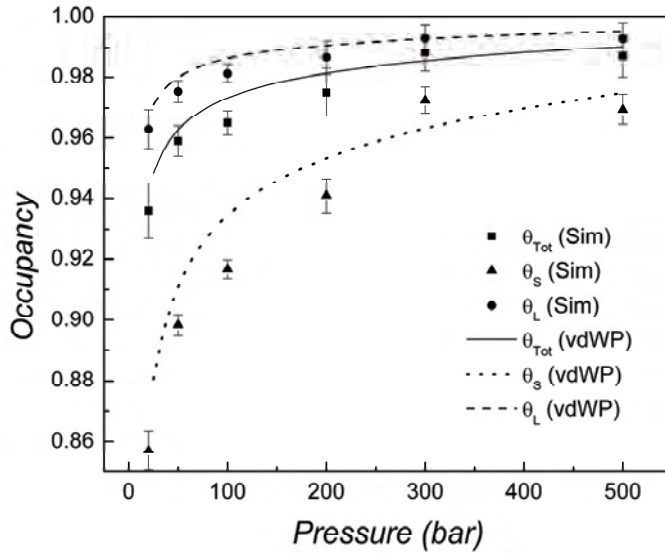


Figure 4.10. Occupancy of structure I methane hydrate as a function of pressure as found from simulations (filled circles) and calculated from the Langmuir adsorption theory applied in the vdWP approach to calculate the L-H-V three-phase equilibria (continuous line). The Langmuir constants applied in the calculations are those reported by Munck and co-workers.¹⁹⁶ The error bars in the occupancy correspond to the uncertainty estimated from the standard deviations of μ_M^H , μ_M^V , $(\mu_W^{Lw} - \mu_W^H)$, and $(\mu_W^H - \mu_W^0)$.

The small differences between occupancies from simulation and those predicted by the vdWP theory may be explained by revisiting some of the underlying assumptions of the vdWP theory. Previous studies have shown that the neglect of long range interactions between methane-methane and methane-water in the vdWP theory can cause minor changes in the occupancies; additionally, the effect of assuming a static hydrate framework can have a significant effect on the occupancy relationship, particularly for the small cage occupancy.¹³⁴

4.8.5 The three-phase equilibria of stoichiometric structure I methane hydrate

In Figure 4.10 it was seen that the hydrate occupancies in general were very high and very close to unity for pressures above 100 bar. Below 100 bar the cage occupancies

started decreasing and in particular the small cage occupancy dropped very fast. Interestingly in Figure 4.9 it was noted that the three-phase coexistence temperatures, also below 100 bar, were shifted towards lower temperatures compared to the trend observed at higher pressures. While this shift could be observed for both the experimental and simulation data the shift was most pronounced in the simulation data. This suggests that the level of linearity of the three-phase equilibrium data in the $\log P$ versus $1/T$ plane depends strongly on the occupancy of the hydrate. In this context it is interesting to investigate the dependence of the hydrate composition on the location of the L-H-V three-phase equilibria. This has been done by calculating the three-phase equilibria of methane hydrate assuming that the hydrate is fully occupied (stoichiometric). Calculating the three-phase equilibrium temperature assuming a stoichiometric hydrate the OF applied is slightly different compared to the one used when accounting for hydrate non-stoichiometry:

$$\text{OF} = G_H(\theta=1) - (N_W \mu_W^L + N_M \mu_M^V) \quad (4.33)$$

where $G_H(\theta=1)$ is the Gibbs free energy of the stoichiometric hydrate and $N_W \mu_W^L$ and $N_M \mu_M^V$ corresponds the free energy of the fluid phase having the same composition as the stoichiometric hydrate ($x_w = 0.852$, $x_m = 0.148$). Other than this the procedure for calculating the three-phase equilibrium temperature is the same as when accounting for hydrate non-stoichiometry. In Figure 4.11 the three-phase equilibria found from experiments and from simulations assuming the hydrate being non-stoichiometric and stoichiometric is shown. In general, there is a better agreement between the experimental results and the simulation results obtained assuming the hydrate is non-stoichiometric (a temperature difference of 4-16 K) compared to the case where a stoichiometric hydrate is assumed (8-16 K).

Interestingly it can be seen that the $\log P$ vs. $1/T$ relationship for the stoichiometric hydrate apparently possesses the same high degree of linearity as the experimental data, i.e., the low pressure data does not deviate as significantly from the expected trend observed for the high pressure data. This suggests that the shift in coexistence temperatures observed at low pressures for the non-stoichiometric hydrate is due to the relatively large decrease in the occupancy of the hydrate at these conditions.

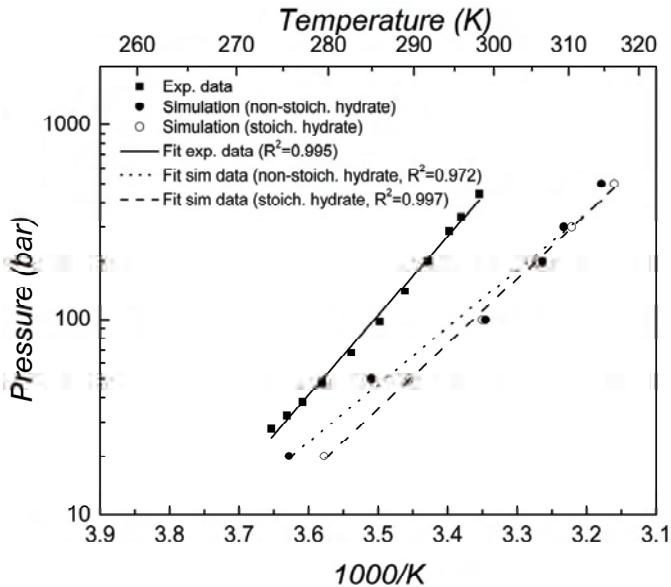


Figure 4.11. Pressure-temperature phase diagram for the liquid water-methane hydrate-methane vapor system comparing experimental data (filled squares)⁹³ and simulations results. Simulations results are shown for the non-stoichiometric hydrate (filled circles) and for the stoichiometric hydrate (open circles). The hydrate structure is structure I. The straight lines correspond to the best fit of the data as found from regression. The standard deviation of the simulation results are in the order of 4 K.

Based on the simulation results and their comparison with experimental data, it can be postulated that the equilibrium occupancies at experimental or simulation (non-stoichiometric) conditions do not decrease to the extent predicted by the Langmuir adsorption theory. Indeed there is also experimental evidence that the occupancy of methane hydrate below 100 bar is nearly constant at a value of 0.96²¹³ despite the fact that the vdWP model and simulations (accounting for non-stoichiometry) predict that the occupancy decreases with pressure. This actually suggests that the Langmuir adsorption theory might not be adequate to describe the filling of gas hydrates as pressure increases.

4.8.6 The three-phase equilibria of stoichiometric structure II methane hydrate

In the nucleation and growth simulations performed very recently by Walsh et al. and Kusalik and it was noticed that sII motifs coexisted with sI through a $5^{12}6^3$ transition cage.^{39,138} It is not known whether the sII and the transition cage is a stable configuration for long simulation times, but determining the three-phase equilibria of the sII methane hydrate will provide more information about the relative stability of these structures. Since it was found for the sI methane hydrate that only the equilibrium temperatures found for pressures below 100 bar were influenced by accounting for hydrate being a non-stoichiometric compound. In performing the calculations here it was assumed that hydrate was fully occupied at all times.

The free energy of the fully occupied sII methane hydrate was found using the FL method. In Table 4.8 a comparison of the free energies found for the sI and sII methane hydrate at 100 bar are shown in the temperature range 270-300 K.

Table 4.8. Gibbs free energy in kJ per mole of water for a fully occupied structure I (sI) and structure II (sII) hydrate calculated with the FL method. A thermal wavelength, $\Lambda = 1\text{\AA}$ has been used. Calculations were performed at 100 bar and the specified temperature. Numbers in parentheses are standard deviations.

Temp (K)	$G_{\text{sI,Full}}^H$ (FL) (kJ/mol)	$G_{\text{sII,Full}}^H$ (FL) (kJ/mol)
270	-47.19 (0.06)	-47.31 (0.03)
280	-46.59 (0.11)	-46.70 (0.03)
290	-45.98 (0.06)	-46.10 (0.05)
300	-45.40 (0.07)	-45.51 (0.04)

As seen in general the Gibbs free energy for the fully occupied sII methane hydrate is slightly lower than the sI methane hydrate indicating that the sII hydrate is a little more stable compared to the sI. This is rather surprising since it is well documented experimentally that methane forms sI hydrate at this condition.

Calculating the three-phase equilibrium temperature for the fully occupied sII hydrate the OF applied is similar to the one presented in eqn. (4.33) however now with $x_w = 0.85$ and $x_m = 0.15$ being the stoichiometric composition of sII hydrate. The results are

presented in Figure 4.12 along with the sI stoichiometric methane hydrate equilibria results.

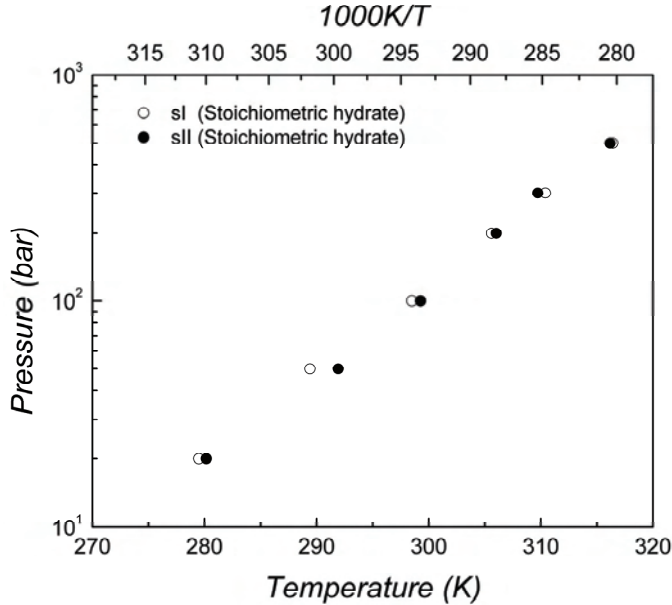


Figure 4.12. Pressure-temperature phase diagram for the liquid water-methane hydrate-methane vapor system assuming that the hydrate phase formed is fully occupied and that the hydrate structure formed is structure I (sI) and II (sII) methane hydrate. The standard deviation of the sI data point is around 4 K and the standard deviation of the sII data points is around 3 K.

Quite surprisingly it is found that equilibrium points of sI and sII methane hydrate are almost identical and that it actually seems as if the sII structure is preferred in particular at low pressures. Obviously assuming that the hydrate is fully occupied will have an impact on the free energies of the hydrate phase and might result in the sII being found to be more stable. If this is the case it is expected that differences in the occupancies of the sI and sII methane hydrate will be found. In Figure 4.13 the fractional occupancies of the small and large cage of sI and sII methane hydrate are shown as a function of the methane chemical potential.

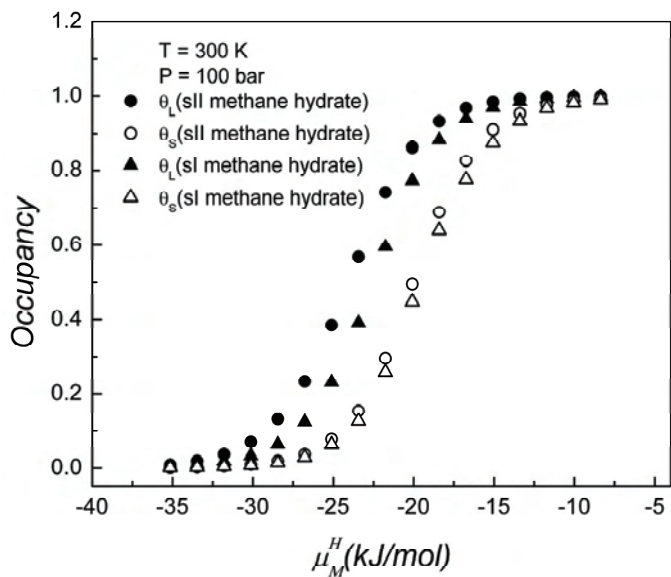


Figure 4.13. The fractional filling of the large and small cages in structure I (sI) and II (sII) methane hydrate as a function of the methane chemical potential at 300 K and 100 bar.

It is seen that the fractional filling of the sII large cage is slightly higher compared to the filling of the sI large cage while the small cage fractional occupancies are almost the same which seems sound since the 5^{12} cage of sI and sII have same number of molecules and are almost identical in terms for size. However due to the lower large to small cage ratio of sII (1:2) compared to sI (3:1) the total occupancy versus methane chemical potential for the sII is actually a little lower than for sI as seen in Figure 4.14. In general it is seen that the two curves have identical occupancies in the limiting regions where the occupancy is either close to 0 or 1. However between a methane chemical potential of -25 to -13 kJ/mol it is seen that the occupancies of the sII hydrate are a little lower than those found for the sI. Such small changes in the occupancy versus methane chemical potential can have a drastic influence on the three-phase hydrate coexistence point, thus it is likely that accounting for variations in the hydrate composition can indeed cause sI to be the structure preferred over sII.

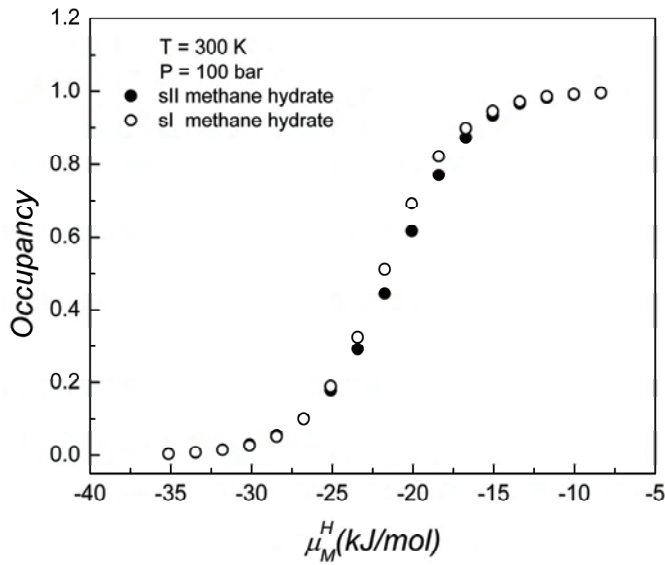


Figure 4.14. The total cage filling of sI and sII methane hydrate as a function of the methane chemical potential. $T = 300$ K and $P = 100$ bar.

Using CSMGem it is possible to perform methane hydrate coexistence point calculations assuming that the structure formed is either sI or sII. The results of these calculations are shown in Table 4.9.

Table 4.9. Liquid water-methane hydrate-methane vapor three-phase equilibrium calculations done for the structure I (sI) and II (sII) hydrate using molecular simulation and CSMGem.

P (bar)	T (K)			
	sI (Sim)	sII (Sim)	sI (CSMGem)	sII (CSMGem)
20	279.5	280.2	265.6	263.3
50	289.4	291.9	279.6	278.6
100	298.5	299.3	286.1	284.6
200	305.6	306.0	291.8	289.6
300	310.4	309.7	294.9	291.9
500	316.4	316.2	299.1	293.9

As seen the hydrate coexistence temperatures found using CSMGem⁷⁹ for the sI and sII methane hydrate are also relatively close however we know sI is the preferred (thermodynamically) structure. Nevertheless there should not be a very big difference in

the coexistence temperature between the two structures. Considering that the standard deviation obtained for the coexistence temperatures from simulations are on the order of 3-4 K it is difficult to conclude which structure will be preferred, since for most cases there will be an overlap between the hydrate coexistence points.

4.8.7 Estimation and calculation of the hydrate dissociation enthalpy

Using the Clapeyron equation it is possible to estimate the enthalpy change, ΔH , that will accompany any phase transition of a pure component (solid→liquid; solid→gas; liquid→gas etc.):

$$\frac{dP}{dT} = \frac{\Delta H}{T\Delta V} \quad (4.34)$$

For the phase transition that goes from the solid/liquid to gas we can make the assumption that the volume of gas is much larger than the volume of an equivalent amount of solid or liquid. Then the volume, ΔV , can be approximated by the volume of gas:

$$\begin{aligned} \Delta V &= V_{Gas} - V_{Liq.} \approx V_{Gas} \text{ or} \\ \Delta V &= V_{Gas} - V_{Sol.} \approx V_{Gas} \end{aligned} \quad (4.35)$$

The volume of gas can then be expressed as:

$$V_{Gas} = \frac{zRT}{P} \quad (4.36)$$

where z is the compressibility of the gas. Substitution of this expression into eqn. 4.32 leads to the following version of the Clapeyron equation:

$$\frac{d \log P}{d(1/T)} = -\frac{\Delta H}{zR} \quad (4.37)$$

Note that in the case of $z = 1$ eqn. (4.37) becomes the Clausius-Clapeyron equation. Eqn. (4.37) is valid for univariant systems like simple hydrates which means that the enthalpy of dissociation, ΔH_d , for hydrates containing only one guest molecule can be

estimated using three-phase equilibrium pressure-temperature data. Plots of $\log P$ versus $1/T$ should in principle approximate straight lines from which it is then possible to estimate $-\Delta H_d / zR$ as the slope of that plot. One of the problems of applying the Clapeyron equation to three-phase coexistence data in general arises from the non-stoichiometric nature of the hydrate phase.^{214,215} This is however not a substantial problem dealing with L-H-V equilibria since the non-stoichiometry does not change significantly over small temperature ranges and again there are indications that the occupancy of the hydrate might not decrease as significantly as proposed by the vdWP model as discussed previously which also seems to justify this assumption.

Previously the enthalpy of methane hydrate dissociation, $\Delta H_{d,M}$, has been determined by Sloan and Fleyfel from experimental pressure-temperature equilibrium data using data in the range up to 100 bar to.²¹⁶ In that work $\Delta H_{d,M}$ was determined to be 56.90 kJ/mol which is very close to the experimental value of 54.20 kJ/mol determined from calorimetry by Handa at 273.15 K and 24.98 bar.^{217,218} Skovborg and Rasmussen tried to reproduce the value determined by Sloan and Fleyfel but found a value of 62.85 kJ/mol and explain the discrepancies as originating in differences in the calculated compressibility factors.

Using the L-H-V equilibrium data found from molecular simulation, $\Delta H_{d,M}$ has been estimated at conditions very close to those used in the calorimetric studies by Handa. Since simulation L-H-V equilibrium data is available up to 500 bar experimental equilibrium data up to 500 bar has also been applied for a fair comparison of the enthalpies found.⁹³ The compressibility factor needed in calculation of $\Delta H_{d,M}$ from experimental equilibrium data was found using the SRK equation of state. The compressibility factors needed to calculate $\Delta H_{d,M}$ from simulated equilibrium data were found by performing methane *NPT* simulations at the pressure and temperature conditions of interest. 4.10 summarizes the results obtained in connection with calculation of $\Delta H_{d,M}$. It should be noted that extrapolation of the simulation L_W-H-V equilibrium data was necessary to calculate $\Delta H_{d,M}$ at 273.15 K.

Table 4.10. Enthalpy of dissociation for methane hydrate determined from the Clapeyron equation using simulation and experimental data for the liquid water – methane hydrate – methane vapor three-phase equilibrium. The experimental value is obtained from calorimetry as reported by Handa.^{217,218}

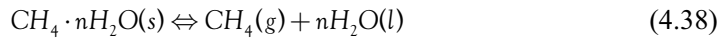
	P/T (bar/K)	Slope	z	$\Delta H_{d,M}$ (kJ/mol)	Abs. deviation (%)
Exp. value	25/273.15	-	-	54.20	-
Exp. P - T data	25/273.15	-9363	0.941	73.28	35.2
Sim. non-stoich.	25/277.95	-6677	0.956	53.10	2.0
Sim. non-stoich.	16.71/273.15	-6677	0.970	53.90	0.6
Sim. stoich.	25/282.20	-7685	0.963	61.56	13.6
Sim. Stoich.	10.16/273.15	-7685	0.982	62.70	15.7

From Table 10 it is noticed that the $\Delta H_{d,M}$ obtained from experimental L-H-V data deviates significantly (35.2 %) from the experimental value and even more compared to the values found by Sloan and Fleyfel and Skovborg and Rasmussen. However as described above, Sloan and Fleyfel used data up to 100 bar while data up to 500 bar is used here, indicating that $\Delta H_{d,M}$ is very sensitive to the range of experimental data used to regress the slope, hence also $-\Delta H_d / zR$. That the slope seems rather sensitive to the pressure-temperature range applied suggests that the non-stoichiometry of the hydrate, unexpectedly, is causing problems in connection with applying the Clapeyron equation for calculation of $\Delta H_{d,M}$. Another reason for the deviations observed could be that the volumes of the condensed phases have been neglected, which in more recent works has been shown to cause $\Delta H_{d,M}$ becoming too large.²¹⁹

Based on the simulation L-H-V equilibrium data assuming a non-stoichiometric methane hydrate, $\Delta H_{d,M}$ is found to be within 2% of the experimental value (either the pressure or temperature match experimental conditions). The reason why $\Delta H_{d,M}$ found at 277.95 K is lower than $\Delta H_{d,M}$ found at 273.15 K, is due to the compressibility factor of methane being smaller at 25 bar compared to 16.71 bar. Assuming a stoichiometric hydrate $\Delta H_{d,M}$ deviates by around 15% from the experimental value. Again the enthalpy at the lower temperature is slightly higher than at the higher temperature value due to the compressibility differences. Interestingly it is the data set showing the least linearity in

the $\log P$ versus $1/T$ plane (showing least Clapeyron behavior) which gives the best estimate of $\Delta H_{d,M}$ (see Figure 4.9).

Alternatively it is possible independently to determine the enthalpy of each species (hydrate, water and methane) by performing individual *NPT* simulations at the pressure and temperature conditions listed in Table 4.10. In this case $\Delta H_{d,M}$ can then be calculated by considering the equation representing the dissociation of methane hydrate to gaseous methane and liquid water:



After dissociation has taken place the liquid water will contain small amounts of methane and the methane will contain small amounts of water which theoretically will impact $\Delta H_{d,M}$. However as was shown in section 4.8.2 the liquid and vapor phases can be assumed pure, to a very good approximation. For the non-stoichiometric hydrate the composition at the chosen conditions has been estimated from fitting a Langmuir type equation to the data in Figure 4.10. From SGMC simulations the enthalpy of the hydrate at the given compositions was determined and the results are presented in Table 4.11.

As seen from the table the enthalpies of methane hydrate dissociation found directly from *NPT* and SGMC simulation assuming the hydrate is non-stoichiometric are very close to the values determined from the simulation *PT* data using the Clapeyron relation and for this reason also in good agreement with the experimental value. It is also noted that the value of $\Delta H_{d,M}$ found at 16.71 bar and 273.15 K is slightly higher compared to the one found at 25 bar and 277.95 K which is consistent with what was found using the Clapeyron relation and is caused by the difference in methane compressibilities as mentioned above. The enthalpies of hydrate dissociation assuming the hydrate has a stoichiometric composition are slightly lower than when the hydrate is assumed non-stoichiometric, however they are still in reasonably good agreement with the experimental value.

Table 4.11. Enthalpies of methane hydrate dissociation, $\Delta H_{d,M}$ found from eqn. (4.38) by calculating the enthalpies of the three species from *NPT* simulations. $\Delta H_{d,M}$ has been determined assuming that the hydrate is non-stoichiometric according to the equilibrium composition given in Figure 4.10 and assuming that the hydrate is stoichiometric.

	P/T (bar/K)	θ	$\Delta H_{d,M}$ (kJ/mol CH ₄)	Abs. deviation (%)
Exp. value	25/273.15	-	54.20	-
Sim. non-stoich.	25/277.95	0.939	50.76	6.35
Sim. non-stoich.	16.71/273.15	0.912	50.86	6.16
Sim. stoich.	25.00/282.20	1	49.87	7.99
Sim. stoich.	10.16/273.15	1	48.54	10.44

Based on these findings it is concluded that the Clapeyron equation should be used with extreme caution for estimating $\Delta H_{d,M}$. This conclusion is supported by the variation in $\Delta H_{d,M}$ values reported in literature using this method as they span from 52.9-67.85 kJ/mol.²¹⁹ On the other hand using the TIP4P/Ice potential model to calculate the enthalpy of melting/dissociation for solids having a high water content should be a relatively good approximation based on the findings here. This is further supported by the fact that the enthalpy of melting of ice has been found using the TIP4P/Ice model to be 5.40 kJ/mol¹⁶⁸ which is close to the experimental value of 6.02 kJ/mol.²²⁰

Chapter 5

Conclusions and recommendations

The kinetics of different gas hydrate forming systems have been investigated experimentally using different experimental apparatuses and methods and analytically using a gas hydrate induction time model. The effect of different KHIs on the formation of gas hydrates has been quantified, including the effect of ice-structuring proteins isolated from insects and fish and considered as novel KHIs.

Using MC simulations the three-phase liquid water-methane hydrate-methane vapor equilibrium was determined over a broad range of temperature and pressure as well as other physical properties of methane hydrate. In the following sections the main conclusions and recommendations for future work is presented.

5.1 Conclusions

The nucleation of sI and sII gas hydrate was investigated experimentally using stirred cells and a high pressure DSC. From the stirred cell experiments it was found that a relatively large scattering of the measured induction times of hydrate formation can be expected stressing that the nucleation of gas hydrates is stochastic. By plotting induction times of propane hydrate formation against supersaturation, information about the formation mechanism and certain microscopic hydrate properties was obtained using an induction time model. The results suggest that the hydrate nucleation mechanism is highly heterogeneous and that the effective surface energy between the hydrate and the

substrate can be regarded as a dynamic surface energy. Adding a KHI to the hydrate forming system will cause the nucleation mechanism to become more homogeneous whereby longer induction times may be expected whereas the effective surface energy between the hydrate and the substrate was found to increase. The reproducibility of the induction time of hydrate formation can be improved significantly by crystal seeding. This was done by adding small amounts of impurities to the hydrate forming system or by forming hydrate precursors in the aqueous solution that constitutes part of the hydrate forming system. Using a crystal seeding procedure the formation rate of sI and sII hydrates was quantified and the effect of introducing NaCl, heptane and two KHIs was investigated. It was found that sI forms more rapidly than sII while both NaCl and heptane were found to promote hydrate formation. PVCap and ISP from the ocean pout were shown capable of prolonging both the induction time of sI and sII quite effectively, the ocean pout ISP being slightly superior compared to PVCap. Despite reports that PVCap is a better KHI of sII hydrate (based on the fact that PVCap can withstand higher subcoolings for sII hydrate), findings in this work suggest that PVCap inhibits sI and sII hydrate equally well - a conclusion reached by including both the formation kinetics and the equilibrium conditions of sI and sII hydrate in the analysis.

Nucleation of gas hydrates was also investigated using a high pressure DSC. The advantage of using this type of equipment is that it allows studying hydrate nucleation in very small samples which is beneficial when studying the KHI potential of novel KHIs which are yet not available in large amounts. The main disadvantage of DSC is that it requires a large subcooling to form hydrate and that isothermal experiments often result in scattered induction time measurements. A test procedure based on the hydrate precursor method was used in the DSC experiments to promote nucleation. This method allowed the study of methane hydrate formation at moderate degrees of subcooling and measurement of the methane hydrate induction time. Addition of very small amounts of the ISP found in the Danish bark beetle to the hydrate forming system, caused the induction time of methane hydrate to increase significantly, thus the bark beetle ISP (which is the most efficient ISP known) also holds great potential as a KHI.

Growth studies of sI and sII hydrate were performed at constant temperature and pressure using a newly designed experimental set-up. The growth profile, (the percentage

of water converted to hydrate as a function of time), of hydrates formed from pure water was found to be linear and again sI hydrate was found to form faster than sII. However where ocean pout ISP or PVCap was added to the aqueous phase the growth profile was found to be split in two stages. Initially the growth pattern followed a second order polynomial but then shifted and became linear. These results suggest that certain KHIs, capable of adsorbing on the surface of the growing hydrate, will minimize the hydrate surface area dramatically enough that the intrinsic kinetics, i.e. mainly the surface reaction process, will control the growth in contrast to when no KHIs are present and mass transfer from the gas to the liquid phase will be the limiting step.

The results suggest that certain ISPs have the potential to substitute the KHIs used by the oil and gas industry today and may even add to the defense against hydrates considering that some of the ISPs are better KHIs than PVCap. Furthermore implementation of ISPs in flow assurance also offers a way to eliminate KHIs with low biodegradability used by the industry today. Currently, however, the production of ISPs is not at a scale where they can be used in practical applications.

Monte Carlo simulations were used to calculate the three-phase liquid water-methane hydrate-methane vapor equilibrium in the pressure range 20-500 bar based on molecular models for water (TIP4P/Ice) and methane (Lennard-Jones united-atom). Vapor-liquid equilibria calculations for the binary methane-water system showed that the fluid phases were nearly pure for the conditions studied, and thus the effect of accounting for mixing in these phases had a negligible contribution to the chemical potential of the majority species. For this reason, the pure component values were used for the chemical potentials of liquid water and methane vapor to simplify the criteria for phase coexistence.

The deviation in the coexistence temperature between the simulation and experimental data increased with pressure, from 4 K at 20 bar to 16 K at 500 bar. The simulation data followed approximately a Clapeyron (linear) behavior in the $\ln P$ versus $1/T$ plot though not as markedly as the experimental data. The hydrate occupancies found at equilibrium from the simulations were in reasonably good agreement with those calculated from the van der Waals and Platteeuw approach, which uses a Langmuir adsorption analogy.

Assuming that the hydrate was fully occupied by methane improved the fit of the simulation data to the Clapeyron equation. This suggests that the composition of the

hydrate might not be accurately represented by the Langmuir adsorption analogy applied in the vdWP theory. This suggestion is further supported by experimental evidence that the occupancy of methane hydrate never falls below 0.96 even in the low pressure ranges. Surprisingly it was found that the fully occupied sII methane hydrate was thermodynamically favored over the sI, however there are indications that accounting for the non-stoichiometric nature of the hydrate will favor the formation of sI. The potential models used were also found to capture the dissociation enthalpy of methane hydrate within 10 % of the experimental value.

Determining the phase equilibrium of a multi-component, multi-phase system is an intricate and computationally intensive process, however, such calculations are essential if proper conclusions are to be made from hydrate simulations defined in terms of subcooling or over-pressurization. The methodology and results reported here serve as a foundation for future studies investigating both equilibrium and dynamic simulations employing molecular models. It should be noted that the results presented are specific to the molecular models used, and phase boundaries may differ significantly between different molecular models; caution should be exercised when determining whether a simulated system is thermodynamically stable within the hydrate phase envelope.

5.2 Recommendations for future work

The nucleation of gas hydrates continues to be a very challenging area, in particular the study of the nucleation mechanism. While molecular simulations have proven quite useful in this study, a true comparison between what is observed in the simulation box and what can be observed experimentally has not been performed. Studying the formation rate of sI and sII hydrate using molecular simulation offers a way of testing the model against experimental data on a qualitative basis since it is known from experiments that formation of sI hydrate is faster than sII hydrate. If such studies are successful this will open up for using molecular simulations to study the effects of known KHIs on the formation of gas hydrates and a comparison with experimental results can be made. In direct continuation of the simulation work done here it is recommended to investigate if the non-stoichiometric sII hydrate is also more stable than the non-stoichiometric sI

methane hydrate or if taking into account the non-stoichiometric nature of methane hydrate will actually alter the preferred thermodynamic structure of methane hydrate.

From an experimental point of view the way in which nucleation results from different apparatuses can be translated and compared is of great interest - not at least how lab scale experiments translate to pilot scale flow lines. In this context and as a continuation of this work it would be interesting to study how the isothermal induction time measurements obtained using the high pressure DSC applying the hydrate precursor method relate to constant cooling rate high pressure DSC experiments or stirred cell experiments. An important goal is ranking how efficient KHIs are found to be using the different methods. In relation to applying the precursor method in high pressure DSC experiments it is also interesting to investigate the effect of superheating and hold time during the production of precursors on the induction time, considering that the method has only been applied for the few studies performed in this work.

Further nucleation studies to investigate the KHI potential of especially the Danish bark beetle ISP should be performed to clarify whether it is actually as promising a KHI as the initial results suggest. In this relation it is also interesting to investigate if it is possible to boost the KHI potential of the ISPs by adding small amounts of (for example) citrate or glycerol to the ISP solution since these compounds have been reported to enhance the ISP antifreeze activity significantly.²²¹

Finally a detailed study and analysis of potential ISP production methods should be performed to reveal if it is possible from a practical point of view to produce ISP in the amounts required if it is to be used as a KHI in oil and gas applications as well as estimating if it can be produced at a price that is comparable to that of PVCap.

References

¹ http://www.pet.hw.ac.uk/research/hydrate/images/hydrates/structures_large.jpg (30.06.10).

² Sloan, E.D., Koh, C.A., Clathrate Hydrates of Natural Gases, 3rd edition, CRC press, Boca Raton, FL (2008).

³ Sloan, E.D., Hydrate Engineering, SPE Inc., Richardson, Texas (2000).

⁴ Sloan, E.D., *Fluid Phase Eq.* 2005, **228–229**, 67.

⁵ Welling and Associates, 1999 Survey, cited by Macintosh, N., Flow Assurance Still Leading Concern among Producers, Offshore, October (2000).

⁶ van der Waals, J. H., *Trans. Faraday SOC.* 1956, **52**, 184.

⁷ van der Waals, J. H., Platteeuw, J. C., *Adv. Chem. Phys.* 1956, **2**, 1.

⁸ Kelland, M., *SPE* 1995, **30420**.

⁹ Cooley, C., Wallace, B.K., Gudimetla, R., *SPE* 2003, **84350**.

¹⁰ Malcolm A. Kelland, *Energy & Fuels* 2006, **20**, 825.

¹¹ Skovborg, P., Rasmussen, P., *Chem. Eng. Sci.* 1994, **49**, 1131.

¹² Natarajan, V., Bishnoi, P. R., Kalogerakis, N., *Chem. Eng. Sci.* 1994, **49**, 2075.

¹³ Christiansen, R.L., Sloan, E.D., Proc. Annual Convention of Gas Processors Association, p. 15, San Antonio, Tx, (1995).

¹⁴ A. Vysniauskas and P. R. Bishnoi, *Chem. Eng. Sci.* 1983, **38**, 1061.

¹⁵ Kashchiev, D. Firoozabadi, A., *J. Cryst. Growth*, 2002, **243**, 476.

¹⁶ Anklam, M.R., Firoozabadi, A., *J. Chem. Phys.*, 2004, **121**, 11867.

¹⁷ Frostman, L.M., Thieu, V., Crosby, D.L., Downs, H.H., *SPE* 2003, **80269**.

¹⁸ Philips, N. J., *Proc. 8th International Oilfield Chemical Symposium*, Geilo, Norway, March (1997).

¹⁹ Argo, C.B., Blaine, R.A., Osborne, C.G., Priestly, I.C., *SPE* 1997, **37255**.

²⁰ Talley, L.D., Mitchell, G.F., *Proc. of the 30th Annual Offshore Technology Conference*, **OTC 11036**, Houston, Tx, (1998).

²¹ Fu, S.B., Cenegy, L.M., Neff, C., *SPE* 2001, **65022**.

-
- ²² Philips, N.J., Grainger, M., *SPE* 1998, **40030**.
- ²³ Leporcher, E.M., Fourest, J.P., Labes-Carrier, C., Lompre, M., *SPE* 1998, **50683**.
- ²⁴ MacDonald, A.W.R., Petrie, M., Wylde, J.J., Chalmers, A.J., Arjmandi, M., *SPE* 2006, **99388**.
- ²⁵ Glenat, P., Peytavy, J. L., Holland-Jones, N., Grainger, M., *SPE* 2004, **88751**.
- ²⁶ Villano, L.D., Kommedal, R., Kelland, M.A., *Energy & Fuels* 2008, **22**, 3143.
- ²⁷ Satyanarayana Gypta, D.W., *Corrosion*, 2007, **04406**, 1.
- ²⁸ Purinton, R.J. Manning, T.S., *SPE* 1996, **35822**.
- ²⁹ Parks-Lee, Bevin, Fidoe, S. In oilfield chemistry, green is the color of progress, *Oil&Gas Financial Journal*, issue 11, volume 6, November 2009.
- ³⁰ Koh, C.A., Savidge, J.L., Tang, C.C., *J. Phys. Chem.* 1996, **100**, 6412.
- ³¹ Koh, C.A., Wisbey, R.P., Wu, X., Westacott, R.E., Soper, A.K., *J. Chem. Phys.* 2000, **113**, 6390.
- ³² Rodger, P.M., Forester, T.R., Smith, W., *Fluid Phase Eq.* 1996, **116**, 326.
- ³³ Baez, L.A., Clancy, P., *Ann. N.Y. Acad. Sci.* 1994, **715**, 177.
- ³⁴ Moon, C., Taylor, P.C., Rodger, P.M., *JACS* 2003, **125**, 4706.
- ³⁵ Nada, H., *J. Phys. Chem.* 2006, **110**, 16526.
- ³⁶ Vatamanu, J., Kusalik, P.G., *J. Phys. Chem.* 2006, **110**, 15896.
- ³⁷ Moon, C., Taylor, P.C., Rodger, P.M., *Faraday Discuss.* 2007, **136**, 367.
- ³⁸ Zhang, J., Hawtin, R.W., Yang, Y., Nakagava, E., Rivero, M., Choi, S.K., Rodger, P.M., *J. Phys. Chem. B* 2008, **112**, 10608.
- ³⁹ Walsh, M.R., Koh, C.A., Sloan, E.D., Sum, A.K., Wu, D.T., *Science* 2009, **326**, 1095.
- ⁴⁰ Devries, A.L., Lin, Y., *Biochem. Biophys. Acta* 1977, **495**, 388.
- ⁴¹ Zeng, H., Ripmeester, J.A., Wilson, L.D., Walker, V.K., *Canadian Journal of Physics* 2003, **81**, 17.
- ⁴² Zeng, H., Moudrakovski, I.L., Ripmeester, J.A., Walker, V.K., *AIChE Journal* 2006, **52**, 3304.
- ⁴³ Zeng, H., Wilson, L.D., Walker, V.K., Ripmeester, J.A., *JACS* 2006, **128**, 2844.
- ⁴⁴ Al-Adel, S., Dick, J.A.G., El-Ghafari R., Servio, P., *Fluid Phase Eq.* 2008, **267**, 92.
- ⁴⁵ Logsdon, J.M., Doolittle, W.F., *Proc. Natl. Acad. Sci.* 1997, **94**, 3485.
- ⁴⁶ Clarke, M., Bishnoi, P.R., *Chem. Eng. Sci.* 2001, **56**, 4715.
- ⁴⁷ Clarke, M., Bishnoi, P.R., *The Canadian Journal of Chemical Engineering* 2001, **79**, 143.
- ⁴⁸ Clarke, M., Bishnoi, P.R., *Chem. Eng. Sci.* 2004, **59**, 2983.
- ⁴⁹ Clarke, M., Bishnoi, P.R., *Chem. Eng. Sci.* 2005, **60**, 695.
- ⁵⁰ Clarke, M., Bishnoi, P.R., *Ann. N.Y. Acad. Sci.* 2000, **912**, 556.

-
- ⁵¹ Bergeron, S., Servio, P., *Fluid Phase Eq.* 2008, **265**, 30.
- ⁵² Ostwald, W., *Zeit fur Physik Chemie* 1900, **34**, 495.
- ⁵³ Miers, H.A., Isaac, F., *Proc. Roy. Soc.* 1907, **A79**, 322.
- ⁵⁴ Wilson, P.W., Heneghan, A.F., Haymet, A.D.J., *Cryobiology* 2003, **46**, 88.
- ⁵⁵ Wilson, P.W., Lester, D. Haymet, A.D.J. *Chem. Eng. Sci.* 2005, **60**, 2937.
- ⁵⁶ Bishnoi, P.R., Natarajan, V., *Fluid Phase Eq.* 1996, **117**, 168.
- ⁵⁷ Davies, S.R., Hester, K.C., Lachance, J.W., Koh, C.A., Sloan, E.D., *Chem. Eng. Sci.* 2009, **64**, 370.
- ⁵⁸ Mullin, J. W., *Crystallization*, 4th edition, Elsevier Science & Technology Books, Amsterdam (2001).
- ⁵⁹ Rahman, A., Stillingner, F.H., *JACS* 1973, **95**, 7943.
- ⁶⁰ Christiansen, R. L., Sloan, E. D., *Ann. N.Y. Acad. Sci.*, **715**, 283 (1994).
- ⁶¹ Long, J. Gas Hydrate Formation Mechanism and Its Kinetic Inhibition, Ph.D. Thesis, Colorado School of Mines, Golden, CO (1994).
- ⁶² Kvamme, B., *Proc. 2nd International Conference on Natural Gas Hydrates*, p. 139, Toulouse, France, June 2-6 1996.
- ⁶³ Baez, L.A., Clancy, P., *Ann. N.Y. Acad. Sci.*, **715**, 177 (1994).
- ⁶⁴ Skovborg, P., Ng, H.J., Rasmussen, P., Mohn, U., *Chem. Eng. Sci.* 1993, **48**, 445.
- ⁶⁵ Arjmandi, M., Tohidi, B., Danesh, A., Todd, A.C., *Chem. Eng. Sci.* 2005, **60**, 1313.
- ⁶⁶ Kashchiev, D., Firoozabadi, A., *J. Cryst. Growth* 250, 2003, 499.
- ⁶⁷ Kozielski, K.A., Becker, N.C., Hartley, P.G., Wilson, P.W., Haymet, A.D.J., Gudimetla, R., Ballard, A.L., Kini, R., *Proc. 6th International Conf. on Natural Gas Hydrates*.
- ⁶⁸ Parent, J.S., Bishnoi, P., *Chem. Eng. Commun.* 1996, **144**, 51-64
- ⁶⁹ Muller-Bongartz, B., Wildeman, T.R., Sloan, E.D., *Proc. 2nd International Offshore and Polar Engineering Conference*, 1992, 628.
- ⁷⁰ Nerheim, A.R., Svartass, T.M., Samuelsen, E.J., *SPE* 1994, **28635**.
- ⁷¹ Cingotti, B., Sinquin, A., Pic, J.S., Herri, J.M., Cournil, M., *SPE* 1999, **50757**.
- ⁷² Jensen, L., Thomsen, K., von Solms, N., *Chem. Eng. Sci.* 2008, **63**, 3069.
- ⁷³ Dalmazzone, D., Hamed, N., Dalmazzone, C., Rousseau, L., *Journal of Thermal Analysis and Calorimetry* 2006, **85**, 361.
- ⁷⁴ Villano, L., Kommedal, R., Fijten, M.W.M., Schubert, U.S., Hoogenboom, R., Kelland, M., *Energy & Fuels* 2009, **23**, 3665.

-
- ⁷⁵ Duchateau, C., Peytavy, J.L., Glenat P., Pou, T.E., Hidalgo, M., Dicharry, C., *Energy & Fuels* 2009, **23**, 962.
- ⁷⁶ Bylov, M., An Experimental Study of the Nucleation and Growth of Gas Hydrates, Ph.D. Thesis, The Technical University of Denmark, Kgs. Lyngby, (1997).
- ⁷⁷ Seo, Y., Ripmeester, A.J., Lee, J., Lee, H., *Environ. Sci. Technol.* 2005, **39**, 2315.
- ⁷⁸ Kashchiev, D., Firoozabadi, A., *J. Cryst. Growth* 2002, **241**, 220
- ⁷⁹ Ballard, A., Sloan, E.D. *Fluid Phase Eq.* 2004, 218, 15.
- ⁸⁰ Chapoy, A., Mokroui, S., Valtz, A., Richon, D., Mohammadi, A.H., Tohidi, B., *Fluid Phase Eq.* 2004, 226, 213.
- ⁸² Kashchiev, D. Nucleation – Basic theory with applications, Butterworth-Heinemann (2000).
- ⁸³ Dufour, L., Defay, R., Thermodynamics of Clouds. Academic Press, New York. (1963).
- ⁸⁴ Englezos, P., Kalogerakis, N., Dholabhai, P.D., Bishnoi, P.R., *Chem Eng Sci* 1987, **42**:2647
- ⁸⁵ Rasmussen, D.H., *J. Chem. Phys.* 1986, **85**, 2272.
- ⁸⁶ Uchida, T., Ebinuma, T., Takeya, S., Nagao, J., Narita, H., *J. Phys. Chem. B* 2002. 106, 820.
- ⁸⁷ van der Leeden, M.C., Kashchiev, D., van Rosmalen, G.M., *Journal of Crystal Growth* 1993, **130**, 221.
- ⁸⁸ Tohidi, B., Burgass, R. W., Danesh, A., Todd, A. C., *Proc. 1st International Conf. on Natural Gas Hydrates, Ann. N. Y. Acad. Sci.* 1994, **715**, 532.
- ⁸⁹ Tohidi, B., Burgass, R. W.; Danesh, A., Østergaard, K. K., Todd, A. C., *Ann. N. Y. Acad. Sci.* 2000, **912**, 924.
- ⁹² Jensen, L., Thomsen, K., Ramløv, H., von Solms, N., *Ind. Eng. Chem. Res.* 2010, 49, 1486.
- ⁹³ Deaton, W. M.; Frost, E. M. Gas hydrates and their relation to the operation of natural-gas pipelines, *U.S. Bureau of Mines Monograph* 1946, 8, 101.
- ⁹⁴ Becke, P., Kessel, D., Rahimian, I., *SPE* 1992, **25032**.
- ⁹⁷ Yousif, M. H., Austvik, T., Berge, L. I., Lysne, D., Coleman, H. W., *Proc. 2nd International Conference. on Gas Hydrates*, p. 291, Toulouse (1996).
- ⁹⁸ Skovborg, P. Gas Hydrate Kinetics, PhD thesis, The Technical University of Denmark, Kgs. Lyngby (1993).
- ⁹⁹ Scauzillo, F. R., *Chem. Eng. Prog.* 1956, **52**, 324.
- ¹⁰⁰ Nygaard, H. F., *Multi-phase Flow-Proceedings of the 4th International Conference*, p. 1-14, 1989.
- ¹⁰¹ Sinquin, A., Bredzinsky, X., Beunat, V., *SPE* 2001, **71543**.

-
- ¹⁰² Sloan, E. D., Subramanian, S., Matthews, P. N., Lederhos, J. P., Khokar, A. A., *Ind. Eng. Chem. Res.* 1998, **39**, 3124.
- ¹⁰³ Larsen, R., Knight, C. A., Sloan, E. D., *Fluid Phase Eq.* 1998, **150-151**, 353.
- ¹⁰⁴ Svartaas, T. M., Kelland, M. A., Dybik, L., *Ann. N.Y. Acad. Sci.* 2000, **912**, 744.
- ¹⁰⁵ Wilkens, C., Ramløv, H., *CryoLetters* 2008, **29**, 293.
- ¹⁰⁶ Prediction of Gas Hydrates Formation with HP-microDSC Technique." Calorimetry conference(2004).
- ¹⁰⁷ Setaram, "Micro DSC VII Commissioning Utilizations" France, Setaram Manual B/DSC7A.
- ¹⁰⁸ Sorai, M., *Comprehensive Handbook of Calorimetry and Thermal Analysis*, Maruzen Company Limited (1998).
- ¹⁰⁹ Noyes, A.A., Whithy, W.R., *Journal of the American Chemical Society* 1897, **19**, 930.
- ¹¹⁰ Berthoud, A., *Journal de Chimique Physique* 1912, **10**, 624.
- ¹¹¹ Valeton, J.J.P., *Zeitschrift für Kristallographie* 1924, **59**, 483.
- ¹¹² Kane, S.G., Evans, T.W., Brian, P.L.T., Sarofim, A.F., *AIChE Journal* 1974, **20**, 855.
- ¹¹³ Malegaonkar, M.B., Dholabhai, P.D., Bishnoi, P.R., *Can. J. Chem. Eng.* 1997, **75**, 1090.
- ¹¹⁴ Chun, M.K., Lee, H., *Korean J. Chem. Eng.* 1996, **13**, 620.
- ¹¹⁵ Mork, M., Gudmundsson, J.S., *Proc. 4th International Conference. on Gas Hydrates*, p. 6, Yokohama (2002).
- ¹¹⁶ Larson, R., Makogon, T., Knight, C., Sloan, E.D., *Proc. 2nd International Conference. on Gas Hydrates*, p. 163, Toulouse (1996)
- ¹¹⁷ Smelik, E.A., King, H.R., *Am. Mineral.* 1997, **82**, 88.
- ¹¹⁸ Udachin, K.A., Ratcliffe, C.I., Ripmeester, J.A., *Supramol. Chemistry* 2002, **2**, 405.
- ¹¹⁹ Makogon, Y., Makogon, T., Holditch, S., *Proc. Japan National Oil Conference*, p. 259, Tokyo (1998).
- ¹²⁰ Uchida, T., Ebinuma, T., Kawabata, J., Narita, H., *J. Cryst. Growth* 1999, **204**, 348.
- ¹²¹ Vysniauskas, A., Bishnoi, P.R., *Chem. Eng. Sci.*, 1985, **40**, 299.
- ¹²² Monfort, J.P., Nzihou, A., *J. Cryst. Growth* 1993, **128**, 1182.
- ¹²³ Bergeron, S., Beltrán, J.G., Servio, P., *Fuel* 2010, **89**, 294.
- ¹²⁴ Laemmli, U.K., *Nature* 1970, **227**, 680.
- ¹²⁵ Scotter, A.J., Marshall, C.B., Graham, L.A., Gilbert, J.A., Garnham, C.P., Davies, P.L., *Cryobiology* 2006, **53**, 229.
- ¹²⁶ Gordienko, R., Ohno, H., Singh, V.K., Jia, Z., Ripmeester, J.A., Walker, V.K., *PLoS ONE*, 5(2): e8953.

-
- ¹²⁷ Allen, M. P., Tildesley, D. J. *Computer Simulation of Liquids*, Clarendon Press, Oxford (1987).
- ¹²⁸ Frenkel, D., Smit, B. *Understanding Molecular Simulation: From Algorithms to Applications*, Academic
- ¹²⁹ Tester, W.J., Bivins, R.L., Herrick, C.C., *AIChE Journal*. 1972, **18**, 1220.
- ¹³⁰ Tse, J.S., Klein, M.L., *J. Chem. Phys.* 1983, **78**, 2096.
- ¹³¹ Tse, J.S., Klein, M.L., *J. Chem. Phys.* 1983, **87**, 4198.
- ¹³² Tse, J.S., Klein, M.L., *J. Chem. Phys.* 1984, **81**, 6146.
- ¹³³ Rodger, P.M., *J. Chem. Phys.* 1990, **94**, 6080.
- ¹³⁴ Wierzchowski, S.J., Monson, P.A., *J. Phys. Chem. B* 2007, **111**, 7274.
- ¹³⁵ Rosenbaum, E.J., English, N.J., Johanson, J.K., Shaw, D.W., Warzinski, R.P., *J. Phys. Chem. B* 2007, **111**, 13194.
- ¹³⁶ Wierzchowski, S.J., Monson, P.A., *Ind. Eng. Chem. Res.* 2006, **45**, 424.
- ¹³⁷ Zheng, J. Hawtin, R.W., Nakagava, E., Rievero, M., Choi, S.K., Rodger, P.M., *J. Phys. Chem. B* 2008, **112**, 10608.
- ¹³⁸ Vatamanu, J., Kusalik, P.G., *J. Am. Chem. Soc.* 2006, **128**, 15588.
- ¹³⁹ McQuarrie, D. A. *Statistical Mechanics*, Harper and Row, New York (1976).
- ¹⁴⁰ Born, M., von Karman, T., *Physik. Z.* 1912, **13**, 297.
- ¹⁴¹ Metropolis, N., Rosenbluth, A.W., Rosenbluth, M.N., Teller, A.H., Teller, E., *J. Chem. Phys.*, 1953, **21**, 1087.
- ¹⁴² Santra, M. Chakrabarty, S., Bagchi, B., *J. Chem. Phys.* 2008, **129**, 234704.
- ¹⁴³ Haile, J.M., *Molecular dynamics simulation, elementary methods*, Wiley Interscience, New York (1990).
- ¹⁴⁴ Ewald, P., *Ann. Phys.* 1924, **64**, 253.
- ¹⁴⁵ Cicotti, G., Frenkel, D., McDonald, I.R., *Simulation of Liquids and Solids: Molecular Dynamics and Monte Carlo Methods in Statistical Mechanics*, North Holland, Amsterdam (1987).
- ¹⁴⁶ De Leeuw, S.W., Perram, J.W., Smith, E.R., *Proc. R. Soc. London A* 1980, **373**, 27.
- ¹⁴⁷ De Leeuw, S.W., Perram, J.W., Smith, E.R., *Proc. R. Soc. London A* 1980, **373**, 56.
- ¹⁴⁸ De Leeuw, S.W., Perram, J.W., Smith, E.R., *Proc. R. Soc. London A* 1983, **388**, 177.
- ¹⁴⁹ Meijer, E. J., Frenkel, D., LeSar, R. A., Ladd, A.J.C., *J. Chem. Phys.* 1990, **92**, 1510.
- ¹⁵⁰ Möller, D., Fischer, J., *Fluid Phase Eq.* 1994, **100**, 35.
- ¹⁵¹ Panagiotopoulos, A., *Mol. Sim.* 1992, **9**, 1.
- ¹⁵² Widom, B., *J. Chem. Phys.* 1963, **39**, 2802.

-
- ¹⁵³ Frenkel, D., Ladd, A.D.C., *J. Chem. Phys.* 1984, **81**, 3188.
- ¹⁵⁴ Kofke, D.A., *Mol. Phys.* 1993, **78**, 1331.
- ¹⁵⁵ Hitchcock, M. R., Hall, C.K., *J. Chem. Phys.* 1999, **110**, 11433.
- ¹⁵⁶ Silva Fernandes, F.M.S, Fartaria, R.P.S., Freitas, F.F.M., *Computer Physics Com.* 2001, **141**, 403.
- ¹⁵⁷ Agrawal, R., Kofke, D.A., *Mol. Phys.* 1995, **85**, 23.
- ¹⁵⁸ Agrawal, R., Kofke, D.A., *Mol. Phys.* 1995, **85**, 43.
- ¹⁵⁹ Lamm, M.H., Hall, C.K., *Fluid Phase Eq.* 2002, **194-197**, 197.
- ¹⁶⁰ Lamm, M.H., Hall, C.K., *Fluid Phase Eq.* 2001, **182**, 37.
- ¹⁶¹ Polson, J.M., Frenkel, D., *J. Chem. Phys.* 1998, 109, 318.
- ¹⁶² Polson, J.M., Frenkel, D., *J. Chem. Phys.* 1999, **111**, 1501.
- ¹⁶³ Lisal, M., Vacek, V., *Mol. Sim.* 1997, **19**, 43.
- ¹⁶⁴ Van't Hof, A. De Leeuw, S.W., Hall, C.K. Peters, C.J., *Mol. Phys.* 2004, **102**, 301.
- ¹⁶⁵ Vega, C., Monson, P., *J. Chem. Phys.* 1998, **109**, 9938.
- ¹⁶⁶ Polson, J.M., Trizac, E., Pronk, S., Frenkel, D., *J. Chem. Phys.* 2000, **112**, 5339.
- ¹⁶⁷ Vega, C., Sanz, E., Abascal, J.L.F., Noya, E.G., *J. Phys. Condens. Matter* 2008, **20**, 153101.
- ¹⁶⁸ Abascal, J.L.F., Sanz, E., Garcia, R., Vega, C., *J. Chem. Phys.* 2005, **122**, 234511.
- ¹⁶⁹ Jorgensen, W.L., *J. Am. Chem. Soc.* 1981, **103**, 335.
- ¹⁷⁰ Chialvo, A., Cummings, P.T., *Adv. Chem. Phys.* 1999, **109**, 115.
- ¹⁷¹ Kalinichev, A.G., Churakov, S.V., *Fluid Phase Eq.* 2001, **183-184**, 271.
- ¹⁷² McBride, C., Vega, C., Sanz, E., MacDowell, L.G., Abascal, J.L.F., *Mol. Phys.* 2005, **103**, 1.
- ¹⁷³ Jorgensen, W.L., Madura, J.D., Swenson, C.J., *J. Am. Chem.Soc.* 1984, **106**, 6638.
- ¹⁷⁴ Baranyai, A., Bartok, A., Chialvo, A.A., *J. Chem. Phys.* 2006, **124**, 74507.
- ¹⁷⁵ Martin, M.G., Siepmann, J.I., *J. Phys. Chem. B* 1998, **102**, 2569.
- ¹⁷⁶ Haar, L., Gallagher, J.S., Kell, G.S., *NBS/NRC Steam Tables*, Hemisphere Publishing Corporation, New York (1984).
- ¹⁷⁷ Teja, A. S., Lee, R. J., Rosenthal, D., Anselme, M., *Fluid Phase Eq.* 1990, **56**, 153.
- ¹⁷⁸ Lorentz, H.A., *Ann. Physik* 1881, **12**, 127.
- ¹⁷⁹ Berthelot, D., *Comptes Rendus de l'Académie des Sciences Paris* 1889, **126**, 1703.
- ¹⁸⁰ Heyes, D. M., *Phys. Rev. B* 1994, **49**, 755.
- ¹⁸¹ Nymand, T. M., Linse, P., *J. Chem. Phys.* 2000, **112**, 6152.
- ¹⁸² Lopez-Lemus, J.; Alejandre, *J. Mol. Phys.* 2003, **101**, 743.

-
- ¹⁸³ Van Der Spoel, D., Lindahl, E., Hess, B., Groenhof, G., Mark, A.E., Berendsen, H.J., *J. Comp. Chem.* 2005, **26**, 1701.
- ¹⁸⁴ Bennett, C.H., *J. Comp. Phys.* 1976, **22**, 245.
- ¹⁸⁵ Lu, N., Singh, J.K., Kofke, D.A., *J. Chem. Phys.* 2003, **118**, 2977.
- ¹⁸⁶ Deitrick, G.L., Scriven, L.E., Davis, H.T., *J. Chem. Phys.* 1989, **90**, 2370.
- ¹⁸⁷ Nagle, J.F., *J. Math. Phys.* 1966, **7**, 1484.
- ¹⁸⁸ McMullan, R. K., Jeffrey, G. A., *J. Chem. Phys.* 1965, **42**, 2725.
- ¹⁸⁹ Mac, T.K., McMullan, R.K., *J. Chem. Phys.* 1965, **42**, 2732
- ¹⁹⁰ Chialvo, A.A., Bartók, A., Baranyai, A., *J. mol. Liq.* 2006, **129**, 120.
- ¹⁹¹ <http://webbook.nist.gov/chemistry/> (19/04/2010).
- ¹⁹² Harvey, A.H., Sengers, J.M.H.L., *AIChE Journal* 1990, **36**, 539.
- ¹⁹³ Harvey, A.H., *AIChE Journal* 1996, **42**, 1491.
- ¹⁹⁴ Docherty, H., Galindo, A., Vega, C., Sanz, E., *J. Chem., Phys.* 2006, **125**, 074510.
- ¹⁹⁵ Keisuke, M., Ryo, O., Sum, A.K., Yasuoka, K., *Proc. 6th International Conference on Natural Gas Hydrates*, Vancouver, British Columbia, Canada, July 6-10 (2008).
- ¹⁹⁶ Munck, J., Skjold-Jørgensen, S., Rasmussen, P., *Chem. Eng. Sci.* 1988, **43**, 2661.
- ¹⁹⁷ Sizov, V., Piotrovskaya, E.M., *J. Chem. Phys. B* 2007, **111**, 2886.
- ¹⁹⁸ Tanaka, H., *J. Chem. Phys.* 1994, **101**, 10833.
- ¹⁹⁹ Ripmeester, J.A., Ratcliffe, C.I., *J. Phys. Chem.*, 1988, **92**, 337.
- ²⁰⁰ Sum, A.K., Burruss, R.C., Sloan, E. D., *J. Phys. Chem. B* 1997, **101**, 7371.
- ²⁰¹ Galloway, T.J., Ruska, W., Chappellear, P.S., Kobayashi, R., *Ind. Eng. Chem. Fundam.* 1970, **9**, 237.
- ²⁰² de Roo, J.L., Peters, C.J., Lichtenthaler, R.N., Diepen, G.A.M., *AIChE Journal* 1983, **29**, 651.
- ²⁰³ Handa, Y.P., *J. Chem. Thermodyn.* 1986, **18**, 915.
- ²⁰⁴ Klauda, J.B., Sandler, S.I., *J. Phys. Chem. B* 2002, **106**, 5722.
- ²⁰⁵ Sun, R., Duan, Z., *Geochim. Cosmochim. Acta* 2005, **69**, 4411.
- ²¹³ Circone, S., Kirby, S.H., Stern, L.A., *J. Chem. Phys. B* 2005, **109**, 9468.
- ²¹⁴ Barrer, R.M. *Nature* 1959, **183**, 463.
- ²¹⁵ Barrer, R.M., Stuart, W.I., *Proc. R. Soc. (London) A* 1957, **243**, 173.
- ²¹⁶ Sloan, E.D., Fleyfel, F., *Fluid Phase Eq.* 1992, **96**, 223.
- ²¹⁷ Handa, Y.P., *J. Chem. Thermo.* 1986, **18**, 891.
- ²¹⁸ Handa, Y.P., Calometric studies of laboratory synthesized and naturally occurring gas hydrates, paper presented at *AIChE Annual meeting* Miami Beach, Nov 2-7 (1986).

²¹⁹ Anderson, G.K., *J. Chem. Thermo.* 2004, **36**, 1119.

²²⁰ Dickenson, D.C., Osborne, N.S., US Bur. Standards 1915, **12**, 49.

²²¹ Cathy, N.L., Andorfer, A., Duman, J.G., *The journal of experimental biology* 1998, **201**, 2243.

Appendix I

Paper 2

J. Phys. Chem. B 2010, 114, 5775–5782

5775

Calculation of Liquid Water–Hydrate–Methane Vapor Phase Equilibria from Molecular Simulations

Lars Jensen,[†] Kaj Thomsen,[‡] Nicolas von Solms,[†] Scott Wierzbowski,^{‡,§} Matthew R. Walsh,[‡] Carolyn A. Koh,[‡] E. Dendy Sloan,[‡] David T. Wu,^{‡,§} and Amadeu K. Sum^{*,§}

Center for Energy Resources Engineering, Department of Chemical & Biochemical Engineering, Technical University of Denmark, 2800 Kgs. Lyngby, Denmark, and Center for Hydrate Research, Department of Chemical Engineering, and Department of Chemistry, Colorado School of Mines, Golden, Colorado 80401

Received: November 20, 2009; Revised Manuscript Received: March 25, 2010

Monte Carlo simulation methods for determining fluid- and crystal-phase chemical potentials are used for the first time to calculate liquid water–methane hydrate–methane vapor phase equilibria from knowledge of atomistic interaction potentials alone. The water and methane molecules are modeled using the TIP4P/ice potential and a united-atom Lennard-Jones potential, respectively. The equilibrium calculation method for this system has three components, (i) thermodynamic integration from a supercritical ideal gas to obtain the fluid-phase chemical potentials, (ii) calculation of the chemical potential of the zero-occupancy hydrate system using thermodynamic integration from an Einstein crystal reference state, and (iii) thermodynamic integration to obtain the water and guest molecules' chemical potentials as a function of the hydrate occupancy. The three-phase equilibrium curve is calculated for pressures ranging from 20 to 500 bar and is shown to follow the Clapeyron behavior, in agreement with experiment; coexistence temperatures differ from the latter by 4–16 K in the pressure range studied. The enthalpy of dissociation extracted from the calculated P – T curve is within 2% of the experimental value at corresponding conditions. While computationally intensive, simulations such as these are essential to map the thermodynamically stable conditions for hydrate systems.

Introduction

Clathrate hydrates, often called gas hydrates, are ice-like inclusion compounds that generally form at low temperatures and high pressures with guest molecules trapped (enclathrated) inside of hydrogen-bonded water cages. Hydrates are relevant in a variety of scientific and industrial contexts, including climate-change modeling, carbon dioxide sequestration, hydrocarbon extraction, hydrogen and natural gas storage, separation and refrigeration technologies, marine biology, and planetary surface chemistry.¹

The prediction of hydrate-phase boundaries as a function of temperature, pressure, and composition for various hydrate-forming mixtures, including simple and mixed gas systems, is often performed using the established semiempirical statistical mechanical theory of van der Waals and Platteeuw (vdWP),^{1–3} which is an exemplar of the common industrial use of statistical mechanics.³ However, it is also possible to compute hydrate thermodynamics using molecular simulations with model intermolecular potentials. Such simulation studies can independently evaluate the vdWP approach and may contribute to improving this model. For example, a recent study compared guest occupancies of the vdWP model to Monte Carlo (MC) simulation using the SPC/E water model in combination with a Lennard-Jones 12–6 potential for methane.⁴ The comparison suggested that the physical significance of the vdWP approach may be improved by including long-range water–methane

interactions while still neglecting guest–guest interactions. This ground-breaking study introduced methods to calculate free energies and chemical potentials in the hydrate phase but did not examine phase boundaries. An earlier study by the same authors did estimate the phase diagram of hydrates but used approximate theories for the fluid-phase calculations.⁵ It would therefore be valuable to have an independent determination of the hydrate-phase boundary based only on knowledge of the intermolecular potentials. The present paper reports the first such study to do so.

The study of gas hydrates using molecular simulation is also appealing because it enables the molecular-level analysis of dynamic phenomena such as hydrate formation and dissociation, providing a level of detail unavailable in typical laboratory investigations. For example, it has recently been shown that molecular dynamics (MD) simulation can be utilized to observe the spontaneous nucleation and growth of methane hydrate starting from a phase-separated water and methane system at elevated pressure and low temperature.⁶ The potential models used in those simulations were the TIP4P/ice model for water⁷ and the united-atom Lennard-Jones model for methane.⁸ Considering that the chosen water model was parametrized based on a fit to the ice–water phase diagram, it is encouraging that MD simulations employing the model lead to the formation of a clathrate structure upon cooling and pressurization in the presence of methane.

Calculating the three-phase equilibrium of a gas hydrate system with molecular models and simulations not only provides useful information for comparison and evaluation of established models but also helps define the thermodynamic state of a system when considering simulations of equilibrium and dynamic phenomena, such as nucleation and growth, in which the temperature and pressure are usually specified. From

* To whom correspondence should be addressed. Tel. +1(303) 273-3873. Fax +1(303) 273-3750. E-mail: asum@mines.edu.

[†] Technical University of Denmark.

[‡] Department of Chemical Engineering, Colorado School of Mines.

[§] Department of Chemistry, Colorado School of Mines.

^{*} Current address: Shell Global Solutions, Westhollow Technology Center, 3333 Highway 6 South, Houston, TX 77082.

experiments, it is well-known that the driving force for the formation of gas hydrates is strongly dependent on the degree of subcooling or overpressurization relative to the equilibrium hydrate formation temperature or pressure.^{9–15} Therefore, it is evident that the driving force, in terms of subcooling/overpressurization, must also be well-defined when considering the formation of gas hydrates in molecular simulations. Nonetheless, all such simulation studies to date have arbitrarily set a temperature and pressure, in the absence of knowledge about the actual hydrate phase boundary, and thus the degree of subcooling or overpressurization for the specific molecular models used.

With these considerations in mind, we have established a procedure to calculate the three-phase equilibrium for the liquid water–hydrate–methane vapor (L_w–H–V) system from molecular simulations. We used different MC simulation methodologies to calculate the chemical potentials of liquid water and methane vapor and the chemical potentials of methane and water in the hydrate phase, from which three-phase equilibrium is determined.

Methods and Models

For a two-component (water and methane), three-phase (L_w–H–V) equilibrium, the chemical potentials (μ) of both species in all phases are equal at a given temperature and pressure, that is

$$\begin{aligned} \mu_{\text{W}}^{\text{L}} &= \mu_{\text{W}}^{\text{H}} = \mu_{\text{W}}^{\text{V}} \\ \mu_{\text{M}}^{\text{L}} &= \mu_{\text{M}}^{\text{H}} = \mu_{\text{M}}^{\text{V}} \end{aligned} \quad (1)$$

where the subscripts W and M refer to water and methane, respectively. At equilibrium conditions, dense ordered (hydrate), dense disordered (liquid), and low-density (vapor) phases coexist; thus, thermodynamic integration along multiple paths is required to obtain all of the necessary chemical potentials. For each phase at a specified temperature and pressure, the chemical potential of each species varies with the composition in that phase. This is illustrated for the solid hydrate phase in Figure 1, which plots the methane and water chemical potentials versus the number of methane molecules at a fixed temperature, pressure, and number of water molecules. Similar plots exist for the liquid and vapor phases. For a given temperature and pressure, equality of chemical potentials between two phases for each species, that is, two-phase equilibrium, will occur only at a specific composition in each phase. In accordance with the Gibbs phase rule, three-phase equilibrium can then only occur at the coexistence temperature at a given pressure (or coexistence pressure at a given temperature). At three-phase coexistence conditions, the composition in the hydrate phase to be in equilibrium with the gas phase will be the same as the hydrate composition to be in equilibrium with the liquid phase.

Considerable simplification can be made, however, when a phase at coexistence is nearly pure, as is the case for the nearly pure liquid water and nearly pure methane vapor phases. In these cases, the chemical potential of the majority species ($\mu_{\text{W}}^{\text{L}}$ or $\mu_{\text{M}}^{\text{V}}$) is well-approximated by its pure-phase chemical potential ($\mu_{\text{W}}^{\text{L}}$ or $\mu_{\text{M}}^{\text{V}}$). The accuracy of this approximation can be assessed by mixture vapor–liquid equilibrium (VLE) simulations and is found to be extremely good for the system studied here, as detailed below. In the present case, this implies that for a given pressure, the coexistence temperature can be determined as that temperature for which the hydrate composi-

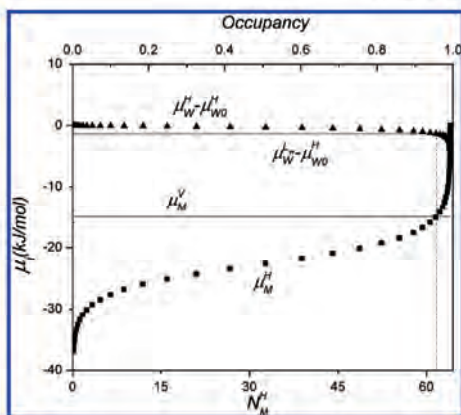


Figure 1. Chemical potential of methane in the vapor phase, $\mu_{\text{M}}^{\text{V}}$ (bottom solid line), methane in the hydrate, $\mu_{\text{M}}^{\text{H}}$ (squares), water in the liquid phase, $\mu_{\text{W}}^{\text{L}} - \mu_{\text{W}}^{\text{H}}$ (top solid line), and water in the hydrate phase, $\mu_{\text{W}}^{\text{H}} - \mu_{\text{W}}^{\text{V}}$ (triangles), plotted as a function of the hydrate occupancy. A thermal wavelength, $\Lambda = 1 \text{ \AA}$, was used in calculating the chemical potential for all phases. The number of methane molecules, N_{M}^{H} , in the hydrate has a maximum value of 64, corresponding to a $2 \times 2 \times 2$ sl hydrate unit cell. The temperature and pressure here are on the three-phase coexistence curve (298.9 K and 100 bar), and therefore, the condition of equal chemical potentials is satisfied at the same composition, as shown by the vertical dashed line.

tion that satisfies $\mu_{\text{W}}^{\text{L}} \approx \mu_{\text{W}}^{\text{H}} = \mu_{\text{W}}^{\text{V}}$ is the same hydrate composition that satisfies $\mu_{\text{M}}^{\text{H}} = \mu_{\text{M}}^{\text{V}} \approx \mu_{\text{M}}^{\text{L}}$.

Figure 1 illustrates this condition of equal water and equal methane chemical potentials at a given composition (dashed vertical line) required to locate the three-phase equilibrium for a methane hydrate system. The chemical potentials of water in the liquid phase and of methane in the vapor phase are shown as straight lines in the plot, as these are fluid-phase properties independent of the occupancy of methane in the hydrate. Equating these two pairs of chemical potentials is thus sufficient to determine the coexistence temperature, pressure, and hydrate composition. The remaining two chemical potential conditions, $\mu_{\text{W}}^{\text{H}} = \mu_{\text{W}}^{\text{V}}$ and $\mu_{\text{M}}^{\text{H}} = \mu_{\text{M}}^{\text{L}}$, serve to determine the (dilute) compositions of the minority species in the fluid phases.

The following simulation methods and calculations were performed to obtain each of the chemical potentials in eq 1, allowing determination of the three-phase coexistence temperatures, pressures, and hydrate compositions (cage occupancies) on the L_w–H–V line. The procedure summarized below for the calculation of chemical potentials in the hydrate phase is detailed elsewhere.⁴

Chemical Potential of Water ($\mu_{\text{W}}^{\text{H}}$) and of Methane ($\mu_{\text{M}}^{\text{H}}$) in the Hydrate. The calculation of chemical potentials in the hydrate phase follows the procedure outlined by Wierzbowski and Monson,⁴ which we briefly summarize here. The calculation proceeds first by the generation of a hypothetical empty hydrate and calculation of the chemical potential of water therein, followed by integration of the change in chemical potential of both water and methane due to the introduction of methane at various compositions. The latter is carried out using semigrand MC simulations described below.

An equilibrated empty hydrate lattice and its density are first obtained from a *NPT* simulation. The Helmholtz free energy of this empty hydrate, A , is then calculated by *NVT* simulations

(at the density determined above) using the methodology described by Frenkel and Ladd;¹⁶ the Frenkel–Ladd method is implemented with modifications to treat the orientational degrees of freedom and the effect of fixed centers of mass.^{17,18} Below, we simply refer to this as the FL method. The method is based on thermodynamic integration of the Helmholtz free energy by taking a reversible path to the system of interest from a classical Einstein crystal for which the Helmholtz free energy can be calculated analytically. Once the Helmholtz free energy for the hydrate is known, the chemical potential of water in the empty hydrate is given by

$$\mu_{w0}^H = \frac{A + PV}{N_W^H} \quad (2)$$

where, N_W^H , V , and P are the number of water molecules, volume, and pressure of the empty hydrate, respectively.

Methane is then introduced into the hydrate lattice at fixed values of methane chemical potential using N_WPT semigrand MC simulations. For each value of the chemical potential, the number of methane molecules in the hydrate, N_M^H , can be calculated (squares in Figure 1).

The Gibbs–Duhem relation for a two-component system implies that the change in the water chemical potential depends on the change in the methane chemical potential, namely, that at constant temperature and pressure, $N_W^H d\mu_W^H + N_M^H d\mu_M^H = 0$. The water chemical potential in the hydrate can thus be obtained as

$$\mu_W^H - \mu_{w0}^H = -\frac{1}{N_W^H} \int_{-\infty}^{\mu_M^H} N_M^H d\mu_M^H \quad (3)$$

and plotted versus N_M^H at the desired temperature and pressure (triangles in Figure 1). From the figure, we can see that the chemical potential of water in the hydrate is less sensitive to the methane occupancy in the hydrate compared to the chemical potential of methane in the hydrate phase. This is understandable as the number of water molecules is much greater than the number of methane molecules.

Finally, note that the Gibbs free energy of the hydrate at any given composition can be expressed as

$$G_H = N_M^H \mu_M^H + N_W^H \mu_W^H = N_M^H \mu_M^H + N_W^H \mu_{w0}^H - \int_{-\infty}^{\mu_M^H} N_M^H d\mu_M^H \quad (4)$$

These values can be compared with direct FL thermodynamic integration as a validation of the semigrand method for accounting for hydrate filling, as shown below.

Chemical Potentials of the Fluid Phases (μ_W^V , μ_W^L , μ_M^V , μ_M^L). The chemical potentials for a mixture can be expressed as

$$\mu_i(T, P, x_i) = \mu_i^0(T, P) + RT \ln(\gamma_i x_i) \quad (5)$$

where μ_i^0 is the pure component (methane or water) chemical potential at the mixture temperature, T , and pressure, P , x_i is the mole fraction of the pure component, and γ_i is the activity coefficient of species i in the mixture. For nearly pure phases, $x_i \approx 1$ for the majority species, and the Lewis–Randall rule, $\gamma_i = 1 + O(x_i^2) \approx 1$, applies.

The chemical potential of a pure component is found from thermodynamic integration (TI). If the chemical potential at one pressure is known, then the chemical potential at any other pressure along an isotherm can be found as

$$\frac{\mu_i(T, P_2)}{k_B T} = \frac{\mu_i(T, P_1)}{k_B T} + \int_{P_1}^{P_2} \frac{1}{\rho_i k_B T} dP \quad (6)$$

where, ρ_i is the number density and k_B is the Boltzmann constant. Likewise, along an isobar, the temperature dependence of the chemical potential is given as

$$\frac{\mu_i(T_2, P)}{k_B T_2} = \frac{\mu_i(T_1, P)}{k_B T_1} - \int_{T_1}^{T_2} \frac{H_i}{k_B T^2} dT \quad (7)$$

where H_i is the molar enthalpy of water or methane. The starting point of the thermodynamic integration can be chosen arbitrarily; however, the ideal gas is often a convenient choice given that its chemical potential can be calculated analytically. The ideal gas chemical potential is given by

$$\frac{\mu_i^{\text{id}}}{k_B T} = \ln(\rho_i \Lambda^3) \quad (8)$$

where $\Lambda = h/(2\pi mk_B T)^{1/2}$ is the thermal wavelength, with h as Planck's constant and m as the molecular mass; this term cancels out when comparing chemical potentials between phases in equilibrium. From NPT simulations along the thermodynamic integration path, the chemical potential of each fluid is calculated in the temperature and pressure regions of interest.

For testing the assumption that the chemical potentials of the pure phases are good approximations to the chemical potentials of the phases with dissolved methane or water, the fluid solubilities were calculated. The mole fraction of a compound in the gas phase (y_i) for near-ideal conditions can be described well in terms of the partial pressure of the compound

$$y_i = \frac{P_i}{P} \quad (9)$$

where the total pressure, P , is the sum of the partial pressures. Likewise, the solubility of a small nonpolar molecule in an aqueous phase (x_i) is well-described by Henry's law, which is given by

$$k_{H,i} = \frac{P_i}{x_i} y_i \quad (10)$$

Henry's constant can also be related to the excess chemical potential of the solute, μ_i^{ex} , by

$$k_{H,i} = \rho_s k_B T \exp(\mu_i^{\text{ex}}/k_B T) \quad (11)$$

where ρ_s is the solvent density. The excess chemical potential of the solute can be calculated from test particle insertion (TPI) simulations.¹⁹ The change in chemical potential resulting from the solubility calculations at various T and P conditions can

then be compared in magnitude relative to the pure phase approximations, as shown below.

Simulation Details and Potential Models

The united-atom Lennard-Jones representation using the optimized parameters (OPLS) by Jorgensen was used to model methane.⁶ The water molecules were modeled using the TIP4P/ice potential.⁷ The cross interactions between methane and water were accounted for with the Lorentz–Berthelot combining rule.^{20,21} The TIP4P/ice potential model accurately describes the solid–liquid equilibrium between hexagonal ice and liquid water up to 2000 bar.⁷ Considering that hydrate is also a solid with a crystal structure mainly composed of water molecules, it is plausible that the TIP4P/ice model, together with a suitable model for the gas molecules, is capable of describing the thermodynamic properties of gas hydrates.

Monte Carlo simulations used the standard Ewald summation method for the long-range electrostatic forces.^{22,23} Similarly, an Ewald summation approach was applied to evaluate the long-range dispersion interactions using a lattice sum method.²⁴ A convergence parameter of $4/L$ was used, where L is the lattice parameter for sl hydrate. For all simulations, the cutoff radius was 10 Å.

For the fluid phase-simulations, 500 water or methane molecules were used. The enthalpy and density of the fluid phases were obtained from *NPT* simulations. Typically 50 000–100 000 equilibration cycles, followed by 100 000–250 000 production cycles were required to obtain statistically acceptable averages of the densities and enthalpies. A cycle corresponded to a set of N trial moves, where N is the number of molecules in the system. The starting point for the integration path was in both cases 1 bar and 800 K, and the ending points of the integration were between 20 and 500 bar and 270 and 320 K. By performing the *NPT* simulations in small steps of temperature and pressure, the chemical potential for water or methane was obtained from eq 6 or 7 by integration using the trapezoidal rule. Step lengths may vary depending on in which region of the P – T diagram the step is done; however, smooth curves must be used in order to get accurate integration. The solubility of methane in water was found from TPI simulations. Using the methodology described by Bennett,²⁵ TPI simulations were performed in the *NPT* ensemble to obtain the solvent (water) densities and solute (methane) excess chemical potentials, from which Henry’s constants were obtained. The Bennett method was used as it has been reported to offer improved accuracy over the Widom method.^{26,27} For these simulations, 500 water molecules were first equilibrated for more than 100 000 cycles, after which four stages of more than 500 000 cycles were performed. In the first stage, insertions of test particles were performed with five insertions attempted per cycle, and in the following three stages, the particles were deleted.

The zero-occupancy empty hydrate lattice consisted of 368 water molecules ($2 \times 2 \times 2$ sl hydrate unit cells); *NPT* simulations were performed for 20 000 equilibration cycles and 200 000 cycles for averaging. The densities obtained were used as input to the semigrand MC and FL simulations. The semigrand MC simulations were conducted over a range of methane chemical potentials ($\mu_{\text{CH}_4}^{\text{H}}$) from states in the neighborhood of the zero-occupancy hydrate (we used an initial value of $\mu_{\text{CH}_4}^{\text{H}} = -36.83$ kJ/mol, which resulted in an occupancy very close to zero) up to states describing a fully occupied hydrate (single occupancy of cages). Integration of eq 3 was done using the trapezoidal rule in intervals of $\delta\mu_{\text{M}} = 0.837$ kJ/mol.

The third simulation type involved the calculation of the chemical potential of water in the zero-occupancy hydrate ($\mu_{\text{H}_2\text{O}}^{\text{H}}$),

TABLE 1: Vapor–Liquid Equilibria for the Binary Water–Methane System at 100 bar and in the Temperature Range of 275–310 K As Found from Experiments and Monte Carlo Simulations^a

T (K)	k_{LM} (kbar)		x_{M}		y_{W} ($\times 10^4$)	
	sim.	exp.	sim.	exp.	sim.	exp.
275	34 (5)	24	0.0030	0.0042	0.0257	0.7037
280	39 (5)	27	0.0025	0.0037	0.0372	0.9775
290	35 (6)	34	0.0028	0.0029	0.0766	1.8538
300	59 (6)	41	0.0017	0.0025	0.1540	3.4402
310	102 (12)	47	0.0010	0.0021	0.3024	6.2558

^a The numbers in parentheses for the simulated Henry’s constants indicate the standard deviation.

which, according to eq 3, is necessary for calculating the chemical potential of water in the occupied hydrate ($\mu_{\text{H}_2\text{O}}^{\text{H}}$). In addition, $\mu_{\text{H}_2\text{O}}^{\text{H}}$ is used for calculating the Gibbs free energy of the hydrate at any given composition according to eq 4. The Helmholtz free energies of the empty and full hydrate were found using the FL method. The coordinates of the oxygen atoms for the perfect crystal used in specifying the Hamiltonian, $H_{\text{E}}(\lambda_{\text{T}}, \lambda_{\text{R}})$ were those given for the sl hydrate.²⁸ The force constants used in the FL method were $\lambda_{\text{T}} = 25000 \text{ k}_B \text{ T} \text{ \AA}^2$ and $\lambda_{\text{R}} = 25000 \text{ k}_B \text{ T}$. Simulations were performed for 5000 relaxation cycles and 50 000 averaging cycles. Calculation of the Helmholtz free energy was performed using a 20 point Gaussian quadrature.

Results and Discussion

We first consider the calculation of the fluid-phase VLE, which was done at 100 bar and in the temperature range of 275–310 K. The solubility of methane in water was found from the TPI simulations. The fraction of water in the vapor phase was estimated using eq 9 and using the vapor pressure data for water modeled using TIP4P/ice as reported by Chialvo et al.²⁹ as the water partial pressure; the methane partial pressure was determined by the equilibrium condition with the hydrate phase. Since only the water vapor pressures of TIP4P/ice in the temperature range of 300–650 K were reported, we extrapolated the data to 275 K. Since the vapor pressures show a high degree of linearity in the $\log P$ versus $1/T$ plane, the error resulting from the extrapolation should be relatively small. Nonideal effects are assumed to be small in the gas phase under the conditions studied, and in any case, the water partial pressure is so low that the effect on the chemical potentials of the majority species is still negligible. The results of the VLE calculations along with experimental values are provided in Table 1. Experimental Henry’s constants were calculated using a semiempirical correlation based on a best fit to experimental data in the temperature range of 273.15–633.15 K.^{30,31} The experimental fractions of water found in the vapor phase are based on experimentally determined vapor pressures of water.³²

As seen from Table 1, the TIP4P/ice water model in combination with the OPLS potential model for methane predicts the solubility of methane in water to be around 30–50% lower than the experimental values, while the amount of water in the vapor phase is on the order of 20–25 times lower than the experimental values. The low solubility of methane (modeled with the OPLS and the TraPPE force fields) in water using other versions of the TIP4P water potential has previously been reported, thus providing additional evidence that the results found here seem reasonable and consistent with existing studies.^{33,34}

TABLE 2: Pure Component Chemical Potential of Water and the Contribution to the Liquid Water Chemical Potential from Accounting for the Solubility of Methane in Water^a

T (K)	μ_w^V (kJ/mol)	$RT \ln(x_w)$ (kJ/mol)
275	-43.887 (0.06)	-0.007 (0.0010)
280	-43.676 (0.06)	-0.006 (0.0008)
290	-43.276 (0.06)	-0.007 (0.0012)
300	-42.895 (0.07)	-0.004 (0.0004)
310	-42.553 (0.07)	-0.003 (0.0003)

^aAll results are for a pressure of 100 bar. The numbers in parentheses are standard deviations.

According to eq 5, the change in the chemical potential of the majority species when accounting for fluid phases mixing is $RT \ln x_i = RT \ln(1 - x_j) \approx -RTx_j$, where $x_j \ll 1$ is the mole fraction of the minority species, as given in Table 1. Since the mixtures are nearly pure, the activity coefficient is extremely close to unity. Therefore, it is obvious from Table 1 that accounting for mixing will have a higher impact on the chemical potential of liquid water, μ_w^V , than on that of methane vapor, μ_M^V , since the mole fraction of methane in liquid water, as predicted using the potential models, is on the order of 100–1000 times larger than the mole fraction of water in methane vapor. In Table 2, the pure component chemical potential of water, found from TI and the additional excess contribution to the total chemical potential due to the dissolved methane, is shown at 100 bar and in the temperature range of 275–310 K. It is evident that the contribution from mixing to the chemical potential of water is negligible compared to the pure water chemical potential (the mixing contribution to the chemical potential is less than the standard deviation from the combined TI steps that were used to calculate the pure water chemical potential). From these considerations, we conclude that the fluid phases can be considered pure for the purposes of determining the chemical potential as the effects of mixing on the pure component chemicals are negligible and consequently have no significant influence when calculating the three-phase (L_w –H–V) equilibrium.

Next, we consider the calculation of the Gibbs free energies of the zero-occupancy and fully occupied hydrates directly using the FL method. The results obtained using semigrand MC simulations, together with eq 4, can also yield the Gibbs free energy of a fully occupied hydrate. Typical results obtained for the semigrand MC simulations correspond to the squares in Figure 1, which shows the methane occupancy of the hydrate as a function of the chemical potential for methane in the hydrate. As seen in the figure, the chemical potential of methane increases as the hydrate is filled with methane. At a chemical potential of about -10 kJ/mol, the number of methane molecules asymptotically approaches full occupancy of the hydrate (64 for the $2 \times 2 \times 2$ unit cells of sI hydrate considered).

Table 3 shows the results of a thermodynamic consistency test. Here, we compare the Gibbs free energy of the fully occupied hydrate found from thermodynamic integration from the zero-occupancy hydrate (using eq 4) with the free energy of an occupied hydrate calculated directly using the FL method. The table shows the results obtained at 100 bar and in the temperature interval of 285–300 K. There is good agreement between the two methods, indicating that these two independent methods for estimating the chemical potential of methane in the hydrate are consistent. These results are also in good agreement with a previous study.⁴

To obtain the three-phase equilibrium temperature at a given pressure, it is necessary to satisfy the constraint on the equality

TABLE 3: Gibbs Free Energy of Water of a Zero-Occupancy and a Full-Occupancy Hydrate Calculated with the FL Method^a

T (K)	zero-occupancy hydrate		
	FL (kJ/mol)	full hydrate FL (kJ/mol)	full hydrate TI (kJ/mol)
285	-42.40 (0.11)	-46.26 (0.06)	-46.34 (0.11)
290	-42.09 (0.05)	-45.98 (0.06)	-46.03 (0.05)
295	-41.81 (0.06)	-45.69 (0.07)	-45.75 (0.06)
300	-41.51 (0.06)	-45.40 (0.07)	-45.45 (0.06)

^aThe full hydrate value calculated from a zero-occupancy hydrate reference by thermodynamic integration (TI) is also shown. A thermal wavelength of $\Lambda = 1 \text{ \AA}$ was used. Calculations were performed at 100 bar and the specified temperature. Numbers in parentheses are standard deviations.

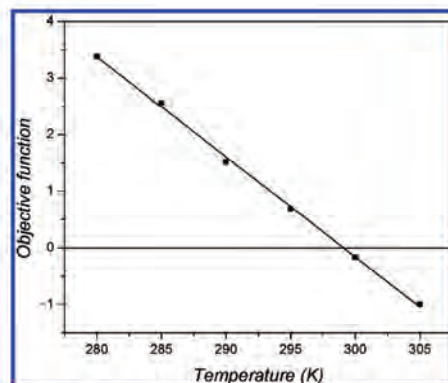


Figure 2. Value of the objective function (OF) defined by eq 12 at the different temperatures explicitly considered at 100 bar (squares). The line corresponds to the best fit of the points. The objective function has an interpolated value of zero (condition for equilibrium) for the liquid water–hydrate–methane vapor equilibrium at 298.9 K.

of the chemical potential for each species in each phase, as shown in eq 1, and with the same hydrate composition as that discussed earlier. Therefore, we employ the following objective function (OF) describing the difference in the methane occupancies at which the chemical potentials of both components are equal

$$OF = N_M(\mu_M^V = \mu_M^H) - N_M(\mu_W^L = \mu_W^H) \quad (12)$$

Conditions for equilibrium are met when the OF has a value of 0. In practice, the OF is calculated at constant pressure for different temperatures, spanning a certain region within the expected equilibrium temperature. Figure 2 shows the values of the OF for the temperatures explicitly considered in the simulations at the fixed pressure of 100 bar. The OF exhibits a high degree of linearity with temperature in the range examined, thus allowing interpolation to obtain the coexistence temperature. The same procedure was applied to determine the equilibrium temperature at the other pressures.

On the basis of this procedure, the calculated three-phase equilibrium temperatures for liquid water–methane hydrate–methane vapor in the pressure range of 20–500 bar are shown in Figure 3 along with experimental data. It can be seen that the linear behavior exhibited by the experimental data is also

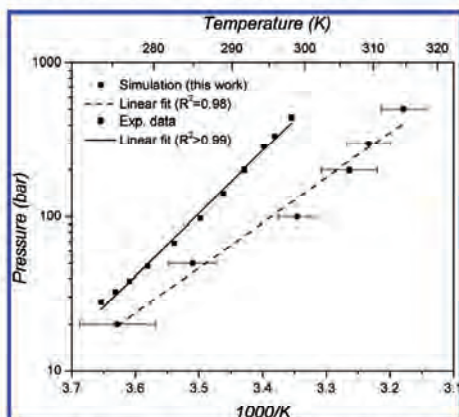


Figure 3. Pressure-temperature phase diagram for the liquid water-methane hydrate-methane vapor system comparing experimental data (squares)³⁵⁻³⁷ and MC simulations results (circles). The straight lines correspond to the best fit of the data as found from a data regression. The error bars on the points found from simulation correspond to uncertainty in the temperature estimated from the standard deviations of $\mu_{\text{H}_2\text{O}}^{\text{L}}$, $\mu_{\text{CH}_4}^{\text{V}}$, $(\mu_{\text{H}_2\text{O}}^{\text{L}} - \mu_{\text{H}_2\text{O}}^{\text{V}})$, and $(\mu_{\text{CH}_4}^{\text{L}} - \mu_{\text{CH}_4}^{\text{V}})$.

seen in the simulation data; it has been shown in general that coexistence curves of simple hydrates approximate straight lines in $\log P$ versus $1/T$ plots. The Clapeyron equation applied to simple hydrates relates the equilibrium pressures and temperatures to the dissociation enthalpy³⁸

$$\frac{d \log P}{d(1/T)} = -\frac{\Delta H}{zR} \quad (13)$$

where ΔH is the dissociation enthalpy of the hydrate, z is the compressibility factor of the gas, and R is the universal gas constant. The experimental value for the enthalpy of dissociation has been reported at 273.15 K and 24.98 bar.^{39,40} For this reason, the equilibrium data calculated from simulation has been extrapolated to 273.15 K, which corresponds to a pressure of 16.71 bar; the enthalpy of dissociation was calculated at these conditions using eq 13. Similarly, we have found the enthalpy of dissociation from simulation at the experimental pressure of 25 bar, which corresponds to a temperature of 277.95 K (that is, the enthalpy of dissociation was determined at both the reported experimental pressure and temperature, at conditions corresponding to the equilibrium temperature or pressure, respectively, as calculated from simulation). The compressibility factor in eq 13 for methane was determined from methane *NPT* simulations at the corresponding temperature and pressure. The results for the enthalpy of dissociation are shown in Table 4. As can be seen from the results, the enthalpy of dissociation of methane hydrate found from simulations is within 2% of the experimental value at similar conditions. The enthalpy of dissociation found at 277.95 K from the simulations is slightly lower than the one found at 273.15 K, which is due to the compressibility factor of methane being smaller at 25 bar compared to that at 16.71 bar.

Figure 4 shows the fractional (small/large cage) and total equilibrium hydrate occupancy as a function of pressure, as determined from the simulations. As seen in the figure, the

TABLE 4: Enthalpy of Dissociation for Methane Hydrate Determined from the Clapeyron Equation Using Simulation Data for the Three-Phase Equilibrium^a

	ΔH (kJ/mol CH ₄)
from simulation data at 273.15 K and 16.71 bar	53.9
from simulation data at 277.95 K and 25 bar	53.1
from experimental data at 273.15 K and 24.97 bar	54.2

^a Experimental values obtained from Handa.^{39,40}

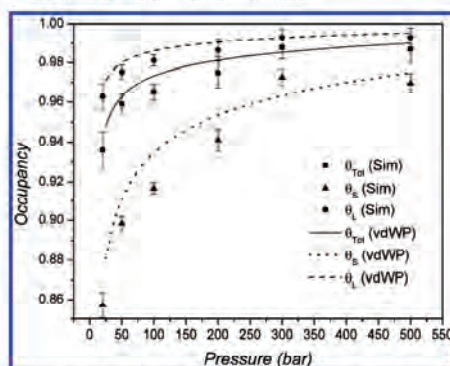


Figure 4. Fractional (small and large cage) and total occupancy of the methane hydrate from MC simulations and calculated from the vdWP approach, which assumes Langmuir adsorption isotherms for methane in the hydrate. The Langmuir constants used to calculate the occupancy are those reported by Munck and co-workers.⁴¹ The error bars in the occupancy correspond to the uncertainty estimated from the standard deviations of $\mu_{\text{H}_2\text{O}}^{\text{L}}$, $\mu_{\text{CH}_4}^{\text{V}}$, $(\mu_{\text{H}_2\text{O}}^{\text{L}} - \mu_{\text{H}_2\text{O}}^{\text{V}})$, and $(\mu_{\text{CH}_4}^{\text{L}} - \mu_{\text{CH}_4}^{\text{V}})$.

occupancy increases as the equilibrium pressure increases. It has previously been shown that the occupancy, $\theta_{i,J}$, of cavity i by type J molecules follows a Langmuir adsorption relation, which is applied in the vdWP theory

$$\theta_{i,J} = \frac{C_{i,J}f_J}{1 + C_{i,J}f_J} \quad (14)$$

where $C_{i,J}$ are the Langmuir constants found from fitting experimental data and f_J are the fugacities of molecule J . Using the Langmuir constants for methane as reported by Munck and co-workers,⁴¹ the fractional and total occupancies of methane hydrate as a function of the equilibrium pressure are also plotted in Figure 4. As seen in the figure, there is good agreement between the trends observed in the occupancy found from simulation and those predicted by the Langmuir adsorption relation applied in the vdWP theory. Similar observations for the methane and propane hydrate occupancy as a function of pressure have been presented in the literature.^{32,43}

In general, the occupancies found from simulations are slightly lower compared to those predicted by the vdWP theory. Compared to that of the large cages, the occupancy of the small cages is seen to be more strongly dependent on the pressure, both as calculated from simulation and from the vdWP theory. At the same time, the small cage occupancies found from simulations deviate more from those predicted by the vdWP theory when compared to the relative deviation in the large cage occupancies. The small/large cage occupancy ratios found from

simulations were between 0.89 and 0.98, and the hydration numbers were found to vary between 6.15 and 5.82 in the pressure region investigated; both of these quantities are not only within the limits reported from theoretical studies but are also within the experimentally reported values.^{1,44–50}

The small differences in occupancy between those from simulation and those predicted by the vdWP theory may be explained by revisiting some of the underlying assumptions of the vdWP theory. Previous studies have shown that the neglect of long-range interactions between methane–methane and methane–water in the vdWP theory can cause minor changes in the occupancy; additionally, the effect of assuming a static hydrate framework can have a significant effect on the occupancy relationship, particularly for small cage occupancy.⁴

Conclusions

Monte Carlo simulations were used to calculate the three-phase liquid water–methane hydrate–methane vapor equilibrium in the pressure range of 20–500 bar based on molecular models for water (TIP4P/ice) and methane (united-atom Lennard-Jones). Vapor–liquid equilibria calculations for the binary methane–water system showed that the fluid phases were nearly pure for the conditions studied, and thus, the effect of accounting for mixing in these phases had a negligible contribution to the chemical potential of the majority species. For this reason, the pure component values could be used for the chemical potentials of liquid water and methane vapor to simplify the criteria for phase coexistence. In general, good agreement between the simulated and experimental three-phase coexistence curves was found. The deviation in the coexistence temperature between the simulation and experimental data increased with pressure, from 4 K at 20 bar to 16 K at 500 bar. The calculated three-phase equilibrium curve was closely fit by a straight line on a log P versus $1/T$ plot, indicating that the data follow a Clapeyron equation relation, a behavior also seen in the experimental data. An enthalpy of hydrate dissociation of about 53 kJ/mol was obtained at 273.15 K or 25 bar, which is within 2% of the experimental value of 54.2 kJ/mol at these conditions. The hydrate occupancies found at equilibrium from the simulations are in reasonably good agreement with those calculated from the van der Waals and Platteeuw approach, which uses a Langmuir adsorption analogy. The results obtained from this study are the first to determine the phase diagram of a gas hydrate system using only the results of atomistic molecular simulations and analytical calculations.

Determining the phase equilibrium of a multicomponent, multiphase system is an intricate and computationally intensive process; however, such calculations are essential if proper conclusions are to be made from hydrate simulations defined in terms of subcooling or overpressurization. The methodology and results reported here serve as a foundation for future studies investigating both equilibrium and dynamic simulations employing molecular models. It should be noted that the presented results are specific to the molecular models used, and phase boundaries may differ significantly between different molecular models; caution should be exercised when determining whether a simulated system is thermodynamically stable within the hydrate phase envelope.

Acknowledgment. The authors would like to thank the Danish Research Council for Technology and Production Sciences for financial support through the project “Gas Hydrates—From Threat to Opportunity” and the Technical University of Denmark for financial support through a Ph.D. scholarship. This

research was supported in part by the Golden Energy Computing Organization at the Colorado School of Mines using resources acquired with financial assistance from the National Science Foundation and the National Renewable Energy Laboratory. A.K.S. and D.T.W. acknowledge the support from the National Science Foundation under Grant CBET-0933856. We acknowledge the financial support from the Center for Hydrate Research Consortium at the Colorado School of Mines (BP, Champion, Chevron, ConocoPhillips, ExxonMobil, Haliburton, Multichem, Nalco, Petrobras, Schlumberger, Shell, StatoilHydro, and Total). A.K.S. acknowledges the support of DuPont for a DuPont Young Professor Award. M.R.W. was supported by funds from U.S. Department of Energy, Basic Energy Sciences (DOE-BES) under Contract DE-FG02-05ER46242.

Note Added after ASAP Publication. This article posted on April 14, 2010. The last sentence in the Acknowledgment section has been added. The correct version posted on April 29, 2010.

References and Notes

- (1) Sloan, E. D.; Koh, C. A., *Clathrate Hydrates of Natural Gases*, 3rd ed.; CRC Press: Boca Raton, FL, 2008.
- (2) van der Waals, J. H. *Trans. Faraday Soc.* 1956, 52, 184.
- (3) van der Waals, J. H.; Platteeuw, J. C. *Adv. Chem. Phys.* 1959, 2, 1.
- (4) Wierzechowski, S. J.; Monson, P. A. *J. Phys. Chem. B* 2007, 111, 7274.
- (5) Wierzechowski, S. J.; Monson, P. A. *Ind. Eng. Chem. Res.* 2006, 45, 424.
- (6) Walsh, M. R.; Koh, C. A.; Sloan, E. D.; Sum, A. K.; Wu, D. T. *Science* 2009, 326, 1095.
- (7) Abascal, J. L. F.; Sanz, E.; Garcia, R.; Vega, C. *J. Chem. Phys.* 2005, 122, 234511.
- (8) Jorgensen, W. L.; Madura, J. D.; Swenson, C. J. *J. Am. Chem. Soc.* 1984, 106, 6638.
- (9) Vysniauskas, A.; Bishnoi, P. R. *Chem. Eng. Sci.* 1983, 38, 1061.
- (10) Skovborg, P.; Rasmussen, P. *Chem. Eng. Sci.* 1994, 49, 1131.
- (11) Natarajan, V.; Bishnoi, P. R.; Kalogerakis, N. *Chem. Eng. Sci.* 1994, 49, 2075.
- (12) Christiansen, R. L.; Sloan, E. D., *Proceedings of the Annual Convention of Gas Processors Association*; San Antonio, TX, 1995; Vol. 74, p 15.
- (13) Kashchiev, D.; Firoozabadi, A. *J. Cryst. Growth* 2002, 243, 476.
- (14) Anklam, A. F.; Firoozabadi, A. *J. Chem. Phys.* 1999, 110, 3977.
- (15) Armandi, M.; Tohidi, B.; Danesh, A.; Todd, A. C. *Chem. Eng. Sci.* 2005, 60, 1313.
- (16) Frenkel, D.; Ladd, A. D. C. *J. Chem. Phys.* 1984, 81, 3188.
- (17) Vega, C.; Monson, P. A. *J. Chem. Phys.* 1998, 109, 9938.
- (18) Polson, J. M.; Trizac, E.; Pronk, S.; Frenkel, D. *J. Chem. Phys.* 2000, 112, 5339.
- (19) Widom, B. *J. Chem. Phys.* 1963, 39, 2802.
- (20) Lorentz, H. A. *Ann. Physik* 1881, 12, 127.
- (21) Berthelot, D. *C.R. Acad. Sci. Paris* 1889, 126, 1703.
- (22) Heyes, D. M. *Phys. Rev. B* 1994, 49, 755.
- (23) Nymand, T. M.; Linse, P. *J. Chem. Phys.* 2000, 112, 6152.
- (24) Lopez-Lemus, J.; Alejandre, J. *Mol. Phys.* 2003, 101, 743.
- (25) Bennett, C. H. *J. Comput. Phys.* 1976, 22, 245.
- (26) Lu, N.; Singh, J. K.; Kofke, D. A. *J. Chem. Phys.* 2003, 118, 2977.
- (27) Deitrick, G. L.; Scriven, L. E.; Davis, H. T. *J. Chem. Phys.* 1989, 90, 2370.
- (28) McMillan, R. K.; Jeffrey, G. A. *J. Chem. Phys.* 1965, 42, 2725.
- (29) Chialvo, A. A.; Bartók, A.; Baranyai, A. *J. Mol. Liq.* 2006, 129, 120.
- (30) Harvey, A. H.; Sengers, J. M. H. L. *AIChE J.* 1990, 36, 539.
- (31) Harvey, A. H. *AIChE J.* 1996, 42, 1491.
- (32) NIST Chemistry WebBook. <http://webbook.nist.gov/chemistry/> (2010).
- (33) Docherty, H.; Galindo, A.; Vega, C.; Sanz, E. *J. Chem. Phys.* 2006, 125, 074510.
- (34) Keisuke, M.; Ryo, O.; Sum, A. K.; Yasuoka, K. Gibbs Ensemble Monte Carlo Simulations for Methane, Liquid Water and Methane/Hydrate Phase Equilibrium. *Proceedings of the 6th International Conference of Gas Hydrates*; Vancouver, British Columbia, Canada, July 6–10, 2008.
- (35) Jhaveni, J.; Robinson, D. B. *Can. J. Chem. Phys.* 1963, 43, 75.

- (36) Deaton, W. M.; Frost, E. M. Gas hydrates and their relation to the operation of natural-gas pipe lines. *U.S. Bur. Mines Monograph* **1946**, *8*, 101.
- (37) Marshall, D. R.; Saito, S.; Kobayashi, R. *AIChE J.* **1964**, *10*, 202.
- (38) Sloan, E. D.; Fleyfel, F. *Fluid Phase Equilib.* **1992**, *96*, 223.
- (39) Handa, Y. P. *J. Chem. Thermodyn.* **1986**, *18*, 891.
- (40) Handa, Y. P. Calometric studies of laboratory synthesized and naturally occurring gas hydrates. AIChE Annual Meeting, Miami Beach, Nov 2–7, 1986.
- (41) Muncck, J.; Skjold-Jørgensen, S.; Rasmussen, P. *Chem. Eng. Sci.* **1988**, *43*, 2661.
- (42) Sizov, V.; Piotrovskaya, E. M. *J. Phys. Chem. B* **2007**, *111*, 2886.
- (43) Tanaka, H. *J. Chem. Phys.* **1994**, *101*, 10833.
- (44) Ripmeester, J. A.; Ratcliffe, C. I. *J. Phys. Chem.* **1988**, *92*, 337.
- (45) Sum, A. K.; Burruss, R. C.; Sloan, E. D. *J. Phys. Chem. B* **1997**, *101*, 7371.
- (46) Galloway, T. J.; Ruska, W.; Chappellear, P. S.; Kobayashi, R. *Ind. Eng. Chem. Fundam.* **1970**, *9*, 237.
- (47) de Roo, J. L.; Peters, C. J.; Lichtenthaler, R. N.; Diepen, G. A. M. *AIChE J.* **1983**, *29*, 651.
- (48) Handa, Y. P. *J. Chem. Thermodyn.* **1986**, *18*, 915.
- (49) Klauda, J. B.; Sandler, S. I. *J. Phys. Chem. B* **2002**, *106*, 5722.
- (50) Sun, R.; Duan, Z. *Geochim. Cosmochim. Acta* **2005**, *69*, 4411.

JP911032Q

Appendix II

Paper 3

1486

Ind. Eng. Chem. Res. 2010, 49, 1486–1492

Inhibition of Methane Hydrate Formation by Ice-Structuring Proteins

Lars Jensen,[‡] Hans Ramløv,[‡] Kaj Thomsen,[‡] and Nicolas von Solms^{*†}

Department of Chemical and Biochemical Engineering, Technical University of Denmark, Søtoftsplads, Building 229 DK-2800 Kgs. Lyngby, Denmark. Department of Science, Systems and Models, Roskilde University, Universitetsvej 1, DK-4000, Roskilde, Denmark

In the oil and gas industry there is ample motivation for moving toward greener kinetic inhibitors of gas hydrates as many of those used today suffer from poor biodegradability. In this work, we have investigated experimentally whether ice-structuring proteins (ISPs) found in fish and insect, assumed biodegradable, are capable of inhibiting the growth of methane hydrate (a structure I hydrate). The ISPs investigated were type III HPLC12 (originally identified in ocean pout) and ISP type III found in meal worm (*Tenebrio molitor*). These were compared to polyvinylpyrrolidone (PVP) a well-known kinetic hydrate inhibitor. The results revealed that adding ISP in sufficient amounts caused the appearance of an initial nonlinear growth period. At a certain point during the growth process the growth pattern changed to linear which is identical to the growth observed for methane hydrate in the absence of inhibitors. The profile of the nonlinear growth was concentration-dependent but also dependent on the stirring rate. ISP type III HPLC12 decreased the growth rate of methane hydrate during the linear growth period by 17–75% at concentrations of 0.01–0.1 wt % (0.014–0.14 mM) while ISP from *Tenebrio molitor* and PVP decreased the growth rate by 30% and 39% at concentrations of 0.004 wt % (0.005 mM) and 0.1 wt % (0.1 mM), respectively. Considering the low concentration of *Tenebrio molitor* ISP used, these results indicate that ISP from *Tenebrio molitor* is the most effective hydrate inhibitor among those investigated. Thermal hysteresis ice formation experiments revealed that ISP from *Tenebrio molitor* causes higher thermal hysteresis for ice formation compared to type III ISP identified in ocean pout while PVP did not cause thermal hysteresis. This indicates that there might be a direct relationship between ISP performance for ice and hydrate inhibition, and that thermal hysteresis experiments can be used to screen ISPs as kinetic inhibitors.

1. Introduction

Gas hydrates are crystalline compounds formed when water and suitably sized gas molecules are combined at high pressure and low temperature. They consist of polyhedral cavities formed from networks of hydrogen-bonded water molecules which small gas molecules can enter. Depending on the type of gas molecules and the thermodynamic conditions present, gas hydrates will form different structures. Of the structures that have been observed experimentally, structure I (sI) and structure II (sII) are the most commonly encountered in practical applications.¹

The gases that form hydrates are normally small molecules, many of which are encountered in natural gas. Examples are methane, ethane, propane, isobutane, butane, carbon dioxide, nitrogen, and hydrogen sulfide.³ Gas hydrate formation is a problem that the oil and gas industry is very concerned about: Oil and gas transmission lines, tie-backs, and off-shore process equipment are prone to being blocked by hydrates, causing potential hazards or economic loss.

Traditionally the formation of hydrates has been prevented by adding thermodynamic hydrate inhibitors such as methanol and glycol. However, the amounts needed to avoid hydrate formation may reach 50 wt % in the water-rich phase.² Water production from fields can be quite severe, especially in cases where water injection has been used to enhance the oil recovery. Therefore very large amounts of hydrate inhibitor are required. For these reasons, a particular interest in finding low dosage hydrate inhibitors (LDHIs) has arisen. These are most often water-soluble polymers. Instead of shifting the hydrate equi-

librium to lower temperatures or higher pressures they affect the kinetics (nucleation and growth rates) of hydrate formation. If the hydrate kinetics are known, and can be controlled, that is, by adding LDHIs, it may then be possible to operate the transmission lines at hydrate formation conditions, while still ensuring that hydrates will not have time to nucleate or grow sufficiently to cause flow blockage. Polymeric compounds such as polyvinylcaprolactam (PVCap) or polyvinylpyrrolidone (PVP) have been shown to be quite effective in retarding both nucleation and growth of gas hydrate at concentrations 10–100 times lower than for thermodynamic inhibitors.³ Nevertheless, their use has been limited owing to their cost or because of environmental restrictions as a result of their poor biodegradability.⁴

Thus there is a particular interest in finding more environmentally friendly LDHIs. One such type could be antifreeze proteins (AFPs). AFPs are compounds that exist naturally in certain species of fish, insect, and plant living at cold conditions. They cause freeze resistance of the plasma and cell material of these living species in a noncolligative manner.⁵ However further research of these proteins has identified that they possess three different properties that are specific to concentration and temperature, that is, recrystallization inhibition, crystal habit modification, and thermal hysteresis freezing. In other words they have an impact on ice crystals that are already formed and may therefore have an effect that is more than just “antifreeze”. Consequently this class of proteins has also been named ice-structuring proteins (ISPs), which is sufficiently general to cover the range of natural functions and potential applications.

ISPs have previously been shown to be able to retard the nucleation and growth of methane hydrates.^{6–9} The degradation rates (biological half-lives) of ISP have been reported to be 4

* To whom correspondence should be addressed. Tel.: +45 4525 2867. Fax: +45 4525 2258. E-mail: nvs@kt.dtu.dk.

[‡] Technical University of Denmark.

[†] Roskilde University.

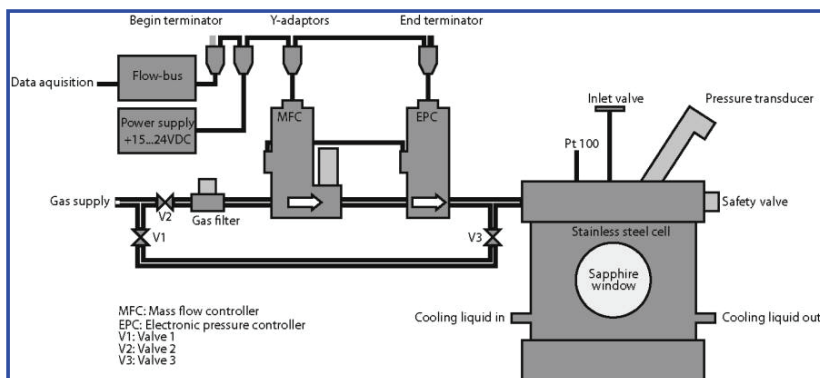


Figure 1. Experimental setup showing the hydrate cell and the back pressure control and flow measurement system.

weeks in an Antarctic fish¹⁰ indicating that ISPs might also possess the desirable property of high enough biodegradability to be used as kinetic hydrate inhibitors (KHI) in the off-shore industry. Fish ISPs can confer freeze resistance in icy seawater down to its freezing point ($-1.9\text{ }^{\circ}\text{C}$), approximately $1\text{ }^{\circ}\text{C}$ colder than the freezing point of fish plasma.¹¹ The millimolar ISP concentrations ($>10\text{--}20\text{ mg/mL}$) found in fish blood lower freezing temperatures below the melting point (a phenomenon termed thermal hysteresis), by about $0.5\text{--}1.0\text{ }^{\circ}\text{C}$. The ISPs found in insects, however, are much more potent. The remarkable specific activities of these proteins were however not fully appreciated until they were purified and expressed as recombinant proteins. The difference in thermal hysteresis (TH) as a function of concentration between insect and fish ISPs is approximately 2 orders of magnitude. For example, a $20\text{ }\mu\text{M}$ concentration of spruce budworm ISP depresses the freezing point by $1.08\text{ }^{\circ}\text{C}$, whereas winter flounder ISP at a 20-fold higher concentration ($400\text{ }\mu\text{M}$) depresses the freezing point by only $0.27\text{ }^{\circ}\text{C}$.¹² Another study has shown that ISP from the mealworm *Tenebrio molitor* (TmISP) depresses the freezing point by $1.4\text{ }^{\circ}\text{C}$ at a concentration of $20\text{ }\mu\text{M}$, whereas more than a 100-fold higher concentration (2.8 mM) of type III ISP from the fish ocean pout is required to produce the same freezing point depression.¹¹

The reason why insect ISP is more effective than fish ISP is most likely because fish ISP only binds to one plane while insect ISP has been shown to bind to prism faces and basal planes of ice even at very low concentrations.^{13,14} Since gas hydrates (just like ice) contain different crystal faces, it is very likely that insect ISPs are also capable of adsorbing strongly onto several faces of the hydrate crystal. If this is the case insect ISP is likely to work as a very effective inhibitor of hydrate growth.

In this work, we have investigated the effect of two types of ISP and the polymeric inhibitor PVP on the growth of methane hydrate. A similar study was performed by Al-Adeel et al.⁹ We have examined more closely the biphasic response of the growth of methane hydrate that is often observed when ISPs or other KHIs are present in the aqueous phase. In particular we have considered the initial nonlinear growth period, as this has not been subject to investigation so far. Methane hydrate was grown at constant pressure and temperature using a newly developed PID-controlled back-pressure and mass-flow setup. The ISPs investigated were type III HPLC12 (originally identified in ocean pout) produced from genetically modified *Saccharomyces*

cerevisiae and that found in the mealworm *Tenebrio molitor* (TmISP). We have also investigated if there is a correlation between the activity of the ISPs toward ice and methane hydrate inhibition by additionally measuring the hysteresis freezing points (HFP) of the different solutions.

2. Materials

The ice inhibition activity of ISP type III HPLC12, TmISP and PVP were measured using a nanoliter osmometer (Otago Osmometers: <http://www.otago-osmometers.com/>) using the procedure of Wharton and co-workers.¹⁵

The growth kinetics of methane hydrate and the effect on adding ISP type III HPLC12, TmISP, and PVP in small amounts to the aqueous phase were investigated experimentally at constant pressure and temperature. This was done using stainless steel hydrate equilibrium cell with a fixed volume of 66.5 cm^3 and a maximum working pressure of 150 bar. The complete experimental setup can be seen in Figure 1.

The cell allows for visual observation of hydrate formation through two sapphire windows. A safety valve is attached to the cell which opens when pressure exceeds an adjustable value ($40\text{--}100\text{ bar}$). The pressure in the cell was monitored using a digital pressure sensor (EPC, Bronckhorst High-Tech) with a range of $0\text{--}100\text{ bar}$ ($\pm 0.5\%$ in full scale). The pressure sensor is connected to a mass flow controller (MFC, Bronckhorst High-Tech EI flow) with a flow range of $0\text{--}10\text{ mL/min N}_2 \pm 2\%$ in full scale (mL is mL at 1 atm and 273.15 K). The MFC has a maximum working pressure of 100 bar and is attached to a gas filter which is attached to a gas reservoir.

The EPC and MFC work as an electronic back-pressure control system which ensures that the pressure in the cell is maintained constant during an experimental run. The pressure sensor receives a digital set point from the flow-bus (High Tech RS232) and when the measured value becomes less than the set point value, that is, pressure drops due to hydrate formation, an analog set point is sent to the mass flow meter. This causes the mass flow meter to open its valve in accordance with the provided set-point. The back-pressure system is PID-controlled and parameters were optimized for the systems of interest to secure the highest level of control. Data logging and instrument control was performed using FlowPlot and FlowView (Bronckhorst technologies). The gas supply can bypass the back-pressure control system by closing valve 2 and opening valve

Table 1. Melting Points (MP), Hysteresis Freezing Points (HFP), and the Thermal Hysteresis (TH) of the Different Solutions

solution	concn (mM/wt%)	Mp (K)	HFP (K)	TH (K)
type III ISP	0.14/0.10	273.06	278.78	0.28
TmISP	0.005/0.004	273.10	272.63	0.47
PVP	0.10/0.10	273.15	273.15	0

1 and 3. This is done when starting up the experiment in order to quickly obtain the required cell pressure.

The temperature in the cell was controlled by circulating coolant (water–ethanol solution) in a jacket surrounding the cell. The temperature was monitored using a platinum resistance probe (± 0.1 K) placed inside the cell and an extra pressure transducer was attached to the cell to verify that a constant pressure was indeed maintained during a run (BD Sensors, 0–100 bar \pm 0.5% in full scale). The cell was placed on a stir plate which allowed a stirrer bar (length 4 cm) to rotate inside the cell. The pressure and temperature in the cell were recorded continuously on a computer.

The experiments were performed using distilled water and methane supplied by AGA with a purity of 99.995%. ISP type III HPLC12 was supplied by UNILEVER as a complex solution containing small amounts of salts, sugars, and proteins (other than ISP), however, in a concentration range not affecting the melting point of ice (see Table 1) nor the phase boundary of methane hydrate. TmISP (8.5 kDa) was isolated from the mealworm *Tenebrio molitor*. The mealworms were homogenized in 50% ethanol and centrifuged for 10 min at 3000 rpm after which the supernatant was decanted. The precipitant was washed twice with a 50% ethanol solution and combined with the supernatant. The solution was filtered and cooled five times in total to remove fat from the solution. The solution was exposed to dialysis against distilled water at 5 °C for 3 \times 24 h while being stirred. The water was changed every 12 h. The remaining solution from dialysis was subsequently freeze-dried. Using SDS-page¹⁶ the purity of the proteins was determined to be around 10%. Among the impurities is a 500000 g/mol protein which was not identified. The measured purity was confirmed by measuring the HFP of the solution containing the protein and comparing it to literature values. This indicates that the impurities do not affect the binding capability of the ISPs on ice. It was therefore deemed unlikely that the impurity would have any impact on the binding capability of the ISP on hydrate. PVP ($M_w = 10,000$) was purchased from Sigma-Aldrich.

3. Methods

The cell was cleaned with distilled water and loaded with 15 g of distilled water or distilled water containing small amounts of ISP. A stirrer bar was placed in the cell. The cell lid was screwed on and the cell evacuated using a vacuum pump for approximately 1 h. The temperature bath was adjusted so the temperature in the cell was 276.9 K. Methane gas was injected into the cell, by bypassing the back-pressure control system (valves 1 and 3 open and valve 2 closed), until the desired pressure at the chosen temperature was obtained.

When adding ISPs to the hydrate forming system nucleation periods can be prolonged quite significantly causing experiments to be very time-consuming. Increasing the subcooling is one way to shorten nucleation periods; however, the effects that ISPs cause on the growth period are better expressed at lower degrees of subcooling. These requirements are contradictory, so in order to perform growth experiments at low degrees of subcooling we need to eliminate or shorten the nucleation period by other means. This was done by allowing hydrate to form and then

melt in the cell before each experiment was initiated. The reason that nucleation periods at second hydrate formation are shorter has been shown through molecular simulation to be associated with the slow equilibration of the aqueous gas concentration.¹⁷ However no experimental evidence confirming this has been published.

When the liquid water is supersaturated with gas more gas molecules will be available for hydrate formation resulting in shorter nucleation periods compared with water that has not experienced hydrate formation.

The procedure was as follows: The pressure was first increased to 90 bar ensuring relatively fast hydrate formation. After a brief period of formation the pressure was lowered to 31 bar. During gas venting caution must be exercised in order not to form ice in the cell. However slowly releasing the gas only causes a minor drop in temperature, which never dropped below the ice point. A pressure of 31 bar corresponds to a superheating degree of 2.2 K compared to the hydrate stability region. This caused the hydrate to melt and the system was maintained at 31 bar and 276.9 K for approximately 2 h—ensuring that all hydrate has melted. The melting process was furthermore visualized through the sapphire windows to ensure the hydrate had melted completely before initiating an experiment. Shortly after dropping the pressure to 31 bar the solution appeared hazy; however, after 2 h it had turned clear indicating that hydrate had melted. The pressure was then increased to the experimental pressure (56 bar). Valves 1 and 3 were closed, and valve 2 was opened. A set-point, corresponding to the start pressure in the cell was given to the EPC. The experiment was then initiated by turning on the stirrer bar in the cell and starting the data acquisition. Data in terms of cell pressure and mL gas injected/min was acquired every 5 s.

A similar experimental technique has been applied previously to measure nucleation periods of gas hydrates, in order to achieve better reproducibility among the measured nucleation periods.¹⁸ Here we move in and out of the hydrate stability area by changing pressure, whereas Dicharry et al.¹⁸ changed the temperature to achieve the same effect.

The amount of gas injected to the cell was based on N₂ mL/n/min. This was subsequently converted to mL/n/min of methane gas using an empirical conversion factor provided by Bronckhorst technologies. The cumulative amount of methane injected to the cell was found by integrating the output volume of the MFC over time using the trapezoidal rule. Each experimental run was repeated three times and the cumulative amounts of methane found for each run were combined to calculate an average amount of gas consumed by the hydrate over time. The average gas consumption rate was then found by performing a linear regression on the combined data. The moles of gas absorbed during the formation process can be changed to % water converted by assuming the hydrate is stoichiometric (CH₄·5.75H₂O) which gives a better idea of the reaction rate.

4. Results

The melting points (MP), HFPs, and the TH of the different solutions are provided in Table 1. As expected TmISP causes a higher TH compared to ISP type III HPLC12. As expected PVP, which is not capable of adsorbing on ice, causes no TH.

The TH value reported for ISP type III HPLC12 is 0.35 K while for TmISP it is 0.52 K—in reasonably good agreement with values found in literature for the concentrations investigated.¹¹

All the methane hydrate growth experiments were performed at 276.9 K and under constant pressure. The back-pressure

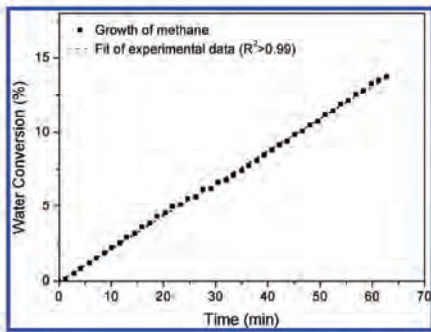


Figure 2. Fraction (%) of the initial amount of liquid water present converted into hydrate over time at $T = 276.9$ K and $P = 56$ bar. Solid points are the data combined from three experiments, and the dashed line indicates the average conversion of water to hydrate. As seen the reproducibility is very high given the R^2 is very close to unity.

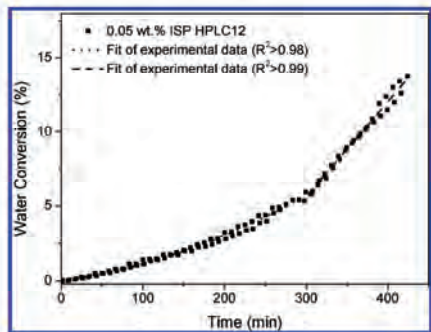


Figure 3. Methane hydrate growth from an aqueous solution containing 0.05 wt % (0.071 mM) ISP type III HPLC12 at $T = 276.9$ K and $P = 56$ bar. Solid points are the data combined from three experiments, and the dashed lines indicate the average growth rate.

control system ensured that the maximum deviation between the experimental pressure and the set-point pressure was never more than 0.25%.

Figure 2 shows the amount of water converted to methane hydrate as a function of time. The solid points are the averages obtained from three different experimental runs. As seen the data shows linearity and in general low scattering among the data points is observed. The dotted line indicates the average amount of water converted to hydrate as found using linear regression.

Figure 3 shows the growth pattern of methane hydrate from an aqueous solution containing 0.05 wt % ISP type III HPLC12. The growth profile is seen to be quite different compared to the case when no inhibitors are present. The initial nonlinear growth period is designated as growth period 1 in the following while the linear growth period is designated as growth period 2. The distinction between growth periods 1 and 2 is quite apparent in the plot, and the interface between the periods is found at around 300 min. The dotted line present in growth period 1 indicates the average conversion of water to hydrate and is based on a second-order poly-

nomial. The dashed line present in growth period 2 also indicates the average conversion of water to hydrate and has been found by linear regression.

Table 2 lists the experimental conditions during the different runs and presence of growth periods 1 and 2. The regressed average growth rate of period 2 (in mole gas/min) has been compared to the average growth rate of methane hydrate with no inhibitor present since these two periods both are linear and likely to be an expression of the same growth mechanism taking place. A comparison of these two indicates the degree of inhibition caused by the ISPs. In the table, the degree of inhibition is shown as a percentage.

From table 2 we can conclude that only addition of ISP type III HPLC12 causes the growth profile to be divided into both a period 1 and a period 2. The addition of TmISP or PVP in all cases results in only linear growth patterns of methane hydrate with moderate reductions in the growth rate.

In Figure 4 the regressed growth curves of methane hydrate at different concentrations of ISP type III HPLC12 and at different stirring rates are presented. The figure shows that growth period 1 is prolonged quite substantially when the ISP concentration is increased. This ISP also decreases the growth rate in period 2—a pattern that also seems to depend on the ISP concentration. Also we note that the amount of water converted into hydrate during the nonlinear growth period decreases with increasing ISP concentration. Another interesting effect observed is that changing the stirring rate will cause changes to both growth period 1 and 2.

5. Discussion

The nature of the methane hydrate growth profile, with and without ISPs/KHIs present, can be explained by looking at the expression for the growth rate in terms of moles of gas absorbed by hydrate over time:

$$\left(\frac{dn}{dt}\right)_{R,T} = C_{w0}K^*(x'_{L,V} - x'_{H,L}) \quad (1)$$

where C_{w0} is the initial concentration of water, $x'_{L,V}$ is the gas solubility in the liquid at experimental conditions, and $x'_{H,L}$ is the gas solubility in the liquid at hydrate liquid equilibrium conditions. K^* is the overall hydrate growth coefficient and is given by

$$\frac{1}{K^*} = \frac{1}{A_p} \left(\frac{1}{k_d} + \frac{1}{k_l} \right) + \frac{1}{k_p A_{L,V}} \quad (2)$$

where A_p is the surface area of the hydrate particles, k_d is the mass transfer coefficient in the diffusion layer surrounding the hydrate particle, k_l is the rate constant for the surface reaction process, k_p is the mass transfer coefficient in the liquid film, and $A_{L,V}$ is the liquid–vapor interfacial area. If no inhibitors are present then $A_p \gg A_{L,V}$ thus the last term in eq 2 will be dominant and result in a constant growth rate. Where sufficient amounts of ISPs or other KHIs are present, these will adsorb onto the hydrate surface thus minimizing the hydrate surface area. The mechanism by which the ISPs adsorb on hydrate may be similar to those suggested for ice, although this is as yet not fully understood. In the literature on antifreeze mechanisms it has long been proposed that the basis for adsorption specificity lies in a hydrogen bonding match between groups on the ice-binding site of the ISP and oxygen atoms on the ice lattice.⁵ It has however been discussed if the number of hydrogen bonds available at very low ISP concentrations is sufficient to bind the ISP tightly enough to the ice surface.^{13,20} Results from the

Table 2. Experimental Conditions, Measured Growth Rates of Methane Hydrate (Numbers in Parentheses Indicate the Standard Error) and the Percentage Inhibition of the Growth Rates by the Ice-Structuring Proteins. The Degree of Subcooling is 4.1 K at 56 bar (Found Using the CSMGem Software¹⁹)

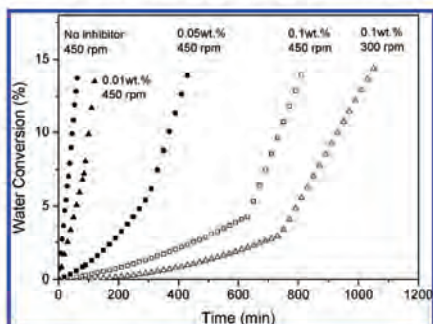
solution	concn (mM/wt %)	stirring rate (rpm)	growth period 1		growth period 2		inhibition (%)
			period occurrence (min)	period occurrence (min)	growth rate (mol/min)	growth rate (mol/min)	
dist. water		450		0–65	3.16×10^{-4} (1.26×10^{-5})		
dist. water + ISP type III HPLC12	0.014/0.01	450	0–85	85–120	2.63×10^{-4} (2.12×10^{-5})		17
			0–300	300–430	9.34×10^{-5} (1.99×10^{-5})		70
			0–620	620–820	7.79×10^{-5} (1.53×10^{-5})		75
dist. water + TmlSP	0.005/0.004	300	0–730	730–1065	5.32×10^{-5} (1.44×10^{-5})		
					0–100	2.20×10^{-4} (4.41×10^{-5})	
dist. water + PVP	0.100/0.10	450		0–105	1.92×10^{-4} (3.04×10^{-5})		39

Table 3. The Amount of Water Converted to Hydrate at the Point Where the Growth Profile Changes from Nonlinear to Linear

stirring rate (rpm)	450	450	450	300
type III ISP concentration (mM/wt %)	0.014/0.01	0.071/0.05	0.14/0.10	0.14/0.10
water converted (%)	7.3	6.20	4.3	2.90
level of linearity (R^2)	0.999	0.944	0.943	0.843

3-D structural analysis of type III ISP^{21,22} and from type I ISP structure function analysis²³ support the notion that hydrogen bonding alone is perhaps inadequate but suggest that significant contributions to the energetics of binding may come from van der Waals interactions and entropic solvation effects resulting from the fit of ISP to ice.

As stated above, when sufficient amounts of ISPs or other KHIs are present these will adsorb to the hydrate surface thus minimizing the hydrate surface area. In this situation we have $A_p \ll A_{L,V}$ and the first term in eq 2 becomes dominant. Since A_p has been shown to be a quadratic function of time, this explains why the curvature of growth period 1 seems to follow a second order polynomial.^{24,25} This suggests that the growth profile of period 1 depends on the surface area of the hydrate particle which again depends on the inhibitor concentration if we assume that the inhibitor adsorbs to the hydrate surface. In Figure 4 we see exactly this effect, namely that the profile of growth period 1 (curvature of the polynomial) levels off and is prolonged significantly when the concentration of ISP type III HPLC12 is increased. An interesting observation during this period is that the amount of hydrate formed decreases as the concentration of type III ISP increases. Another interesting observation is that changing the stirring rate will also change the profile of growth period 1, that is, decreasing the stirring rate from 450 to 300 rpm levels off and prolongs the profile of growth period 1 at the same ISP concentration (0.14 mM). The amount of hydrate formed at the point of transition between

**Figure 4.** Regressed growth curves of methane hydrate at $T = 276.9$ K and $P = 56$ bar at different concentrations of ISP type III HPLC12 and at different stirring rates.

growth period 1 and 2 is shown in Table 3. A linear regression, giving indications of the level of experimental reproducibility in terms of R^2 has been performed for each experiment and is also provided in Table 3.

When any adsorption process takes place the initial concentration of the adsorbing compound and the surface area of the substrate on which the adsorption takes place are key parameters. When the ISP concentration is very low it is likely that only a small part of the growing hydrate will be covered by the ISPs thus leaving more surface area to grow freely (linear). If this is the case one would expect that the initial nonlinear growth period would exhibit a higher degree of linearity, although the growth rate would still be smaller compared to growth period 2, since small parts of the hydrate surface are adsorbed to by ISPs. In other words there is competition between which of the growth patterns is dominant. As the concentration of ISP increases one would then expect to observe more and more nonlinear behavior of the initial growth period, and this is what is seen here. The fact that the amount of hydrate formed during this period diminishes with increasing ISP concentration is simply due to more ISPs being available for adsorption per hydrate surface area. This also explains why less hydrate is formed during the nonlinear growth period when the stirring rate is lowered—surface and interfacial areas are lowered and thus more ISP is available per unit surface area. Decreasing the stirring rate also causes the growth profile of period 2 to become more nonlinear. We know that $k_d A_{L,V}$ is lowered when lowering the stirring rate so it is likely that this causes the term $1/A_p (1/k_r + 1/k_d)$ in eq 2 to become even more dominant though it is not possible to assess if and to what extent k_r and k_d are influenced by the stirring rate. However the result surely indicates that the relationship between $k_d A_{L,V}$ and $1/A_p (1/k_r + 1/k_d)$ is changed.

Another reason why less hydrate is formed during the nonlinear growth period could be that the ISP adsorbs on any active nucleation sites, for example, dust particles in the solution, which thereby reduces the number of available sites for hydrate nucleation and growth which would limit the amount of gas that can be consumed during this period. Such a mechanism for inhibiting hydrate nucleation has been proposed in an earlier study.²⁶

Only linear growth of methane hydrate was observed for TmlSP and PVP. A comparison plot of the linear growth periods of methane hydrate, in presence of ISP type III HPLC12, TmlSP, and PVP is shown in Figure 5. As can be seen the growth rates of ISP type III HPLC12, TmlSP and PVP are

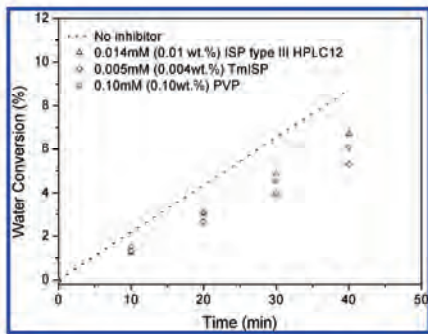


Figure 5. Regressed growth curves for the linear growth period of methane hydrate with no inhibitor present and in presence of TmISP, PVP, and ISP type III HPLC12. $T = 276.9$ K and $p = 56$ bar.

similar even though the concentrations are very different. Thus it can be definitively concluded that PVP is not as efficient an inhibitor as ISP type III HPLC12 and TmISP, their concentration being a factor 10 and 25 lower by wt % than that of PVP. This is perhaps not surprising considering that PVP is better known as an inhibitor of sII hydrate.

Overall the TmISP at these quite low concentrations shows the best performance toward inhibiting growth period 2 of methane hydrate. The inhibition by 0.004 wt % TmISP is 30% or almost twice that of ISP type III HPLC12 at a concentration of 0.01 wt %. Al Adeel and co-workers⁹ reported an inhibition for methane hydrate growth of 25% for a 0.007 wt % winter flounder ISP solution at similar conditions (4 K subcooling) to those studied here. However they did not report whether a nonlinear growth period was present and to what extent.⁹

It is surprising that the nonlinear growth period is not present in the case when testing TmISP which could give indications that it might not bind as effectively to the hydrate surface as ISP type III HPLC12. This may seem contradictory, since TmISP was shown to inhibit growth period 2 more than ISP type III HPLC. It is believed that the lack of the initial nonlinear growth period in the TmISP experiments is because the concentration of TmISP is simply too low to ensure an efficient covering of the hydrate surface. Looking at Figure 4 it can be seen that the nonlinear growth profile at an ISP type III HPLC12 concentration of 0.01 wt % was very short and almost linear. Considering that the concentration used in that case is 2.5 times higher by wt % compared to the TmISP experiments, it is not surprising that a nonlinear growth period is not present in those experiments. With these considerations in mind we claim that TmISP is actually a better hydrate growth inhibitor than ISP type III HPLC12 though we have not been able to confirm that the addition of TmISP to the aqueous phase can provoke a nonlinear growth period. This conclusion is in good agreement with what was observed in the thermal hysteresis experiments for ice—namely that TmISP is being a better inhibitor than ISP type III HPLC12.

It is also possible that the staged growth pattern present in the case of ISP type III HPLC12 is due to the way the ISP adsorbs on the hydrate. sI hydrate exhibits growth primarily at the {110} plane which will result in crystals having large facets. In cases where a kinetic inhibitor is added the crystal growth changes from exhibiting large facets to having no visible facets and being highly irregularly branched.²⁷ This is very similar to

what is observed when ISPs inhibit the formation of ice—namely that the growth morphology changes.²⁸

6. Conclusion

The capabilities of two different types of ice-structuring proteins and polyvinylpyrrolidone to inhibit methane hydrate growth have been reported. The ice-structuring proteins investigated were ISP type III HPLC12 (originally identified in ocean pout) produced from genetically modified *Saccharomyces cerevisiae* and ISP type III found in mealworm (*Tenebrio molitor*). The average growth rate of methane hydrate was determined using an experimental setup that allowed measurement of gas absorption, due to methane hydrate growth, over time at constant pressure and temperature. All experiments were performed at 276.9 K and 56 bar corresponding to 4.1 K of subcooling. The results of these studies revealed that if the concentration of ice-structuring protein was sufficiently high a nonlinear growth profile would appear initially. The extent and shape of this initial growth period was concentration dependent. This initial nonlinear growth profile was attributed to adsorption of the ice-structuring proteins on the surface of the growing hydrate crystals, limiting the surface area available for growth. It has previously been argued that the resistance to hydrate growth during this initial period should be ascribed to the rate constant of the surface reaction taking place and the available surface area of the growing particle. From conducting experiments at different inhibitor concentrations and stirring rates, we showed that profile of the nonlinear growth period is likely to be a result of both the mass-transfer coefficient in the liquid film, the mass-transfer coefficient in the diffusion layer around the hydrate particle and the rate constant for the surface reaction process.

The initial nonlinear growth period changed into a linear growth profile after a certain time indicating that ISPs initially available for adsorbing on the hydrate surface were no longer present. The linear growth period was also inhibited depending on the initial ISP concentration. The linear growth period was inhibited by 75% at a concentration of 0.1 wt % ISP type III HPLC12. The addition of *Tenebrio molitor* ISP, even though added in a very small amount (0.004 wt %) inhibited the linear growth period by 30%, whereas ISP type III HPLC12 at 0.01 wt % only caused 17% inhibition. Polyvinylpyrrolidone added in 0.10 wt % caused an inhibition of 39%. This indicated that *Tenebrio molitor* was actually a more effective inhibitor of methane hydrate compared to both ISP type III HPLC12 and polyvinylpyrrolidone. This is in good agreement with *Tenebrio molitor* ISP also being a more effective inhibitor of ice formation, measured in terms of thermal hysteresis, compared to ISP type III HPLC12.

Acknowledgment

The authors would like to thank the Danish Research Council for Technology and Production Sciences for financial support through the project "Gas Hydrates—from Threat to Opportunity" and the Technical University of Denmark for financial support through a Ph.D. scholarship. The type III ISP was made available as a gift by Unilever PLC, for which the authors are very thankful.

Nomenclature

Abbreviations

AFP = antifreeze protein
CSMGem = Colorado School of Mines Gibbs free energy minimization

EPC = electronic pressure controller
 HFP = hysteresis freezing point
 ISP = ice-structuring protein
 KHI = kinetic hydrate inhibitor
 LDHI = low dosage hydrate inhibitor
 MFC = mass flow controller
 MP = melting point
 PVCap = polyvinylcaprolactam
 PVP = polyvinylpyrrolidone
 TH = thermal hysteresis
 Tm = *Tenebrio molitor*

Notation

$A_{L,V}$ = liquid–vapor interfacial area
 A_p = surface area of hydrate particle
 C_{w0} = initial water concentration
 k_d = mass transfer coefficient in diffusion layer surrounding hydrate particle
 k_l = mass transfer in liquid film
 k_r = rate constant for surface reaction on hydrate particle
 K^* = hydrate growth coefficient
 x_i = gas solubility

Literature Cited

- (1) Sloan, E. D.; Koh, C. A. *Clathrate Hydrates of Natural Gases*, 3rd ed.; CRC Press: New York, 2008.
- (2) Kelland, M. Studies on new gas hydrate inhibitors. *Soc. Pet. Eng. 1995*, 30420, 531.
- (3) Sloan, E. D.; Lederhos, J. P.; Long, J. P.; Sum, A.; Christiansen, R. L. Effective kinetic inhibitors for natural gas hydrates. *Chem. Eng. Sci.* 1996, 51, 1221.
- (4) Villano, L. D.; Kommedal, R.; Kelland, M. A. A class of kinetic hydrate kinetic inhibitor with good biodegradability. Proceedings of the 6th International Conference on Gas Hydrates, Vancouver, British Columbia, Canada, July 6–10, 2008.
- (5) Devries, A. L.; Lin, Y. Structure of peptide antifreeze and mechanism of adsorption to ice. *Biochem. Biophys. Acta* 1977, 495, 388.
- (6) Zeng, H.; Ripmeester, J. A.; Wilson, L. D.; Walker, V. K. The inhibition of tetrahydrofuran clathrate–hydrate formation with antifreeze protein. *Can. J. Phys.* 2003, 81, 17.
- (7) Zeng, H.; Moudakovski, I. L.; Ripmeester, J. A.; Walker, V. K. Effect of antifreeze protein on nucleation, growth and memory of gas hydrates. *AIChE J.* 2006, 52, 3304.
- (8) Zeng, H.; Wilson, L. D.; Walker, V. K.; Ripmeester, J. A. Effect of antifreeze proteins on the formation and reformation of tetrahydrofuran clathrate hydrate. *J. Am. Chem. Soc.* 2006, 128, 2844.
- (9) Al-Adel, S.; Dick, J. A. G.; El-Ghafari, R.; Servio, P. The effect of biological and polymeric inhibitors on methane gas hydrate growth kinetics. *Fluid Phase Equilib.* 2008, 267, 92.
- (10) Fletcher, G. L.; Addison, R. F.; Slaughter, D.; Hew, C. L. Antifreeze proteins in the Arctic Shorthorn Sculpin. *Arctic* 1982, 35, 302.
- (11) Scotter, A. J.; Marshall, C. B.; Graham, L. A.; Gilbert, J. A.; Gamham, C. P.; Davies, P. L. The basis for hyperactivity of antifreeze proteins. *Cryobiology* 2006, 53, 229.
- (12) Græther, S. P.; Kuiper, S. M.; Gagne, M. J.; Walker, V. K.; Jia, Z.; Sykes, B. D.; Davies, P. L. β -Helix structure and ice-binding properties of a hyperactive antifreeze protein from an insect. *Nature* 2000, 406, 325.
- (13) Knight, C. A.; Cheng, C. C.; Devries, L. Adsorption of α -helical antifreeze peptides on specific crystal surface planes. *Bioophys. J.* 1991, 59, 409.
- (14) Græther, S. P.; Sykes, B. D. Cold survival in freeze-intolerant insect. The structure and function of β -helical antifreeze proteins. *Eur. J. Biochem.* 2004, 271, 3285.
- (15) Wharton, D. A.; Barrett, J.; Goodall, G.; Marshall, C. J.; Ramløv, H. Ice-active proteins from the Antarctic nematode *Panagrolaimus davidi*. *Cryobiology* 2005, 51, 198.
- (16) Laemmli, U. K. Cleavage of structural proteins during the assembly of the head of bacteriophage T4. *Nature* 1970, 227, 680.
- (17) Hawtin, R. W.; Quigley, D.; Rodger, P. M. Gas hydrate nucleation and cage formation at a water/methane interface. *Phys. Chem. Chem. Phys.* 2008, 10, 4855.
- (18) Dichary, C.; Duchateau, C.; Glénet, P.; Hidalgo, M.; Peytavy, J.-L.; Pou, T.-E. Laboratory evaluation of kinetic hydrate inhibitors: A new procedure for improving reproducibility of measurements. Proceedings of the 6th International Conference on Gas Hydrates, Vancouver, British Columbia, Canada, July 6–10, 2008.
- (19) Ballard, A.; Sloan, E. D. The next generation of hydrate prediction: Part III. Gibbs energy minimization formalism. *Fluid Phase Equilib.* 2004, 218, 15.
- (20) Wen, D.; Laursen, R. A. A model for binding of an antifreeze polypeptide to ice. *Bioophys. J.* 1992, 63, 1659.
- (21) Sönnichsen, F. D.; DeLuca, C. I.; Davies, P. L.; Sykes, B. D. Refined solution structure of type III antifreeze protein: Hydrophobic groups may be involved in the energetics of the protein–ice interaction. *Structure* 1996, 4, 1325.
- (22) Jia, Z.; DeLuca, C. I.; Chao, H.; Davies, P. L. Structural basis for the binding of a globular antifreeze protein to ice. *Nature* 1996, 284, 285.
- (23) Chao, H.; Houston, M. E.; Hodges, R. S.; Kay, C. M.; Sykes, B. D.; Loewen, M. C.; Davies, P. L.; Sönnichsen, F. D. A diminished role for hydrogen bonds in antifreeze protein binding to ice. *Biochemistry* 1997, 36, 14652.
- (24) Kane, S. G.; Evans, T. W.; Brian, P. L. T.; Sarofim, A. F. Determination of the kinetics of secondary nucleation in batch crystallizers. *AIChE J.* 1974, 20, 855.
- (25) Bergeron, S.; Servio, P. Reaction rate constant of propane hydrate formation. *Fluid Phase Equilib.* 2008, 265, 30.
- (26) Jensen, L.; Thomsen, K.; von Soms, N. Propane hydrate nucleation: Experimental investigation and correlation. *Chem. Eng. Sci.* 2008, 63, 3069.
- (27) Larsen, R.; Knight, C. A.; Rider, K. T.; Sloan, E. D. Melt growth and inhibition of ethylene oxide clathrate hydrate. *J. Cryst. Growth* 1999, 204, 376.
- (28) Strom, C. S.; Liu, X. Y.; Jia, Z. Why does insect antifreeze protein from *Tenebrio molitor* produce pyramidal ice crystallites. *Bioophys. J.* 2005, 89, 2618.

Received for review August 24, 2009

Revised manuscript received December 18, 2009

Accepted December 18, 2009

IE901321P

Appendix III

Paper 4

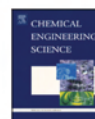
Chemical Engineering Science 63 (2008) 3069–3080



Contents lists available at ScienceDirect

Chemical Engineering Science

journal homepage: www.elsevier.com/locate/ces



Propane hydrate nucleation: Experimental investigation and correlation

Lars Jensen, Kaj Thomsen, Nicolas von Solms*

Department of Chemical and Biochemical Engineering, Centre for Phase Equilibria and Separation Processes (IVC-SEP), Technical University of Denmark, Søtofts Plads, Building 229, DK-2800 Lyngby, Denmark

ARTICLE INFO

Article history:

Received 10 October 2007

Received in revised form 12 February 2008

Accepted 5 March 2008

Available online 8 March 2008

Keywords:

Aqueous solutions

Interfacial energy

Nucleation

Crystallization

Gas hydrate

Polymers

ABSTRACT

In this work the nucleation kinetics of propane gas hydrate has been investigated experimentally using a stirred batch reactor. The experiments have been performed isothermally recording the pressure as a function of time. Experiments were conducted at different stirring rates, but in the same supersaturation region. The experiments showed that the gas dissolution rate rather than the induction time of propane hydrate is influenced by a change in agitation. This was especially valid at high stirring rates when the water surface was severely disturbed.

Addition of polyvinylpyrrolidone (PVP) to the aqueous phase was found to reduce the gas dissolution rate slightly. However the induction times were prolonged quite substantially upon addition of PVP.

The induction time data were correlated using a newly developed induction time model based on crystallization theory also capable of taking into account the presence of additives. In most cases reasonable agreement between the data and the model could be obtained. The results revealed that especially the effective surface energy between propane hydrate and water is likely to change when the stirring rate varies from very high to low. The prolongation of induction times according to the model is likely to be due to a change in the nuclei–substrate contact angle.

© 2008 Elsevier Ltd. All rights reserved.

1. Introduction

Gas hydrates are crystalline compounds formed when water and suitably sized gas molecules are combined at high pressure and low temperature. They consist of polyhedral cavities formed from networks of hydrogen-bonded water molecules in which small gas molecules can enter. Depending on the type of gas molecules present gas hydrates form different structures, known as structure I (sl), structure II (sII) and in special cases structure H (sH) (Sloan, 1998).

The gases that form hydrates are normally small molecules, many of which are encountered in natural gas. Examples are methane, ethane, propane, iso-butane, butane, carbon dioxide, nitrogen and hydrogen sulfide (Sloan, 1998). Gas hydrate formation is a problem that the oil and gas industry is most concerned with. Oil- and gas transmission lines, tie-backs and off-shore process equipment are prone to being blocked by hydrates, causing potential hazards or economic loss.

Traditionally, the formation of hydrates has been prevented by addition of thermodynamic hydrate inhibitors such as methanol and glycol. However, the amounts needed to avoid hydrate formation may reach 50 wt% in the water rich phase (Kelland, 1995). Since

water production from fields can be quite severe, especially in cases where water injection has been used to enhance the oil recovery, large amounts of hydrate inhibitor are required. For these reasons a particular interest in hydrate formation kinetics has arisen. If the hydrate kinetics are known, and can be controlled, it may then be possible to operate the transmission lines at hydrate formation conditions, while still ensuring that hydrates will not grow sufficiently to cause flow blockage. If the kinetics of gas hydrate formation is very fast, it is possible to slow their formation by the addition of low dosage hydrate inhibitors (LDHI). These are most often water soluble polymers and are effective at concentrations 10–100 times less than conventional thermodynamic inhibitors (Sloan et al., 1996).

From a thermodynamic point of view there is a good understanding of gas hydrate formation conditions and several methods for accurate prediction of hydrate formation conditions exist (Munck et al., 1988; Ng and Robinson, 1976; Parrish and Prausnitz, 1972). The kinetics of hydrate formation is less well understood, although it is clear that they are a very important property of gas hydrates. Hydrate formation is usually divided into two periods. The first period, the nucleation or induction period, deals with formation of small hydrate nuclei. When these small nuclei have grown to a critical size a second period, the growth period, commences.

Gas hydrate nucleation and growth has been investigated experimentally using different approaches and analytical expressions have been derived to describe the obtained data (Englezos et al., 1987;

* Corresponding author. Tel.: +45 4525 2867; fax: +45 4588 2258.
E-mail address: nvs@kt.dtu.dk (N. von Solms).

Kashchiev and Firoozabadi, 2003; Natarajan et al., 1994; Skovborg et al., 1993; Vysniaskas and Bishnoi, 1983). It is the general conception that the nucleation process of gas hydrates has a stochastic nature (Natarajan et al., 1994) and that induction periods are quite hard to reproduce. One reason for this is that the presence of even very small impurities in the hydrate forming system can have drastic influence on the induction time. The reason for this is that the nucleation mechanism of hydrates is primarily heterogeneous (Bishnoi and Natarajan, 1996). However, identification of the important factors affecting the nucleation process of gas hydrates is vital in order to gain understanding of the area.

In this work we investigate the effect that the driving force in terms of supersaturation, has on nucleation of slI propane gas hydrate. The supersaturation is here represented as the difference in the chemical potentials of a hydrate building unit in solution and in the hydrate crystal (Kashchiev and Firoozabadi, 2002a).

We begin by investigating the effect that the magnitude of the driving force has on the induction period of propane hydrate in pure water. The influence of the agitation Reynolds number was subsequently investigated. Finally investigation on how the nucleation period is influenced when a kinetic inhibitor, polyvinylpyrrolidone (PVP), is added to the aqueous phase was performed. The nucleation data are used to investigate different physical properties of propane hydrate like critical size, hydrate–water interfacial energy and hydrate–substrate contact angle. This is done by using a newly described model for the induction time of gas hydrates (Kashchiev and Firoozabadi, 2003).

2. Theory of hydrate nucleation

Nucleation of hydrates is a microscopic stochastic phenomenon where gas–water clusters (nuclei) grow and disperse until the nuclei have grown to a critical size (Natarajan et al., 1994). Primarily hydrate nucleation takes place at the vapor–liquid (V–L_w) interface (Sloan, 1998), thus the theories dealing with describing this phenomenon have focused on this surface. Two theories dealing with describing the nucleation mechanism have gained acceptance in literature although they are hypothetical. One of these is the cluster nucleation theory which proposes that water molecules form labile clusters around dissolved gas molecules. These clusters combine due to hydrophobic bonding between the apolar molecules inside the clusters, to form hydrate unit cells. The other theory assumes that nucleation is taking place on the vapor side at the V–L_w interface. First gas molecules are transported to the interface and adsorbed by the aqueous surface. At suitable adsorption sites water molecules will form first partial and then complete cages around the adsorbed gas molecules. Clusters will join and grow on the vapor side until the critical size is reached.

The time taken from when supersaturation is obtained to the appearance of a hydrate crystal is referred to as the induction period (t_{ind}). The induction period is considered to be made up by several parts. Time is required for the system to relax to achieve a quasi steady-state distribution of molecular clusters, t_r , the formation of stable clusters, t_n , and the growth of these to a detectable size, t_g . Based on these considerations, the induction time can be expressed as (Mullin, 2004):

$$t_{ind} = t_r + t_n + t_g \quad (1.1)$$

However, during the induction period, it is not possible to distinguish these separate quantities from each other.

From observing the pressure–time relationship for a hydrate-forming system the induction time can be identified. In Fig. 1 such a relationship is presented. The initial pressure drop from P_0 to P_{sol} is due to absorption of gas in the aqueous phase. After equilibrium is reached the pressure stabilizes until t equals t_{ind} where a sudden

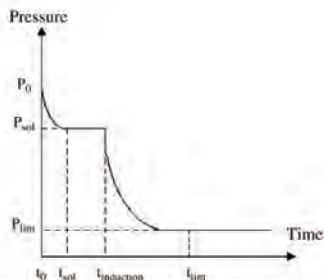


Fig. 1. Illustration of a typical pressure recording for a hydrate forming system. Important parameters which can be deduced from the recording are indicated with dashed lines. The initial pressure drop is due to gas dissolution followed by an isobaric period where nucleation takes place. The sudden pressure drop during the nucleation period is caused by hydrate formation.

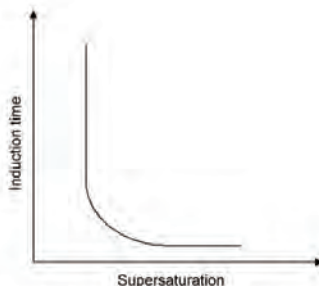


Fig. 2. Stylistic plot of the typical relationship between the induction time and the supersaturation for a gas hydrate nucleating system. When the supersaturation reaches a critical value the induction time increases dramatically.

pressure drop appears as hydrate starts to form. The pressure keeps decreasing as gas is consumed during the hydrate formation process until it reaches P_{lim} where no more hydrate forms. The induction time should be corrected for the initial time taken for gas to dissolve. The induction time is then found as

$$t_{ind}^* = t_{ind} - t_{sol} \quad (1.2)$$

The curve presented here is slightly idealized and deviation from the shape can appear if $t_{ind} < t_{sol}$ or if the gas solubility in water is sufficiently low.

A typical relationship between the induction time and the supersaturation is presented in Fig. 2. At low supersaturation the induction time goes up very sharply (critical region) while it approaches zero at higher supersaturations.

Heterogeneous nucleation plays an important role in the formation of ice (Mullin, 2004) and has been shown also to be thermodynamically favored over homogeneous nucleation of gas hydrates (Kashchiev and Firoozabadi, 2002b). This causes the induction time to be very sensitive to any heterogeneities in solution, i.e. impurities can possibly cause significant deviation among measured induction times.

2.1. Single component driving force

A number of different approaches for calculating the driving force of hydrate nucleation have been described in the literature and summarized by Sloan (1998). We use the definition that the driving force is equal to the difference between the chemical potentials of the old and the new phases upon hydrate formation from an aqueous solution. The expression for the driving force for nucleation of simple hydrates has been described on the basis of the following phase reaction occurring in the aqueous solution (Kashchiev and Firoozabadi, 2002a):



where n_w is the number of water molecules in a hydrate building unit. The resulting expression for the driving force in terms of supersaturation is given below. The derivation of this expression can be found in the work of Kashchiev and Firoozabadi (2002a):

$$\Delta\mu = kT \ln \left(\frac{f(P, T)}{f(P_e, T)} \right) + \Delta v_e (P - P_e) \quad (1.4)$$

where k is Boltzmann's constant, f is the fugacity of the gas in the gas phase and Δv_e is the volume difference between a water molecule in solution and a hydrate building unit in the hydrate lattice. A hydrate building unit is constituted by a single gas molecule and x water molecules, x depending on the hydrate structure. For propane hydrate the volume difference has been reported to be $-1.370 \times 10^{-28} \text{ m}^3$ (Kashchiev and Firoozabadi, 2002a). The fugacities of the gas have been calculated using the SRK equation of state. The three-phase equilibrium pressure has been calculated using the program HYDOFF (Sloan, 2000).

3. Experimental equipment and procedure

3.1. Experimental equipment

The kinetic measurements were performed in a stainless steel hydrate equilibrium cell with a fixed volume of 66.5 cm^3 and a maximum working pressure of 150 bar. The cell allows for visual observation of hydrate formation through two sapphire windows. A safety valve was attached to the cell which opens when pressure exceeds an adjustable value (40–100 bar). The cell is attached to a gas reservoir and a vacuum pump. The temperature in the cell was controlled by circulating coolant (water–ethanol solution), in a jacket surrounding the cell. The temperature was monitored by using a platinum resistance probe ($\pm 0.01 \text{ K}$) placed inside the cell. The pressure of the cell was monitored by a single pressure transducer (BD Sensors, 0–40 bar). The cell was placed on a stir plate which allowed a stirring bar ($L = 4 \text{ cm}$) to rotate within the cell. The pressure and temperature in the cell were recorded continuously on a computer. A schematic layout of the experimental equipment used to investigate gas hydrate nucleation is shown in Fig. 3. The experiments were performed using distilled water, propane with a purity of 99.5 supplied by Intergas (<http://www.intergas.co.uk/>). In the experiments concerning kinetic inhibition of the nucleation process PVP (Mw 10,000) supplied by Sigma-Aldrich was used.

3.2. Experimental procedure

The cell was cleaned with distilled water and loaded with distilled water or distilled water containing PVP. A stirring bar was placed in the cell. The cell lid was screwed on and the cell evacuated using a vacuum pump for approximately 1 h. The temperature bath was adjusted so the temperature in the cell was 273.75 K . When the temperature in the cell was constant the propane gas was injected

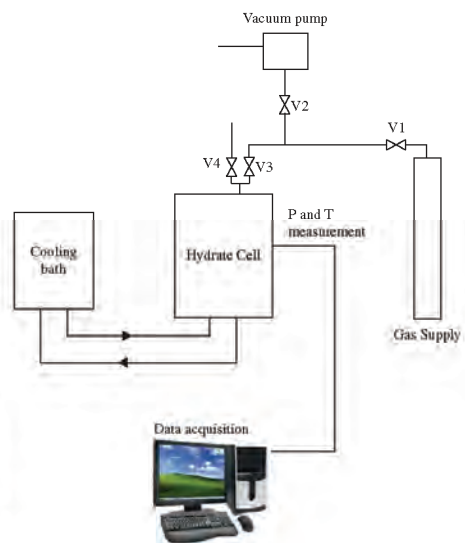


Fig. 3. Layout of experimental equipment used in the study of gas hydrate nucleation. The hydrate cell is attached to a gas supply unit and a vacuum pump. The temperature is controlled by a cooling bath. Data are collected continuously on a computer.

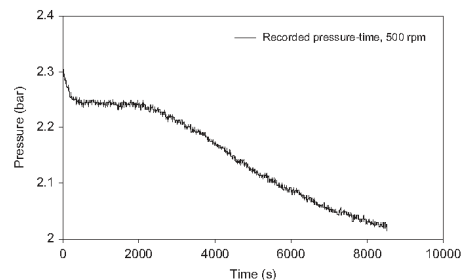


Fig. 4. Typical pressure–time recording for the propane hydrate forming system. The plot is in very good agreement with the idealized plot shown in Fig. 1.

through the inlet until the desired pressure at the chosen temperature was obtained. Three experimental series using distilled water were performed. For each series the stirring rate was altered in the range 200–500 rpm in order to investigate the effect of the stirring rate on the nucleation kinetics. The stirring rate interval will result in agitation Reynolds's numbers varying in the range from 3254 to 8134 found from the following relation:

$$Re_A = \frac{n \cdot D_{\text{imp}}^2 \cdot \rho}{\eta} \quad (1.5)$$

where n is the rotation speed of the impeller (s^{-1}), D_{imp} is the diameter of the impeller, ρ is the density and η is the viscosity of the

Table 1

Results of the nucleation experiments; calculated dissolution rate and supersaturation, measured pressure characteristics, dissolution and induction time at 273.75 K and 500 rpm of agitation

System	rpm	P_0 (bar)	P_{sol} (bar)	t_{sol} (min)	$K_{L-V}a_{L-V}$ (s^{-1})	t_{ind} (min)	$\Delta\mu/kT$
Propane 273.75 K 1.890bar	500	2.140	2.081	7.68	7.5	> 1200	0.73
		2.195	2.113	10.87	5.0	630.6	0.85
		2.193	2.127	10.53	7.2	411.6	0.90
		2.200	2.130	9.11	5.0	408.0	0.91
		2.200	2.133	8.33	7.5	113.4	0.92
		2.208	2.148	6.67	10.0	166.8	0.97
		2.208	2.143	9.02	7.1	217.6	0.96
		2.213	2.155	9.26	6.5	361.8	1.00
		2.223	2.158	5.68	9.0	75.0	1.01
		2.223	2.165	7.76	8.0	101.5	1.03
		2.268	2.185	8.02	6.5	76.7	1.10
		2.268	2.193	6.67	7.5	93.0	1.16
		2.273	2.210	6.93	6.0	39.0	1.19
		2.298	2.223	11.12	6.5	41.2	1.22
		2.306	2.243	5.76	8.0	34.4	1.29
		2.320	2.248	6.02	9.0	41.3	1.32
		2.336	2.271	6.10	8.0	30.6	1.39
		2.366	2.316	7.18	8.0	21.0	1.56
		2.426	2.364	5.60	8.0	14.4	1.69
		2.511	2.441	10.00	3.5	165	1.97
2.576	2.509	7.17	8.0	11.6	2.15		
2.586	2.544	5.35	9.0	8.70	2.24		
2.667	2.592	8.33	8.0	7.20	2.38		

Table 2

Results of the nucleation experiments; calculated dissolution rate and supersaturation, measured pressure characteristics, dissolution and induction time at 273.75 K and 300 rpm of agitation

System	rpm	P_0 (bar)	P_{sol} (bar)	t_{sol} (min)	$K_{L-V}a_{L-V}$ (s^{-1})	t_{ind} (min)	$\Delta\mu/kT$
Propane 273.75 K 1.890bar	300	2.170	2.100	22.87	2.0	> 1200	0.10
		2.200	2.130	25.58	2.2	192.75	0.11
		2.250	2.180	24.17	2.5	100.83	0.13
		2.273	2.195	17.00	2.8	85.48	0.14
		2.298	2.225	23.48	2.8	81.13	0.16
		2.312	2.248	20.90	2.8	61.05	0.17
		2.295	2.210	19.12	3.0	54.22	0.15
		2.340	2.270	18.33	2.7	33.33	0.17
		2.380	2.301	19.61	2.4	32.52	0.19
		2.379	2.298	23.33	2.8	24.62	0.19
		2.351	2.268	16.67	2.8	28.27	0.17
		2.426	2.349	21.67	2.8	22.18	0.21
		2.406	2.326	19.58	2.8	19.58	0.18
		2.430	2.360	18.60	2.8	8.68	0.20
		2.400	2.320	23.00	2.5	11.12	0.22
		2.432	2.365	18.33	3.0	8.95	0.21
		2.582	2.504	18.33	2.5	5.16	0.27

Table 3

Results of the nucleation experiments; calculated dissolution rate and supersaturation, measured pressure characteristics, dissolution and induction time at 273.75 K and 200 rpm of agitation

System	rpm	P_0 (bar)	P_{sol} (bar)	t_{sol} (min)	$K_{L-V}a_{L-V}$ (s^{-1})	t_{ind} (min)	$\Delta\mu/kT$ (min)
Propane 273.75 K 1.890bar	200	2.298	2.220	72.27	0.8	209.00	0.15
		2.340	2.250	53.33	0.9	780.00	0.17
		2.300	2.230	34.28	1.2	118.20	0.16
		2.328	2.253	35.43	1.1	101.36	0.17
		2.33	2.255	40.21	1.1	293.33	0.17
		2.331	2.256	43.33	1.0	92.23	0.17
		2.356	2.278	58.33	0.7	29.41	0.18
		2.373	2.298	30.91	1.3	27.00	0.19
		2.380	2.300	41.67	1.0	91.33	0.19
		2.391	2.310	51.43	0.9	9.0	0.19
		2.404	2.320	53.58	0.8	56.42	0.20
		2.480	2.420	26.67	1.0	13.33	0.24
		2.521	2.442	59.33	0.7	11.20	0.24
		2.610	2.520	31.25	1.0	4.20	0.27

fluid being agitated. The flow will be laminar for numbers lower than 10 and turbulent for numbers above 10,000. The impeller is 4 cm in diameter and the water density and viscosity equals 1000 kg/m³ and 0.000922 kg/(m s). In these cases the flow can be said to be in

the intermediate region between laminar and turbulent, the 500 rpm being very close to turbulent.

For nucleation experiments involving PVP as a kinetic inhibitor two experimental series at PVP concentrations of 0.05 and 0.025 wt%

Table 4

Results of the nucleation experiments; calculated dissolution rate and supersaturation, measured pressure characteristics, dissolution and induction time at 273.75 K and 500 rpm of agitation

System	rpm	P_0 (bar)	P_{sol} (bar)	t_{sol} (min)	$K_{L-V}a_{L-V}$ (s^{-1})	t_{ind} (min)	$\Delta\mu/kT$
Propane 273.75 K 1.890 bar	500	3.89	3.47	15.05	5.00	844.23	0.58
		3.96	3.50	11.53	4.00	878.68	0.58
		4.07	3.66	16.67	5.00	610.00	0.62
		4.13	3.71	8.68	6.20	334.90	0.64
		4.25	3.86	10.62	6.00	318.23	0.67
		4.29	3.94	8.68	5.80	253.52	0.69
		4.39	4.06	7.60	6.50	181.35	0.72
		4.49	4.20	7.50	6.00	131.50	0.75
		4.54	4.11	7.52	5.80	191.25	0.73
		4.59	4.24	7.85	7.00	76.35	0.76
		4.59	4.34	7.35	6.20	82.33	0.78
		4.68	4.50	8.52	6.00	67.25	0.81
		4.76	4.64	5.93	6.00	39.80	0.84
		4.83	4.70	5.00	8.00	22.58	0.85
4.85	4.75	5.00	6.20	30.47	0.86		

The water phase has a PVP concentration of 0.05 wt%.

Table 5

Results of the nucleation experiments; calculated dissolution rate and supersaturation, measured pressure characteristics, dissolution and induction time at 273.75 K and 500 rpm of agitation

System	rpm	P_0 (bar)	P_{sol} (bar)	t_{sol} (min)	$K_{L-V}a_{L-V}$ (s^{-1})	t_{ind} (min)	$\Delta\mu/kT$
Propane 273.75 K 1.890 bar	500	3.11	2.73	25.83	2.0	885.22	0.35
		3.18	2.85	9.02	8.0	520.04	0.39
		3.19	2.87	10.87	7.0	682.33	0.40
		3.21	2.85	16.63	5.0	486.33	0.39
		3.24	2.93	12.95	6.5	534.30	0.42
		3.27	3.05	5.93	8.5	109.27	0.46
		3.30	2.91	8.33	8.5	496.22	0.41
		3.35	3.15	5.00	8.5	25.88	0.49
		3.36	3.20	7.10	8.0	40.60	0.50
		3.36	3.08	7.35	7.0	166.60	0.46
		3.46	3.29	5.77	7.0	32.73	0.53
		3.52	3.30	6.77	7.0	19.88	0.53
		3.56	3.45	16.67	3.0	38.75	0.57
		3.65	3.45	4.17	9.0	16.18	0.57
		4.24	4.07	4.17	7.0	7.00	0.72
		4.56	4.40	5.10	9.0	5.43	0.79

The water phase has a PVP concentration of 0.025 wt%.

were performed both at a stirring rate of 500 rpm. In all the experiments the pressure and temperature was recorded in a time interval of 5 s. The data obtained in an experimental run can typically be represented from the pressure–time relationship provided in Fig. 4. As seen it is in quite good agreement with the idealized schematic provided in Fig. 1.

4. Results and discussion

A series of 54 experiments investigating how the driving force, $\Delta\mu/(kT)$, influences the nucleation period of propane hydrate and investigating the role of the stirring rate has been performed. The series investigating the role of PVP in connection to propane hydrate nucleation involved in total 31 experiments. P_0 , t_{sol} , P_{sol} and t_{ind}^* for each experiment have been extracted from the recorded data. $\Delta\mu/(kT)$ was calculated at $P=P_{sol}$. The results for all series are summarized in Tables 1–5. In these tables the gas dissolution rate, $K_{L-V}a_{L-V}$ has also been provided.

In Figs. 5 and 6 the induction times have been plotted against the supersaturation for the different stirring rates and at two different PVP concentrations, respectively.

From Fig. 5 the nucleation periods can be seen to be more or less independent of the stirring rate when this is varied in the range of 300–500 rpm. The consistency in the data is quite well, i.e. the data follows the typical pattern of Fig. 2. However for the lower stirring rate this tendency is not as regular, i.e. there is quite some scattering

among the data points. This indicates that in case of less convection, the system will act more randomly which could be due to lower $V-L_w$ interfacial area or a less favorable distribution of gas in the bulk liquid phase.

Tables 1–3 show that the time from the initial loading of the gas until growth is observed ($t_{sol}+t_{ind}$) depends on the stirring rate. This is due to differences in the time required for gas to dissolve into the bulk water, i.e. gas dissolution time decreases with increasing stirring rate. This demonstrates that as turbulence intensity increases, so does mass-transfer velocity (Xu et al., 2006).

When PVP is added in even very small amounts the induction time/supersaturation relationship is shifted to the right as can be observed from Fig. 6. There seems to be quite steady agreement among the two data sets, i.e. the higher PVP concentration data are shifted to the right with approximately the same value in the $\Delta\mu$ range investigated compared to the data for the lower PVP concentration.

The dissolution rate at the $V-L_w$ interface has been determined from the two film theory neglecting the resistance on the gas side of the $V-L_w$ interface using the following expression:

$$\left(\frac{dx}{dt}\right) = K_{L-V}^i a_{L-V} (x_{L-V}^i - x) \quad (1.6)$$

where x_{L-V}^i is the gas solubility of the hydrate former in the liquid phase at the $V-L_w$ interface at T_{exp} and P_{exp} and a_{L-V} is the vapor–liquid interfacial area per volume of dispersion (A_{L-V}/V_L).

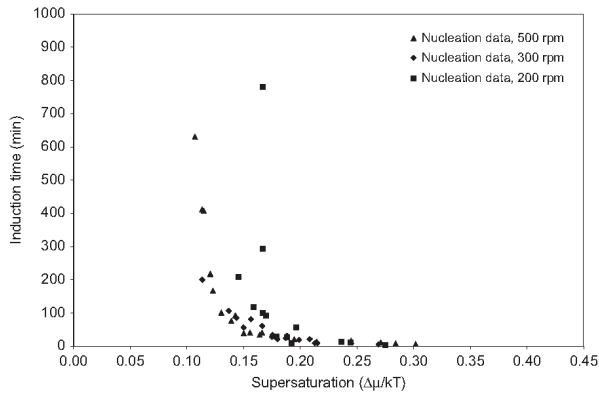


Fig. 5. Plot of nucleation period vs. driving force at 273.75 K for propane hydrate at different stirring rates. The induction times measured at stirring rates of 500 and 300 rpm are very similar. At 200 rpm more scattering among the measured induction times is observed. At this stirring rate the induction times are also seen to be prolonged compared to those measured at 300 and 500 rpm.

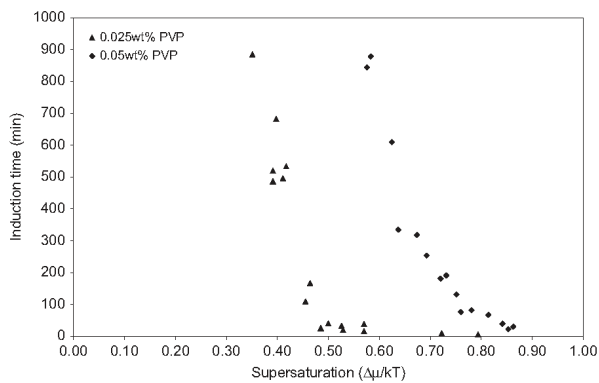


Fig. 6. Plot of nucleation period vs. driving force at 273.75 K for propane hydrate for two different concentrations of PVP and a stirring rate of 500 rpm. PVP is seen to cause longer induction times compared to nucleation of propane hydrate from a pure aqueous phase. When the concentration of PVP is increased the induction time of propane hydrate is increased.

Integrating from $x=x_0$ at t_0 to the equilibrium concentration $x=x_{\text{sol}}$ at t_{sol} yields the final expression:

$$\ln \left(\frac{x_{L-V}^i - x_{\text{sol}}}{x_0 - x_{\text{sol}}} \right) = -k_{L-V}^i a_{L-V} t \quad (1.7)$$

All variables in Eq. (1.7) were obtained experimentally except for the dissolution rate which was calculated using a least-square analysis. The mole fraction of propane gas dissolved in water was in all cases calculated using the fugacity of the pure component in the vapor phase and Henry's constant:

$$x_i = \frac{f_i(p_{\text{exp}}, T_{\text{exp}})}{H_{iW}} \quad (1.8)$$

Henry's constant was calculated using the empirical expression found by Chapoy et al. (2004):

$$\ln(H_{iW})(\text{KPa}) = 552.64799 + 0.078453T - \frac{21,334.4}{T} - 85.89736 \ln(T) \quad (1.9)$$

It was assumed that the addition of PVP did not have any impact on the magnitude of Henry's constant as the concentration was very low.

From Tables 1–5 it is seen that different values for the dissolution rate were obtained for different stirring rates. The reason for this is primarily due to the difference in the interfacial area at different stirring rates. From observing the dissolution rates in Tables 1–5 it can be seen that they are more or less independent of

pressure in the pressure range investigated. The average values are listed in Table 6 along with the calculated Reynolds numbers. When the Reynolds number increases so does the dissolution rate. Addition of PVP causes the dissolution rate to lower slightly, the higher concentration causing the dissolution rate to decrease most. The Reynolds numbers are in the intermediate range between laminar and turbulent, the 500 rpm being very close to turbulence. However, as the number only refers to the conditions in the vicinity of the impeller, it does not give any indication of how well the water surface is stirred nor how good contact between water and gas there is. From a visual point of view 200 rpm corresponds to a situation where a vortex on the water surface has just appeared and 500 rpm corresponds to a vigorous mixing of the complete water phase.

The dissolution rate of propane gas in distilled water has been plotted as a function of the agitation Reynolds number and can be seen in Fig. 7. It is assumed that the dissolution rate will be very small at zero agitation, thus $K_{L-V}^i a_{L-V} = 0$ at $Re_A = 0$. From the plot it is seen that the data follow a second-order polynomial.

A dissolution rate ($K_{L-V}^i a_{L-V}$) of $2.15 \times 10^{-3} \text{ s}^{-1}$ at 150 kPa, 274.2 K and 750 rpm using a similar approach to the one used here has been reported in literature (Bergeon and Servio, 2007). This value is slightly less compared to the findings here. However, using an iterative procedure they optimized the dissolution rate and found a value of $1.73 \times 10^{-2} \text{ s}^{-1}$. This value is in better agreement with the findings in this work taking into account that the stirring rate they use is faster. Using the polynomial trend line the obtained dissolution rate at 750 rpm will be $1.70 \times 10^{-2} \text{ s}^{-1}$.

To summarize the conclusions that can be made from the nucleation experiments: The stirring rate is primarily of importance for the dissolution rate of propane gas—the induction period is not influenced significantly by the stirring rate. This tendency is especially evident for the two higher stirring rates, 300 and 500 rpm, where

the water surface is highly disturbed. In these cases similar induction periods are obtained even though a difference in the dissolution rate can be observed. For a stirring rate of 200 rpm which causes the water surface to rotate slowly the induction periods are shifted slightly to higher supersaturations compared to the experiments using a higher stirring rate. This is especially true in the range of the critical supersaturation where the induction time increases rapidly. At higher supersaturations where the induction time comes close to zero the stirring rate seems to have less influence on induction times. Using a stirring rate of 200 rpm also result in slightly more scattering in the measured induction times compared to the results obtained at higher stirring rates. PVP was found to decrease the dissolution rate of propane gas in water, and also showed quite active toward shifting the induction time/supersaturation relationship to higher supersaturations.

5. Surface energy and volumetric properties of propane hydrate

In this section we use the obtained nucleation data to calculate the effective surface energy of the propane hydrate/water interface. The size of the critical nucleus, i.e. the size of the hydrate nucleus just before it starts to grow has been determined also from the nucleation data.

Different models to describe the nucleation process and in particular the induction period have been presented in the literature. Most of these are based on crystal growth theory in which the fitting parameters often are found to be system specific (Mullin, 2004; Natarajan et al., 1994). More recently an induction time model has been proposed by Kashchiev and Firoozabadi (2003). The model is also based on crystallization theory thus accounts for proportionality between the induction time and the nucleation rate. Also the model assumes that progressive nucleation is taking place, i.e. hydrate crystallites are continuously nucleated during the process. The model can be expressed as

$$t_i = K e^{-\Delta\mu/kT} (1 - e^{-\Delta\mu/kT})^{-3m/(1+3m)} \times \exp\left[\frac{4c^3 v_h^2 \sigma_h^3}{27(1+3m)kT\Delta\mu^2}\right] \quad (1.10)$$

in which K is a kinetic constant, $\Delta\mu$ is the supersaturation, k is Boltzmann's constant, T is the temperature, m is a number that relates to the growth type, c is a shape factor, v_h is the volume of a

Table 6
Reynolds numbers and dissolution rates for the different experimental series

Stirring rate	Re_A	$K_{L-V}^i a_{L-V} (\times 10^3 \text{ s}^{-1})$
500	8134	7.38
300	4881	2.66
200	3254	0.96
500 (0.05 wt% PVP)	8134	5.98
500 (0.025 wt% PVP)	8434	6.94

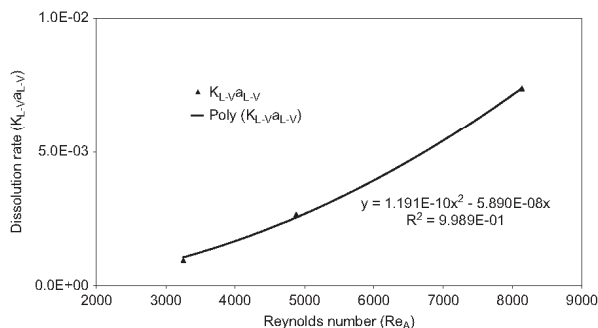


Fig. 7. Dissolution rate of propane in distilled water as a function of the agitation Reynolds number. The dissolution rate is seen to follow a second-order polynomial trend in the agitation Reynolds number interval investigated here.

hydrate building unit and σ_{ef} is the effective surface energy between hydrate and solution. For a thorough explanation of this expression see Kashchiev and Firoozabadi (2003).

In order to assess the interfacial properties of the hydrate forming system, i.e. the effective surface energy between hydrate and solution, and the hydrate substrate contact angle (1.10) is linearized. This is done by substituting the following expression into Eq. (1.10):

$$B = \frac{4c^3 v_h^2 \sigma_{ef}^3}{2l(kT)^3} \quad (1.11)$$

The supersaturation can be represented as the supersaturation ratio, S :

$$S = \left[\frac{\varphi(P, T)P}{\varphi(P_e, T)P_e} \right] \cdot \exp \left[\frac{\Delta v_e (P - P_e)}{kT} \right] \quad (1.12)$$

Using Eq. (1.12) as the driving force, Eq. (1.10) can be expressed on the following form:

$$t_i = K[S(S-1)^{3m}]^{-1/(1+3m)} \cdot \exp \left[\frac{B}{(1+3m) \ln^2 S} \right] \quad (1.13)$$

This expression is appropriate for plotting induction times against supersaturation ratios whereby B and K can be obtained from a regression as the slope and the intercept.

If growth by volume diffusion of dissolved gas, through a stagnant layer formed around the nucleus is assumed then $m = 1$ (Kashchiev and Firoozabadi, 2003). Hereby Eq. (1.13) becomes

$$\ln[S^{1/4}(S-1)^{3/4}t_i] = \ln K + \frac{B}{4 \ln^2 S} \quad (1.14)$$

5.1. Propane hydrate properties

Using Eq. (1.14) the dependence of the induction time on the supersaturation ratio for propane hydrate has been investigated. The results using the experimentally obtained induction periods at different supersaturation ratios at a stirring rate of 500 rpm and the best linear fit are presented in Fig. 8.

The intercept and the slope of the best fit allows for determination of the constants K and B as $\ln(K) = 4.8746$ and $B/4 = 0.044$ according to Eq. (1.14) thus it follows that $K = 130.92$ s (1.1080) and $B = 0.1764$ (0.0082). The values in parenthesis state the standard error of K and B , respectively.

The magnitude of K is rather high for a process taking place on a molecular level; however it is likely that it indicates that nucleation

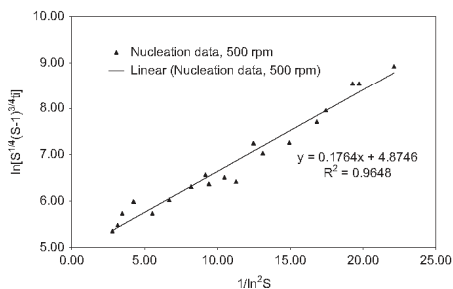


Fig. 8. Linearized dependence of the induction time on the supersaturation ratio for nucleation of propane hydrate in aqueous solution at $T = 273.75$ K and 500 rpm. A very low degree of scattering in the measured data can be observed.

is following a polynuclear crystallization mechanism and that heterogeneous nucleation is taking place. For an operative mononuclear mechanism and homogeneous nucleation very low K values would be expected, < 5 ns (Kashchiev and Firoozabadi, 2003).

Previously it has been demonstrated that heterogeneous nucleation of cap-shaped hydrate clusters on hydrate wetted solid surfaces in solution is thermodynamically favored over homogeneous nucleation (Kashchiev and Firoozabadi, 2002a). From Eq. (1.11) the hydrate–solution effective surface energy can be calculated by inserting $c^3 = 36\pi$ for cap-shaped hydrate nuclei on solid substrate, $v_h = 0.647 \times 10^{-27}$ m³ which is the volume of a propane hydrate building unit, thus it follows that $\sigma_{ef} = 1.11$ mJ/m². This low effective surface energy indeed implies a heterogeneous nucleation mechanism is taking place as for homogeneous nucleation a surface energy of 20 mJ/m² between water and ice would be expected (Dufour and Defay, 1963). For heterogeneous nucleation in general σ_{ef} is given as

$$\sigma_{ef} = \psi \sigma \quad (1.15)$$

The shape factor ψ can then be determined to be 0.055. The expression for this factor for cap-shaped clusters is given as

$$\psi = \left[\left(\frac{1}{4} \right) (2 + \cos \theta) (1 - \cos \theta)^2 \right]^{1/3} \quad (1.16)$$

Using this expression it follows that the contact angle between the hydrate and the hydrate wetted solid is equal to 10°.

The number of building units that constitutes the hydrate nucleus can be calculated using the following expression:

$$n^* = \frac{2B}{\ln^3 S} \quad (1.17)$$

The number of building units constituting the hydrate nucleus in the supersaturation ratio range of 1.35–1.11 has been found to be 13–294. Using the stoichiometric formula for propane hydrate (C₃H₈·17H₂O) this means that the smallest propane hydrate nuclei will consist of 237 molecules. The size of the critical nucleus can be found from the relation (Anklam and Firoozabadi, 2004)

$$R^* = \frac{2\sigma n_w v_{hw}}{\Delta g} \quad (1.18)$$

v_{hw} is the molecular volume of water in the hydrate (hydrate unit cell volume divided by the number of water molecules in the unit cell) and n_w is the number of water molecules in a hydrate unit cell. Δg for simple hydrate forming systems is given by

$$\Delta g = n_i(T, P_e, y)kT \ln \left[\frac{f_{gi}(T, P, y)}{f_i(T, P_e, y)} \right] + \Delta v_e(P - P_e) \quad (1.19)$$

n_i being the number of gas molecules in the unit cell. Given these relations the critical radius of the hydrate nuclei has been determined to vary between 1.70 and 4.70 nm for S in the interval of 1.35–1.11. These values are slightly lower than the critical radii of methane and ethane hydrate for homogeneous nucleation (Englezos et al., 1987), thus agrees with the nucleation theory and also indicates heterogeneous nucleation.

In contradiction to these findings the critical radius of propane hydrate at $S = 1.26$ and $T = 274.1$ K has been reported to be 56.5 nm (Bergeon and Servio, 2007). This finding is based on measuring the particle size at the onset of hydrate growth using a particle size analyzer. As the system is likely to contain small impurities the value measured experimentally comprises both the hydrate layer and the impurity. In other words, the value reported is that of the hydrate layer and the impurity located underneath thus not comparable with the value which can be calculated from Eq. (1.18).

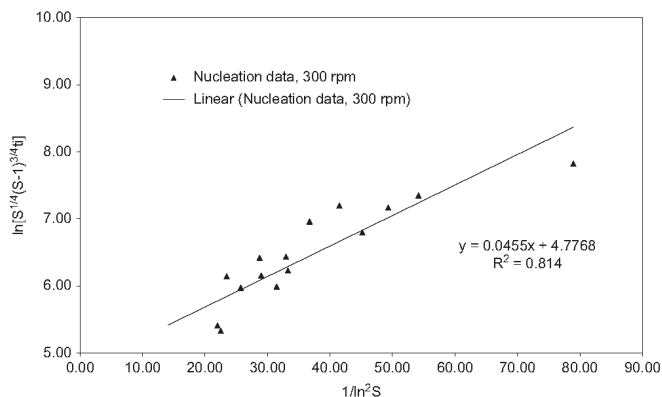


Fig. 9. Linearized dependence of the induction time on the supersaturation ratio for nucleation of propane hydrate in aqueous solution at $T = 273.75\text{ K}$ and 300 rpm. More scattering in the data compared to the measured data at 500 rpm can be observed.

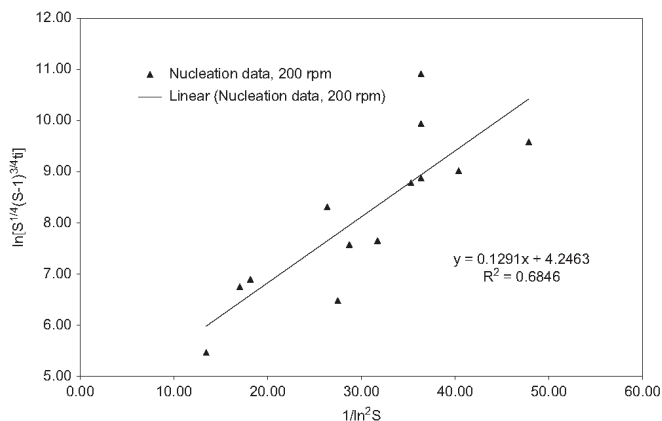


Fig. 10. Linearized dependence of the induction time on the supersaturation ratio for nucleation of propane hydrate in aqueous solution at $T = 273.75\text{ K}$ and 200 rpm. A rather high degree of scattering among the measured data is observed indicating more stochastic nature of nucleation at low stirring rate.

The effect of the stirring rate on these properties of propane hydrate has been investigated using the two data sets at lower stirring rates. In Figs. 9 and 10 the linearized plots at 200 and 300 rpm are presented.

The induction time model parameters, critical number of building units, critical nucleus radius for the supersaturation ratio interval investigated, the hydrate–solution effective surface energy and the hydrate–substrate contact angles are all presented in Table 7 at the different stirring rates. The model parameters obtained are deviating slightly from each other. When the stirring rate is decreased K decreases however most pronounced when going from 300 to 200 rpm. The opposite trend is seen for the B -values, thus also for the effective surface energy. The standard error of the model parameters also

increases when the stirring rate is lowered thus indicating that the lower stirring rate causes the system to act more stochastic.

The surface energy in nucleation processes can in general be regarded as a dynamic surface energy and not an equilibrium surface energy (Rasmussen, 1986). This means that the surface energy is likely to be depending on diffusion of gas molecules in the bulk and geometry of the nuclei surfaces. Equilibrium conditions are reached more rapid in fast stirred systems compared to stagnant systems. This suggests that the interfacial tension in the case of 500 rpm is closer to a given equilibrium interfacial tension compared with the interfacial tensions at 300 and 200 rpm. As seen this is the actual case as the higher stirring rate interfacial tension is also attaining the lowest value.

Table 7
Induction model parameters, hydrate–solution effective surface energy, hydrate–substrate contact angle

rpm	S	n^*	R^* (nm)	K (s)	B	σ_{ef} (mJ/m ²)	Angle (°)
500	1.11–1.36	294–13	4.1–1.50	130.92 (1.11)	0.176 (0.008)	1.11	10
300	1.12–1.31	255–19	3.9–1.68	118.73 (1.25)	0.182 (0.023)	1.12	10
200	1.16–1.31	341–55	4.35–2.34	69.85 (2.32)	0.516 (0.107)	1.58	13

Numbers in parenthesis indicates the standard error.

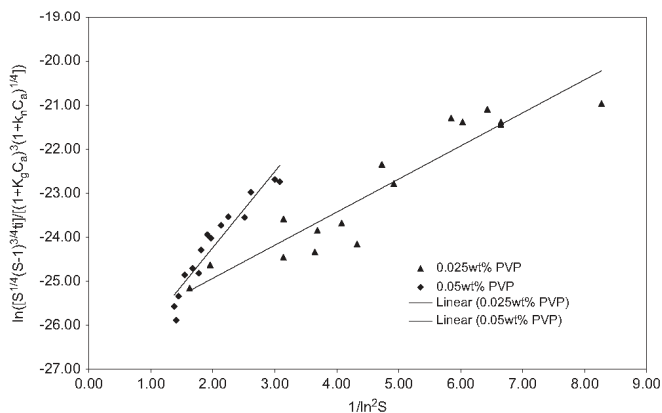


Fig. 11. Linearized dependence of the induction time on the supersaturation ratio for nucleation of propane hydrate in aqueous solutions containing PVP at $T = 273.75$ K and 500 rpm. When the PVP concentration is increased the slope is increased while the intercept decreases.

In literature the water–propane hydrate interfacial tension has been reported to be 25 mJ/m² from fitting experimental phase equilibrium data to the Gibbs–Thompson equation (Uchida et al., 2002). Oppositely the water–CO₂ hydrate interfacial tension has been reported to be 1.5 mJ/m² using an approach much similar to the one used in this work and in much better agreement with the value found here (Zatsepina and Buffett, 2002).

As a consequence of the slight increase in the effective surface energy between water and hydrate the critical radius will also increase slightly. The contact angle is not influenced significantly by the stirring rate and in general the overall influence of the stirring rate on the nucleation period can be regarded as minor.

5.2. Effect of PVP on the propane hydrate properties

Different mechanisms of hydrate inhibition using kinetic inhibitor molecules have been suggested (Armandi et al., 2005; Rodger et al., 1996; Storr et al., 2004). A hypothesis based on a lock-and-key model has been proposed stating that adsorption of shape-specific compounds onto the hydrate crystal surface prevents further growth (Storr and Rodger, 2000). Kinetic inhibitors are not only able to inhibit the growth of gas hydrates but also to prolong the induction times. The mechanism behind this is not likely to be due to adsorption of the molecules on the nuclei surface because the lifetime of the nuclei is too short for the additive to reach them by diffusion and because their surface area is too small (van der Leeden et al., 1993).

The effective surface energy and the size of the critical nuclei were calculated for the system containing PVP. This was done by

introducing a term taking into account adsorption of molecules on nucleation sites and the surface of growing hydrate to Eq. (1.13). Expression (1.13) thereby becomes

$$t_i = K[(1 + k_g C_d)^{3m}(1 + k_n C_d)^{1/(1+3m)}] \times [S(S-1)^{3m}-1/(1+3m)] \cdot \exp\left[\frac{B}{(1+3m)\ln^2 S}\right] \quad (1.20)$$

where k_g and k_n (m³) are adsorption constants and C_d (molecules/m³) is the concentration of the additive in solution. This expression is valid for additive molecules that (1) do not adsorb on the surface of the hydrate nuclei, but adsorb on the surface of the growing hydrate crystallites, (2) do not provide new nucleation sites in the system and (3) block existing nucleation sites by adsorbing at the solution/gas interface or onto the surface of the nucleation-active microparticles and solid substrates present in the solution (Kashchiev and Firoozabadi, 2003). This expression is likewise rearranged to a form that is suitable for regression:

$$\ln\left[\frac{S^{1/4}(S-1)^{3/4}t_i}{(1+k_g C_d)^3(1+k_n C_d)^{1/4}}\right] = \ln K + \frac{B}{4\ln^2 S} \quad (1.21)$$

The result of using the linearized induction time model for the data obtained in the nucleation experiments with PVP are shown in Fig. 11. Exemplary values of $k_g = k_n = 10^{-18}$ m³, also reported elsewhere in literature (Kashchiev and Firoozabadi, 2003) have been used. As seen there is a reasonable good linear relationship for the two data sets. The regressed K and B parameters, the calculated

Table 8
Induction model parameters, hydrate–solution effective surface energy, hydrate–substrate contact angle based on PVP inhibited experiments

rpm	C_{PVP}	S	n^*	R^* (nm)	K (s)	B	σ_{ef} (mJ/m ²)	Angle (°)
500	0	1.11–1.36	294–13	4.1–1.50	130.92 (1.11)	0.176 (0.008)	1.11	10.0
500	1.50×10^{22}	1.42–2.19	143–12	3.33–1.57	3.31×10^{-12} (1.45)	3.010 (0.297)	2.85	20.4
500	3.51×10^{22}	1.77–2.35	75–22	2.76–1.93	9.44×10^{-13} (1.38)	6.910 (0.607)	3.76	25.2

Numbers in parenthesis indicates the standard error.

effective surface energies, the hydrate substrate contact angle and the critical radii of the nuclei are given in Table 8.

The addition of PVP to the aqueous phase causes the kinetic constant K to decrease substantially compared to the K value when PVP is absent. When homogeneous nucleation is taking place a K value of 5 ns would be expected however the presence of PVP is here seen to cause even smaller values of K . The B parameter has on the opposite increased compared to the B value when no PVP is present. When the PVP concentration is increased the B parameter also increases. This implies that adsorption of PVP on hydrate nuclei does not take place as this would result in a decrease of the surface energy according to the equilibrium adsorption theory. The explanation of why B increases when PVP is added could be various. It is possible that the contact angle between the hydrate nuclei and substrate is influenced if for example PVP adsorbs onto the nucleation sites on the substrate. This would be in agreement with the third consideration listed above. Accordingly from Eq. (1.16) it can be seen that for this to be true the contact angle should increase when PVP is added. Another reason could be that the additive is a second type of nucleation site being less active compared to the original heterogeneous nucleation sites. The effective surface energy of the nuclei that forms on this type of substrate could indeed be different from that of nuclei forming on the original substrate. In fact if the substrate is less active this will result in a higher surface energy (van der Leeden et al., 1993). Following it would result in an increase of the nuclei sizes which indeed are also observed. It was found that at $S=1.77$ the critical radius was 2.76 and 2.11 nm for the 0.05 and 0.025 wt% PVP solution, respectively. As the model does not account for molecules that themselves acts as nucleation sites this last consideration should be perceived only as a suggestion for the inhibiting mechanism of additives like PVP.

6. Conclusion

We have shown that the induction time of propane hydrate is only influenced to some degree by a change in the stirring rate. Especially the induction times measured at very low stirring rates are expected to exhibit poorer reproducibility and will be slightly prolonged compared to induction times measured under well-agitated conditions. On the other hand, a notable difference in the propane dissolution rate was observed when the stirring rates were varied. Correlation of the measured induction times to an induction time model developed from crystallization theory revealed that the stirring rate is likely to influence the effective hydrate–solution surface energy, i.e. higher stirring rates give lower surface energies. This was especially observed when comparing well agitated with poor agitated systems. The value of the surface energy between hydrate and water was found to highly depend on the way it was calculated—surface energies calculated using kinetic information were found to be much lower compared to surface energies calculated from phase equilibrium data. Addition of a very small amount of PVP to the aqueous phase caused the induction times to be prolonged quite substantially. The induction times were correlated to an induction time model taking into account the presence of additives. The

results revealed that the prolongation was likely to be due to a change in the nuclei–substrate contact angle.

Notation

c	shape factor
C_d	concentration
D	diameter
f	fugacity
Δg	supersaturation, nucleus
H	Henry's constant
k	Boltzmann's constant
K	kinetic constant
$K_{g,n}$	adsorption constants
K_{L-V}/a_{L-V}	gas dissolution rate
m	growth type number
n	rotation speed
n^*	number of building units constituting the hydrate nucleus
n_w	number of water molecules in a hydrate unit cell
P	pressure
R^*	critical radius of nucleus
Re	Reynolds number
S	supersaturation ratio
t	time
T	temperature
v_h	volume of hydrate building unit
v_{hw}	molecular volume of water in the hydrate
Δv_e	volume difference between water molecule and hydrate building unit
x	gas solubility

Greek letters

η	viscosity
θ	contact angle
$\Delta\mu$	supersaturation, building unit
ρ	density
σ	surface energy
ψ	shape factor

Acknowledgments

The authors would like to thank the Danish Research Council for Technology and Production Sciences for financial support through the project "Gas Hydrates—from Threat to Opportunity" and the Technical University of Denmark for financial support through a Ph.D. scholarship.

References

- Anklam, M.R., Firoozabadi, A., 2004. Driving force and composition for multicomponent gas hydrate nucleation from supersaturated aqueous solutions. *Journal of Chemical Physics* 121, 11867–11875.

- Armandi, M., Ren, S.R., Tohidi, B., 2005. Anti-agglomerant and synergism effect of quaternary ammonium zwitterions. In: Proceedings of the Fifth International Conference on Gas Hydrates, Trondheim.
- Bergeon, S., Servio, P., 2007. Intrinsic kinetics of propane hydrate formation. In: Proceedings of the 11th International Conference on Properties and Phase Equilibria for Product and Process Design, Crete, Greece.
- Bishnoi, P.R., Natarajan, V., 1996. Formation and decomposition of gas hydrates. *Fluid Phase Equilibria* 117, 168–177.
- Chapoy, A., Mokroui, S., Valtz, A., Richon, D., Mohammadi, A.H., Tohidi, B., 2004. Solubility measurement and modeling for the system propane–water from 277.62 to 368.16 K. *Fluid Phase Equilibria* 226, 213–220.
- Dufour, L., Defay, R., 1963. Thermodynamics of Clouds. Academic Press, New York.
- Englezos, P., Kalogerakis, N., Dholabhai, P.D., Bishnoi, P.R., 1987. Kinetics of formation of methane and ethane gas hydrates. *Chemical Engineering Science* 42, 2647–2658.
- Kashchiev, D., Firoozabadi, A., 2002a. Driving force for crystallization of gas hydrates. *Journal of Crystal Growth* 241, 220–230.
- Kashchiev, D., Firoozabadi, A., 2002b. Nucleation of gas hydrates. *Journal of Crystal Growth* 243, 476–489.
- Kashchiev, D., Firoozabadi, A., 2003. Induction time in crystallization of gas hydrates. *Journal of Crystal Growth* 250, 499–515.
- Kelland, M., 1995. Studies on new gas hydrate inhibitors. SPE 30420, pp. 531–539.
- Mullin, J.W., 2004. Crystallization. Elsevier-Butterworth Heinemann, London.
- Munck, J., Jørgensen, S., Rasmussen, P., 1988. Computations of the formation of gas hydrates. *Chemical Engineering Science* 43, 2662–2672.
- Natarajan, V., Bishnoi, P.R., Kalogerakis, N., 1994. Induction phenomena in gas hydrate nucleation. *Chemical Engineering Science* 49, 2075–2087.
- Ng, H.J., Robinson, D.B., 1976. Measurement and prediction of hydrate formation in liquid hydrocarbon–water systems. *Industrial & Engineering Chemistry Fundamentals* 15, 293–298.
- Parrish, W.R., Prausnitz, J.M., 1972. Dissociation pressures of gas hydrates formed by gas mixtures. *Industrial & Engineering Chemistry Process Design and Development* 11, 26–35.
- Rasmussen, D.H., 1986. Dynamic surface tension and classical nucleation theory. *Journal of Chemical Physics* 85, 2272–2276.
- Rodger, P.M., Carver, T., Drew, M.G.B., 1996. Characterisation of the (111) growth planes of a type II gas hydrate and study of the mechanism of kinetic inhibition by poly(vinylpyrrolidone). *Journal of the Chemical Society-Faraday Transactions* 92, 5029–5034.
- Skovborg, P., Rasmussen, P., Mohn, U., 1993. Measurement of induction times for the formation of methane and ethane gas hydrates. *Chemical Engineering Science* 48, 445–453.
- Sloan, E.D., 1998. Clathrate Hydrates of Natural Gases. Marcel Dekker, New York.
- Sloan, E.D., 2000. Hydrate Engineering. SPE Inc., Texas.
- Sloan, E.D., Lederhos, J.P., Long, J.P., Sum, A., Christiansen, R.L., 1996. Effective kinetic inhibitors for natural gas hydrates. *Chemical Engineering Science* 51, 1221–1229.
- Storr, M.T., Rodger, P.M., 2000. A molecular dynamics study of the mechanism of kinetic inhibition. *Annals of the New York Academy of Sciences* 912, 669–677.
- Storr, M.T., Taylor, P.C., Monfort, J.P., Rodger, P.M., 2004. Kinetic inhibitor of hydrate crystallization. *Journal of the American Chemical Society* 126, 1569–1576.
- Uchida, T., Ebinuma, T., Takeya, S., Nagao, J., Narita, H., 2002. Effects of pore sizes on dissociation temperatures and pressures of methane, carbon dioxide, and propane hydrates in porous media. *Journal of Physical Chemistry B* 106, 820–826.
- van der Leeden, M.C., Kashchiev, D., van Rosmalen, G.M., 1993. Effect of additives on nucleation rate, crystal growth rate and induction time in precipitation. *Journal of Crystal Growth* 130, 221–232.
- Vysniaskas, A., Bishnoi, P.R., 1983. A kinetic study of methane hydrate formation. *Chemical Engineering Science* 38, 1061–1072.
- Xu, Z.F., Khoo, B.C., Carpenter, K., 2006. Mass transfer across the turbulent gas–water interface. *AIChE Journal* 52, 3363–3374.
- Zatsepin, O.Y., Buffett, B.A., 2002. Nucleation of CO₂-hydrate in a porous medium. *Fluid Phase Equilibria* 200, 263–275.

Appendix IV

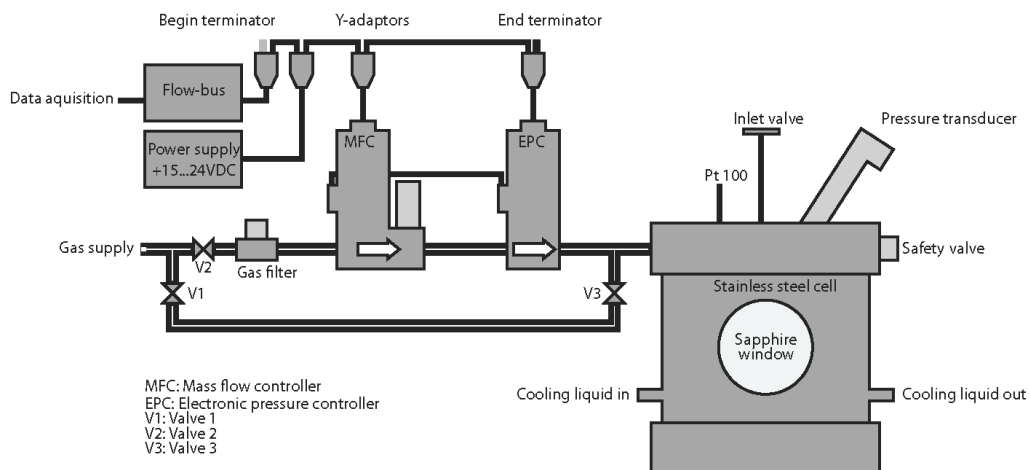
Apparatus operations

This section is a guideline for operating the experimental set-up for measurement of gas hydrate growth rates. The set-up consists of a high-pressure stainless steel cell attached to an electronic back-pressure and mass-flow control system. The idea behind this set-up is to measure the formation rate of gas hydrates at constant pressure and temperature by measuring the amount of gas consumed by the hydrate over time.

Equipment and instruments

The experimental set-up consists of a high-pressure stainless steel cell with two sapphire windows. The temperature of the cell is controlled by circulating coolant from a cooling bath through a cooling jacket surrounding the cell. The cell lid which can easily be detached is connected to a pressure transducer, a temperature probe and a safety valve. The cell lid is also connected to an electronic pressure controller (Bronkhorst Technologies, EI-Press, P-512C-100A-RGD-22-V) and a digital thermal mass flow meter (Bronkhorst Technologies, EI-Flow, F-211CV-020-RGD-22-Z). Brochures describing in detail the specifications of the instruments and the technology they rely on can be downloaded from Bronkhorst's homepage.ⁱⁱ The thermal mass flow meter is connected to a gas filter which is attached by a thin steel tube to a gas reservoir. The gas can also bypass the mass flow meter and pressure controller by closing valve 2 and opening valve 1 and 3. This is necessary during start-up as will be explained later. A schematic of the set-up can be seen below.

ⁱⁱ http://www.bronkhorst.com/en/downloads/brochures_and_leaflets/



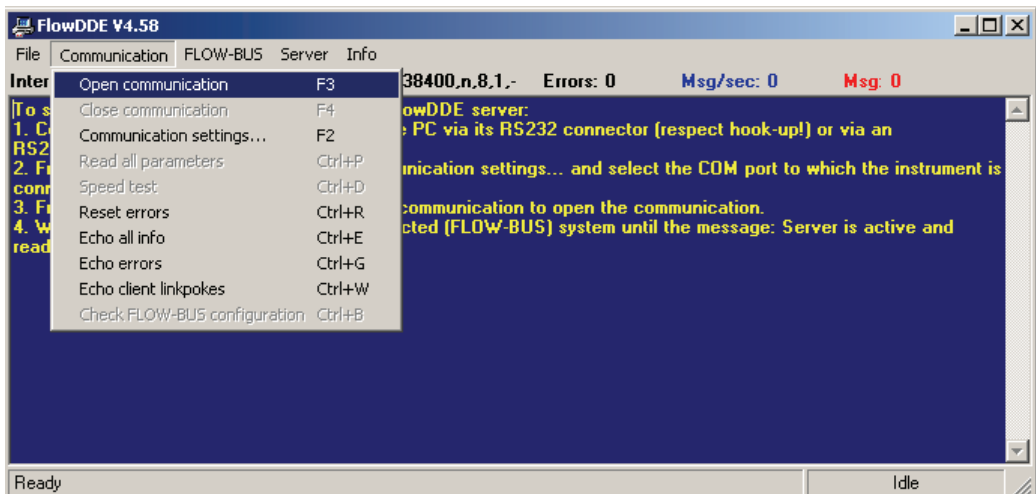
The pressure controller and the mass flow meter are connected to the flow-bus interface module through RJ45 Y-adaptor cables. The flow-bus is connected through a RS232 to a computer enabling communication between the two instruments and the computer. In the Y-adaptor cable attached to the flow-bus interface a begin terminator is placed in the RJ45 sockets which is not used and likewise an end terminator is placed in the free RJ45 socket of the Y-adaptor attached to the pressure controller. The pressure controller and the mass flow meter are connected directly to each other through a Sub-D9 cable. It is thus possible to operate the pressure controller as a master while the mass flow meter can be used as a slave. The advantage of such an instrument configuration in this type of experiment will be explained later. Power supply (+15...24VDC) is hooked on the Y-adaptor through a Sub-D9/RJ45 converter. The pressure controller has a maximum operating pressure of 100 bar and the mass flow meter has a maximum flow throughput of 10 mln/min N₂. How to convert this unit into something representative for the gas used in the specific experiments will be explained below. The maximum allowable pressure difference over the mass flow meter is 15 bar.

Instrument control and data logging

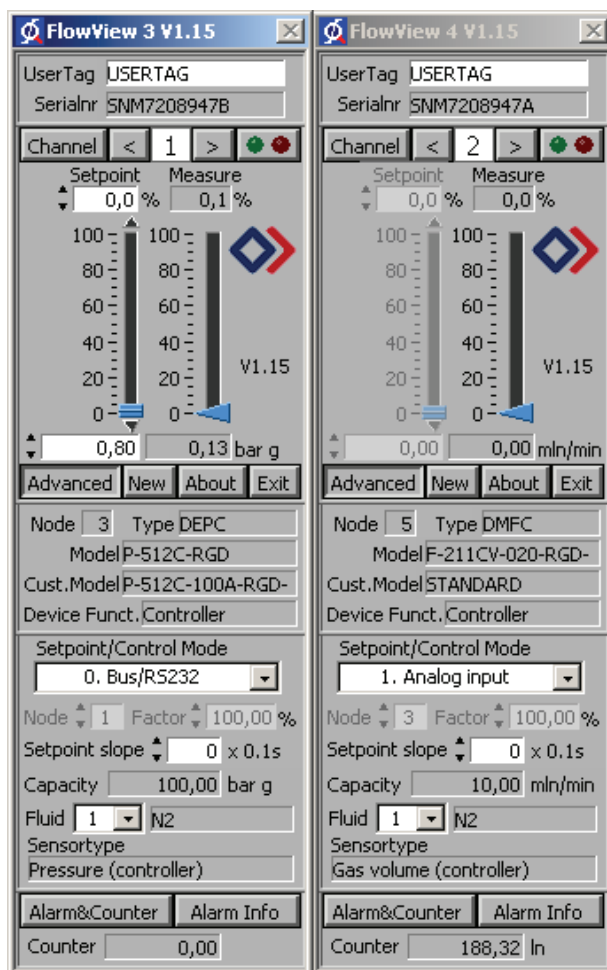
Control of the mass flow meter and the pressure controller is done using a computer on which the software provided along with the instruments has been installed. Three types of

software have to be installed on the computer namely the FlowDDE, FlowView and FlowPlot .

FlowDDE Server is a small program which assures that the communication between the instruments and FlowView and FlowPlot is maintained. By clicking the FlowDDE icon on the computer desktop → communication → open communication as illustrated on the picture below the communication between the computer and the instruments will be started.



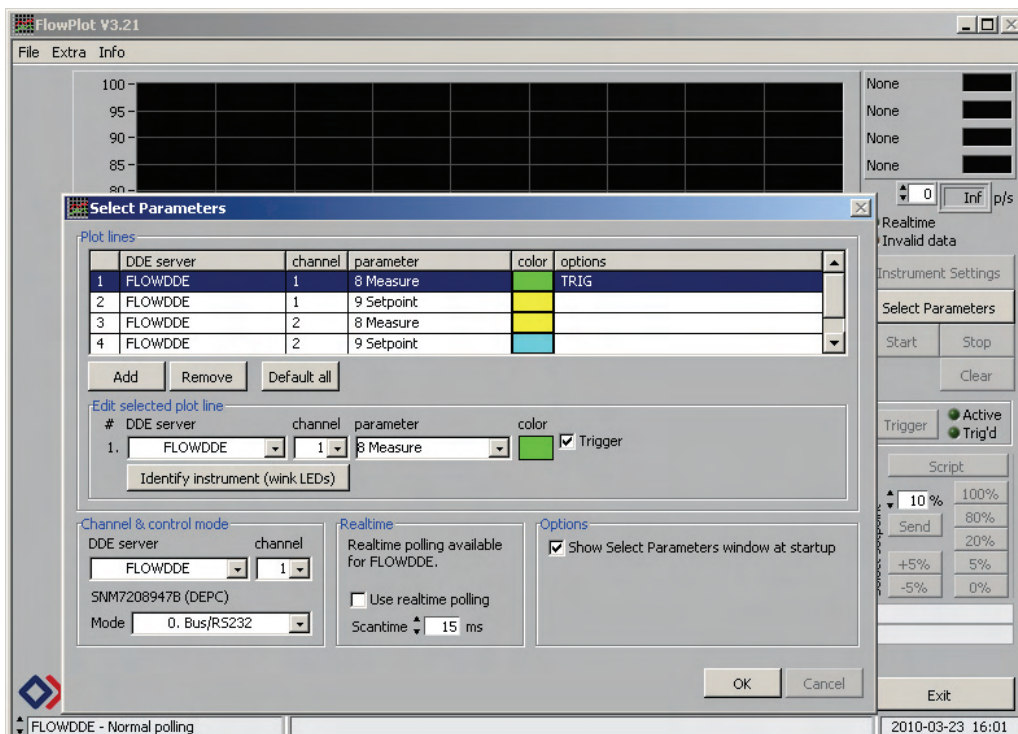
FlowView can be used to change the setpoint and read the measured value quickly. FlowView only works if the DDE-server is running. A screenshot of FlowView can be seen below.



The serial number indicates which instrument is being monitored. In this case the pressure controller communicates through channel 1 and the mass flow meter communicates through channel 2 (channel preferences can be changed in FlowPlot – see below). Currently in the picture the pressure is at atmospheric pressure i.e. there is no gas in the hydrate cell. Once gas is let in to the cell the “Measure” of channel 1 will start increasing. The setpoint pressure will specify the pressure at which the experiment is conducted. The “Setpoint” and “Measure” should always be very close to each other in a constant pressure hydrate growth experiment. The “Control Mode” of the pressure controller should be set to Bus/RD232 whereby the pressure controller will work as a “Master”.

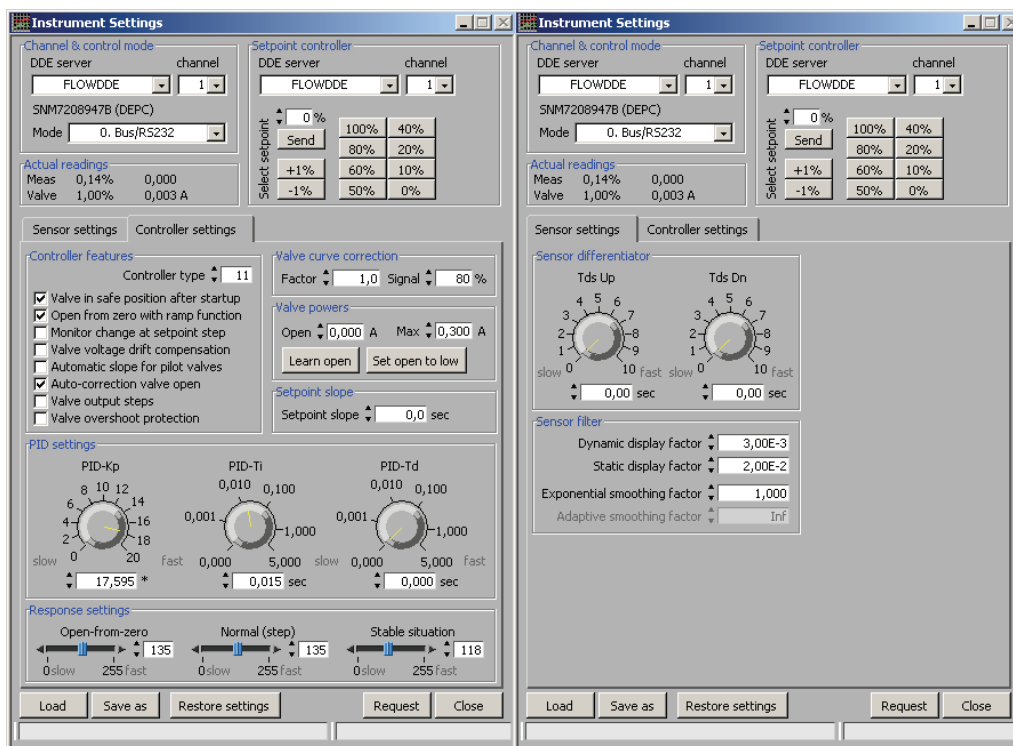
Channels 2 is the mass flow meter. The “Setpoint” of the mass flow meter will be received from the pressure controller as an analog input thus the “Control Mode” of channel 2 should be set correspondingly. In this way the mass flow meter works as a slave of the pressure controller. When the pressure in the hydrate cell starts decreasing due to hydrate formation a “Setpoint” will be sent from the pressure controller to the mass flow meter which will then open its valve in accordance with the “Setpoint” received. Other information such as the capacity of the instruments and the fluid type which the mass flow meter is calibrated to (N₂) can also be obtained from looking at FlowView.

FlowPlot is the program used to monitor the instrument signals and tune the instrument settings to provide a good of control over system. When attempting to open the program a box “Select Parameters” will immediately pop up. In this box it is possible to add and assign instruments to certain channels and also specify which parameters/output signals (Measure and Setpoint) should be displayed during the data logging. A screenshot of this is seen below.



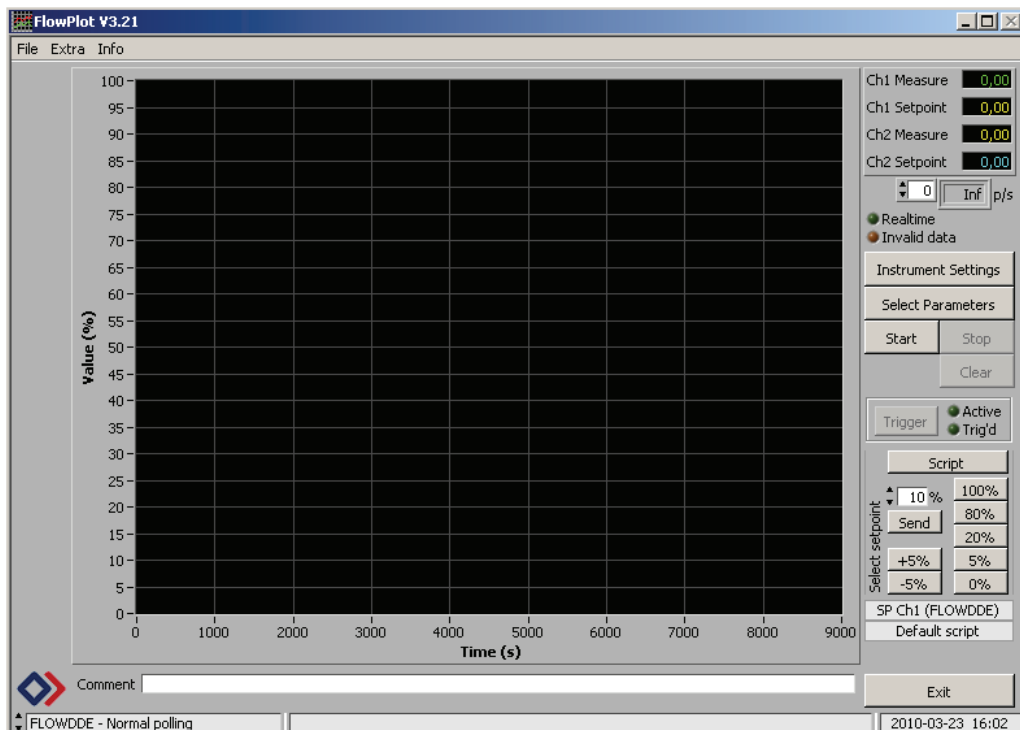
When parameters have been selected and the box has been closed it is possible to adjust the “Instrument Settings” by clicking this icon. In “Instrument Settings” it is possible to specify the optimized configuration for the instruments. For example the PID settings can be optimized to obtain a fast and stable response of the mass flow meter. In the screenshot below the settings for the pressure controller is provided. The following PID and response settings can be used for good instrument control. Note however that it might be necessary to optimize these parameters when changing experimental conditions.

Channel	Instrument	PID settings			Response settings		
		PID-Kp	PID-Ti	PID-Td	Open from zero	Normal	Stable
1	Pressure Controller	18	0.015	0	135	135	118
2	Mass flow meter	10	0.03	0	115	115	108



Once the instrument settings have been adjusted the “Instrument Settings” is closed. If the experiment is ready to start data logging can be initiated by pressing “Start”. The

output signals of the pressure controller and the mass flow meter will be logged every 5 seconds (default position). A screenshot of the FlowPlot is shown below.



Starting up an experiment

Before starting up an experiment the inside of the stainless steel cell should be carefully cleaned using ultra pure water. A magnet bar is placed in the cell and water is poured in the cell chamber and the lid is screwed on. The cooling bath is switched on and adjusted to the value at which the experiment is conducted. The setpoint temperature of the cooling bath should be around 2 K less than the temperature wanted in the cell because of heat loss. The cell can then either be evacuated using a vacuum pump or be flushed a couple of times with the gas used for the experiment. After this the cell is pressurized by by-passing the mass flow meter and pressure controller (valve 2 in closed position and valve 1 and 3 in open position) to a pressure slightly below the three-phase equilibrium pressure at the given temperature. This is to saturate the water phase with gas. After this the pressure is increased to the experimental pressure (also done by by-passing the gas).

Valve 1 and 3 are closed and valve 2 is opened. **Remember that the pressure difference over the mass flow controller must not be more than 15 bar.** The software for monitoring and controlling the instruments is opened. Before the experiment is started the mass flow meter is calibrated to the pressure provided from the gas reservoir. This is simply done by setting the “Control Mode” of channel 2 to Bus/RS232 and providing a setpoint of 50% for example. This will force the mass flow meter to open its valve and adjust to the pressure provided. After a minute the setpoint can be changed to 0 and the Control Mode changed to analog. The experiment is now ready to be started. This is done by starting the stirring and pressing start in FlowPlot.

Converting Instrument Output

The pressure output is straightforward to convert into bar. The pressure controller operates with a maximum pressure of 100 bar thus for example 20% in output corresponds to 20 bar, 50% to 50 bar and so on. It is not as straightforward to convert the output of the mass flow meter to something representative for gas used in the experiments. The mass flow meter used here is calibrated on N₂ and has a maximum capacity of 10 normal milliliters per minute (mln/min). The normal refer to standard conditions of 273.15 K and 1 atm. The following equation can be used to convert the mass flow meter output to a specific gas volume of a component *i*:

$$V_{\text{Flow}, i} = V_{\text{Measure}} \cdot \frac{C_i}{C_{\text{N}_2}}$$

where V_{Measure} is the maximum capacity of the mass flow meter times the output signal in percentage and C is a gas conversion factor. Gas conversion factors for a broad selection of gases can be found in the tables below. Consider the following example:

Mass flow meter calibrated on 10 mln/min N₂

Gas flow passing the meter is CH₄

The mass flow meter output signal is 80%

$$V_{CH_4} = \frac{80 * 10 \frac{\text{mln}}{\text{min}}}{100} \cdot \frac{0.76}{1} = 0.61 \frac{\text{mln}}{\text{min}}$$

In case a gas flow passing the mass flow meter consist of several components the following equation for calculating the mixture conversion factor can be used with good assumption:

$$\frac{1}{C_{\text{Mix}}} = \frac{V_1}{C_1} + \frac{V_2}{C_2} + \dots + \frac{V_n}{C_n}$$

where C_{Mix} is the mixture conversion factor, V_n is the volume component n in the mixture and C_n is the conversion factor of component n.

Nr.:	Name:	Symbol	Density ρ_n [g / l] 0°C, 1 atm.	Heat capacity* c_p – cal[cal / g.K] 20°C, 1 atm.	Conversion factor 20°C, 1 atm.
1	Acetylene (Ethyne)	C ₂ H ₂	1.172	0.438	0.61
2	Air	Air	1.293	0.241	1.00
3	Allene (Propadiene)	C ₃ H ₄	1.832	0.392	0.43
4	Ammonia	NH ₃	0.7693	0.524	0.77
5	Argon	Ar	1.784	0.125	1.40
6	Arsine	AsH ₃	3.524	0.133	0.66
7	Boron trichloride	BCl ₃	5.227	0.136	0.44
8	Boron trifluoride	BF ₃	3.044	0.188	0.54
9	Bromine pentafluoride	BrF ₅	7.803	0.156	0.26
10	Butadiene (1,3-)	C ₄ H ₆	2.504	0.405	0.31
11	Butane	C ₄ H ₁₀	2.705	0.457	0.25
12	Butene (1-)	C ₄ H ₈	2.581	0.415	0.29
13	Butene (2-) (Cis)	C ₄ H ₈	2.503	0.387	0.32
14	Butene (2-) (Trans)	C ₄ H ₈	2.503	0.421	0.30
15	Carbonylfluoride	COF ₂	2.983	0.194	0.54
16	Carbonylsulfide	COS	2.724	0.175	0.65
17	Carbon dioxide	CO ₂	1.977	0.213	0.74
18	Carbon disulfide	CS ₂	3.397	0.152	0.60
19	Carbon monoxide	CO	1.25	0.249	1.00
20	Chlorine	Cl ₂	3.218	0.118	0.82
21	Chlorine trifluoride	ClF ₃	4.125	0.188	0.40
22	Cyanogen	C ₂ N ₂	2.376	0.275	0.48
23	Cyanogen chloride	ClCN	2.743	0.185	0.61
24	Cyclopropane	C ₃ H ₆	1.919	0.374	0.43
25	Deuterium	D ₂	0.1798	1.73	1.00
26	Diborane	B ₂ H ₆	1.248	0.577	0.43
27	Dibromo difluoromethane	Br ₂ CF ₂	9.361	0.17	0.20
28	Dichlorosilane	SiH ₂ Cl ₂	4.506	0.17	0.41
29	Dimethylamine	C ₂ H ₇ NH	2.011	0.417	0.37
30	Dimethylpropane (2,2-)	C ₅ H ₁₂	3.219	0.462	0.21
31	Dimethylether	C ₂ H ₆ O	2.105	0.378	0.39
32	Disilane	Si ₂ H ₆	2.857	0.352	0.31
33	Ethane	C ₂ H ₆	1.355	0.468	0.49
34	Ethylene (Ethyne)	C ₂ H ₄	1.261	0.414	0.60
35	Ethylene oxide	C ₂ H ₄ O	1.965	0.303	0.52
36	Ethylacetylene (1-Butyne)	C ₄ H ₆	2.413	0.401	0.32
37	Ethylchloride	C ₂ H ₅ Cl	2.878	0.263	0.41
38	Fluorine	F ₂	1.696	0.201	0.91
39	Freon-11	CCl ₃ F	6.129	0.145	0.35
40	Freon-113	C ₂ Cl ₃ F ₃	8.36	0.174	0.21
41	Freon-1132A	C ₂ H ₂ F ₂	2.889	0.244	0.44
42	Freon-114	C ₂ Cl ₂ F ₂	7.626	0.177	0.23
43	Freon-115	C ₂ ClF ₅	7.092	0.182	0.24
44	Freon-116	C ₂ F ₆	6.251	0.2	0.25
45	Freon-12	CCl ₂ F ₂	5.547	0.153	0.37
46	Freon-13	CClF ₃	4.72	0.165	0.40
47	Freon-13B1	CBrF ₃	6.768	0.12	0.38
48	Freon-14	CF ₄	3.946	0.18	0.44
49	Freon-21	CHCl ₂ F	4.592	0.154	0.44
50	Freon-22	CHClF ₂	3.936	0.168	0.47
51	Freon-23	CHF ₃	3.156	0.191	0.52
52	Freon-C318	C ₄ F ₈	9.372	0.222	0.15
53	Germane	GeH ₄	3.45	0.16	0.56

Nr.:	Name:	Symbol	Density ρ_n [g / l] 0°C, 1 atm.	Heat capacity* c_p – cal[cal / g.K] 20°C, 1atm.	Conversion factor 20°C, 1atm.
54	Helium	He	0.1785	1.24	1.41
55	Helium (3-)	3He	0.1346	1.606	1.44
56	Hydrogen	H ₂	0.08991	3.44	1.01
57	Hydrogen bromide	HBr	3.646	0.0869	0.98
58	Hydrogen chloride	HCl	1.639	0.192	0.99
59	Hydrogen cyanide	HCN	1.206	0.345	0.75
60	Hydrogen fluoride	HF	0.8926	0.362	0.96
61	Hydrogen iodide	HI	5.799	0.0553	0.97
62	Hydrogen selenide	H ₂ Se	3.663	0.109	0.78
63	Hydrogen sulfide	H ₂ S	1.536	0.246	0.82
64	Isobutane	C ₄ H ₁₀	2.693	0.457	0.25
65	Isobutylene (Isobutene)	C ₄ H ₈	2.60	0.429	0.28
66	Krypton	Kr	3.749	0.058	1.43
67	Methane	CH ₄	0.7175	0.568	0.76
68	Methylacetylene	C ₃ H ₄	1.83	0.399	0.43
69	Methylbromide	CH ₃ Br	4.35	0.118	0.61
70	Methylchloride	CH ₃ Cl	2.3	0.212	0.64
71	Methylfluoride	CH ₃ F	1.534	0.29	0.70
72	Methylmercaptan	CH ₃ SH	2.146	0.272	0.53
73	Molybdenum hexafluoride	MoF ₆	9.366	0.156	0.21
74	Mono-ethylamine	C ₂ H ₅ NH ₂	2.011	0.436	0.36
75	Monomethylamine	CH ₃ NH ₂	1.419	0.424	0.52
76	Neon	Ne	0.9002	0.246	1.41
77	Nitric oxide	NO	1.34	0.239	0.97
78	Nitrogen	N ₂	1.250	0.249	1.00
79	Nitrogen dioxide	NO ₂	2.053	0.204	0.74
80	Nitrogen trifluoride	NF ₃	3.182	0.194	0.50
81	Nitrosyl chloride	NOCl	2.984	0.17	0.61
82	Nitrous oxide	N ₂ O	1.978	0.221	0.71
83	Oxygen	O ₂	1.429	0.222	0.98
84	Oxygen difluoride	OF ₂	2.417	0.201	0.64
85	Ozone	O ₃	2.154	0.207	0.70
86	Pentane	C ₅ H ₁₂	3.219	0.455	0.21
87	Perchlorylfluoride	ClO ₂ F	4.653	0.165	0.41
88	Perfluoropropane	C ₃ F ₈	8.662	0.22	0.16
89	Performa- ethylene	C ₂ F ₄	4.523	0.206	0.33
90	Phosgene	COCl ₂	4.413	0.149	0.47
91	Phosphine	PH ₃	1.53	0.277	0.73
92	Phosphorus pentafluoride	PF ₅	5.694	0.183	0.30
93	Propane	C ₃ H ₈	2.012	0.456	0.34
94	Propylene (Propene)	C ₃ H ₆	1.915	0.408	0.40
95	Silane	SiH ₄	1.443	0.349	0.62
96	Silicon tetrafluoride	SiF ₄	4.683	0.18	0.37
97	Sulfuryl fluoride	SO ₂ F ₂	4.631	0.175	0.38
98	Sulfur dioxide	SO ₂	2.922	0.157	0.68
99	Sulfur hexafluoride	SF ₆	6.626	0.175	0.27
100	Sulfur tetrafluoride	SF ₄	4.821	0.192	0.34
101	Trichlorosilane	SiHCl ₃	6.044	0.157	0.33
102	Trimethylamine	C ₃ H ₉ N	2.637	0.424	0.28
103	Tungsten hexafluoride	WF ₆	13.29	0.092	0.25
104	Vinylbromide	C ₂ H ₃ Br	4.772	0.141	0.46
105	Vinylchloride	C ₂ H ₃ Cl	2.865	0.229	0.47
106	Vinylfluoride	C ₂ H ₃ F	2.08	0.305	0.49
107	Xenon	Xe	5.899	0.0382	1.38

Appendix V

MCHydrate: Monte Carlo simulation of clathrate hydrates

MCHydrate is a Monte Carlo based program with capabilities of simulating fluid and solid phases. For the fluid phase, the density, chemical potential, energy, and enthalpy values are averaged in a simulation for a number of different components. In the solid phase, the Gibbs free energy is calculated along with the lattice parameter value, energy, and enthalpy. These properties are available for ice (Ic and Ih) and hydrate (structures - sI, sII, and sH). Nonstoichiometric hydrate occupation number is calculated as a function of chemical potential. A comparison of the simulation value is made with three different versions of the van der Waals and Platteeuw theory. Fluctuation properties, including heat capacity, thermal expansivity and isothermal compressibility of the fluid and solid phases are also calculated.

The input file (State.dat)

Line (1): The type of simulation will direct the simulation to a particular methodology. The code is broken into three sections, a) solid phase properties excluding Gibbs free energy, b) Gibbs free energy calculation of a solid, and c) chemical potential of a fluid (multi component systems included).

Line (2): The lattice type directs the simulation to a starting configuration.

Line (3): The long range corrections (LRC) and cross-interactions are specified in line 3. The code handles possibilities such as no LRC, Ewald corrections for charge-charge interactions, LSM for Lennard-Jones terms, and an integration approach by assuming $g=1$ (typically used in a fluid).

Line (4): The simulation is capable of starting from preset coordinates or coordinates after a number of simulation cycles. The simulation also can restart averaging or continue averaging in the event the code is halted.

Line (5): The pressure in bar.

Line (6): The temperature in Kelvin.

Line (7): A character of length 3 in which the run output is saved to.

Line (8): A character of length 2 in which the series output is saved to.

Line (9): The number of cycles that are required to relax the initial coordinates.

Line (10): The number of cycles that are required to produce the final averages.

Line (11-13): The number of unit cells in the x, y, and z directions, respectively. In a fluid, only one cell in each direction is needed.

Line (14-16): For special cases the length of the cells can be specified. The length is the total length of the simulation box. As an example if the x-direction length of the 2 unit cell structure I hydrate is 22 Angstroms, we reference this to 3 Angstroms. The value in the input file will be 7.33333 for the length and 2 from the number of boxes.

Line (17): Total number of molecules in system.

Line (18): Interface only: specifies the density of fluid at solid interface.

Line (19): Interface only: specifies the fraction of the slab being hydrate z dir

Line (20): Specifies the number of different components. In the solid phase a maximum of 6 components can be specified including water. In the fluid phase a maximum of 3 components can be specified.

Line (21): Specifies the molecular types. One special case, in a double hydrate the sequence should be water, small guest, large guest.

Line (22): Specifies the chemical potential for a nonstoichiometric hydrate. The first number should be kept at zero. This is for water and will not play into the simulation. The order should correspond to the definition of the molecular type. The chemical potential is reduced by 4 kcal/mol.

Line (23): The mole fractions are specified only for the fluid phase. All other mole fractions will be calculated based on simulation type and in the nonstoichiometric hydrate, the chemical potential.

In the table below an example of the input file for MCHydrate is shown. The placement of the number is not important. Integers are specified in the example without a decimal, otherwise they are floating points.

7							Simulation type
2							Lattice type
1							Periodic and interaction type
0							Trigger to restart
1.00000							Pressure -Bar
240.00000							Temperature -Kelvin
004							Run Number
a0							Series Number
1000							Number of relaxation cycles
5000							Number of production cycles
100							Number of cycles in a block ave
1							Number of cells in the x dir
1							Number of cells in the y dir
1							Number of cells in the z dir
3.93000							Cell length in the x direction
3.93000							Cell length in the y direction
3.93000							Cell length in the z direction
54							Number of molecules in system
0.00000							Density of fluid reduce
0.00000							Frac. hydrate in slab
2							Number of molecule type
6	11	0	0	0	0	Molecule types	
0.00000	0.00000	0.00000	0.00000	0.00000	0.00000	Chemical potentials	
0.851852	0.148148	0.00000	0.00000	0.00000	0.00000	Mole fractions	

Ensembles and property calculations - line 1 in input file

- (1) NVT (Canonical Ensemble).
- (2) NPT (Isothermal -Isobaric Ensemble) Box Length in x-y-z adjusted the same.
- (3) NPT (Isothermal -Isobaric Ensemble) Rahman-Parrinello simulation.
- (4) Semigrand simulation fixed chemical potential-VT.
- (5) Semigrand simulation fixed chemical potential-PT Box Length in x-y-z adjusted the same.
- (6) Semigrand simulation fixed chemical potential-PT Rahman-Parrinello simulation.
- (7) Gibbs Free Energy calculation. Thermodynamic integration from Einstein Crystal.
- (8) NPT chemical potential calculation.
- (9) NVT chemical potential calculation.

When the options are set to negative values, the reduced box lengths are user inputs.

Original free energy calculation – Frenkel, D, Ladd A.J.C., New Monte Carlo method to compute the free energy of arbitrary solids. Application to the fcc and hcp phases of hard spheres *Journal of chemical physics*, 81, 1984, 3188.

Free energies for solids with orientational contributions – Vega, C, Paras, E.P.A., Monson,

P.A., Solid-fluid equilibrium for hard dumbbells via Monte Carlo simulation, *Journal of chemical physics*, 96, 1992, 9060.

Free energies for a water model - Vega, C, Monson, P.A., Solid-fluid equilibrium for a molecular model with short ranged directional forces, *Journal of chemical physics*, 109, 1998, 9938.

Finite size corrections - Polson J.M, Trizac, E, Pronk, S, Frenkel, D., Finite-size corrections to the free energies of crystalline solids, *Journal of chemical physics*, 112, 2000, 5339.

Residual entropy of ice - Pauling, L, *The Structure and Entropy of Ice and of Other Crystals with Some Randomness of Atomic Arrangement*, *JACS*, 57, 1935, 2680.

Wu, D., Kofke, D.A., Phase-space overlap measures. I. Fail-safe bias detection in free energies calculated by molecular simulation, *Journal of chemical physics*, 123, 2005, 054103.

Wu, D., Kofke, D.A., Phase-space overlap measures. II. Design and implementation of staging methods for free energy calculations, *Journal of chemical physics*, 123, 2005, 084109.

Lu, N., Singh, J.K., Kofke, D.A., Appropriate methods to combine forward and reverse free-energy perturbation averages, 118, 2003, 2977.

Parrinello, M., Rahman, A., Crystal Structure and Pair Potentials: A Molecular-Dynamics Study, *Phys. Rev. Lett.*, 45, 1980, 1196.

Parrinello, M., Rahman, A., Polymorphic transitions in single crystals: A new molecular dynamics method, *J. Appl. Phys.*, 52, 1981, 7182.

A. NVT - Option (1)

A Monte Carlo canonical ensemble (NVT) simulation consists of a fixed volume, displacement moves and rotation moves. Option 1 is for a solid phase.

B. NPT - Option (2) and (3)

A Monte Carlo isothermal-isobaric ensemble (NPT) simulation consists of a varying volume, displacement moves and rotation moves. Option 2 is a simulation where the lengths of x-y-z are varied with equal distance $dx=dy=dz$. Option 3 is a simulation where the length x, y, and z are varied each with different dx, dy, and dz.

C. Semigrand ensemble - Option (4), (5), and (6)

A semigrand ensemble consists of rotation moves, displacement moves, insertion moves, deletion moves, and volume moves for an isobaric system. Option 4 is a semigrand simulation with constant volume. Option 5 is a semigrand simulation with varying volume of the type $dx=dy=dz$. Option 6 is a semigrand simulation with varying volume with different dx, dy, and dz. The chemical potential must be specified.

D. Solid free energy - Option (7)

Solid free energies, option 7, are found through a thermodynamic integration from an Einstein crystal. The simulation steps through a number of spring constants and then

integrates the results with Gauss-Legendre integration. Only displacement moves and rotation moves are performed.

E. Fluid chemical potential - Option (8) and (9)

Option 8 and 9 perform chemical potential calculation on a fluid. Option 8 is an isothermal-isobaric simulation. Option 9 is a canonical ensemble simulation. Three methodologies are used, Widom insertions, overlap distributions, and Bennett's method. The method consists of a fluid fixed at a given composition, and for each component they are inserted in one stage and then deleted in another. 3 components leads to 4 staged simulation, one to insert each molecule, and 3 to delete N+1 molecules.

Initial configurations and lattice types – line 2

- (1) sI- no guest molecules
- (2) sI- S and L filled- one guests
- (3) sI- S and L filled- two guests
- (4) sI- L filled- one guest
- (5) sI(rigid lat.)-S and L filled- one guests
- (6) sI(rigid lat.)-S and L filled- two guests
- (7) sI(rigid lat.)-L filled- one guest
- (8) sII- no guest molecules
- (9) sII- S and L filled- one guests
- (10) sII- S and L filled- two guests
- (11) sII- L filled- one guest
- (12) sII(rigid lat.)-S and L filled- one guests
- (13) sII(rigid lat.)-S and L filled- two guests
- (14) sII(rigid lat.)-L filled- one guest
- (15) sH- no guest molecules
- (16) sH- S and L filled- two guests
- (17) sH(rigid lat.)-S and L filled- two guests
- (18) Ice H
- (19) Ice C
- (20) Fluid - Liquid FCC initial config.

- (21) Fluid - Vapor FCC initial config.
 - (22) Interface sI- S and L filled- one guest
 - (23) Interface sII- L filled- one guest
 - (24) Interface sII- S and L filled- two guests
- See code output for crystal structures.
- S - small cage
 - M - medium cage
 - L - large cage

Option (5)-(7) and (12) - (14): The simulation type must be at fixed volume. Useful when a rigid water lattice is needed to compare with predictions of hydrate occupancies found from the vdWP theory. Option (18)-(19): The simulation of ice. Option (20): The simulation of a fluid phase of specified composition. Option (21)-(23): Interface simulations – not yet implemented.

Long range corrections and mixing rules - Line 3

A. Options

Two mixing rule are applied here. In option (0) - (2), and Option (6), geometric combining

rules are used. In option (3) - (5), and option (7), arithmetic combining rules are used.

- (0) no ewald summation, use A-C
- (1) ewald sum on qq and lattice sum method (LSM) on A-C
- (2) ewald sum on qq only, use A-C
- (3) no ewald summation, use LJ
- (4) ewald sum on qq and lattice sum method (LSM) on LJ
- (5) ewald sum on qq only, use LJ
- (6) ewald sum on qq only, use A-C, $g=1$
- (7) ewald sum on qq only, use LJ, $g=1$

B. Lennard Jones potential mixing rules

Geometric combination rules, use A-C:

$$u(r_{ij}) = 4\sqrt{\varepsilon_i \varepsilon_j} \left(\left[\frac{\sqrt{\sigma_i \sigma_j}}{r_{ij}} \right]^{12} - \left[\frac{\sqrt{\sigma_i \sigma_j}}{r_{ij}} \right]^6 \right)$$

Arithmetic combination rules LJ:

$$u(r_{ij}) = 4\sqrt{\varepsilon_i \varepsilon_j} \left(\left[\frac{\sigma_i \sigma_j}{2r_{ij}} \right]^{12} - \left[\frac{\sigma_i \sigma_j}{2r_{ij}} \right]^6 \right)$$

Implementing Arithmetic combination rules LJ:

$$u(r_{ij}) = 4\sqrt{\varepsilon_i \varepsilon_j} \left(\left[\frac{\sigma_i \sigma_j}{2r_{ij}} \right]^{12} \right) - \lambda_{ij}$$

$$\lambda_{ij} = - \left(\frac{1}{2^6} \right) \sum_{k=0}^6 \frac{6!}{k!(6-k)!} \lambda_{k,i} \lambda_{6-k,j}$$

$$\lambda_{k,i} = 2\varepsilon_i^{1/2} \sigma_i^k$$

Lopez-Lemus J, Alejandro J, Mol. Phys., 101, 743-751 (2003).

C. Long-range corrections

Option (0): Geometric combining rules with no long range correction.

Option (1): Geometric combining rules with Ewald sum on charges and lattice sum on the Lennard Jones term.

Option (2): Geometric combining rules with Ewald sum on charges.

Option (3): Arithmetic combining rules with no long range correction.

Option (4): Arithmetic combining rules with Ewald sum on charges and lattice sum on the Lennard Jones term.

Option (5): Arithmetic combining rules with Ewald sum on charges.

Option (6) and (7): Ewald summation is used on the charge interactions. Long range correction on Lennard Jones term is dealt with through an integral. See Frenkel and Smit,

$$u^{tail} = 2\pi\rho \int_{r_c}^{\infty} u(r)r^2 dr$$

Molecular species - Line 18

- (1) Water SPC
- (2) Water SPCE
- (3) Water TIP4P
- (4) Water TIP4P-EW
- (5) Water TIP4P/2005
- (6) Water TIP4P/ICE
- (11) Methane 1-site (Jorgensen)
- (12) Methane 5-site (Siepmann)
- (13) Methane 5-site (Tse)
- (14) Ethane 1-site (Hirschfelder)
- (13) Ethane 3-site (Jorgensen)
- (16) Ethane 9-sites (Siepmann)
- (17) Propane 1-site (Hirschfelder)
- (18) Propane 3-sites (Jorgensen)
- (19) Helium 1-site (Hirschfelder)
- (20) Neon 1-site (Hirschfelder)
- (21) Argon 1-site (Zeile)
- (22) Krypton 1-site (Zeile)
- (23) Xenon 1-site (Pashek)
- (24) Hydrogen 1-site (Hirschfelder)
- (25) Hydrogen 3-sites (Alavi)
- (26) EO - UA 4-sites (Wielpolski)
- (27) EO - AA 8-sites (Mountain)
- (28) TMO- UA 5-sites (In-house)
- (29) TMO- AA 8-sites (In-house)
- (30) THF- UA 5-sites (Girard)

- (31) THF- AA 14-sites (Alavi)
- (32) THP- UA 7-sites (In-house)
- (33) THP- AA 17-sites (In-house)
- (34) CO₂ 3-sites (Jorgensen)
- (35) MCH 1-site (Prausnitz)
- (36) Na⁺ 1-site (Smith)
- (37) Cl⁻ 1-site (Smith)
- (38) C₅H₁₀ 5-site (Martin)
- (39) C₆H₁₄ 6-site (Martin)

A. Water molecular models

- (1) SPC Water Ref: Berendsen, HJC, Postma, JPM, von Gunster, WF, Hermans, J Intermolecular Forces, Pullman, B, Ed. (1981).
- (2) SPCE Water Berendsen, HJC, Grigera, JR, Straatsma, TP JPC, 91, 6269 (1987).
- (3) TIP4P Water Jorgensen, WL, Chandrasekhar, JD, Madura, RW, Impey, RW, Klein, ML, JCP, 79, 926 (1983).
- (4) TIP4P-EW Water Horn, HW, et al., JCP, 120, 9665 (2005).
- (5) TIP4P/2005 Water Abascal, JLK, Vega, C, JCP, 123, 234505 (2005).
- (6) TIP4P/ICE Water Abascal, JLF, Sanz, E, Fernandez, G, Vega, C JCP, 122, 234511 (2005).

B. Guest molecular models

- (11) Methane United atom: 1-site Jorgensen, WL, JACS, 103, 335-340 (1981)
Siepmann, JI, Martin, MG, JPCB, 102, 2569 (1998).
- (12) Methane All atom: 5-sites Chen, B, Siepmann, JI, JPCB, 1003, 5370 (1999).
- (13) Methane All-atom: 5-sites Tse, Klein, MacDonald, JCP, 81, 6146.
- (14) Ethane United-atom: 1-site Hirschfelder, JO, Curtiss, CF, Bird, RB Molecular Theory of Gases and Liquids John Wiley, NY (1954).
- (15) Ethane United-atom: 3-sites Jorgensen, WL, JACS, 103, 335 (1981).
- (16) Ethane All-atom: 9-sites Chen, B, Siepmann, JI, JPCB, 103, 5370 (1999).
- (17) Propane United-atom: 1-site Hirschfelder, JO, Curtiss, CF, Bird, RB Molecular Theory of Gases and Liquids John Wiley, NY (1954).

- (18) Propane United-atom: 3-sites Jorgensen, WL, JACS, 103, 335 (1981).
- (19) Helium: 1-site Hirschfelder, JO, Curtiss, CF, Bird, RB Molecular Theory of Gases and Liquids John Wiley, NY (1954).
- (20) Neon: 1-site Hirschfelder, JO, Curtiss, CF, Bird, RB Molecular Theory of Gases and Liquids John Wiley, NY (1954).
- (21) Argon: 1-site Zele, SR, Lee, SY, Holder, GD JPCB, 103, 10250 (1999).
- (22) Krypton: 1-site Zele, SR, Lee, SY, Holder, GD JPCB, 103, 10250 (1999).
- (23) Xenon: 1-site Pashek, D, JCP, 120, 6674.
- (24) Hydrogen: 1-site Hirschfelder, JO, Curtiss, CF, Bird, RB Molecular Theory of Gases and Liquids John Wiley, NY (1954).
- (25) Hydrogen: 3-sites Alavi, S, Ripmeester, JA, Klug, DD JCP, 123, 024507 (2005)
- (26) Ethylene oxide United-atom: 4-sites Wielopolski, PA, Smith, ER Mol. Phys, 54, 467 (1985).
- (27) Ethylene oxide All-atom: 8-sites Mountain, RD, JPCB, 109, 13353 (2005).
- (28) Trimethylene oxide United-atom: 5 sites In-house potential Geometry from <http://srdata.nist.gov/cccbdb> MP2FC/6-311G** LJ parameters CH₂O from: Wielopolski, PA, Smith, ER Mol. Phys, 54, 467 (1985) Charges from expt dipole - 1.94 D.
- (29) Trimethylene oxide All-atom: 11 sites In-house potential Geometry from <http://srdata.nist.gov/cccbdb> MP2FC/6-311G** LJ parameters C,O,H from: Mountain, RD, JPCB, 109, 13353 (2005) Charges from expt dipole - 1.94 D.
- (30) Tetrahydrofuran United-atom: 5-sites Zhao, X, Leng, Y, Cummings, PT Langmuir, 22,4116 (2006) Girard, S;Muller-Plathe,F,Mol. Phys.,101,779 Geometry from <http://srdata.nist.gov/cccbdb> HF.6-31G**.
- (31) Tetrahydrofuran All-atom: 14-sites Alavi, S, Ripmeester, JA, Klug, DD JCP, 123, 024507 (2005) Geometry from <http://srdata.nist.gov/cccbdb> HF.6-31G**.
- (32) Tetrahydropyran United-atom: 7 sites In-house potential Geometry from <http://srdata.nist.gov/cccbdb> MP2FC/6-311G** LJ parameters CH₂O from: Girard, S; Muller-Plathe,F, Mol. Phys., 101, 779 Charges from expt dipole - 1.58 D.
- (33) Tetrahydropyran All-atom: 11 sites In-house potential Geometry from

<http://srdata.nist.gov/cccbdb> MP2FC/6-311G** LJ parameters C,O,H from: Alavi, S, Ripmeester, JA, Klug, DD JCP, 123, 024507 (2005) Charges from expt dipole - 1.94 D.

(34) Carbon dioxide: 3 sites Jorgensen, WL; JACS, 103, 335-340 (1981).

(35) Methylcyclohexane: 1-site Reid, RC; Prausnitz, JM; The Properties of Gases and Liquids (Prentice Hall, NJ, 1987).

(36) Sodium ion : 1-site Smith DE, Dang, LX, JCP, 100, 3757 (1994).

(37) Chlorine ion : 1-site Smith DE, Dang, LX, JCP, 100, 3757 (1994).

(38) Cyclopentane : 5-site Geometry from <http://srdata.nist.gov/cccbdb> MP2FC/6-311G** Martin, MG, Siepmann, JI 102, 2569 (1998).

(39) Hexane : 6-site Geometry from <http://srdata.nist.gov/cccbdb> MP2FC/6-311G** Martin, MG, Siepmann, JI 102, 2569 (1998).

The iofile.f

In the iofile.f (input/output file) it is possible to change a large number of input parameters used in the simulation. However one should be very careful when modifying this file. The cutoff radius used in the simulations is specified in this file and can be changed here if necessary. The default value is 10 Å.

Another useful feature in the iofile is that it allows switching on and of the vdWP module. The vdWP module when running semigrand ensemble simulations will calculate the occupancy of the hydrate according to the vdWP theory which can then be compared to those found from simulation. The vdWP module can be switched on by setting `icgrev = 1`. It should only be switched on if the results are really of interest since it is computationally quite heavy. If a cage analysis (splits the occupancy into small and large) in connection with the vdWP study is necessary the semigrand simulation should simply be started from a fully occupied hydrate which by default will set `icagestudy = 10` and `icgst = 1`. Otherwise these can also be set in the iofile.

Compilation

It is possible to compile the program by running “`compile.cmd`” which will create an executable file which along with the state file will run a given simulation. By default the

executable file created is named "mchhydrate" however this is easily changed in "compile.cmd".

Center for Energy Resources Engineering
Department of Chemical and
Biochemical Engineering
Technical University of Denmark
Søltofts Plads, Building 229
DK-2800 Kgs. Lyngby
Denmark

Phone: +45 4525 2800
Fax: +45 4525 4588
Web: www.kt.dtu.dk

ISBN : 978-87-92481-29-0